

MINISTRY OF EDUCATION AND TRAINING
HCMC UNIVERSITY OF TECHNOLOGY AND EDUCATION

VAN-THIEN TRAN

**DEVELOPMENT OF STOCHASTIC COMPOSITE PLATE
MODELS SUBJECTED TO MECHANICAL
AND THERMAL LOADS**

**DOCTORAL DISSERTATION OF
ENGINEERING MECHANICS**

Ho Chi Minh City, 7/2025

MINISTRY OF EDUCATION AND TRAINING
HCMC UNIVERSITY OF TECHNOLOGY AND EDUCATION

VAN-THIEN TRAN

**DEVELOPMENT OF STOCHASTIC COMPOSITE PLATE
MODELS SUBJECTED TO MECHANICAL
AND THERMAL LOADS**

MAJOR: ENGINEERING MECHANICS - 9520101

Supervisor 1: Prof. Dr. Trung-Kien Nguyen

Supervisor 2: Dr. Van-Hau Nguyen

Ho Chi Minh City, 7/2025

LÝ LỊCH CÁ NHÂN

I. LÝ LỊCH SƠ LƯỢC

Họ và tên: Trần Văn Thiên

Giới tính: Nam

Ngày, tháng, năm sinh: 25/04/1992

Nơi sinh: Bình Định

Quê quán: Hoài Nhơn đông – Gia Lai

Dân tộc: Kinh

Địa chỉ: 11.13 Block A, Khu căn hộ Bcons Garden, 25A Phạm Hữu Lầu, khu phố
Thống Nhất 1, phường Dĩ An, Tp. Hồ Chí Minh.

Điện thoại: 0932847629

Email: thientv@hcmute.edu.vn

Đơn vị công tác: Trường Đại học Sư phạm Kỹ thuật Tp. Hồ Chí Minh

Địa chỉ cơ quan: 01 Võ Văn Ngân, Phường Thủ Đức, Tp. Hồ Chí Minh.

II. QUÁ TRÌNH ĐÀO TẠO

- 2011-2015: Sinh viên ngành Công nghệ kỹ thuật công trình xây dựng, Trường Đại học Sư phạm Kỹ thuật Tp. Hồ Chí Minh.
- 2016-2018: Học viên cao học ngành Công nghệ kỹ thuật công trình xây dựng, Trường Đại học Sư phạm Kỹ thuật Tp. Hồ Chí Minh.
- Từ 2020 đến nay: Nghiên cứu sinh ngành Cơ kỹ thuật, Trường Đại học Sư phạm Kỹ thuật Tp. Hồ Chí Minh.

III. QUÁ TRÌNH CÔNG TÁC

- Từ 4/2021 đến nay làm việc tại bộ môn Kết cấu công trình, Khoa Xây dựng, Trường Đại học Sư phạm Kỹ thuật Tp. Hồ Chí Minh.

Tp. Hồ Chí Minh, ngày tháng 01 năm 2025



Trần Văn Thiên

DECLARATION

I certify that this thesis is entirely the result of my efforts, following the direction of Professor Trung-Kien Nguyen and Dr. Van-Hau Nguyen.

The content presented in this thesis has not been previously submitted for any other award.

Name: Van-Thien Tran

Signature:

A handwritten signature in black ink, consisting of a stylized 'V' followed by a series of loops and a long horizontal stroke.

ACKNOWLEDGEMENT

I sincerely appreciate my advisor, Professor Trung-Kien Nguyen from HUTECH University, for his invaluable guidance, insightful suggestions, and unwavering support throughout my study. His influence on my career has been significant, as he has provided advice and mentorship in cultivating a strong work ethic and a sense of responsibility. Additionally, he has imparted valuable research skills essential for excelling as a researcher. The successful completion of this project would not have been feasible without the invaluable contributions of his meticulous guidance, constructive feedback, unwavering support, and enduring patience.

I sincerely thank Dr. Van-Hau Nguyen from the HCMC University of Technology and Education for generously dedicating a significant amount of time to engaging in fruitful discussions and offering valuable alternative perspectives on my ideas.

I want to convey my sincere gratitude to my colleagues in the research process. Their intellectual contributions, camaraderie, and nurturing atmosphere have been invaluable to me.

Lastly, I extend my profound gratitude to my family and wife for their unwavering encouragement and support throughout my academic pursuits. Their absence would have rendered this work unattainable.

Van-Thien Tran



ABSTRACT

Due to their superior hardness and lightness, laminated composite materials are widely utilized in fields like mechanical engineering, aerospace, and construction. However, their layered structure leads to stress concentrations and potential delamination at the interfaces. Thus, functionally graded materials (FGMs) have been developed to address this, offering a continuous variation in material properties along specific directions. FGMs excel in thermal resistance, corrosion resistance, and toughness, providing unique properties beyond those of their components. Recent advancements have also enabled the production of functionally graded porous materials and porous metal foam materials, which enhance sound dampening and reduce structural weight, making them highly valuable for modern applications. However, the development of such materials accompanied efficiently computational methods and models in order to predict accurately their responses at different structural scales. Therefore, this dissertation carried out the development of stochastic composite plate models subjected to mechanical load and thermal buckling. For this aim, the following main research topics have been studied in the thesis:

Firstly, this thesis utilized the Ritz method's orthogonal polynomial to generate shape functions as the hybrid function. It was built by combining a polynomial with a series of orthogonal polynomial functions such as the Hermite and Laguerre polynomials. Besides, orthogonal polynomials (OP) were also created using the Gram-Schmidt orthogonalization process. Shape functions were designed to fulfill the necessary boundary conditions. Therefore, the thesis proposed new computational algorithms, which combined the Ritz method with novels OP, unified higher-order shear deformation plate theory (HSDT), the modified couple stress (MCT), and the modified gradient strain (MST) theory for analysis of microplates. Based on the findings of this study, the OP-Ritz shape functions proposed in this thesis are suitable for the behaviors analysis of microplates. There is an important

difference in the behaviors of microplates derived from the MST and MCT for the MLSP-to-thickness ratio. This showed that the MST was good at catching the size effects of microplates.

Secondly, the practical application of materials is subject to various unforeseen factors that can significantly influence and modify their properties, thereby resulting in alterations to their static and dynamic behaviors. Hence, in order to deal with the above challenges, this study developed stochastic models (the polynomial chaos expansion (PCE) and Stochastic collocation (SC)) to examine the behaviors of microplates with uncertain material properties. In which, PCE speeds up the computing process while still maintains the accuracy. The key idea of this technique is to approximate random outputs as a series of basis functions and their corresponding coefficients in orthogonal space. SC is known as one of the stochastic expansion methods similar to the popular PCE. It derives the Lagrange interpolation polynomials for a set of collocation points and reproduces the model responses at these collocation points as expansion coefficients. The Monte Carlo Simulation (MCS) method was also considered as the exact solution and used to investigate the performance of the proposed PCE and SC models. The obtained numerical results showed that the PCE and SC give much better computation times than the MCS.

Thirdly, with the aim of reducing the computational cost in solving the stochastic problems of microplates with high accuracy. The dissertation developed two novel intelligent computation algorithms by using the neural network systems (artificial neural network (ANN) and deep neural network (DNN)) integrated with the balancing composite motion optimization (BCMO) and improved BCMO to give the so-called BCMO-ANN and iBCMO-DNN algorithms for solving stochastic problems. The accuracy and efficiency of the proposed BCMO-ANN and iBCMO-DNN algorithms are validated through stochastic behaviors of microplates subjected to uncertainties in material properties.

Lastly, this thesis proposed meta-heuristic optimization algorithms for behaviors analysis of laminated composite plates. It is a combination of unified higher-order shear deformation theory, the Ritz method, and two optimization algorithms, namely shrimp and goby association search algorithm (SGA), balancing composite motion optimization (BCMO). The SGA and BCMO are employed for the first time to ascertain the optimal buckling loads and frequencies of laminated composite plates. The numerical findings demonstrate that the increase of side to thickness ratios and Young's modulus ratios leads to the rising of the natural frequencies and critical buckling loads of the laminated composite plates. The performance the BCMO and SGA algorithms, which are better than a differential evolution (DE) algorithm when compared with the convergence rate and computation cost.

TÓM TẮT

Do độ cứng và độ nhẹ vượt trội, vật liệu composite nhiều lớp được sử dụng rộng rãi trong các lĩnh vực như kỹ thuật cơ khí, hàng không vũ trụ và xây dựng. Tuy nhiên, cấu trúc nhiều lớp của chúng dẫn đến sự tập trung ứng suất và khả năng tách lớp tại các điểm giao nhau giữa các lớp. Vì vậy, vật liệu phân loại chức năng (FGM) đã được phát triển để giải quyết vấn đề này, FGM cung cấp sự thay đổi liên tục về các đặc tính vật liệu theo các hướng cụ thể. FGM vượt trội về khả năng chịu nhiệt, chống ăn mòn và độ bền, cung cấp các đặc tính độc đáo vượt xa các thành phần của chúng. Những tiến bộ gần đây cũng đã cho phép sản xuất các vật liệu xốp phân loại chức năng và vật liệu bọt kim loại xốp, giúp tăng cường khả năng giảm âm và giảm trọng lượng kết cấu, khiến chúng trở nên cực kỳ có giá trị đối với các ứng dụng hiện đại. Tuy nhiên, trong thực tế, sự phát triển của các vật liệu này đi kèm với các phương pháp và mô hình tính toán hiệu quả nhằm dự đoán chính xác đáp ứng của chúng ở các quy mô cấu trúc khác nhau. Luận án này đã thực hiện nhằm xây dựng mô hình tấm composite ngẫu nhiên chịu tác dụng của tải trọng cơ học và nhiệt độ. Để đạt được mục đích này, luận án đã nghiên cứu các nội dung chính sau:

Thứ nhất, luận án này đã sử dụng phương pháp Ritz, trong đó hàm hình dạng là hàm lai với chuỗi số là các đa thức trực giao. Các hàm lai này đã được xây dựng bằng cách kết hợp một đa thức với một chuỗi đa thức trực giao như đa thức Hermite và Laguerre. Ngoài ra, các đa thức trực giao cũng được tạo bằng quá trình trực giao hóa Gram-Schmidt. Các hàm hình dạng được thiết kế để đáp ứng các điều kiện biên cần thiết. Do đó, luận án đề xuất các thuật toán tính toán mới, kết hợp phương pháp Ritz với các hàm dạng lai mới (OP), lý thuyết tấm biến dạng cắt bậc cao thống nhất (HSDT), ứng suất cặp biến dạng (MCT) và lý thuyết gradient biến dạng (MST) để phân tích các tấm vi mô. Dựa trên các phát hiện của nghiên cứu này, các hàm hình dạng OP-Ritz được đề xuất trong luận án này phù hợp để phân tích tĩnh, dao động và ổn định của các tấm vi mô. Có một sự khác biệt quan trọng về giá trị tính toán của chuyển vị, tần số và ổn định của các tấm vi mô có nguồn gốc từ MST và MCT

đối với tham số vật liệu. Điều này cho thấy MST và MCT có hiệu quả trong việc nắm bắt các hiệu ứng kích thước của các tấm vi mô.

Thứ hai, ứng dụng thực tế của vật liệu phải chịu nhiều yếu tố không lường trước được có thể ảnh hưởng và thay đổi đáng kể các đặc tính của chúng, từ đó dẫn đến thay đổi hành vi tĩnh và động của kết cấu. Chính vì vậy, để giải quyết những thách thức trên, nghiên cứu này đã phát triển các mô hình ngẫu nhiên (PCE và SC) để kiểm tra ứng xử của các tấm vi mô có đặc tính vật liệu không chắc chắn. Trong đó, PCE có quá trình tính toán nhanh mà vẫn duy trì được độ chính xác cao. Ý tưởng chính của kỹ thuật này là tính gần đúng các đầu ra ngẫu nhiên dưới dạng một chuỗi các hàm cơ sở và các hệ số tương ứng của chúng trong không gian trực giao. SC được biết đến là một trong những phương pháp khai triển ngẫu nhiên tương tự như PCE. Phương pháp mô phỏng Monte Carlo (MCS) cũng được coi là giải pháp chính xác và được sử dụng để nghiên cứu hiệu suất của các mô hình PCE và SC đã đề xuất. Kết quả số thu được cho thấy PCE và SC cho thời gian tính toán tốt hơn nhiều so với MCS.

Thứ ba, với mục đích giảm chi phí tính toán trong việc giải các bài toán ngẫu nhiên của tấm vi mô với độ chính xác cao. Luận án đã phát triển hai thuật toán tính toán thông minh mới bằng cách sử dụng hệ thống mạng nơ-ron (ANN và DNN) tích hợp với thuật toán tối ưu hóa chuyển động tổng hợp cân bằng (BCMO) và BCMO cải tiến được gọi là BCMO-ANN và iBCMO-DNN để giải các bài toán ngẫu nhiên. Độ chính xác và hiệu quả của thuật toán BCMO-ANN và iBCMO-DNN được xác thực thông qua các ứng xử ngẫu nhiên của các tấm vi mô với sự không chắc chắn về tính chất vật liệu.

Cuối cùng, luận án này áp dụng hai thuật toán tối ưu hóa meta-heuristic để phân tích hành vi của tấm composite nhiều lớp. Nó là sự kết hợp giữa lý thuyết biến dạng cắt bậc cao hiệu chỉnh, phương pháp Ritz với hai thuật toán tối ưu hóa mới (SGA và BCMO). SGA và BCMO lần đầu tiên được sử dụng để xác định trạng thái bất ổn định và tần số của các tấm composite nhiều lớp. Kết quả tính toán số chứng minh rằng việc tăng tỷ lệ cạnh trên độ dày và tỷ lệ mô đun Young dẫn đến sự gia tăng tần số tự nhiên và buckling của các tấm composite nhiều lớp. Hiệu suất của thuật toán BCMO và SGA tốt hơn thuật toán DE khi so sánh về tốc độ hội tụ và chi phí tính toán.

TABLE OF CONTENT

LÝ LỊCH CÁ NHÂN	i
DECLARATION	ii
ACKNOWLEDGEMENT	iii
ABSTRACT	iv
TÓM TẮT	vii
TABLE OF CONTENT	ix
NOMENCLATURE AND ABBREVIATIONS	xiii
LIST OF FIGURES	xvi
LIST OF TABLES	xxii
CHAPTER 1	1
INTRODUCTION	1
1.1 Research motivation	1
1.2 Literature review	2
1.3 Objectives of the dissertation	12
1.4 Scope of the dissertation	13
1.5 Thesis outline	13
CHAPTER 2	15
OVERVIEW OF THEORETICAL BASIS	15
2.1 Advanced composite materials for analysis of plates	15
2.1.1 Laminated composite materials	15
2.1.2 Functionally graded materials	15
2.1.3 Functionally graded sandwich materials	18
2.1.4 Porous metal foam materials	20
2.2 Plate theories	21
2.2.1 Classical plate theory	22
2.2.2 First-order shear deformation theory	22

2.2.3 Higher-order shear deformation theory	23
2.2.4 A Quasi-3D theory	24
2.3 Size dependent analysis of microplates	25
2.4 Ritz solution.....	27
2.4.1 Product of trigonometric functions	28
2.4.2 Static beam functions.....	28
2.4.3 Characteristic functions	29
2.4.4 Modified characteristic functions	30
2.4.5 Orthogonal polynomials	31
2.4.6 Non-orthogonal polynomials	32
2.4.7 Hybrid shape function.....	33
2.5 Stochastic method.....	33
2.5.1 Monte Carlo Simulation	34
2.5.2 Probabilistic spectral methods for the propagation of uncertainty	34
2.6 Neural network systems	37
2.6.1 Single layer neural network	38
2.6.2 Multilayer-recurrent neural networks	38
2.6.3 Activation function	39
2.6.4 Loss function	39
2.6.5 Backpropagation and mini-batch gradient descent.....	40
2.7 Meta-heuristic algorithms.....	41
2.7.1. DE algorithm	41
2.7.2. SGA algorithm.....	43
2.7.3. BCMO algorithm	43
2.8 Conclusion	45
CHAPTER 3.....	46
A RITZ-BASED COMPUTATIONAL METHOD FOR SIZE-DEPENDENT ANALYSIS OF ADVANCED COMPOSITE MICROPLATES UNDER THERMO-MECHANICAL LOADS	46
3.1 Introduction	46
3.2 Theoretical formulation	49
3.2.1 Advanced functionally graded materials	49

3.2.2 Modified strain gradient theory based on a framework of unified high-order shear deformation theory	52
3.2.3 Ritz-type series solution	64
3.3 Numerical results	74
3.3.1 Convergence study of solution	74
3.3.2 Analysis of PMF microplates	77
3.3.3 Analysis of FG sandwich microplates	92
3.3.4 Analysis of FGP microplates	101
3.4 Conclusions	128
CHAPTER 4	130
INTELLIGENT COMPUTATIONAL ALGORITHMS FOR STOCHASTIC ANALYSIS OF FUNCTIONALLY GRADED MICROPLATES WITH UNCERTAINTIES OF MATERIAL PROPERTIES	130
4.1 Introduction	131
4.2 Polynomial chaos expansion	133
4.3 Stochastic collocation	137
4.4 Intelligent stochastic computational algorithms based on optimization and machine learning methods	138
4.4.1 Balancing composite motion optimization: BCMO	138
4.4.2 Artificial neural network (ANN) and BMCO algorithm: BCMO-ANN	140
4.4.3 Deep neural network (DNN) and improved BMCO algorithm: iBCMO-DNN	142
4.5 Numerical results	145
4.5.1 Stochastic vibration analysis of FG microplates using polynomial chaos expansion	145
4.5.2 Stochastic thermal buckling analysis of FG sandwich microplates using stochastic collocation	155
4.5.3 Stochastic vibration analysis of FGP microplates using BCMO-ANN algorithm	161
4.5.4 Stochastic thermal buckling analysis of FGP microplates using iBCMO-DNN algorithm	169
4.6. Conclusions	182
CHAPTER 5	184

META-HEURISTIC OPTIMIZATION ALGORITHMS FOR VIBRATION AND BUCKLING ANALYSIS OF LAMINATED COMPOSITE PLATES	184
5.1. Introduction	184
5.2. Theoretical formulation	187
5.3. Ritz method	191
5.4. Optimization solution	196
5.5. Numerical examples	196
5.5.1. Verification study	197
5.5.2. Optimization study	202
5.6. Conclusions	208
CHAPTER 6.....	210
CONCLUSIONS AND RECOMMENDATIONS	210
6.1 Conclusions	210
6.2. Recommendations	211
REFERENCES	213
LIST OF PUBLICATIONS	229

NOMENCLATURE AND ABBREVIATIONS

C:	Damping matrix
M:	Mass matrix
K:	Stiffness matrix
F:	Force
d:	Displacement field
$\dot{\mathbf{d}}$:	Velocity
$\ddot{\mathbf{d}}$:	Acceleration
E:	Young's modulus
h:	The thickness
ρ:	Mass density
V_c:	The volume fraction of the ceramic
β:	The porosity volume fraction
p:	The power-law index
x_1, x_2, x_3:	The coordinate system
ν:	Poisson's ratio
Π_U:	The strain energy
Π_V:	Work done by membrane forces
Π_K:	Kinetic energy
ϵ:	Strains
χ:	Symmetric rotation gradients
ξ:	Dilatation gradient
η:	Deviation stretch gradient
σ:	Cauchy stress
\mathbf{m}:	The high-order stress corresponding with strain gradients χ

$\mathbf{p}, \boldsymbol{\tau}$:	High-order stresses corresponding with strain gradients $\boldsymbol{\xi}, \boldsymbol{\eta}$, respectively.
δ_{ij} :	Kronecker delta
e_{imn} :	Permutation symbol
λ, μ :	Lamé constants
l :	Material length scale parameters
α :	The coefficient of thermal expansion
$R_i(x_1), P_j(x_2)$:	The shape functions in direction in $x_1 - , x_2 -$
φ :	The activation function
BCs:	Boundary conditions
BCMO:	Balance composite motion optimization
CPT:	Classical plate theory
FSDT:	First-Order shear deformation theory
HSDT:	High-Order shear deformation theory
Quasi-3D:	Quasi-three dimensional plate theory
FG:	Functionally graded
FGMs:	Functionally graded materials
PMF:	Porous metal foam
FGP:	Functionally graded porous
LC:	Laminate composite
MAT:	Material
MCT:	Modified couple stress theory
MST:	Modified strain gradient theory
MLSP:	Material length scale parameter
SD:	Standard deviation
CoV:	Coefficient of variation
ANN:	Artificial neural network
DNN:	Deep neural network

MCS:	Monte Carlo simulation
PCE:	Polynomial chaos expansion
SC:	Stochastic collocation method
PDF:	Probability density function
PoE:	Probability of exceedance
UTR:	Uniform distribution
LTR:	Linear distribution
MSE:	The mean square error
LSTM:	Long short-term memory network

LIST OF FIGURES

Figure 1.1: Geometry of a structures microplate	3
Figure 2.1: The geometric of laminated composite plates	15
Figure 2.2: Functionally grade materials	16
Figure 2.3: Geometry of FGP microplates	16
Figure 2.4: The volume fraction of material $V_c(x_3)$ follow Power-law	17
Figure 2.5: The volume fraction of material $V_c(x_3)$ follow Sigmoid.....	18
Figure 2.6: Geometric of functionally grade sandwich plate.....	19
Figure 2.7: The volume fraction of the ceramic material $V_c(x_3)$ of sandwich FG plate (1–2–1)	19
Figure 2.8: Porosity is uniformly distribution.....	20
Figure 2.9: Porosity is asymmetric distribution	20
Figure 2.10: Porosity is symmetric distribution.....	21
Figure 2.11: Un-deformed and deformed geometries of an edge of a plate	22
Figure 2.12: Un-deformed and deformed geometries of an edge of a plate	23
Figure 2.13: Deformation of a transverse normal according to the higher-order plate theory.....	24
Figure 2.14: The simple architecture of a neural network	38
Figure 2.15: The architecture of a deep neural network	38
Figure 3.1: The first five algorithm polynomials for series type solution	65
Figure 3.2: The first five orthogonal polynomials based on GS process.....	67
Figure 3.3: Comparison with both convergence speed of number of series of porous metal foam PMF microplates with full clamped boundary condition for normalized fundamental frequency ($a/h=10$, $\beta=0.3$, $h/l=\infty$)	76
Figure 3.4: Distance of normalized fundamental frequency of porous metal foam PMF microplates with full clamped boundary condition ($a/h=10$, $\beta=0.3$, $h/l=\infty$).....	77

Figure 3.5: Variation of normalized fundamental frequencies with respect the length scale-to-thickness ratio h/l and $a/h=10$ under uniform distribution	82
Figure 3.6: Variation of normalized fundamental frequencies with respect the length scale-to-thickness ratio h/l and $a/h=10$, $\beta=0.2$	83
Figure 3.7: Variation of normalized critical buckling load for uniaxial compression with respect the length scale-to-thickness ratio h/l and $a/h=10$ under symmetric distribution	88
Figure 3.8: Convergence study of series solution of Al/Al ₂ O ₃ FGP microplates with different BCs ($a/h=20$, $p=5$, $\beta=0.1$, $h/l=5$)	107
Figure 3.9: Variation of normalized center deflection with respect the power index p and thickness-to-length scale h/l of FGP microplates ($\beta=0.2$, $a/h=10$)	111
Figure 3.10: Variation of normalized fundamental frequencies with respect the power index p and thickness-to-MLSP ratio h/l ($a/h=10$, $\beta=0.2$)	115
Figure 3.11: Size effect of the MCT and MST for the normalized fundamental frequencies with respect to the length scale-to-thickness ratio h/l ($\beta=0.2$, $p=5$, $a/h=10$)	115
Figure 3.12: Variation of normalized critical buckling load for axial compression with respect the power index p and length scale-to-thickness ratio h/l ($a/h=10$, $\beta=0.1$)	119
Figure 3.13: Size effect of the MST for the normalized critical buckling load with respect to the length scale-to-thickness ratio h/l under simply supported and axial compression, $a/h=10$, and power – law index $p=1$	120
Figure 3.14: Size effect of the MCT and MST for the normalised critical buckling load with respect to the length scale-to-thickness ratio h/l under simply supported and axial compression, $a/h=10$	121
Figure 3.15: The normalized critical buckling under impacting size effect of the MST and MCT with axial compression, $a/h=10$, $\beta=0.2$, $p=1$	122

Figure 3.16: Variation of normalized thermal buckling load with respect the length scale-to-thickness ratio h/l ($a/h=20$) with biaxial compression under uniform distribution	126
Figure 3.17: Variation of normalized thermal buckling load with respect the length scale-to-thickness ratio h/l ($a/h=20$) with biaxial compression under linear distribution	127
Figure 3.18: Variation of normalized thermal buckling load with respect the length scale-to-thickness ratio h/l ($a/h=20$) with biaxial compression under nonlinear distribution	128
Figure 4.1: Flowchart of stochastic free vibration and buckling analysis of the microplates using PCE and MCS	136
Figure 4.2: An artificial neural network structure.....	141
Figure 4.3: Deep neural network.....	142
Figure 4.4: The flowchart of the stochastic response of FGP microplates	144
Figure 4.5: PDF and PoE of MCS and PCE methods for the fundamental frequency (Hz) of the FG microplates with SSSS BC ($p=5$, $h/l=1$, $a/h=10$)	146
Figure 4.6: PDF and PoE of MCS and PCE methods for the fundamental frequency (Hz) of the FG microplates with SSSS, CSCS, CCCC BCs ($p=5$, $h/l=1$, $a/h=10$).....	149
Figure 4.7: Probability density function (PDF) for the natural frequencies and critical buckling loads of SSSS FG microplates ($a/h=10$) with various power-law index p (PCE order-3).....	150
Figure 4.8: Coefficient of variation (COV) with respect the power-law index p of the FG microplates ($a/h=10$) with various BCs and h/l	151
Figure 4.9: Quantile-quantile plot of PCE and MCS method for the fundamental frequencies of the FG microplates with various BCs ($p=5$, $h/l=1$, $a/h=10$)	152
Figure 4.10: First Sobol index of the random input variables with respect to the fundamental frequencies of SSSS FG microplates ($p=5$, $a/h=10$)	153

Figure 4.11: Total Sobol index of the random input variables with respect to the fundamental frequencies of the CCCC FG microplates ($a/h = 10$)	154
Figure 4.12: Quantile-quantile, PDF and PoE of MCS and SC for the critical buckling temperature of the (1-1-1) FG sandwich microplates under uniform distribution with SSSS, CCCC BCs (MAT 1, $p = 0.5$, $a/h = 10$)	157
Figure 4.13: Quantile-quantile, PDF and PoE of MCS and SC for the critical buckling temperature of the (2-1-2) FG sandwich microplates under linear distribution with SSSS, CCCC BCs (MAT 1, $p = 2$, $a/h = 10$)	158
Figure 4.14: Probability density function (PDF) for the critical buckling temperature and free vibration of (1-2-1) FG sandwich microplates under uniform distribution with various ratio thickness to material h/l , ($a/h = 10$, $p = 0.5$)	159
Figure 4.15: Probability density function (PDF) for the natural frequencies and critical buckling temperature of (1-2-1) FG sandwich microplates under uniform distribution with various power-law index p ($a/h = 10$)	160
Figure 4.16: Coefficient of variation (COV) of critical buckling temperature (MAT 1) with respect to the power-law index p of the FG sandwich microplates (1-2-1) with various BCs and h/l , $a/h = 10$ under uniform distribution	160
Figure 4.17: Scatter plot of the Ritz-BCMO model with ANN-BCMO one on the normalized fundamental frequencies for FGP microplates with different boundary conditions, $p = 1$, $a/h = 10$ and $h/l = 1$	165
Figure 4.18: Probability density function (PDF) of Ritz-BCMO and BCMO-ANN methods for normalized fundamental frequencies of FGP microplates with different boundary conditions, $p = 1$, $a/h = 10$ and $h/l = 10$	166
Figure 4.19: Loss function of the normalized fundamental frequencies for FGP microplates with different boundary conditions, $p = 10$, $a/h = 10$ and $h/l = 5$..	167
Figure 4.20: Regression of the normalized fundamental frequencies with log transfer function for FGP microplates with full clamped boundary condition, $p = 10$ and $a/h = 10$	168

Figure 4.21: Comparison of the efficiency of the <i>rand</i> coefficient differences for iBCMO algorithm of normalized thermal buckling load with biaxial compression, simply supported , $a/h = 20$, $p = 1$, $h/l = 10$, $\beta = 0.1$ under uniform distribution	171
Figure 4.22: Comparison of the efficiency of the probabilistic threshold (TV) differences for iBCMO algorithm of normalized thermal buckling load with biaxial compression, simply supported , $a/h = 20$, $p = 1$, $h/l = 10$, $\beta = 0.1$ under uniform distribution	172
Figure 4.23: Comparison of the efficiency of iBCMO with the BCMO algorithm of normalized thermal buckling load , $a/h = 20$, $p = 1$, $h/l = 10$ with biaxial compression under uniform distribution	174
Figure 4.24: Quantile-quantile plot of the Ritz-iBCMO model with DNN-iBCMO, $a/h = 20$, $p = 1$, $h/l = 5$, biaxial compression under uniform distribution	179
Figure 4.25: Probability density function (PDF) of Ritz-iBCMO and iBCMO-DNN methods the normalized thermal buckling with $a/h = 20$, $p = 1$, $h/l = 5$, biaxial compression under uniform distribution	180
Figure 4.26: Loss function of the normalized critical buckling temperature with $a/h = 20$, $h/l = 5$, $\beta = 0.3$	181
Figure 5.1: The geometric of laminated composite plates	188
Figure 5.2: The first five orthogonal polynomials	193
Figure 5.3: Mode shapes of vibration of laminated composite plates $a/h = 10$, $E_1/E_2 = 40$, $[0^\circ/90^\circ/0^\circ]$, $\bar{\omega}_1 = (\omega a^2/\pi^2)/\sqrt{\rho h/(E_2 h^3/(12(1-\nu_{12}\nu_{21})))}$	202
Figure 5.4: Comparison the maximum buckling load (uniaxial compression) of SSSS square laminated composite plates with size population $NP = 20$ ($E_1/E_2 = 40$)	206
Figure 5.5: Comparison the maximum fundamental frequencies for SSSS square laminated composite plates with size population $NP = 20$ ($E_1/E_2 = 40$)	206
Figure 5.6: Comparison the minimum results of SSSS square laminated composite plates with size population $NP = 20$ ($E_1/E_2 = 40$)	207

Figure 5.7: Comparison the minimum results of SSSS and CCCC square laminated composite plates with size population $NP = 50$ ($E_1 / E_2 = 40$).....	207
Figure 5.8: Comparison the minimum results for CSCS square laminated composite plates with size population $NP = 50$ ($E_1 / E_2 = 40$)	208

LIST OF TABLES

Table 3.1: Approximation functions of series solutions with different BCs	67
Table 3.2: Comparison with convergence speed of the series solution ($n = n_1 = n_2$) of porous metal foam PMF microplates with full clamped boundary condition for ($a/h = 10$, $\beta = 0.3$, $h/l = \infty$)	76
Table 3.3: Convergence study of the series solution of porous metal foam PMF microplates with different boundary conditions ($a/h = 10$, $\beta = 0.1$, $h/l = 1$) under uniform distribution and Hermite polynomial	78
Table 3.4: Normalized fundamental frequencies of PMF rectangular microplates for simply supported boundary condition with $a/h = 10$	79
Table 3.5: Normalized fundamental frequencies of PMF rectangular microplates for full clamped boundary condition with $a/h = 10$	80
Table 3.6: Normalized fundamental frequencies of rectangular porous metal foam microplates with $a/h = 10$ and SCSC boundary condition	81
Table 3.7: The normalized critical buckling load of the SSSS metal foam square microplate under uniaxial compression $a/h = 10$	84
Table 3.8: The normalized critical buckling load of the SSSS metal foam square microplate under biaxial compression $a/h = 10$	85
Table 3.9: The normalized critical buckling load of the metal foam square microplates under biaxial compression with many boundary conditions, $a/h = 10$	86
Table 3.10: The normalized critical buckling load of the metal foam square microplates under uniaxial compression with many boundary conditions, $a/h = 10$	87
Table 3.11: Normalized fundamental frequencies of PMF rectangular microplates for simply supported boundary condition with $a/h = 10$	89
Table 3.12: Normalized critical buckling load under uniaxial compression of PMF rectangular microplates for simply supported boundary condition with $a/h = 10$.90
Table 3.13: Normalized critical buckling load under biaxial compression of PMF rectangular microplates for simply supported boundary condition with $a/h = 10$.91

Table 3.14: Comparison of non-dimensional fundamental frequency $\bar{\omega}$ of square SSSS FG sandwich microplates (MAT 2, $a/h=10$)	93
Table 3.15: Non-dimensional critical buckling loads of square SSSS FG sandwich microplates (MAT 2) ($a/h=10$) with biaxial compression.....	94
Table 3.16: Non-dimensional critical buckling temperature \bar{T}_{cr} of square SSSS FG sandwich microplates (MAT 1) under uniform distribution with biaxial compression	95
Table 3.17: Non-dimensional critical buckling temperature \bar{T}_{cr} of square SSSS FG sandwich microplates (MAT 1) under linear distribution with biaxial compression, $T_b = 25^\circ C$	96
Table 3.18: Non-dimensional critical buckling temperature \bar{T}_{cr} of square FG sandwich microplates (MAT 1) under uniform distribution with biaxial compression	97
Table 3.19: Non-dimensional critical buckling temperature \bar{T}_{cr} of square FG sandwich microplates (MAT 1) under linear distribution with biaxial compression, $T_b = 25^\circ C$	98
Table 3.20: Non-dimensional critical buckling temperature \bar{T}_{cr} of square FG sandwich microplates (MAT 1) under uniform distribution with biaxial compression, $a/h=10$	99
Table 3.21: Non-dimensional critical buckling temperature \bar{T}_{cr} of square FG sandwich microplates (MAT 1) under linear distribution with biaxial compression, $T_b = 25^\circ C$, $a/h=10$	100
Table 3.22: Non-dimensional natural frequency of the FG square microplates	101
Table 3.23: Non-dimensional critical buckling loads of the FG square plates	102
Table 3.24: Non-dimensional critical buckling loads of SSSS FG square microplates with biaxial compression.....	103
Table 3.25: Convergence study of the series solution of Al/Al ₂ O ₃ FGP microplates with different boundary conditions ($a/h=10$, $p=10$, $\beta=0.1$, $h/l=1$)	104

Table 3.26: Normalized fundamental frequencies of simply supported FGP microplates with $a/h = 20$	105
Table 3.27: Normalized critical buckling loads of FGP plates with biaxial compression, $a/h = 20$ and CCCC boundary condition	106
Table 3.28: Normalized transverse center displacements of FGP microplates under sinusoidal load ($\beta = 0$, SSSS).....	108
Table 3.29: Normalized transverse center displacements of FGP microplates under sinusoidal load with $a/h = 10$ $\beta = 0$ and different boundary conditions.....	109
Table 3.30: Normalized transverse center displacements of FGP square microplates under sinusoidal load with different boundary conditions.....	110
Table 3.31: Normalized fundamental frequencies $\bar{\omega} = \omega h \sqrt{\rho_c / E_c}$ of Al/Al ₂ O ₃ FGP square microplates ($\beta = 0$, $a/h = 10$, SSSS).....	112
Table 3.32: Normalized fundamental frequencies of Al/Al ₂ O ₃ FGP square microplates ($\beta = 0$, $a/h = 10$, CCCC and SCSC).....	113
Table 3.33: Normalized fundamental frequencies of Al/Al ₂ O ₃ FGP square microplates	114
Table 3.34: Normalized critical buckling load $\bar{N}_{cr} = (N_{cr}^m a^2 / h^3 E_m)$ of Al/Al ₂ O ₃ FGP square microplates ($\beta = 0$, $a/h = 10$, SSSS).....	116
Table 3.35: Normalized critical buckling load $\bar{N}_{cr} = (N_{cr}^m a^2 / h^3 E_m)$ of Al/Al ₂ O ₃ FGP square microplates with axial compression $(N_1^{(m)}, N_2^{(m)}, N_{12}^{(m)} = 1, 0, 0)$, $\beta = 0$, $a/h = 10$, SCSC and CCCC boundary conditions	117
Table 3.36: Normalized critical buckling load $\bar{N}_{cr} = (N_{cr}^m a^2 / h^3 E_m)$ of Al/Al ₂ O ₃ FGP square microplates ($a/h = 10$, SSSS), $(N_1^{(m)}, N_2^{(m)}, N_{12}^{(m)} = 1, 0, 0)$	118
Table 3.37: Normalized thermal critical buckling load \bar{T}_{cr} of Al/Al ₂ O ₃ FGP square microplates with biaxial compression $(N_1^{(tr)}, N_2^{(tr)}, N_{12}^{(tr)} = 1, 1, 0)$ and $a/h = 20$ under uniform distribution	123

Table 3.38: Normalized thermal critical buckling load \bar{T}_{cr} of Al/Al ₂ O ₃ FGP square microplates with biaxial compression $(N_1^{(tr)}, N_2^{(tr)}, N_{12}^{(tr)} = 1, 1, 0)$ and $a/h = 20$ under linear temperature distribution	124
Table 3.39: Normalized thermal critical buckling load \bar{T}_{cr} of Al/Al ₂ O ₃ FGP square microplates with biaxial compression $(N_1^{(tr)}, N_2^{(tr)}, N_{12}^{(tr)} = 1, 1, 0)$ and $a/h = 20$ under nonlinear temperature distribution	125
Table 4.1: Comparison study between MCS (10.000 samples) and PCE (256 samples) for the mean, standard deviation (SD), Kurtosis and Skewness for the fundamental frequency of the FG plates ($a/h = 5$, MAT 1)	147
Table 4.2: Comparison study between MCS (10.000 samples) and PCE (256 samples) for the mean, standard deviation (SD), Kurtosis and Skewness for the fundamental frequency of the FG microplates ($a/h = 10$, MAT 1)	148
Table 4.3: The standard deviation (SD), mean, Skewness, Kurtosis for the biaxial thermal buckling of FG sandwich microplates (MAT 3, $a/h = 10$) under linear distribution of SC (256 samples) and MCS (10.000 samples), $T_b = 25^\circ C$	156
Table 4.4: Mean and standard deviation (SD) of normalized fundamental frequencies for FGP microplates with $a/h = 10$ and SSSS boundary condition...	162
Table 4.5: Mean and standard deviation (SD) of normalized fundamental frequencies for FG microplates with $a/h = 10$ and CSCS boundary condition	163
Table 4.6: Mean and standard deviation (SD) of normalized fundamental frequencies for FG microplates with $a/h = 10$ and CCCC boundary condition ...	164
Table 4.7: Comparison of the <i>rand</i> coefficient of the Ritz-iBCMO algorithm for the normalized critical buckling temperature \bar{T}_{cr} of Al/Al ₂ O ₃ FGP square microplates with $a/h = 20$, $\beta = 0.1$, $p = 1$, $h/l = 10$ with biaxial compression $(N_1^{(tr)}, N_2^{(tr)}, N_{12}^{(tr)} = 1, 1, 0)$ under uniform temperature distribution and simply supported	170

Table 4.8: Comparison between BCMO and iBCMO algorithms for the normalized critical buckling temperature \bar{T}_{cr} of Al/Al ₂ O ₃ FGP square microplates with $a/h=20$, $\beta=0.1$, $p=1$ with biaxial compression under uniform temperature distribution	173
Table 4.9: Mean and standard deviation (SD) of normalized critical buckling temperature for FGP microplates with biaxial compression, $a/h=20$, SSSS under uniform temperature distribution	176
Table 4.10: Mean and standard deviation (SD) of normalized critical buckling for FGP microplates with biaxial compression, $a/h=20$, SCSC under uniform temperature distribution	177
Table 4.11: Mean and standard deviation (SD) of normalized critical buckling for FGP microplates with biaxial compression, $a/h=20$, CCCC under uniform temperature distribution	178
Table 5.1: Approximation functions of series-type solution	193
Table 5.2: Convergence study for $[0^\circ/90^\circ/90^\circ/0^\circ]$ plates with different BCs..	197
Table 5.3: The normalize fundamental frequencies of $[0^\circ/90^\circ/90^\circ/0^\circ]$ plates.	198
Table 5.4: The normalize fundamental frequencies of $[0^\circ/90^\circ/0^\circ]$ plates $(\bar{\omega}_1 = (\omega a^2 / \pi^2) / \sqrt{\rho h / (E_2 h^3 / (12(1 - \nu_{12}\nu_{21})))})$	199
Table 5.5: The normalize fundamental frequencies of $[0^\circ/90^\circ]$ plates	200
Table 5.6: The normalize critical buckling of $[0^\circ/90^\circ/90^\circ/0^\circ]$ plates under uniaxial compression $(N_1^0, N_2^0, N_{12}^0 = 1, 0, 0)$	200
Table 5.7: The normalize critical buckling of $[0^\circ/90^\circ/0^\circ]$ plates under biaxial compression $(N_1^0, N_2^0, N_{12}^0 = 1, 1, 0)$	201

Table 5.8: Normalized shear buckling of $[0^\circ/90^\circ/90^\circ/0^\circ]$ plates $(N_1^0, N_2^0, N_{12}^0 = 0, 0, 1)$, $a/h = 10$	201
Table 5.9: Optimization critical buckling of symmetric SSSS square laminated composite plates with four layers ($a/h = 10$, $E_1/E_2 = 40$, $NP = 20$) under uniaxial compression $(N_1^0, N_2^0, N_{12}^0 = 1, 0, 0)$	203
Table 5.10: Optimization critical buckling of SSSS square laminated composite plates with four layers ($a/h = 10$, $E_1/E_2 = 40$, $NP = 20$) under uniaxial compression $(N_1^0, N_2^0, N_{12}^0 = 1, 0, 0)$	204
Table 5.11: Optimization fundamental frequencies of SSSS square laminated composite plates with four layers ($a/h = 10$, $E_1/E_2 = 40$, $NP = 20$).....	205

CHAPTER 1

INTRODUCTION

This chapter composes five sections that present the research motivation, general literature review of stochastic composite microplates, objectives, scopes, research method, and dissertation structures.

1.1 Research motivation

Due to its many advantages in hardness and lightness, laminated composite (LC) materials have been widely used in many fields such as mechanical engineering, aerospace, construction, etc. The disadvantage of this type of material is that material discontinuity at the interface between the layers can lead to significant stress concentrations and delamination phenomena. In order to overcome this drawback, functionally graded (FG) materials have been developed, and the properties of the component materials change continuously in the required directions of the coordinate system. FGMs excel in thermal resistance, corrosion resistance, and toughness, providing unique properties beyond those of their components. Besides, based on the high technology in the fabrication of materials, functionally graded porous materials (FGP) and porous metal foam materials (PMF) can increase sound dampening while reducing the overall weight of the structures that can be manufactured. These materials have become more valuable as a new material for structures. In practice, the constituent size effects, uncertainties of material characteristics, geometries and loads of microplates provided significant challenges in predicting their behaviors. Therefore, the development of advanced computational methods to anticipate and optimize the behaviors of such microplates is crucial to effectively harness the potential of microplates. It is known that the classical elasticity theory of plates is suitable for the macro level. Still, it could not be used to accurately analyze responses of microplates or nanoplates due to the size effects. As structures are reduced to the nanoscale or microscale, the influence of constituent size, microstructural geometry, and boundary conditions become

increasingly prominent. To fully understand and predict the behaviors of nano and micro structures, it is essential to develop models that include size-dependent phenomena, among which the strain gradient elasticity and nonlocal elasticity theories have been commonly used. In this context, the consideration of the effects of shear strains, material distributions, geometry, boundary conditions, constituent size and non-classical elasticity theories on static and dynamic behaviors of LC, FG, FGP and PMF plates is still an interesting topic that needs to be studied further. Moreover, it is essential to note that the variations in manufacturing processes, fluctuations in ambient conditions, and exposure to radiation or severe temperatures, could lead to uncertainties of geometries, material properties and loads of the structures. It therefore requires appropriate stochastic models to tackle these uncertainties and enhance the performance of plates.

Given the aforementioned issues, the author has selected the research subject for this dissertation, titled **“Development of stochastic composite plate models subjected to mechanical and thermal loads”**. In this context, the thesis will develop new computational approaches for deterministic and stochastic analysis of LC, FG, FGP, PMF microplates in thermo-mechanical environments. The present research will provide a low computational time and high accuracy.

1.2 Literature review

Due to its many advantages in hardness and lightness, composite materials have been widely used in many fields, such as aviation and construction. Laminated composite materials are the first type of structure formed from two or more layers of component materials bonded together at the interfaces between the layers in which the direction of reinforcing fibers at the layers can be changed to meet the given requirements. The disadvantage of this type of material is that material discontinuity at the interface between the layers can lead to significant stress concentrations and delamination phenomena. In order to overcome this drawback, functionally graded materials (Fig.1.1) have been developed, and the properties of the component materials change continuously in the required directions of the

coordinate system ([1]). Moreover, with the advancements in material fabrication technology, FGP and PMF can enhance sound dampening while decreasing the overall weight of manufactured structures. These qualities have made them increasingly valuable as a new material for structural applications. However, the development of such materials accompanied efficiently computational methods and models in order to predict accurately their responses at different structural scales.

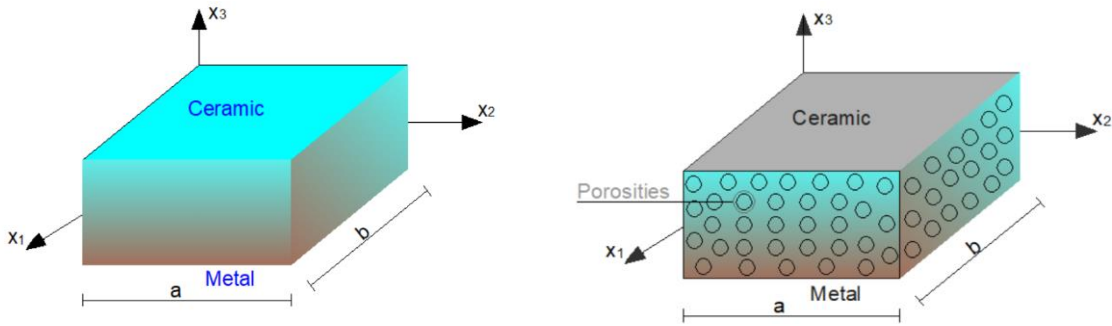


Figure 1.1: Geometry of a structures microplate

Regarding computational techniques, many methods have been developed to predict the behavior of plates. Two main approaches can be distinguished: analytical methods and numerical methods. Numerical methods have many advantages, such as the fact that they can solve complex problems with arbitrary boundary conditions. The finite method element (FEM) is the most commonly used method, attracting many research teams to analyze the behavior of LC and FG plates [2]. However, the FEM has difficulties in meshing problems, and overcoming the shear-locking effect. In order to avoid the use of meshing issues, the mesh-free methods can also be used by the geometry domain separation into points without the need for rejoining elements [3]. There are numerous methods for addressing the shear-locking phenomenon, such as Hughes and Tezduyar's hypothetical natural deformation method [4], which enables defining the shear strain independently from the kinematic approximation. Based on this approach, many finite elements have been developed such as DKT [5], DSG [6], MIN3 [7]. The mixed interpolation of tensorial components (MITC3) [8] method has been used successfully as a shear-locking removal technique for shell and plate finite elements. Compared with other

shear-locking removal techniques, the MITC3 technique exhibits spatially isotropic behavior which does not depend on the nodal numbering. This technique has been used for studies of plate/shell ([9-11]). Additionally, to increase the accuracy of FEM, Liu et al.[12] developed the smooth FEM method (S-FEM), which consists of four types of mains (element-domain smoothing (CS-FEM), element-node smoothing (NS-FEM), element-edge smoothing (ES-FEM), and element-facet smoothing (FS-FEM)). Many research groups have developed this technique for several finite elements and applied different structural behavior analysis of plates ([13-18]). Moreover, Hughes et al. [19] proposed the integration of computer-aided design (CAD) and finite element analysis (FEA) into a single model, referring to this strategy as isogeometric analysis (IGA). This method uses B-splines or NURBS functions to model geometric domains consistently in CAD and get close to FEA solutions. For example, Pham et al. [20] analyzed PMF microplates using a refined HSDT, MST and IGA. Le et al. [21] utilized the MCT and IGA to investigate the linear bending and geometrically nonlinear responses of PMF microplates. Thai et al. [22] analysed the post-buckling of FG microplates subject to mechanical and thermal loads using IGA and third-order shear deformation theory (IGA-TSDT) based on the MST. Farzam et al. [23] investigated the size-dependent analysis of FG microplates with temperature-dependent material properties using MST and IGA- refined plate theory (RPT). Furthermore, the precise geometric representation is preserved even at the most basic discretization level. For the analytical approach, Navier's solution method is the simplest one. It uses trigonometric functions that meet the boundary conditions to approximate the displacement field variables. Although this method can only be applied to simple presumptive boundary conditions, because of its simplicity, this approach has been used by many authors ([24-28]). To overcome this drawback, the Levy method can be used. For rectangular plates, this solution applies to the plate with two simply supported edges and the other two with different boundary conditions [29]. The differential quadrature method (DQM) developed by Bellman and Casti [30] and has been

successfully applied in solving systems of nonlinear differential equations. This method is also applied in the behavior analysis of beams and plates composite ([31-33]). Airy's stress function method has been used to investigate behaviors of composite structure ([34, 35]). However, the selection of the stress function that satisfies both the biharmonic equation (a fourth-order partial differential equation) and boundary conditions could be challenging. Another approach, the Ritz method can be considered as the most general analytical method that allows solving problems with different boundary conditions in which the displacement field variable is approximated through form functions. The Ritz method was initially introduced by Walter Ritz [36] to analyze the free vibrations of structures. Since then, a multitude of researchers have used this method to investigate the static and dynamic responses of beams, plates, and shells. It is worthy to noticing that the Ritz solution's precision, numerical instabilities and convergence rates are dependent on the construction of approximation functions. Consequently, it is essential to meticulously select a set of functions that not only produce physically accurate results but also possess favorable numerical properties. The set of approximation functions must not violate the essential or geometric boundary conditions and should be linearly independent and complete [37]. A brief literature shows that a number of researches have been performed in developing the shape functions of Ritz method in which it can be categorized into two typical types: orthogonal polynomials (OP) and non-orthogonal polynomials (NOP). For the OP shape function, Chebyshev's polynomial has commonly used for analysis of composite structures owing to its convergence rate and numerical robustness [38]. It is noted that the orthogonal polynomials for the Ritz method could be formulated from Gram-Schmidt procedure [39]. In practice, the approximation functions of Ritz method could be a series of non-orthogonal polynomials [40]. This particular set does not exhibit orthogonality, resulting in the loss of certain computational benefits. However, the primary benefit of these functions lies in their ability to eliminate the requirement for intricate generation procedures compared to the

creation of orthogonal polynomials. The evaluation of the integrals is significantly simpler when compared to those involving orthogonal polynomials. Moreover, it is also worthy to noticing that the shape functions should be selected to satisfy the boundary conditions ([41]), which are found to be efficient in the convergence's rate. Alternatively, the penalty function method could be used to incorporate the boundary condition, however this approach leads to an increase in the dimension of the mass and stiffness matrices and thus causes increasingly computational cost. Therefore, the accuracy of the Ritz solution depends on choosing a suitable form function. These shape functions can be chosen to satisfy the boundary conditions; otherwise, the penalty function method can be used. Shape functions can be also the orthogonal polynomial or non-orthogonal polynomial. A series-type solution of the Ritz method can be one-dimensional or two-dimensional. A literature review reveals that numerical methods have many advantages. However, the FEM has difficulties in meshing problems and overcoming the shear-locking effect. Therefore, this thesis will focus on the Ritz method which is the analytical solution. It can be seen that Ritz's OP functions offer significant advantages in numerical computations; thus, there is a need for further studies on the Ritz method for microplate problems.

In addition to the calculation method, the selection of the appropriate plate model significantly impacts the study results. An overview of the displacement fields can be found in the study of Sayyad and Ghugal [42], Khandan et al [43]. Many plate theories have been developed, which include main categories such as: classical plate theory (CPT), first-order shear deformation theory (FSDT), higher-order shear deformation theory (HSDT), a quasi-3D theory, and three-dimensional theory. The CPT ignores the effect of the transverse shear deformation and is only suitable for thin plates. To overcome this shortcoming, the FSDT is the simplest method, but it requires a shear correction factor to properly handle the free-traction boundary conditions for shear stresses [44]. In contrast, the HSDTs [45] with higher-order variations of in-plane displacements or both in-plane and out-of-plane

displacements (Quasi-3D) [46] do not need such correction factors. However, the HSDTs ignore the thickness-stretching effect, resulting in a uniform transverse displacement across the plate's thickness. The significance of considering the thickness-stretching effect has been highlighted by Carrera et al. [2]. Besides, the three-dimensional elasticity theory was also developed, in which the field displacement is directly approximated via shape functions, which is difficult to compute in practice. Although plate models incorporating higher-order variations of both in-plane and out-of-plane displacements generally provide more accurate predictions than the HSDTs, they are more complex and costly to implement due to the increased number of variables. Thus, it is important to use unified HSDT for various shear deformation plate theory.

Moreover, the structures at small scales require advanced computational models to capture size effects. The earlier experimental works revealed that the classical elasticity theory could not accurately predict responses of microstructures at small scale, advanced computations theories with length scale parameters have been therefore developed with different approaches. A number of studies have been performed to predict accurately static, buckling and vibration behaviors of the FG microplates ([47-49]) in which the modified coupled stress theory (MCT) and modified strain gradient theory (MST) are mostly used for various theories (CPT, FSDT, HSDT, three dimensional elasticity theory). The MCT initiated by Yang et al. [50] was known as the simplest one to include the size effects with only one material length scale parameter (MLSP) associated with rotation gradient in the constitutive equations. The MST proposed by Lam et al. [51] modified the classical strain gradient theory of Mindlin [52], Mindlin and Eshel [53] to establish a new set of high-order metrics, where the total number of MLSP was reduced from five to three. The MST can be reduced to MCT if two MLSPs related to dilatation gradient and deviatoric stretch gradient were set to be zero. It should be mentioned that although the MST predicts more accurate than the MCT, it appears to be complicated to implement. Kim et al. [54] presented static, free vibration and

buckling behaviors of FGP simply-supported microplates by using the MCT, classical and FSDT. Fan et al. [55], Thanh et al. [56] investigated the nonlinear buckling and vibration responses of FGP microplates using the MCT, isogeometric approach and HSDT. Guo et al. [57] investigated forced vibration responses of exponentially FGP microplates under moving loads. Moreover, another way to capture size effects of nanostructures is to use the nonlocal elasticity theory (NET) known as Eringen's one ([58]). By involving the nonlocal parameter in constitutive equations, the NET has been employed for analysis of the FG nanoplates ([59-61]). However, it is complicated to implement different boundary conditions for nanostructures. Besides, thermal load can have various effects on plates, depending on the material and temperature range it is exposed to. Thus, the study of size-dependent FG microstructures in this environment have been attracted by many researchers. Aria et al. [62] demonstrated the hygro-thermal behavior of FG sandwich microbeams using nonlocal elasticity theory. Shojaeefard et al. [63] used CPT and FSDT to investigate the temperature-dependent of FG porous circular microplates under a nonlinear thermal load. The study of how temperature affects the behavior of FG plates has generated significant interest ([64, 65]). Zenkour and Sobhy [66] studied the thermal buckling of various types of FG sandwich plates using the sinusoidal shear deformation theory. Fazzolari et al. [67] studied thermal buckling of FG sandwich plates using a refined quasi-3D theory. Daikh et al. ([68]) studied the thermal buckling, bending analysis of FG sandwich beams/plates resting on elastic foundations using a HSDT. The enhanced radial point interpolation mesh-free technique was used by Do et al. [69] to study the thermal buckling of FG sandwich plates. Sahoo et al. [70] investigated nonlinear vibration of FG sandwich structures under thermal loadings. The hydro-thermo-mechanical effects on static responses of FG plates have been studied by Mudhaffar et al. [71] by using a HSDT and Navier method. Daikh et al. [72] studied the thermal buckling of FG sandwich cylindrical shells with the simply supported boundary conditions by using the Donnell theory. Non-local elastic theories are also considered when analyzing

structural size effects at the microstructural level. Nevertheless, the implementation of this theory for microplates with different boundary conditions, porous parameters, size-scale-thickness ratio, uncertain material, etc, is quite complicated. Therefore, the next goal will be to propose a size-dependent microplate model based on a general framework of higher-order shear deformation plate theory, MCT, and MST under mechanical and thermal loads.

Moreover, it needs to be noted that, due to the manufacturing process or other unexpected factors, the material properties of the structures can be uncertain ([73, 74]), which leads to the change on their static and dynamic behaviors. Hence, it is imperative to develop a stochastic model to examine the behavior of microplate with uncertain material properties. Monte Carlo Simulation (MCS) method [75] is the simplest and most popular approach to solve this complicated problem. It was used for analysis of the FG and LC plates ([76-79]). Nonetheless, this approach is infeasible in different cases due to its expensive computational cost, especially when a complicated physical model is considered. In order to overcome this adverse, Kumar et al. [80] proposed an artificial neural network-based-MCS approach for stochastic buckling analysis of LC sandwich plates. Another approach is to use polynomial chaos expansion (PCE) which speeds up the computing process while still maintains the accuracy. This approach has been employed for static and dynamic analysis of LC and FG plates with uncertainty of materials properties. Peng et al. [81] studied a uncertainty analysis of LC plate with data-driven PCE method under insufficient input data of uncertain parameters based on FEM to solve the natural frequency. Umesh and Ganguli [82] presented the material uncertainty effect on vibration control of smart composite plate using PCE and FEM. Chakraborty et al. [83] analysed the stochastic free vibration analysis of LC plates using polynomial correlated function expansion. Sasikumar et al. [84] proposed a data-driven PCE method for stochastic analysis of LC plates. Shaker et al. [85] studied the stochastic FEM to perform reliability analysis of the free vibration of LC plates with material and fabrication uncertainties using the first-order and

second-order reliability method based on the third-order shear deformation theory (TSDT). Li et al. [86] investigated stochastic thermal buckling characteristics of LC plates with the random system properties using the first-order perturbation technique. For FG plates, Li et al. [87] investigated stochastic static responses of FG plates with uncertainty of material properties using the PCE, FSDT and isogeometric approach. García et al. [88] illustrated the meta model-based approach for stochastic free vibration analysis of FG carbon nanotube reinforced plates using the FEM. Stochastic collocation (SC)[89] is known as one of stochastic expansion method similar to the popular PCE. It method allows for the efficient and accurate computation of statistics and solutions of mathematical models that involve stochastic input parameters. It is particularly useful in the field of uncertainty quantification, where it can be used to estimate the propagation of uncertainties in physical systems or to quantify the sensitivity of system response to uncertain parameters. It derives the Lagrange interpolation polynomials for a set of collocation points and reproduces the model responses at these collocation points as of expansion coefficients. A literature review shows that although many studies on the stochastic analysis of composite/FG plates have been performed, as far as the authors are aware the similar research on the porous FG/FGP microplates is still very limited. Therefore, developing stochastic models to investigate the behaviors of microplates with uncertain material properties is essential in practice.

Besides the traditional stochastic models, optimization meta-heuristic algorithms and artificial intelligence are also used to analyze stochastic behaviors of structures. There has been significant scholarly interest in the optimal design of FG plates, as evidenced by numerous studies ([90, 91]). Optimization algorithms can be classified into two primary categories: gradient-based methods such as sequential quadratic programming, optimality criterion, force method, and non-gradient-based methods. Algorithms in the first group ([92-94]) quickly find the best solutions. However, a common limitation of these algorithms is their tendency to become stuck at local optimal solutions. Furthermore, it is imperative to conduct sensitivity analyses on

both the fitness and constraint functions, as they play a crucial role in the optimization process. However, it is worth noting that performing these analyses can be intricate and resource-intensive. In order to mitigate these limitations, a variety of by natural phenomena simulation algorithms have been devised, such as Moth-Fame Algorithm (MFA) [95], Gravitational Search Algorithm (GSA) [96], Firefly Algorithms (FA) [97], Memetic Algorithm (MA) [98], Ant Colony Optimization (ACO) [99], Particle Swarm Optimization (PSO) [100], Differential Evolution (DE) [101], Genetic Algorithms (GA) [102], Spotted Hyena Optimizer [103], etc. Owing to its advantages, these optimization algorithms have been applied for the optimization of FG plates [104] nanoplates [105] and micro-beams [106]. In practice, the algorithms require dependent parameters and high computational costs. In order to overcome this adverse, the Balancing Composite Motion Optimization algorithm (BCMO) [107] has been recently developed, in which no dependent parameters are required. This method is inspired by the fact that the solution space is assumed to be in Cartesian coordinates and the searching movements of candidate solutions are compositely equalized in both global and local ones. In fact, a candidate solution can move closer to better ones to exploit the local regions, and move further to explore the search space. Thus, the best-ranked individual in each generation can jump immediately from space to space or intensify its current local space. The BCMO has been applied to optimize behaviors of FG plates and a rectangular concrete-filled steel tube short columns ([108, 109]). The shrimp and goby association search algorithm (SGA)[110] has already been developed without depending on input parameters. Its concept is inspired by the symbiotic relationship between shrimp and goby fishes in their natural habitat. In this ecosystem, the goby uses the shrimp's burrow as a haven during the day and a regular resting place at night. Essentially, the security level of the shelter is contingent upon the shrimp's capacity to allure the gobiid fish. It is noted that the efficacy of these algorithms relies on the synchronization of a collective of particles, which impedes the ability to discern and independently assess individual particles.

Instead, particles participate in collective communication to determine their subsequent course of action. A collective of agents engaged in continuous movement and interaction across several activities is often known as a particle swarm. Furthermore, the machine learning, which involves an artificial neural network (ANN), has been used to predict the behaviors of materials [111] . A literature review [112] shows that although many investigations on the optimization analysis of composite/FG plates have been done, as far as the authors are aware, similar research on the microplates with uncertain materials is still very limited. Moreover, a literature survey indicates that the BCMO and SGA algorithms are recognized as efficient methods for optimization of structures. Besides, the combination between the BCMO algorithm and neural networks system to determine optimal responses for microplates with uncertainties of material properties has not been developed yet, this interesting topic needs to be investigated. Therefore, in order to fill in the research mentioned above gap, this study proposes novel intelligent computation algorithms for solving the stochastic problems of microplates.

1.3 Objectives of the dissertation

The primary objective of this dissertation is to develop stochastic models for microplates under mechanical and thermal loading conditions. To achieve the desired objective, the dissertation focuses on the following key research topics:

- Develop the shape functions for the series-type solution of the Ritz method.
- Develop stochastic models to investigate the behaviors of microplates with uncertain material properties: polynomial chaos expansion, stochastic collocation method and Monte Carlo simulation.
- Propose novel intelligent computation algorithms for solving the stochastic problems of microplates.
- Provide optimization methods to search the optimal fiber directions of laminated composite plates.

1.4 Scope of the dissertation

This dissertation's research scope is restricted to the following aspects:

- The hybrid shape function will be developed in which combination the series of exponential or orthogonal polynomial and a polynomial to satisfy the boundary conditions of the Ritz method.
- Functionally graded materials, functionally graded porous materials, porous metal foam and laminated composite material are used.
- Composite plate models subjected to mechanical load and thermal buckling.
- A size-dependent model for microplates based on a general framework of higher-order shear deformation plate theory, the modified strain gradient theory and the modified couple stress theory are employed.
- The utilization of surrogate models, namely polynomial chaos expansion, stochastic collocation method, and Monte Carlo simulation, are employed in this study.
- To achieve efficient evaluations for optimal responses, the meta-heuristic algorithms Balancing Composite Motion Optimization (BCMO), Shrimp and Goby association Search algorithm (SGA), and Differential evolution (DE) are developed.
- Ritz-BCMO, Ritz-SGA, Ritz-DE, BCMO-ANN, Ritz-iBCMO and iBCMO-DNN algorithms are developed for investigation of the impacts of material distribution, material length scale parameters, porosity density, temperature variations and boundary conditions on the static, natural frequencies, critical buckling loads and the critical buckling temperatures of plates.

1.5 Thesis outline

This dissertation is structured into seven chapters. A concise overview of each chapter is provided in the following section.

- **Chapter 1** describes the motivation, the literature review of the problem research, objectives, the scope, and the research approaches of the dissertation.

- **Chapter 2** provides an overview of the theoretical basis.
- **Chapter 3** presents a Ritz-based computational method for size-dependent analysis of advanced composite microplates under thermo-mechanical loads.
- **Chapter 4** illustrates the intelligent computational algorithms for stochastic analysis of functionally graded microplates with uncertainties of material properties.
- **Chapter 5** provides the meta-heuristic optimization algorithms for vibration and buckling optimization of laminated composite plates.
- **Chapter 6** closes this dissertation with remarkable main conclusions and provides recommendations for future research.

CHAPTER 2

OVERVIEW OF THEORETICAL BASIS

This chapter focuses on presenting the main contents including advanced composite materials, plate theories, Ritz solution, size-dependent analysis, stochastic methods, neural network systems, meta-heuristic algorithms.

2.1 Advanced composite materials for analysis of plates

2.1.1 Laminated composite materials

Due to their many advantages in stiffness and lightness, laminated composite materials have been widely applied in many engineering fields, such as aviation and construction, mechanical engineering, etc. The LC structure is made of two or more layers of component composite materials that are bonded together at the interface between the layers (Fig.2.1).

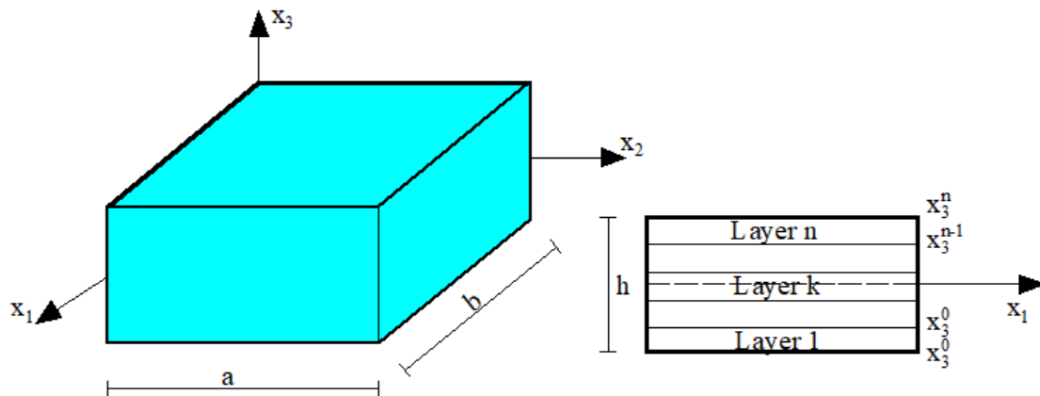


Figure 2.1: The geometric of laminated composite plates

The disadvantage of this type of material is that material discontinuity at the interface between the layers can lead to significant stress concentrations and delamination phenomena.

2.1.2 Functionally graded materials

In order to overcome drawbacks of LC materials, functionally graded materials (FGMs) have been made in which the properties of the different materials vary

continuously in one direction (Fig.2.2) to improve and optimize the structure's ability to withstand mechanical and thermal loads according to desired requirements. The concept of FGM first appeared in 1984 in Japan by a group of materials scientists in aviation [113].

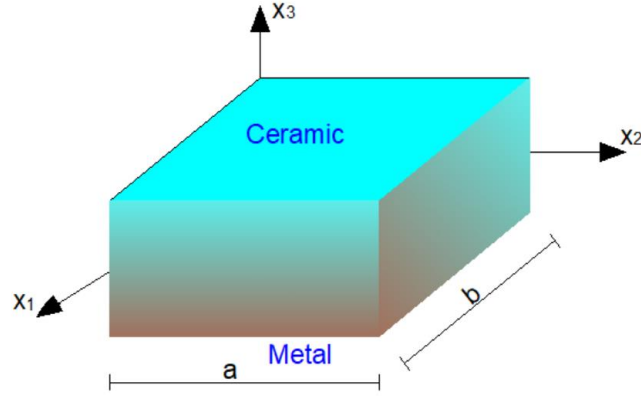


Figure 2.2: Functionally grade materials

Moreover, porosity can occur within materials during the process of manufacture. Functionally graded materials with porosity parameters (FGP) (Fig.2.3) have seen wide utility in various systems. The material properties such as Young's modulus E , mass density ρ , Poisson's ratio ν of FGP material can be approximated by the following expressions ([114]):

$$P(x_3) = (P_c - P_m)V_c(x_3) + P_m - 0.5\beta(P_c + P_m) \quad (2.1)$$

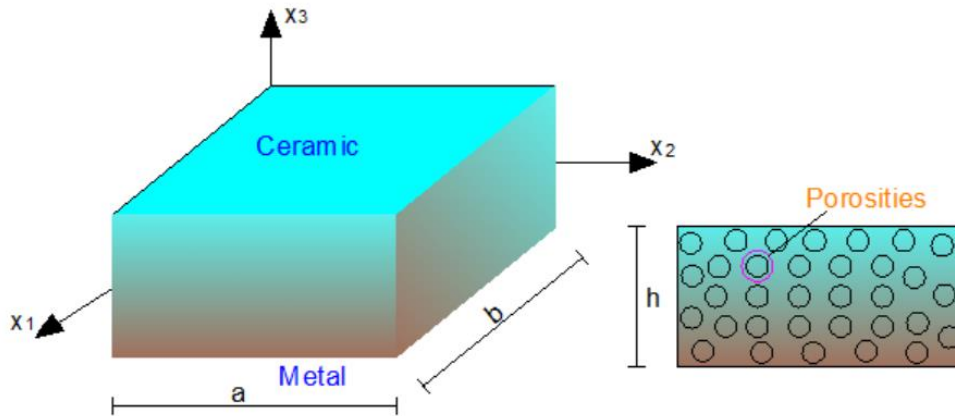


Figure 2.3: Geometry of FGP microplates

where P_c and P_m are the material properties of ceramic and metal; V_c is the volume fraction of material, $0 \leq \beta \ll 1$ is the porosity volume fraction; $x_3 \in [-h/2, h/2]$.

The investigation of the material properties involves the analysis of a series of functions that are associated with the distribution of volume fractions within these materials. Many models have been developed to solve the distribution of volume fractions: power-law model, Sigmoid model, exponential function law, and Mori-Tanaka scheme.

Power-law model [115]:

$$V_c(x_3) = \left(\frac{1}{2} + \frac{x_3}{h} \right)^p \quad (2.2)$$

with p is the power-law index which is positive and $x_3 \in [-h/2, h/2]$.

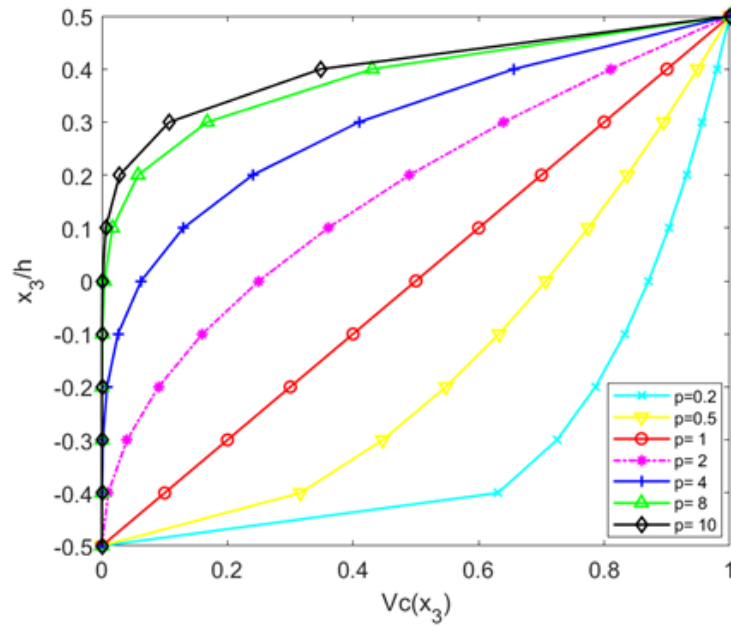


Figure 2.4: The volume fraction of material $V_c(x_3)$ follow Power-law

The material properties according to the Sigmoid model are determined as follows [115]:

$$V_c(x_3) = \begin{cases} 1 - \frac{1}{2} \left(1 - \frac{2x_3}{h} \right)^p & ; \quad 0 \leq x_3 \leq \frac{h}{2} \\ \frac{1}{2} \left(1 + \frac{2x_3}{h} \right)^p & ; \quad -\frac{h}{2} \leq x_3 \leq 0 \end{cases} \quad (2.3)$$

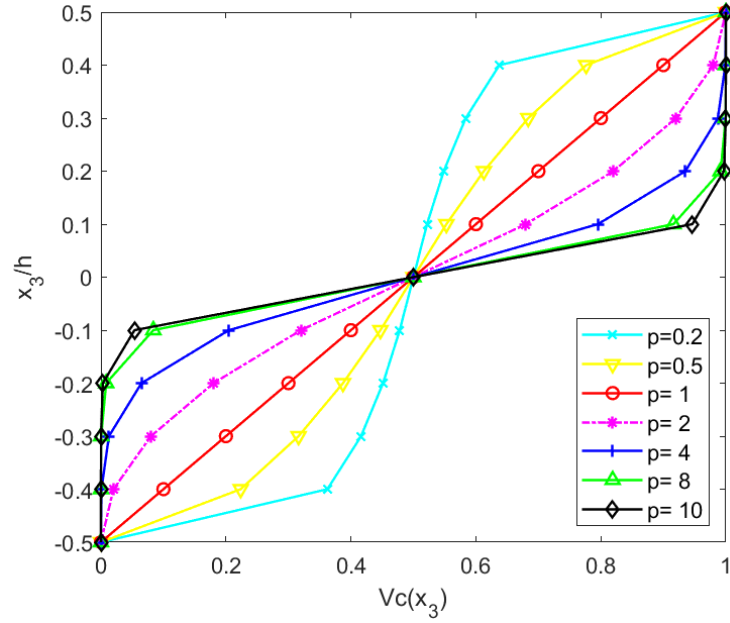


Figure 2.5: The volume fraction of material $V_c(x_3)$ follow Sigmoid

The material properties according to the exponential function law are determined as follows [26] :

$$V_c(x_3) = e^{p\left(\frac{1}{2} + \frac{x_3}{h}\right)} \quad (2.4)$$

Furthermore, the Mori-Tanaka scheme [116] predicts the accurate material properties:

$$\frac{K - K_1}{K_2 - K_1} = \frac{V_c}{1 + \frac{3V_m(K_2 - K_1)}{3K_1 + 4G_1}} ; \frac{G - G_1}{G_2 - G_1} = \frac{V_c}{1 + \frac{V_m(G_2 - G_1)}{G_1 + f_1}} \quad (2.5a)$$

$$f_1 = \frac{G_1(9K_1 - 8G_1)}{6(K_1 + 2G_1)} ; E = \frac{9KG}{3K + G} ; \nu = \frac{3K - 2G}{6K + 2G} \quad (2.5b)$$

with ν , G , K are the Poisson's ratio, local shear modulus local, and bulk modulus, respectively.

2.1.3 Functionally graded sandwich materials

In addition, functionally graded sandwich materials have been designed to optimize structures performance through a controlled gradation of properties across the material's thickness. Sandwich structures offer numerous advantages, such as being lightweight and having high bending stiffness, making them ideal for use in aircraft,

aerospace, flexible electronics, and biomedical applications. A typical sandwich structure consists of two FGMs face sheets with a homogeneous core in between.

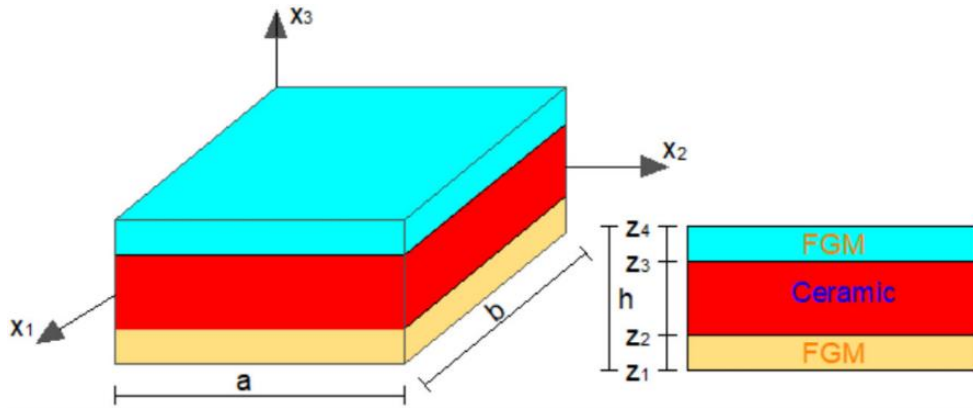


Figure 2.6: Geometric of functionally grade sandwich plate

The FG sandwich materials with thickness h as shown in Fig. 2.6 It is composed of a mixture of ceramic and metal materials whose material properties vary continuously in the thickness direction. The plate is made up of two FG faces comprised of ceramic-metal components and a homogenous core which called sandwich FG plate in which the volume fraction of the ceramic material $V_c(x_3)$ across the plate thickness is determined by ([117]):

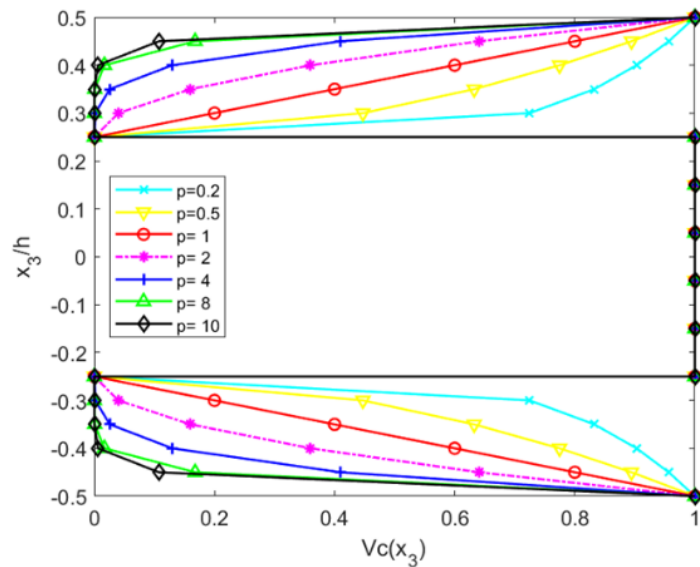


Figure 2.7: The volume fraction of the ceramic material $V_c(x_3)$ of sandwich FG plate (1-2-1)

$$V_c(x_3) = \begin{cases} \left(\frac{z_4 - x_3}{z_4 - z_3} \right)^p, & z_3 \leq x_3 \leq z_4 & \text{FG} & \text{top} & \text{layer} \\ 1 & z_2 \leq x_3 \leq z_3 & \text{ceramic} & \text{core} & \text{layer} \\ \left(\frac{x_3 - z_1}{z_2 - z_1} \right)^p & z_1 \leq x_3 \leq z_2 & \text{FG} & \text{bottom} & \text{layer} \end{cases} \quad (2.6)$$

2.1.4 Porous metal foam materials

Besides, based on the high technology in the fabrication of materials, porous metal foam materials can increase sound dampening while reducing the overall weight of the structures that can be manufactured. An effective material properties of porous metal foam materials are expressed as follows ([118]):

- Distribution of uniform porosity (UD)

$$\rho(x_3) = \rho_{\max} \sqrt{(1 - \beta v)}; E(x_3) = E_{\max} (1 - \beta v) \quad (2.7)$$

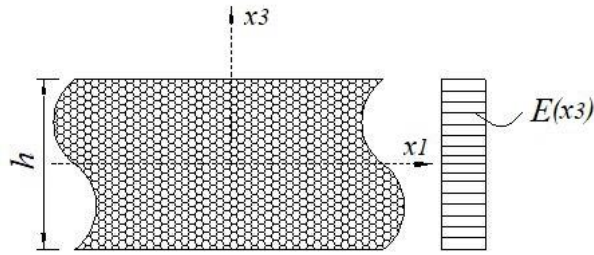


Figure 2.8: Porosity is uniformly distribution

- Distribution of asymmetric porosity (AD)

$$\rho(x_3) = \rho_{\max} \left[1 - \beta_m \cos \left(\frac{\pi z}{2h} + \frac{\pi}{4} \right) \right]; E(x_3) = E_{\max} \left[1 - \beta \cos \left(\frac{\pi z}{2h} + \frac{\pi}{4} \right) \right] \quad (2.8)$$

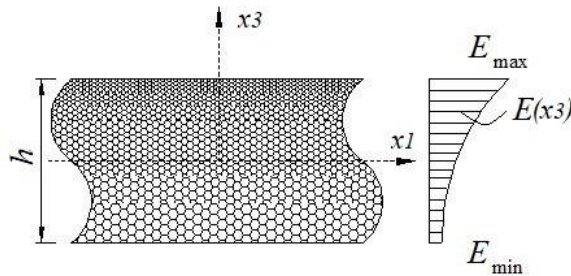


Figure 2.9: Porosity is asymmetric distribution

- Distribution of symmetric porosity (SD)

$$\rho(x_3) = \rho_{\max} \left(1 - \beta_m \cos\left(\frac{\pi z}{h}\right) \right); E(x_3) = E_{\max} \left(1 - \beta \cos\left(\frac{\pi z}{h}\right) \right) \quad (2.9)$$

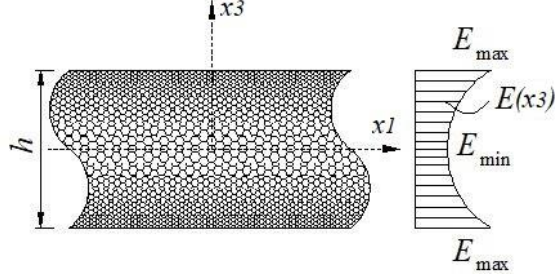


Figure 2.10: Porosity is symmetric distribution

where E_{\max} and ρ_{\max} are maximum values of Young's modulus and mass density, respectively; β and β_m denote the porosity parameters and mass density, respectively, which are given by:

$$\beta = 1 - \frac{E_{\min}}{E_{\max}}, 0 < \beta < 1; \beta_m = 1 - \frac{\rho_{\min}}{\rho_{\max}}, 0 < \beta_m < 1; \beta_m = 1 - \sqrt{1 - \beta} \quad (2.10)$$

where E_{\min} and ρ_{\min} are minimum Young's modulus and mass density, respectively. It is noted that the material characteristics in the case of a uniform distribution of porosity remain constant in the thickness direction and depend only on the porosity coefficient β . Thereafter, the coefficient ν is written as follows:

$$\nu = \frac{1}{\beta} - \frac{1}{\beta} \left(\frac{2}{\pi} \sqrt{1 - \beta} - \frac{2}{\pi} + 1 \right)^2 \quad (2.11)$$

2.2 Plate theories

Plate theories are formulated by using the semi-inverse approach, which involves making an informed assumption about the shape of the displacement field or stress field. This assumption allows for sufficient flexibility in the assumed field to ensure compliance with the equations of elasticity. In the context of plates, the displacement field is expressed in terms of unknown functions ϕ_i^j of the surface coordinates (x_1, x_2) and time t [119]:

$$u_i(x_1, x_2, x_3, t) = \sum_{j=0}^N (x_3)^j \phi_i^j(x_1, x_2, t) \quad (2.12)$$

The explicit form of Eq. (2.12) varies depending on the kinematics of the deformation being considered including CPT, FSDT, HSDT, Quasi-3D, and three-dimensional elasticity.

2.2.1 Classical plate theory

The classical plate theory ignores the effect of shear deformation, so it is only suitable for thin plates.

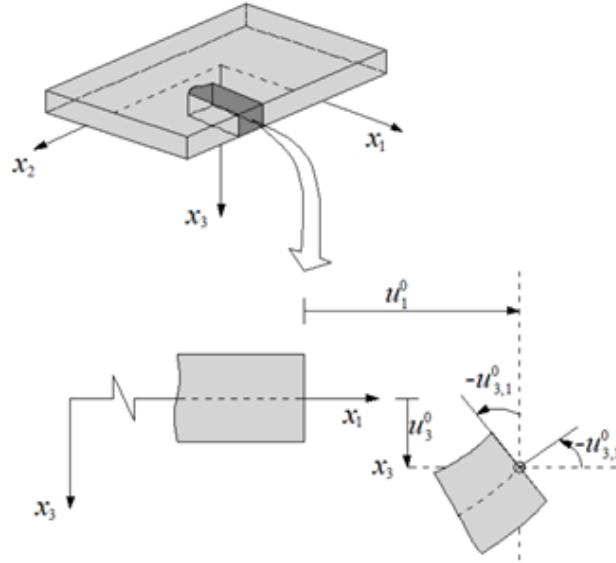


Figure 2.11: Un-deformed and deformed geometries of an edge of a plate

However, due to the simplicity of the approximate displacement field, this is the simplest approach to analyzing the behaviors of LC and FG plates [115], the displacement field of CPT can be shown as follows:

$$u_1(x_1, x_2, x_3, t) = u_1^0(x_1, x_2) - x_3 u_{3,1}^0 \quad (2.13a)$$

$$u_2(x_1, x_2, x_3, t) = u_2^0(x_1, x_2) - x_3 u_{3,2}^0 \quad (2.13b)$$

$$u_3(x_1, x_2, x_3, t) = u_3^0(x_1, x_2) \quad (2.13c)$$

where u_1^0 , u_2^0 , u_3^0 are the displacement components according to x_1 , x_2 , x_3 coordinates at the neutral surface.

2.2.2 First-order shear deformation theory

To address the effect of shear deformation in plates, the first-order shear deformation theory is the simplest method, but it requires a shear correction factor

to properly handle the free-traction boundary conditions for shear stresses ([44]), the displacement field can be expressed as follows:

$$u_1(x_1, x_2, x_3, t) = u_1^0(x_1, x_2) + x_3 \varphi_1(x_1, x_2) \quad (2.14a)$$

$$u_2(x_1, x_2, x_3, t) = u_2^0(x_1, x_2) + x_3 \varphi_2(x_1, x_2) \quad (2.14b)$$

$$u_3(x_1, x_2, x_3, t) = u_3^0(x_1, x_2) \quad (2.14c)$$

with φ_1, φ_2 are the angle of rotation with respect to the x_1 and x_2 axes, respectively. Besides, the FSDT can return to the CPT when the angle of rotations is derivative transverse displacement.

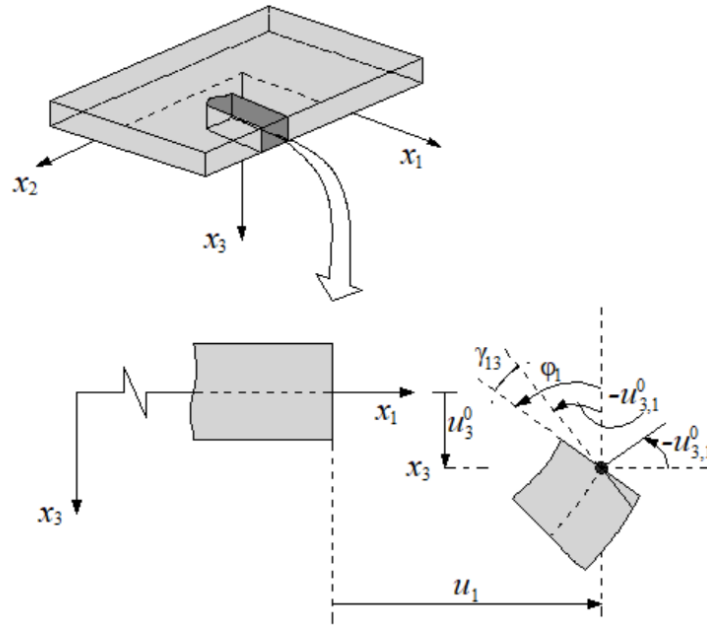


Figure 2.12: Un-deformed and deformed geometries of an edge of a plate

2.2.3 Higher-order shear deformation theory

The higher-order shear deformation theory does not require a shear transverse factor and behaves better than FSDT. Many groups of authors have proposed HSDT theories with various degrees of success [120] in which some studies have developed some models and some techniques to reduce the number of variables in the computational model ([121, 122]). It can be seen that building the HSDT including the membrane and transverse displacements, rotations, with high

accuracy, simplicity, and efficiency is a topic that attracts many researchers. It is derived from the plate theory as follows:

$$u_1(x_1, x_2, x_3, t) = u_1^0(x_1, x_2) - x_3 u_{3,1}^0 + f(x_3) \varphi_1(x_1, x_2) \quad (2.15a)$$

$$u_2(x_1, x_2, x_3, t) = u_2^0(x_1, x_2) - x_3 u_{3,2}^0 + f(x_3) \varphi_2(x_1, x_2) \quad (2.15b)$$

$$u_3(x_1, x_2, x_3, t) = u_3^0(x_1, x_2) \quad (2.15c)$$

where $f(x_3)$ is a high-order term whose first derivative satisfies the free-stress boundary condition at the top and bottom surfaces of the plates, i.e. $f_{,3}(x_3 = \pm 0.5h) = 0$.

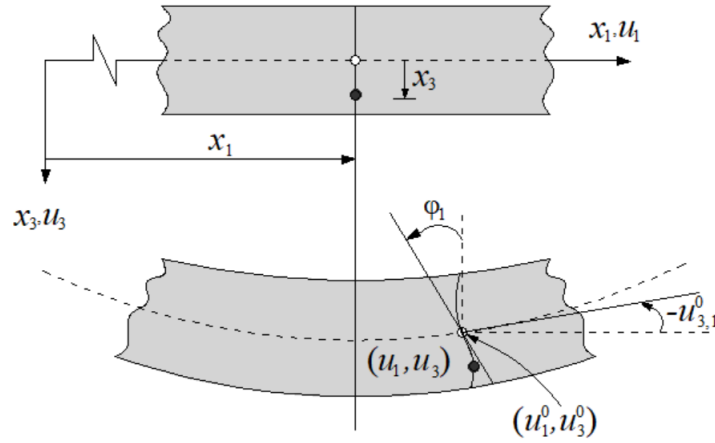


Figure 2.13: Deformation of a transverse normal according to the higher-order plate theory

Besides, it is well-known that the HSDT generally predicts more accurate than the FSDT, however, its accuracy depends on a choice of the shear functions [123].

2.2.4 A Quasi-3D theory

In recent years, researchers ([124, 125]) also proposed various quasi-3D theories which displacement field is described as shows:

$$u_1(x_1, x_2, x_3, t) = u_1^0(x_1, x_2) - x_3 u_{3,1}^0 + f(x_3) \varphi_1(x_1, x_2) \quad (2.16a)$$

$$u_2(x_1, x_2, x_3, t) = u_2^0(x_1, x_2) - x_3 u_{3,2}^0 + f(x_3) \varphi_2(x_1, x_2) \quad (2.16b)$$

$$u_3(x_1, x_2, x_3, t) = u_3^0(x_1, x_2) + f_{,3}(x_3) \varphi_3(x_1, x_2) \quad (2.16c)$$

Although plate models incorporating higher-order variations of both in-plane and out-of-plane displacements generally provide more accurate predictions than the HSDTs, they are more complex and costly to implement due to the increased number of variables.

In particular, three-dimensional (3D) [126] analysis, based on linear and small strain elasticity theory, does not rely on any hypotheses involving the kinematics of deformation. Such analysis provides realistic results that the two-dimensional theories cannot otherwise predict. However, constructing form functions for this theory is a challenge.

2.3 Size dependent analysis of microplates

The recent development of FG microplates with continuous material variations in a required direction and significant porosity density requires advanced computational theories and models. However, it is well known that the classical elasticity theory could not accurately predict the behaviors of such structures at a small scale. To overcome this problem, the material size-dependent theory has been proposed to predict static and dynamic behaviors of nano- and micro-structures using different approaches. The nonlocal elasticity theory initiated by Eringen [58] can be used to capture the size effects of nanostructures. The nonlocal stress components can be defined as:

$$t_{ij}(x) = \int_V \alpha(|x' - x|, \tau) \sigma_{ij}(x') dx' \quad (2.17)$$

where t_{ij} is the total nonlocal stress, τ is a length scale parameter, σ_{ij} is the local Cauchy stress tensor, and $\alpha(|x' - x|, \tau)$ is the nonlocal kernel function. Nevertheless, the implementation of this theory for microplates with different boundary conditions appears to be quite complicated. Another way to investigate the size effects is to use the classical strain gradient theory of Mindlin ([52, 53]) defined the density of strain energy as:

$$\delta \Pi_{UB} = \int_A (\boldsymbol{\sigma} \delta \boldsymbol{\epsilon} + \mathbf{m} \delta \boldsymbol{\chi} + \tilde{\mathbf{m}} \delta \tilde{\boldsymbol{\chi}} + \hat{\mathbf{m}} \delta \hat{\boldsymbol{\chi}} + \bar{\mathbf{m}} \delta \bar{\boldsymbol{\chi}} + \bar{\bar{\mathbf{m}}} \delta \bar{\bar{\boldsymbol{\chi}}}) dA \quad (2.18)$$

where $\boldsymbol{\varepsilon}, \boldsymbol{\chi}, \tilde{\boldsymbol{\chi}}, \hat{\boldsymbol{\chi}}, \bar{\boldsymbol{\chi}}, \bar{\bar{\boldsymbol{\chi}}}$ are strains, rotation, second gradient of displacement, gradient of strain, gradient of rotation, symmetric part of gradient strain, respectively; $\boldsymbol{\sigma}$ is Cauchy stress; $\mathbf{m}, \tilde{\mathbf{m}}, \hat{\mathbf{m}}, \bar{\mathbf{m}}, \bar{\bar{\mathbf{m}}}$ are high-order stresses corresponding with strain gradients $\boldsymbol{\chi}, \tilde{\boldsymbol{\chi}}, \hat{\boldsymbol{\chi}}, \bar{\boldsymbol{\chi}}, \bar{\bar{\boldsymbol{\chi}}}$, respectively. The components of strain ε_{ij} and strain gradients $\chi_{ij}, \tilde{\chi}_{ijk}, \hat{\chi}_{ijk}, \bar{\chi}_{ij}, \bar{\bar{\chi}}_{ijk}$ are defined as follows:

$$\chi_{ij} = (u_{n,mj}e_{imn} + u_{n,mi}e_{jmn})/4; \tilde{\chi}_{ijk} = u_{k,ij}; \hat{\chi}_{ijk} = (u_{k,ji} + u_{j,ki})/2 \quad (2.19a)$$

$$\bar{\chi}_{ijk} = \frac{1}{2}e_{jlk}u_{k,li}; \bar{\bar{\chi}}_{ijk} = \frac{1}{3}(u_{k,ij} + u_{i,jk} + u_{j,ki}); \varepsilon_{ij} = (u_{i,j} + u_{j,i})/2 \quad (2.19b)$$

with e_{ijk} is the alternator.

The modified strain gradient theory (MST) reduces the number of independent higher-order length scale parameters for the second strains in Mindlin's strain gradient theory from five to three ([51]). The process of reduction is a crucial advancement in facilitating the experimental analysis of strain gradient behavior. By solely employing bending and torsion, it becomes possible to fully characterize the elastic strain gradient of a material that is approximately incompressible. The strain energy variation of the system $\delta\Pi_{UB}$ is obtained by the MST theory:

$$\delta\Pi_{UB} = \int_A (\boldsymbol{\sigma}\delta\boldsymbol{\varepsilon} + \mathbf{p}\delta\boldsymbol{\xi} + \boldsymbol{\tau}\delta\boldsymbol{\eta} + \mathbf{m}\delta\boldsymbol{\chi})dA \quad (2.20)$$

where $\boldsymbol{\varepsilon}, \boldsymbol{\chi}, \boldsymbol{\xi}, \boldsymbol{\eta}$ are strains, symmetric rotation gradients, dilatation gradient and deviation stretch gradient, respectively; $\boldsymbol{\sigma}$ is Cauchy stress; $\mathbf{m}, \mathbf{p}, \boldsymbol{\tau}$ are high-order stresses corresponding with strain gradients $\boldsymbol{\chi}, \boldsymbol{\xi}, \boldsymbol{\eta}$, respectively.

The components of strain ε_{ij} and strain gradients $\xi_i, \eta_{ijk}, \chi_{ij}$ are defined as follows:

$$\varepsilon_{ij} = (u_{i,j} + u_{j,i})/2; \xi_i = \varepsilon_{mm,i} \quad (2.21a)$$

$$\eta_{ijk} = (\varepsilon_{jk,i} + \varepsilon_{ki,j} + \varepsilon_{ij,k})/3 - \left[(\xi_i + 2\varepsilon_{mi,m})\delta_{jk} + (\xi_k + 2\varepsilon_{mk,m})\delta_{ij} + (\xi_j + 2\varepsilon_{mj,m})\delta_{ki} \right]/15 \quad (2.21b)$$

$$\chi_{ij} = (u_{n,mj}e_{imn} + u_{n,mi}e_{jmn})/4 \quad (2.21c)$$

where δ_{ij} is Kronecker delta; e_{imn} is permutation symbol. The constitutive equations are used to determine the stress components as follows:

$$\sigma_{ij} = \lambda \varepsilon_{kk} \delta_{ij} + 2\mu \varepsilon_{ij}; \quad m_{ij} = 2\mu l_1^2 \chi_{ij}; \quad p_j = 2\mu l_2^2 \xi_j; \quad \tau_{ijk} = 2\mu l_3^2 \eta_{ijk} \quad (2.22)$$

where λ, μ are Lamé constants; l_1, l_2, l_3 are three material length scale parameters (MLSP) which should be practically determined by experimental works. In the absence of stretch and dilatation gradients in the MST theory, the modified couple stress (MCT) initiated by Yang et al. [50] was known as the simplest one to include the size effects with only one MLSP associated. The strain energy of the system Π_{UB} is given by:

$$\delta \Pi_{UB} = \int_A (\boldsymbol{\sigma} \delta \boldsymbol{\varepsilon} + \mathbf{m} \delta \boldsymbol{\chi}) dA \quad (2.23)$$

2.4 Ritz solution

The Ritz method was initially introduced by Walter Ritz [36] to analyze the free vibrations of structures. Since then, a multitude of researchers have used this method to investigate the static and dynamic responses of beams, plates, and shells. According to the Ritz technique, the following series type solution of approximation functions and related series values may be used to represent the transverse and membrane displacements, rotations, $(u_1^0, u_2^0, u_3^0, \varphi_1, \varphi_2)$ of the plates:

$$\{u_1^0(x_1, x_2, t), \varphi_1(x_1, x_2, t)\} = \sum_{j=1}^{N_1} \sum_{i=1}^{N_2} \{u_{1ji}(t), x_{ji}(t)\} F_{j,1}(x_1) P_i(x_2) \quad (2.24a)$$

$$\{u_2^0(x_1, x_2, t), \varphi_2(x_1, x_2, t)\} = \sum_{j=1}^{N_1} \sum_{i=1}^{N_2} \{u_{2ji}(t), y_{ji}(t)\} F_j(x_1) P_{i,2}(x_2) \quad (2.24b)$$

$$u_3^0(x_1, x_2, t) = \sum_{j=1}^{N_1} \sum_{i=1}^{N_2} u_{3ji}(t) F_j(x_1) P_i(x_2) \quad (2.24c)$$

where $u_{1ji}, u_{2ji}, u_{3ji}, x_{ji}, y_{ji}$ are variables that need to be calculated; the shape functions in the x_1 – and x_2 – directions are represented by $F_j(x_1), P_i(x_2)$.

It can be noted that the Ritz solution's precision, numerical instabilities and convergence rates are dependent on the construction of approximation functions

[127], which must be orthogonal and satisfy the conditions for stress freedom. Consequently, it is essential to meticulously select a set of functions that not only produce physically accurate results but also possess favorable numerical properties. Therefore, developing new hybrid shape functions for the Ritz method is necessary.

2.4.1 Product of trigonometric functions

Admissible functions as product of trigonometric functions. The initial implementation of this particular function was conducted by Chai [41]. The investigation conducted by this researcher focused on the analysis of the free vibration characteristics exhibited by plates, both with and without the presence of a concentrated mass. The investigation is predicated upon the utilization of the Rayleigh method, wherein a solitary term of the trigonometric function product is employed.

$$F_j(x_1) = \sin\left(\frac{\pi x_1}{a}\right) \sin\left(\frac{j\pi x_1}{a}\right) \quad (2.25)$$

Nguyen et al. [128] utilized the Ritz method to investigate the buckling, bending, and vibration of laminated composite beams using the trigonometric-series solution as a shape function with a number of series which is 14 for deflection for simply supported as follow:

$$\varphi_j(x_1) = \sin \frac{j\pi}{L} x_1; \quad \psi_j(x_1) = \cos \frac{j\pi}{L} x_1; \quad \xi_j(x_1) = \cos \frac{j\pi}{L} x_1 \quad (2.26)$$

Where L is length of beam.

2.4.2 Static beam functions

Zhou Ding [129] was the first to propose the utilization of static beam functions as admissible functions in the Ritz method. The above functions come from the basic solution of the differential equation that describes what happens to a Euler-Bernoulli beam when a concentrated load is put on it. A collection of third-order polynomial functions can be established by altering the placement of the point load exerted on the beam. The determination of the coefficients of the polynomials is based on the boundary conditions. In addition to determining the frequency

parameters of a clamped beam, the eigenvalues of five plates with distinct boundary conditions are also computed. There is a notable level of concurrence with the precise solution, along with a commendable level of accuracy when compared to outcomes obtained using characteristic functions. Static Beam Functions (SBF):

$$F_j(x_1) = A_j + B_j x_1 + C_j x_1^2 + D_j x_1^3 + \sin\left(\frac{jx_2}{L}\right) \quad (2.27)$$

$$\text{with } A_j = 0; B_j = -\frac{j\pi}{L}; C_j = \frac{j\pi((-1)^j + 2)}{L^2}; D_j = -\frac{j\pi((-1)^j + 1)}{L^3}.$$

Lee et al. [130] utilized static beam functions to investigate the free vibration analysis of rectangular plates supported by elastic point supports. The researchers present an analysis of the initial three modes exhibited by a square plate that is subjected to simple support along all four edges, while also incorporating a central elastic point support. This study examines the impact of both the stiffness and the placement of the elastic point support on the frequency parameter.

2.4.3 Characteristic functions

Young [131] utilized characteristic functions or eigen-functions as a means of examining the free vibrations exhibited by different plate configurations. These configurations encompassed clamped plates, cantilever plates, as well as plates with two adjacent edges clamped and the remaining two edges left free. The aforementioned functions establish the normal modes of vibration for a beam. Characteristic Functions (CF) as below:

$$F_j(x_1) = \sin \alpha_j x_1 - \sinh \alpha_j x_1 - \phi_j (\cos \alpha_j x_1 - \cosh \alpha_j x_1) \quad (2.28)$$

$$\text{with } \phi_j = \frac{\sin \alpha_j a - \sinh \alpha_j a}{\cos \alpha_j a - \cosh \alpha_j a}; \alpha_j = \frac{(j + 0.5)\pi}{a}.$$

Kim [132] conducted an analysis of the vibration characteristics of fully clamped rectangular plates composed of a functionally graded material consisting of both metal and ceramic components. The present study investigates the influence of temperature on the material properties, which exhibit a variation across thickness.

This variation follows a power-law distribution based on the volume fractions of the constituents. The application of the Ritz method involves utilizing the characteristic functions of clamped beams while incorporating a third-order shear deformation theory to accurately consider the effects of rotary inertia and transverse shear strains. The presented numerical findings indicate that the vibration characteristics are notably impacted by the composition of the materials, the geometry of the plate, and the increase in temperature.

2.4.4 Modified characteristic functions

Gartner and Olgac [133] introduced a revised set of characteristic functions for beams to address the numerical challenges associated with their original formulation. This modification ensures that the magnitudes of the terms fall within the range of $[-1, 1]$. The modified Characteristic Functions as follow:

$$F_j(x_1) = \cos \alpha_j x_1 + A_j \sin \alpha_j x_1 + B_j e^{-\alpha_j x_1} + C_j e^{-\alpha_j (L-x_1)} \quad (2.29)$$

$$\text{with } \alpha_j = \frac{(j+0.5)\pi}{a}; A_j = -\frac{1+(-1)^j e^{-\alpha_j}}{1-(-1)^j e^{-\alpha_j}}; B_j = -\frac{1}{1-(-1)^j e^{-\alpha_j}}; C_j = -\frac{(-1)^j}{1-(-1)^j e^{-\alpha_j}}$$

Pao and Peterson [134] employed a collection of altered characteristic functions within the framework of the Ritz method to graphically represent the contours of free vibration and buckling mode shapes of plates. The plates that were examined in this study possessed a square shape and were subjected to full clamping. These plates were constructed using both isotropic and composite materials. In addition to illustrating the amplitude variations of the first six mode shapes, the contour plots also provide insights into the orientation of the fibers in the single-layer laminate plate under analysis. In their study, Dasgupta and Huang [135] introduced a layer-wise approach to analyze the free vibration of thick, arbitrarily laminated spherical panels. The panels were subjected to various boundary conditions at their four edges, including combinations of simply supported, free, clamped, and guided conditions in each lamina. The proposed model uses a displacement field that is defined by finite element interpolation shape functions in the thickness direction

and modified characteristic functions in both the in-plane and latitudinal directions. According to the authors, the utilization of both the Ritz and finite element methods offers substantial computational resource savings compared to a sole three-dimensional finite element analysis while maintaining a given level of accuracy.

2.4.5 Orthogonal polynomials

This task will discuss the admissible functions known as orthogonal polynomials (OP) proposed by Bhat [136], which are constructed using the Gram-Schmidt method [137]. These functions exhibit a rapid convergence rate, although they encounter challenges in determining the initial function. The initial polynomial $\phi_0(x_1)$ exhibits adherence to both the essential geometric conditions and the inherent boundary conditions, $x \in [c, d]$. Using the Gram-Schmidt approach as follow:

$$\phi_1(x_1) = (x_1 - A_1)\phi_0(x_1), \quad \phi_k(x_1) = (x_1 - A_k)\phi_{k-1}(x_1) - D_k\phi_{k-2}(x_1) \quad (2.30a)$$

$$A_k = \frac{\int_c^d x_1 w(x_1) \phi_{k-1}^2(x_1) dx}{\int_c^d w(x_1) \phi_{k-1}^2(x_1) dx}; \quad D_k = \frac{\int_c^d x_1 w(x_1) \phi_{k-1}(x_1) \phi_{k-2}(x_1) dx}{\int_c^d w(x_1) \phi_{k-2}^2(x_1) dx} \quad (2.30b)$$

where $w(x_1)$ being the weighting function. Orthogonality is satisfied by the polynomials $\phi_k(x_1)$ as below:

$$\int_c^d w(x_1) \phi_k(x_1) \phi_l(x_1) dx = \begin{cases} 0 & \text{if } k \neq l \\ a_{kl} & \text{if } k = l \end{cases} \quad (2.31)$$

Sun et al. [39] proposed a method for calculating the vibration of rotating cylindrical shells featuring arbitrary edges via the Ritz method with orthogonal polynomials as the shape function for series-type solutions, which are resolved from the Gram-Schmidt procedure in which the first function (SSSS BC: $\phi_0''(\xi) = 1; \phi_0^v(\xi) = \phi_0^w(\xi) = \xi^2 - \xi$) is carried out in a way that satisfies the cylindrical shell's geometric boundary constraints. Song et al. [138] showed the traveling wave analysis of rotating cross-ply laminated cylindrical shells based on

Donnel's shell theory and the Ritz approach for boundary conditions, in which, a set of orthogonal polynomials as the shape function is produced via the Gram-Schmidt process. Parashar et al. [139] employed the Ritz method to study the free vibration of piezoceramic cylindrical shells based on a three-dimensional model, the starting functions satisfying the electric boundary conditions which are used for the Gram-Schmidt technique to build the shape function, with the starting functions satisfying the electric boundary conditions.

2.4.6 Non-orthogonal polynomials

This particular set does not exhibit orthogonality, resulting in the loss of certain computational benefits. However, the primary benefit of these functions lies in their ability to eliminate the requirement for intricate generation procedures, such as those employed in the creation of orthogonal polynomials. The evaluation of the integrals is significantly simpler when compared to those involving orthogonal polynomials. For example, Non-orthogonal polynomials (NOP) which constitute a set of polynomials that are derived by increasing the exponent of the multiplying variable ([140]) for full clamped BC, the flexural vibration of rectangular plates approached by using simple polynomials in the Rayleigh-Ritz method as follow:

$$F_j(x_1) = (a - x_1)^2 x_1^{j+1} \quad (2.32)$$

Nguyen et al. ([141, 142]) presented the free vibration and buckling and analysis of functionally graded sandwich beams based on the Ritz solution in which the admissible functions was derived from non-orthogonal polynomial series.

$$\psi(x_1) = x_1^{j-1} \quad (2.33)$$

Aydogdu ([143, 144]) investigated the vibration and buckling of laminated composite beams based on the Ritz approach therein the shape function is determined in a series of simple algebraic polynomials that are not orthogonal, the shape function for full clamped as below:

$$\psi(\zeta) = \zeta^j (\zeta - 1)^2, \zeta = x_1 / L \quad (2.34)$$

with L is the length of beams.

2.4.7 Hybrid shape function

Recently, there has been development in the utilization of the admissible function as a hybrid form. This development has shown rapid convergence in the analysis of natural frequency, buckling, and displacement for both plates and beams. For instance, Mantari and Canales [145] studied the buckling and free vibration of LC beams using the Ritz method with shape functions that are built from a hybrid polynomial-trigonometric series compared with pure polynomial series:

$$T_j = x_1^{j-1} \begin{cases} \left(\frac{x_1}{L}\right)^{j-1} & j = 1, 2, 3 \\ \cos\frac{(j-3)\pi x_1}{L} & j = 4, \dots, n \end{cases} \quad (2.35)$$

Nguyen Duong et al. [146] studied the for the buckling and frequency behavior of I-beams by employing the Ritz method in which the form function as a hybrid with a series of exponential functions combined with a polynomial to satisfy the boundary conditions. The shape function for edges clamped CC as follow:

$$T_j = \left(1 - \frac{x_1}{L}\right)^2 \left(\frac{x_1}{L}\right)^2 e^{-\frac{jx_1}{L}} \quad (2.36)$$

with L is the length of beams.

Li et al. [117] demonstrated the frequency of rectangular FG plates via the Ritz method in a three-dimensional model using the Chebyshev polynomial- type one series multiplied by appropriate functions to satisfy the essential boundary conditions:

$$T_j(x_1) = \cos\left[(j-1)\arccos\left(\frac{x_1}{L}\right)\right], j = 1, 2, 3 \quad (2.37)$$

2.5 Stochastic method

The properties of the material may be uncertain in actuality, owing to the manufacturing process or other unexpected situations. This uncertainty alters the static and dynamic behaviors of the structures, necessitating the use of sophisticated computational techniques.

The mean or expected value of a function $f(x)$ of an n dimensional random variable vector can be expressed as [147] :

$$\mu_f = E[f(x)] = \int_{\Omega} f(x) \Phi(x) dx \quad (2.38)$$

Similarly the variance of the random function $f(x)$ is given by the integral below:

$$\sigma_f^2 = Var[f(x)] = \int_{\Omega} (f(x) - \mu_f)^2 \Phi(x) dx \quad (2.39)$$

with $\Phi(x)$ is distribution specified.

2.5.1 Monte Carlo Simulation

The most common and straightforward approach for addressing this challenging issue is the Monte Carlo Simulation (MCS) method [75]. In this approach, a set of P samples is randomly selected from the given distribution. The system's responses are assessed for each sample, denoted as u_i , where i ranges from 1 to P . Therefore, the mean μ value and standard deviation (SD) are as follow:

$$\mu = \frac{1}{P} \sum_{i=1}^P u_i \quad (2.40a)$$

$$SD = \sqrt{\frac{1}{P-1} \sum_{i=1}^P (u_i - \mu)^2} \quad (2.40b)$$

However, this method can result in high computing costs, especially when a complex physical model is considered.

2.5.2 Probabilistic spectral methods for the propagation of uncertainty

An alternative approach is to use polynomial chaos expansion (PCE), which can accelerate the computation while maintaining accuracy, as a way to overcome the limitations of MCS. The fundamental goal of this technique is to approximate random outputs as a series of basis functions and their corresponding coefficients in orthogonal space. Stochastic collocation (SC) is known as one of stochastic expansion method similar to the popular PCE. It derives the Lagrange interpolation

polynomials for a set of collocation points and reproduces the model responses at these collocation points as of expansion coefficients. The series is comprised of two essential elements: the basis functions and their corresponding coefficients:

$$\hat{u}(\mathbf{x}) = \sum_{i=0}^{\infty} c_i \kappa_i(\mathbf{q}) \quad (2.41)$$

where κ_i are multivariate orthogonal basis functions; \mathbf{q} is a vector of independent random variables;

2.5.2.1 Polynomial chaos expansion

The above series Eq. (2.41) in terms of a truncated orthogonal series as follows by Askey's scheme ([148, 149]):

$$P = \frac{(n+d)!}{n!d!} \quad (2.42)$$

in which P is the permutation of the qualified order of the polynomial n , and the number of random variable d .

Eq. (2.41) becomes:

$$\hat{u}(\mathbf{x}) = \sum_{i=0}^{P-1} c_i \kappa_i(\mathbf{q}) + r \quad (2.43)$$

with c_i are coefficients to be determined so that the residual r is minimized;

Spectral projection approach: This task can be easily obtained by forcing the residual minimum resulting in the inner product of the residual and each basis function becomes zero. By taking the inner product of both sides of Eq. (2.41) with respect to κ_j :

$$\langle \hat{u}, \kappa_j \rangle = \sum_{i=0}^{P-1} c_i \langle \kappa_i, \kappa_j \rangle \quad (2.44)$$

then enforcing the orthogonality of κ_j , Eq. (2.47) becomes:

$$c_i = \frac{\langle \hat{u}, \kappa_i \rangle}{\langle \kappa_i, \kappa_i \rangle} = \frac{1}{\langle \kappa_i, \kappa_i \rangle} \int \hat{u} \kappa_i \rho_Q(\mathbf{q}) d\mathbf{q} \quad (2.45)$$

The “truth” response \hat{u} is unknown, thus Gauss quadrature approach is implemented for computing c_i as follows:

$$c_i = \frac{1}{\gamma_i} \sum_{j_1=1}^{N_{gp}^1} \dots \sum_{j_d=1}^{N_{gp}^d} (w_{j_1}^1 \times \dots \times w_{j_d}^d) \times \hat{u}(q_{j_1}^1, \dots, q_{j_d}^d) \times \kappa_i(q_{j_1}^1, \dots, q_{j_d}^d) \quad (2.46)$$

where $\gamma_i = \langle \kappa_i, \kappa_i \rangle$ can be analytically computed; N_{gp}^i is the number of quadrature point; q_j^i and w_j^i are the set of quadrature points and their weights, respectively for the random variable i^{th} .

Linear regression approach: The estimation of the vector of residuals can be derived from Eq. (2.41) as follow:

$$\psi = U - c^T \kappa \quad (2.47)$$

Where U is corresponding output evaluations; κ is the matrix whose elements are given by $\kappa_{ij} = \kappa_j(\mathbf{q}^i)$. The estimation of the coefficients c is achieved by minimizing the L2-norm, also known as least-square regression, of the residual that follows:

$$c = \text{Arg} \min \|U - c^T \kappa\|_2^2 \quad (2.48)$$

The coefficients can be determined by solving Eq. (2.51).

$$c = (\kappa^T \kappa)^{-1} \kappa^T U \quad (2.49)$$

2.5.2.2 Stochastic collocation method

For 1-D problem (i.e., one random input X) and n_i interpolation points, it approximates the stochastic response u by forming the Lagrange functions and estimating the model response at interpolation points $u(q_i)$ as follows ([150, 151]):

$$\hat{u}(X) = \sum_{i=1}^{n_i} u(q_i) L_i(q) \quad (2.50)$$

where q is a standard variable mapping to the physical variable X and for maximizing performance of this approach q_i are defined as appropriate Gauss quadrature points corresponding to the distribution of q . The 1-D Lagrange interpolation $L_i(q)$ is defined as:

$$L_i(q) = \prod_{\substack{j=1 \\ j \neq i}}^{n_i} \frac{q - q_j}{q_i - q_j} \quad (2.51)$$

A tensor product of 1-D functions is applied to expand the SC approximation to the multi-dimensional space. Particularly, the expansion of d -variable and n_k collocation points for the k^{th} variable can be expressed as:

$$\hat{u}(\mathbf{q}) = \sum_{j_1=1}^{n_1} \dots \sum_{j_d=1}^{n_d} u(q_{j_1}^1, \dots, q_{j_d}^d) \times (L_{j_1}^1 \otimes \dots \otimes L_{j_d}^d) \quad (2.52)$$

where $\mathbf{q} = [q^1, q^2, \dots, q^d]^T$ is a vector of random inputs.

2.6 Neural network systems

A neural network, also known as an artificial neural network (ANN), is a dynamic system that acquires knowledge through interconnected nodes or neurons arranged in a layered structure that bears a resemblance to the human brain. A neural network possesses the capability to acquire knowledge from data, thereby enabling it to undergo training processes aimed at pattern recognition, data classification, and future event prediction. A neural network decomposes the input into hierarchical layers of abstraction. The process of training involves utilizing numerous examples to enable the recognition of patterns in speech or images, akin to the cognitive abilities of the human brain. The behavior of a neural network is determined by the configuration of its constituent elements, specifically, the manner in which they are interconnected and the relative magnitudes of the connection weights. The weights of the artificial neural network are dynamically modified during the training process, adhering to a predetermined learning rule, until the network achieves the desired task with accuracy. In engineering applications, three prevalent types of neural networks are commonly employed such as feedforward neural network (FNN), Convolutional neural network (CNN), Recurrent neural network (RNN).

2.6.1 Single layer neural network

An artificial neural network is composed of an input layer, one hidden layer, and an output layer.

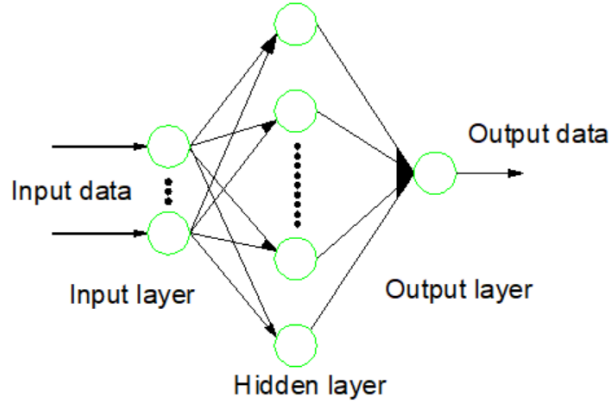


Figure 2.14: The simple architecture of a neural network

2.6.2 Multilayer-recurrent neural networks

Recurrent neural networks (RNNs) [152] exhibit significant efficacy in cases where a model is specifically engineered to handle sequential data. The proposed model uses a mechanism in which data is sent forward and then back-propagated to earlier stages of the artificial neural network. This is done in order to improve task performance and improve the network's ability to predict.

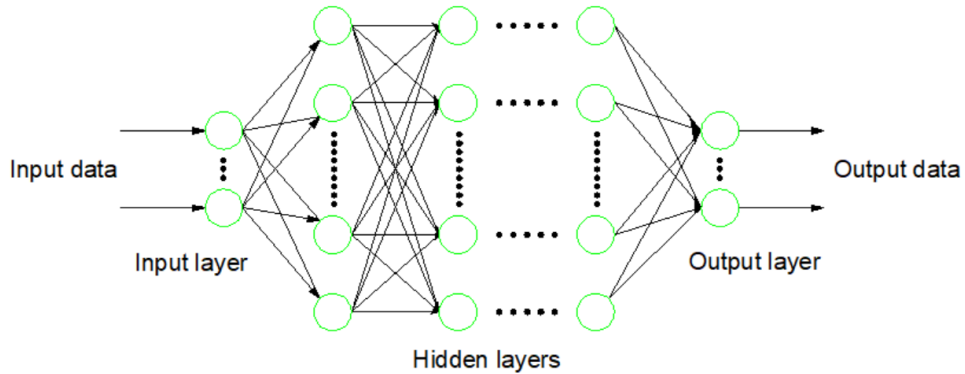


Figure 2.15: The architecture of a deep neural network

The intermediate layers situated between the input and output layers exhibit a recurrent nature, as they incorporate a mechanism to cyclically transmit and preserve pertinent information. The memory of outputs from a layer is recurrently connected back to the input, where it is stored and utilized to enhance the processing of subsequent inputs.

Nevertheless, the sensitivity of RNNs to the problems of exploding and vanishing gradients is considered a significant drawback of this methodology [153]. In the context of the training process, it is worth noting that the reduplications of various derivatives, whether they are large or small in magnitude, have the potential to result in the exponential amplification or attenuation of gradients. Upon the introduction of novel inputs, the network ceases to consider the initial ones, resulting in a gradual decline in its sensitivity over time. Moreover, the resolution of this matter can be addressed through the utilization of Long-short-term memory (LSTM) [154]. The methodology employed incorporates recurrent connections to memory blocks within the network. Each memory block is comprised of multiple memory cells that possess the capacity to store the temporal states of the network.

2.6.3 Activation function

Before reaching the nodes, the input data from the outside is multiplied by the weights. Each node in the succeeding layers will get the total of the preceding nodes' output values multiplied by their respective weights, and the activation function's output data for the sum is supplied as follows ([155]):

$$y_i^n = \varphi(x_i^n) = \varphi\left(\sum_{j=1}^{L_{n-1}} w_{ij}^{n-1} \times y_j^{n-1} + b_i^n\right) \quad (2.53)$$

where φ is activation function. Different activation functions have been, therefore, developed in the literature ([156]).

2.6.4 Loss function

The role of the loss function is crucial in the process of reducing the various components of a complex model into a single scalar value. This scalar value serves as an indicator of the model's quality, with improvements in this value reflecting a better-performing model [157]. The objective of the loss function is to assess the disparity between the desired target values and the predicted values. During the training phase of a neural network, the internal parameters of the network are iteratively adjusted in order to minimize the loss function. This refers to the phenomenon where the disparity between the anticipated outcome and the actual

outcome gradually diminishes, ultimately converging towards zero. The construction of loss functions is therefore undertaken to address various types of optimization problems. The mean square error (MSE) is a widely employed metric in practical applications for assessing the precision of prediction models [158]. The utilization of this function is also acknowledged as a loss function in the training phase of neural networks. The statement of MSE is depicted as follows:

$$MSE = \frac{1}{P} \sum_i^P (y_i - \hat{y}_i)^2 \quad (2.54)$$

where P is the number of training samples; y_i is the actual output data; \hat{y}_i is the predicted value of the i^{th} – sample.

2.6.5 Backpropagation and mini-batch gradient descent

The technique of backpropagation is extensively employed in the domain of supervised learning, with a specific focus on the training of neural networks. Backpropagation involves figuring out the relationship between the weights and biases in the neural network and the gradient of the loss function [159]. In the backpropagation process, the gradient of the loss function is sent from the output layer to the input layer of the network over and over again. This lets you figure out the loss function's derivative with respect to the network's input layer. In the training phase of the neural network, the primary goal is to minimize the loss function through the utilization of a specialized backpropagation algorithm. Several algorithms have been developed for network training to date, such as stochastic gradient descent (SGD) [160], the adaptive gradient algorithm [161], adaptive moment estimation (Adam) [162].

In the conventional approach, the parameters are typically updated in gradient descent by computing the gradient of the loss function for each individual training sample. Consequently, it is not possible to employ vectorization in the code to eliminate the need for iterating over the training set. In contrast, batch gradient descent is a method that involves updating the parameters by computing the gradient of the loss function with respect to the entire training set before making

any updates. Therefore, a significant amount of time is required to complete a single update. To address these concerns, Hinton [163] introduced a method known as mini-batch gradient descent. The mini-batch gradient descent algorithm involves updating the parameters by computing the gradient of the loss function with respect to a small batch of the training set and subsequently adjusting the parameters accordingly. This enables the rapid updating of model parameters while also leveraging the benefits of vectorization. Therefore, the mini-batch gradient descent algorithm is able to achieve a trade-off between fast convergence and the presence of noise in the gradient update process. This results in the algorithm acquiring flexibility and robustness.

2.7 Meta-heuristic algorithms

In contrast to optimization algorithms and iterative methods, meta-heuristics algorithms do not ensure the discovery of a globally optimal solution for certain problem classes. Instead, many meta-heuristics algorithms employ stochastic optimization [164], making the solution contingent on the random variables generated. Consequently, they offer valuable avenues for addressing optimization problems. Therefore, metaheuristic algorithms can be used to analyze the stochastic behaviors of structures with uncertain material properties. Three algorithms including differential evolution (DE), shrimp and goby association search algorithm (SGA) and balancing composite motion optimization (BCMO) are used to solve the above problem.

2.7.1. DE algorithm

Initiated by Storn and Price [165, 166], DE algorithm has numerically shown efficacy and robustness in identifying an optimum solution throughout a defined continuous domain.

Initialization: The initial distribution of the population is created in a stochastic way as follows:

$$x_{i,j} = x_j^{\min} + rand(1, d) \times (x_j^{\max} - x_j^{\min}) \quad (2.55)$$

with d represents the count of design variables.

Mutation: A mutated vector \mathbf{v}_i^t derives from the goal vectors \mathbf{x}_i^t in the current iteration through mutation. The five frequently employed mutation choices are as follows:

$$\begin{aligned}
\text{rand/1} : \mathbf{v}_i^t &= \mathbf{v}_{T_1}^t + F(\mathbf{v}_{T_2}^t - \mathbf{v}_{T_3}^t); \text{ best/1} : \mathbf{v}_i^t = \mathbf{v}_{best}^t + F(\mathbf{v}_{T_1}^t - \mathbf{v}_{T_2}^t) \\
\text{current - to - best/1} : \mathbf{v}_i^t &= J(\mathbf{x}_{T_1}^t - \mathbf{x}_{T_2}^t) + J(\mathbf{x}_{best}^t - \mathbf{x}_i^t) + \mathbf{x}_{best}^t \\
\text{rand/2} : \mathbf{v}_i^t &= \mathbf{x}_{T_1}^t + J(\mathbf{x}_{T_2}^t - \mathbf{x}_{T_3}^t) + J(\mathbf{x}_{T_4}^t - \mathbf{x}_{T_5}^t) \\
\text{best/2} : \mathbf{v}_i^t &= J(\mathbf{x}_{T_3}^t - \mathbf{x}_{T_4}^t) + J(\mathbf{x}_{T_1}^t - \mathbf{x}_{T_2}^t) + \mathbf{x}_{best}^t
\end{aligned} \tag{2.56}$$

where T_1, T_2, T_3, T_4 and T_5 consist of randomly selected integer values from within the range of $[1, NP]$, NP is a population size; J is randomly chosen $[0,1]$, when each of them is entirely distinct from the index i , $v_{i,j}^t$ is determined:

$$v_{i,j}^t = \begin{cases} 2x_{\min,j} - v_{i,j}^t & \text{if } v_{i,j}^t < x_{\min,j} \\ 2x_{\max,j} - v_{i,j}^t & \text{if } v_{i,j}^t < x_{\max,j} \\ v_{i,j}^t & \text{otherwise} \end{cases} \tag{2.57}$$

Crossover: During this stage, a crossover mechanism enhances the variety among individual vectors \mathbf{u}_i^t within the present population.

$$u_{i,j}^t = \begin{cases} u_{i,j}^t & \text{if } j = L \text{ or } rand \leq [0.1,1] \\ x_{i,j}^t & \text{otherwise} \end{cases} \tag{2.58}$$

Selection: This process aims to pick superior individuals from the current population for the subsequent iteration.

$$\mathbf{x}_i^{t+1} = \begin{cases} \mathbf{x}_i^t & \text{if } f(\mathbf{u}_i^t) \leq f(\mathbf{x}_i^t) \\ \mathbf{u}_i^t & \text{otherwise} \end{cases} \tag{2.59}$$

2.7.2. SGA algorithm

Sang-To et al. [110] first has introduced SGA algorithm, which showed the efficacy in addressing high-dimensional single-objective issues of varying complexity.

The initial population:

$$B_i^{t+1} = B_i^t + \beta r_1 \otimes (S * -B_i^t) \quad (2.60)$$

where B is the position vector of an individual; $S *$ denotes the positional vector of the finest burrow; d is number of items; $\beta \in [2,1]$ is linear function; $r_1 \in (0,1)$.

Global Search: the mathematical modeling of signal transmission is expressed as:

$$B_{m,d}^{t+1} = r_2 \times G_{m,d}^t ; B_{i,d}^{t+1} = r_2 \times (ub_d - lb_d) + lb_d \quad (2.61)$$

with lb and ub are lower and upper boundaries. $B_{i,d}^t$ indicates the d^{th} information component of shrimp ; $B_{m,d}^t$ is the d^{th} information of gobiid fish.

Local Search: The weakest candidates are placed into the top two shelters to enhance survival, concurrently bolstering the efficacy of local search process.

$$B_i^{t+1} = S_1^t \otimes (1 + \varsigma \times r_3) ; B_i^{t+1} = S_2^t \otimes (1 + \varsigma \times r_3) \quad (262)$$

where S_1^t, S_2^t represents the optimal positions of neighboring burrows; $\varsigma \in [2,1]$; $r_3 \in (-1,1)$.

More details regarding the SGA algorithm can be found in Ref.[110].

2.7.3. BCMO algorithm

Le-Duc et al. [107] proposed the BCMO algorithm, which is a population-based optimization technique that aims to achieve a global optimum by skillfully balancing the composite motion properties of individual entities. The process of achieving a balance between global and local search is facilitated by employing a probabilistic model of selection, which in turn creates a mechanism for movement for each individual.

Initialization: The population is established in a random manner shows that:

$$x_i = x_j^L + rand(1, d) \times (x_i^U - x_j^L) \quad (2.63)$$

where x_i^U and x_i^L are the upper and lower bounds of the i^{th} -individual; d is number of parameter applied.

Immediate global point and optimal individual: The global point x_{Oin}^t , which represents the current global optimum, is determined by the previous best point x_1^{t-1} , in relation to a trial u_1^t , utilizing the objective function.

$$x_{Oin}^t = \begin{cases} u_1^t & \text{if } f(u_1^t) < f(x_1^{t-1}) \\ x_1^{t-1} & \text{otherwise} \end{cases} \quad (2.64)$$

where u_1^t is calculated as follows based on data about the current generation's population:

$$u_1^t = (x^U + x^L) / 2 + v_{k1/k2}^t + v_{k2/1}^t \quad (2.65)$$

where $v_{k1/k2}^t$ and $v_{k2/1}^t$ are determined using $L_{LS} = 1$ as follows:

$$v_{i/j} = -(x_i + x_j) L_{LS} \times \begin{cases} rand(1, d) & \text{if } TV_j > 0.5 \\ -rand(1, d) & \text{otherwise} \end{cases}, \quad (2.66)$$

Coordinated movement of individuals within the solution space: In the context of BCMO, the motion of the global search v_j which is determined:

$$v_j = -(x_j + x_{Oin}) L_{GS} \times \begin{cases} e^{-\frac{1}{d} \frac{j}{NP} r_j^2} & \text{if } TV_j > 0.5 \\ e^{-\frac{1}{d} (1 - \frac{j}{NP}) r_j^2} & \text{otherwise} \end{cases} \quad (2.67)$$

where NP is the population size; $r_j = \|x_j - x_{Oin}\|$

The probabilities for these v_{ik} cases are identical and can be calculated in the following manner:

$$G(v_{in}) = G(v_{i/j}) \times G(v_j) = 0.5 \times 0.5 = 0.25 \quad n = 1, \dots, 4 \quad (2.68)$$

The i^{th} individual's revised position in the succeeding generation is as follows:

$$x_i^{t+1} = x_i^t + v_{i/j} + v_j \quad (2.69)$$

Further information regarding the BCMO algorithm is available in Ref. [107].

2.8 Conclusion

A literature review shows that it is necessary to develop stochastic composite plate models subjected to mechanical and thermal loads. For this aim, the dissertation will focus on the contents:

- Develop the new hybrid shape functions for the Ritz method.
- Develop stochastic models to investigate the behaviors of microplates with uncertain material properties.
- Develop new computation algorithms using artificial intelligence to solve the stochastic problems of microplates.
- Applying optimization methods to search the optimal fiber directions of laminated composite plates.

CHAPTER 3

A RITZ-BASED COMPUTATIONAL METHOD FOR SIZE-DEPENDENT ANALYSIS OF ADVANCED COMPOSITE MICROPLATES UNDER THERMO- MECHANICAL LOADS

Based on equations of the elasticity, this chapter proposes a new size-dependent computational method of advanced composite microplates under thermo-mechanical loads by combine unified higher-order shear deformation theory and modified strain gradient theory. The governing equations of motions are derived from Hamilton's principle. The solution Ritz are approximated by bi-directional series in which new hybrid shape functions are proposed, then the stiffness and mass matrix are explicitly derived. By demonstrating superior convergence speed and stability compared to alternative shape functions, these methods represent a significant advancement in computational techniques. Numerical results are presented for different configurations of the microplates such as the power-law index, material length scale parameter, length-to-thickness ratio and boundary conditions on their critical buckling load thermal buckling and natural frequencies.

3.1 Introduction

Owing to distinctive properties in the energy absorption capacities, high strength and lightweight, porous materials have been applied in various engineering fields such as aerospace, petrochemical industry, etc ([167-169]). In practice, the development of such materials accompanied efficiently computational methods and models in order to predict accurately their responses at different structural scales.

The earlier experimental work showed that the constituent size effects need to be considered in computing responses of micro and nano structures. In this context, it is well-known that the classical elasticity theory is inadequate, hence surrogate theories accounting for size effects have been exploring to calculate the responses of nano and micro structures. One such theory is the MCT proposed by Yang [50], which used a single material length scale parameter (MLSP) to account for the size effects. Because of its simplicity, the MCT has been used for size dependent analysis of FG and FGP microplates with different porosity densities. Saber et al. [170] investigated free vibration analysis of FG microplates using the FSDT and Levy solution. Tran et al. ([171, 172]) developed a unified HSDT using the MCT and Ritz method to analyze vibration and buckling behaviors of FGP microplates. An alternative approach for exploring the size effects is to utilize the modified strain gradient theory (MST) by introducing the effects of rotation, dilatation and deviatoric stretch gradients in constitutive equations [51], which incorporates three MLSPs. This methodology has been applied to forecast the behaviors of microstructures. In comparison, the MST could predict microstructures' responses more accurate than the MCT owing to accounting for three MLSPs, however this method is complicated in theoretical formulation and implementation. The exceptional material attributes of porous metal foam (PMF) have increasingly enticed researchers to explore its characteristics and behaviors for various structures. Wang et al. [173] investigated static and buckling behaviors of 3D PMF plates within the context of a refined HSDT, and Galerkin method. Pham et al. [174] examined bending, free vibration, and forced vibration transient responses of PMF plate by using the IGA and a refined HSDT. Tu et al. [175] analyzed the buckling and post-buckling responses of thin PMF plates using Galerkin's analytical solution and CPT. Sobhy et al. [176] investigated the phase velocity of the waves and wave frequency of PMF nanoplates using a refined HSDT and wave propagation analysis.

In addition to plate models and size-dependent theories, computational methods significantly influence the analysis of porous structures. These methods are generally divided into numerical and analytical approaches, among which the Ritz method stands out due to its accuracy and simplicity in both formulation and implementation. First introduced by Walter Ritz to study free vibrations, this method has since been widely applied to analyze the static and dynamic behavior of beams, plates, and shells. The effectiveness of the Ritz method depends largely on the choice of approximation functions, which must be complete, linearly independent, and satisfy essential or geometric boundary conditions. Research has shown that these functions typically fall into two categories: orthogonal polynomials (OP) and non-orthogonal polynomials (NOP). Chebyshev polynomials, a type of OP, are commonly used for their excellent convergence and numerical stability. Moreover, the OP often generated via the Gram-Schmidt process. In contrast, NOPs are easier to construct and simplify integral evaluations, though they sacrifice certain numerical benefits. While penalty methods can enforce boundary conditions, they increase matrix dimensions and computational cost. Ultimately, the accuracy and efficiency of the Ritz method rely heavily on selecting appropriate shape functions that ensure both physical correctness and numerical stability. A literature review reveals that though the OP offer significant advantages in numerical computations, their development for analysis of microplates is still a gap. This chapter will fill this gap, and that is its main motivation.

This chapter proposes various new computational algorithms, which combined the Ritz method under novel shape functions with unified higher- order shear deformation theory and modified strain gradient for analysis of microplates. The characteristic equations are derived using Hamilton's principle and solved by using Ritz solutions. Numerical instability and converge rate of the proposed solutions, the effects of materials, geometry, porosity and boundary conditions on free vibration, buckling and thermal buckling responses are investigated and evaluated.

3.2 Theoretical formulation

3.2.1 Advanced functionally graded materials

Laminated composite materials, known for their exceptional hardness and low weight, are widely used in mechanical engineering, aerospace, and construction. However, their layered architecture can result in stress concentrations and delamination at the interfaces. To overcome these limitations, functionally graded materials (FGMs) have been developed. FGMs feature a gradual variation in material properties along specific directions. They offer enhanced thermal resistance, corrosion resistance, and toughness—delivering performance beyond that of conventional composites. Recent innovations have further led to the creation of functionally graded porous materials and porous metal foams, which provide excellent sound insulation and reduced structural weight, making them highly suitable for modern, high-performance applications.

3.2.1.1 Porous metal foam material

Consider PMF rectangular microplate, which has three types of porosity distributions as seen in Fig. 2.8-2.10, with the thickness h and sides $a \times b$. The effective material properties are expressed via porosity parameter β and maximum Young's modulus E_{\max} as well as the corresponding coefficients β_m and ρ_{\max} of mass density as follows ([118]):

- Distribution of uniform porosity

$$\rho(x_3) = \rho_{\max} \sqrt{(1 - \beta v)} \quad (3.1a)$$

$$E(x_3) = E_{\max} (1 - \beta v) \quad (3.1b)$$

- Distribution of asymmetric porosity

$$\rho(x_3) = \rho_{\max} \left[1 - \beta_m \cos\left(\frac{\pi z}{2h} + \frac{\pi}{4}\right) \right] \quad (3.2a)$$

$$E(x_3) = E_{\max} \left[1 - \beta \cos\left(\frac{\pi z}{2h} + \frac{\pi}{4}\right) \right] \quad (3.2b)$$

- Distribution of symmetric porosity

$$\rho(x_3) = \rho_{\max} \left(1 - \beta_m \cos\left(\frac{\pi z}{h}\right) \right) \quad (3.3a)$$

$$E(x_3) = E_{\max} \left(1 - \beta \cos\left(\frac{\pi z}{h}\right) \right) \quad (3.3b)$$

where E_{\max} and ρ_{\max} are maximum values of Young's modulus and mass density, respectively; β and β_m denotes the porosity parameters and mass density, which are given by:

$$\beta = 1 - \frac{E_{\min}}{E_{\max}}, 0 < \beta < 1 \quad (3.4a)$$

$$\beta_m = 1 - \frac{\rho_{\min}}{\rho_{\max}}, 0 < \beta_m < 1 \quad (3.4b)$$

where E_{\min} and ρ_{\min} are minimum Young's modulus and mass density.

In which

$$\beta_m = 1 - \sqrt{1 - \beta} \quad (3.5)$$

The material characteristics in the case of a distribution of uniform porosity remain constant in the thickness direction and depend only on the porosity coefficient β .

Thereafter, the coefficient ν is written as follows:

$$\nu = \frac{1}{\beta} - \frac{1}{\beta} \left(\frac{2}{\pi} \sqrt{1 - \beta} - \frac{2}{\pi} + 1 \right)^2 \quad (3.6)$$

3.2.1.2 Functionally graded sandwich materials

In the coordinate system (x_1, x_2, x_3) , the FG sandwich rectangular microplate as seen in Fig.2.6 with thickness h and the sides $a \times b$.

The plate is made up of two FG faces comprised of ceramic-metal components and a homogenous core. The following formulas can be used to evaluate the effective material properties of FG sandwich microplates:

$$P(x_3) = (P_c - P_m)V_c(x_3) + P_m \quad (3.7)$$

where the volume fraction of the ceramic material $V_c(x_3)$ across the plate thickness is determined by ([117]):

$$V_c(x_3) = \begin{cases} \left(\frac{z_4 - x_3}{z_4 - z_3} \right)^p, & z_3 \leq x_3 \leq z_4 & \text{FG} & \text{top} & \text{layer} \\ 1 & z_2 \leq x_3 \leq z_3 & \text{ceramic} & \text{core} & \text{layer} \\ \left(\frac{x_3 - z_1}{z_2 - z_1} \right)^p & z_1 \leq x_3 \leq z_2 & \text{FG} & \text{bottom} & \text{layer} \end{cases} \quad (3.8)$$

with the power-law index p , P_c and P_m are the characteristics of ceramic and metal materials, respectively, such as the Young's moduli E , mass density ρ , and Poisson's ratio ν .

3.2.1.3 Functionally graded porous materials

Considering a rectangle FGP microplate in the coordinate system (x_1, x_2, x_3) with thickness h , sides $a \times b$ as provided in Fig. 2.3.

The effective material properties of FGP microplates are given by [114]:

$$P(x_3) = (P_c - P_m) \left(\frac{2x_3 + h}{2h} \right)^p + P_m - \frac{\beta}{2} (P_c + P_m) \quad (3.9)$$

where P_c and P_m are the Poisson's ratio ν , Young's moduli E of ceramic and metal materials, respectively; p is the power-law index; $0 \leq \beta \ll 1$ is the porosity volume fraction; $x_3 \in [-h/2, h/2]$.

3.2.1.4 Properties of materials and temperature distribution

Moreover, in order to investigate the effect of temperature on the buckling responses, three types of temperature distribution are considered as below ([107, 108]):

- For uniform distribution (UTR): $T(z) = T_o + \Delta T$ where the bottom surface's reference temperature is T_o .
- For linear distribution (LTR): $T(z) = (T_t - T_b) \left(\frac{z}{h} + \frac{1}{2} \right) + T_b$ where the

temperatures at the top and bottom surfaces of FGP microplates are represented by T_t and T_b , respectively.

- For the nonlinear temperature rise (NLTR): the expression of the current temperature is derived from the Fourier equation of steady-state heat

conduction as follows:
$$T(z) = T(b) + \frac{T_t - T_b}{\int_{-h/2}^{h/2} 1/k(z) dz} \int_{-h/2}^z \frac{1}{k(\xi)} d\xi$$

where $k(z)$ is the coefficient of thermal conductivity.

3.2.2 Modified strain gradient theory based on a framework of unified high-order shear deformation theory

For simplicity purpose, the effects of transverse normal strain are neglected, i.e. $u_3(x_1, x_2, x_3) = u_3^0(x_1, x_2)$ where $u_3^0(x_1, x_2)$ is transverse displacement at the mid-surface of the microplates. Moreover, it is supposed that the transverse shear stresses are expressed in terms of the transverse shear forces as follows:

$$\sigma_{13} = f_{,3}(x_3) Q_1(x_1, x_2) \quad (3.10a)$$

$$\sigma_{23} = f_{,3}(x_3) Q_2(x_1, x_2) \quad (3.10b)$$

where $f(x_3)$ is a higher-order term whose first derivative satisfies the free-stress boundary condition at the top and bottom surfaces of the microplates, i.e.

$$f_{,3}\left(x_3 = \pm \frac{h}{2}\right) = 0; \quad Q_1(x_1, x_2), Q_2(x_1, x_2) \quad \text{are the transverse shear forces.}$$

Additionally, transverse shear strains are linearly related to the membrane displacements $u_1(x_1, x_2, x_3), u_2(x_1, x_2, x_3)$ and transverse one $u_3^0(x_1, x_2)$ by:

$$\gamma_{13} = u_{1,3} + u_{3,1}^0 = \frac{\sigma_{13}}{\mu} = \frac{f_{,3} Q_1}{\mu} \quad (3.11a)$$

$$\gamma_{23} = u_{2,3} + u_{3,2}^0 = \frac{\sigma_{23}}{\mu} = \frac{f_{,3} Q_2}{\mu} \quad (3.11b)$$

where $\mu(x_3) = \frac{E(x_3)}{2(1+\nu)}$ is the shear modulus. Furthermore, integrating Eq. (3.11)

in x_3 - direction leads to a general displacement field of the microplates as follows:

$$u_1(x_1, x_2, x_3) = u_1^0(x_1, x_2) - x_3 u_{3,1}^0 + \Psi(x_3) Q_1(x_1, x_2) \quad (3.12a)$$

$$u_2(x_1, x_2, x_3) = u_2^0(x_1, x_2) - x_3 u_{3,2}^0 + \Psi(x_3) Q_2(x_1, x_2) \quad (3.12b)$$

$$u_3(x_1, x_2, x_3) = u_3^0(x_1, x_2) \quad (3.12c)$$

where $\Psi(x_3) = \int_0^{x_3} \frac{f_3}{\mu(x_3)} dx_3$. It is observed that Eq. (3.12) can be considered as a

general zeroth-order shear deformation theory in which displacement field of Shimpi ([177]), Ray ([178]) can be obtained by the assumption of homogeneous

materials and $f(x_3) = \frac{3}{2h} \left(z - \frac{4z^3}{3h^2} \right)$. Moreover, it is known that the transverse

shear forces can be expressed in terms of the rotation (φ_1, φ_2) and gradients of the transverse displacement as follows:

$$Q_1(x_1, x_2) = H^s (\varphi_1 + u_{3,1}^0) \quad (3.13a)$$

$$Q_2(x_1, x_2) = H^s (\varphi_2 + u_{3,2}^0) \quad (3.13b)$$

where $H^s = k^s \int_{-h/2}^{h/2} \mu(x_3) dx_3$ is the transverse shear stiffness of the microplates;

$k^s = 5/6$ is shear coefficient factor. Substituting Eq. (3.13) into Eq. (3.12) leads to a general HSDT as follows:

$$u_1(x_1, x_2, x_3) = u_1^0(x_1, x_2) + \Phi_1(x_3) u_{3,1}^0 + \Phi_2(x_3) \varphi_1(x_1, x_2) \quad (3.14a)$$

$$u_2(x_1, x_2, x_3) = u_2^0(x_1, x_2) + \Phi_1(x_3) u_{3,2}^0 + \Phi_2(x_3) \varphi_2(x_1, x_2) \quad (3.14b)$$

$$u_3(x_1, x_2, x_3) = u_3^0(x_1, x_2) \quad (3.14c)$$

where $\Phi_1(x_3) = H^s \Psi(x_3) - x_3$, $\Phi_2(x_3) = H^s \Psi(x_3)$. Similarly, it is from Eq. (3.14) that the displacement field of Reissner [179], Shi et al. [180] can be derived with $f(x_3) = \frac{3}{2h} \left(z - \frac{4z^3}{3h^2} \right)$, and Reddy's theory [181] with $f(x_3) = \frac{6}{5h} \left(z - \frac{4z^3}{3h^2} \right)$.

The microplates' total potential energy is calculated by using Hamilton's principle as follows:

$$\int_{t_1}^{t_2} (\delta \Pi_{UB} + \delta \Pi_{VB} + \delta \Pi_{FB} - \delta \Pi_{KB}) dt = 0 \quad (3.15)$$

where $\delta \Pi_{VB}$, $\delta \Pi_{UB}$, $\delta \Pi_{FB}$ and $\delta \Pi_{KB}$ are the variations of work done by membrane compressive forces, strain energy, work done by external forces and kinetic energy, respectively. The strain energy variation of the system $\delta \Pi_{UB}$ is obtained by the MST ([51]):

$$\delta \Pi_{UB} = \int_A (\boldsymbol{\sigma} \delta \boldsymbol{\varepsilon} + \mathbf{p} \delta \boldsymbol{\xi} + \boldsymbol{\tau} \delta \boldsymbol{\eta} + \mathbf{m} \delta \boldsymbol{\chi}) dA \quad (3.16)$$

where $\boldsymbol{\varepsilon}, \boldsymbol{\chi}, \boldsymbol{\xi}, \boldsymbol{\eta}$ are strains, symmetric rotation gradients, dilatation gradient and deviation stretch gradient, respectively; $\boldsymbol{\sigma}$ is Cauchy stress; $\mathbf{m}, \mathbf{p}, \boldsymbol{\tau}$ are high-order stresses corresponding with strain gradients $\boldsymbol{\chi}, \boldsymbol{\xi}, \boldsymbol{\eta}$, respectively.

The components of strain ε_{ij} and strain gradients $\xi_i, \eta_{ijk}, \chi_{ij}$ are defined as follows:

$$\varepsilon_{ij} = (u_{i,j} + u_{j,i}) / 2; \quad \xi_i = \varepsilon_{mm,i} \quad (3.17a)$$

$$\chi_{ij} = (u_{n,mj} e_{imn} + u_{n,mi} e_{jmn}) / 4 \quad (3.17b)$$

$$\eta_{ijk} = (\varepsilon_{jk,i} + \varepsilon_{ki,j} + \varepsilon_{ij,k}) / 3 - \left[(\xi_i + 2\varepsilon_{mi,m}) \delta_{jk} + (\xi_k + 2\varepsilon_{mk,m}) \delta_{ij} + (\xi_j + 2\varepsilon_{mj,m}) \delta_{ki} \right] / 15 \quad (3.17c)$$

where δ_{ij} is Kronecker delta; e_{imn} is permutation symbol. The constitutive equations are used to determine the stress components as follows:

$$\sigma_{ij} = \lambda \varepsilon_{kk} \delta_{ij} + 2\mu \varepsilon_{ij}; \quad m_{ij} = 2\mu l_1^2 \chi_{ij}; \quad p_j = 2\mu l_2^2 \xi_j; \quad \tau_{ijk} = 2\mu l_3^2 \eta_{ijk} \quad (3.18a)$$

$$p_j = 2\mu l_2^2 \xi_j; \tau_{ijk} = 2\mu l_3^2 \eta_{ijk} \quad (3.18b)$$

where λ, μ are Lamé constants; l_1, l_2, l_3 are three material length scale parameters (MLSP) which should be practically determined by experimental works. Substituting Eq. (3.17a) into Eq. (3.14), the strains $\boldsymbol{\epsilon}^T = [\boldsymbol{\epsilon}^{(i)} \quad \boldsymbol{\epsilon}^{(ss)}]$ are achieved as follows:

$$\boldsymbol{\epsilon}^{(ss)} = \Phi_3(x_3) \boldsymbol{\epsilon}^{(3)}; \boldsymbol{\epsilon}^{(i)} = \Phi_2(x_3) \boldsymbol{\epsilon}^{(2)} + \Phi_1(x_3) \boldsymbol{\epsilon}^{(1)} + \boldsymbol{\epsilon}^{(0)} \quad (3.19a)$$

$$\boldsymbol{\epsilon}^{(i)} = \Phi_2(x_3) \boldsymbol{\epsilon}^{(2)} + \Phi_1(x_3) \boldsymbol{\epsilon}^{(1)} + \boldsymbol{\epsilon}^{(0)} \quad (3.19b)$$

where $\Phi_3(x_3) = H^s f_{,3}(x_3) / \mu(x_3)$ and,

$$\boldsymbol{\epsilon}^{(0)} = \begin{Bmatrix} \epsilon_{11}^{(0)} \\ \epsilon_{22}^{(0)} \\ \gamma_{12}^{(0)} \end{Bmatrix} = \begin{Bmatrix} u_{1,1}^0 \\ u_{2,2}^0 \\ u_{1,2}^0 + u_{2,1}^0 \end{Bmatrix}; \quad \boldsymbol{\epsilon}^{(1)} = \begin{Bmatrix} \epsilon_{11}^{(1)} \\ \epsilon_{22}^{(1)} \\ \gamma_{12}^{(1)} \end{Bmatrix} = \begin{Bmatrix} u_{3,11}^0 \\ u_{3,22}^0 \\ 2u_{3,12}^0 \end{Bmatrix} \quad (3.20a)$$

$$\boldsymbol{\epsilon}^{(3)} = \begin{Bmatrix} \gamma_{13}^{(0)} \\ \gamma_{23}^{(0)} \end{Bmatrix} = \begin{Bmatrix} \varphi_1 + u_{3,1}^0 \\ \varphi_2 + u_{3,2}^0 \end{Bmatrix}; \quad \boldsymbol{\epsilon}^{(2)} = \begin{Bmatrix} \epsilon_{11}^{(2)} \\ \epsilon_{22}^{(2)} \\ \gamma_{12}^{(2)} \end{Bmatrix} = \begin{Bmatrix} \varphi_{1,1} \\ \varphi_{2,2} \\ \varphi_{1,2} + \varphi_{2,1} \end{Bmatrix} \quad (3.20b)$$

The non-zero components of dilatation gradients $\boldsymbol{\xi} = [\xi_1 \quad \xi_2 \quad \xi_3]^T$ are given by:

$$\boldsymbol{\xi} = \boldsymbol{\xi}^{(0)} + \Phi_1 \boldsymbol{\xi}^{(1)} + \Phi_2 \boldsymbol{\xi}^{(2)} + \Phi_{1,3} \boldsymbol{\xi}^{(3)} + \Phi_{2,3} \boldsymbol{\xi}^{(4)} \quad (3.21)$$

where

$$\boldsymbol{\xi}^{(0)} = \begin{Bmatrix} \xi_1^{(0)} \\ \xi_2^{(0)} \\ \xi_3^{(0)} \end{Bmatrix} = \begin{Bmatrix} u_{1,11}^0 + u_{2,12}^0 \\ u_{1,12}^0 + u_{2,22}^0 \\ 0 \end{Bmatrix}; \quad \boldsymbol{\xi}^{(1)} = \begin{Bmatrix} \xi_1^{(1)} \\ \xi_2^{(1)} \\ \xi_3^{(1)} \end{Bmatrix} = \begin{Bmatrix} u_{3,111}^0 + u_{3,122}^0 \\ u_{3,112}^0 + u_{3,222}^0 \\ 0 \end{Bmatrix} \quad (3.22a)$$

$$\xi^{(2)} = \begin{Bmatrix} \xi_1^{(2)} \\ \xi_2^{(2)} \\ \xi_3^{(2)} \end{Bmatrix} = \begin{Bmatrix} \varphi_{1,11} + \varphi_{2,12} \\ \varphi_{1,12} + \varphi_{2,22} \\ 0 \end{Bmatrix}; \xi^{(3)} = \begin{Bmatrix} \xi_1^{(3)} \\ \xi_2^{(3)} \\ \xi_3^{(3)} \end{Bmatrix} = \begin{Bmatrix} 0 \\ 0 \\ u_{3,11}^0 + u_{3,22}^0 \end{Bmatrix} \quad (3.22b)$$

$$\xi^{(4)} = \begin{Bmatrix} \xi_1^{(4)} \\ \xi_2^{(4)} \\ \xi_3^{(4)} \end{Bmatrix} = \begin{Bmatrix} 0 \\ 0 \\ \varphi_{1,1} + \varphi_{2,2} \end{Bmatrix} \quad (3.22c)$$

The non-zero components of deviatoric stretch gradients η_{ijk} are given by:

$$\eta_{111} = \varepsilon_{11,1} - \frac{1}{5}(\xi_1 + 2\varepsilon_{11,1} + \gamma_{12,2} + \gamma_{13,3}) \quad (3.23a)$$

$$\eta_{222} = \varepsilon_{22,2} - \frac{1}{5}(\xi_2 + 2\varepsilon_{22,2} + \gamma_{12,1} + \gamma_{23,3}); \eta_{333} = -\frac{1}{5}(\xi_3 + \gamma_{13,1} + \gamma_{23,2}) \quad (3.23b)$$

$$\eta_{112} = \eta_{211} = \eta_{121} = \frac{1}{3}(\varepsilon_{11,2} + \gamma_{12,1}) - \frac{1}{15}(\xi_2 + \gamma_{12,1} + 2\varepsilon_{22,2} + \gamma_{23,3}) \quad (3.23c)$$

$$\eta_{113} = \eta_{311} = \eta_{131} = \frac{1}{3}(\gamma_{13,1} + \varepsilon_{11,3}) - \frac{1}{15}(\xi_3 + \gamma_{13,1} + \gamma_{23,2}) \quad (3.23d)$$

$$\eta_{221} = \eta_{122} = \eta_{212} = \frac{1}{3}(\gamma_{12,2} + \varepsilon_{22,1}) - \frac{1}{15}(\xi_1 + 2\varepsilon_{11,1} + \gamma_{12,2} + \gamma_{13,3}) \quad (3.23e)$$

$$\eta_{223} = \eta_{322} = \eta_{232} = \frac{1}{3}(\gamma_{23,2} + \varepsilon_{22,3}) - \frac{1}{15}(\xi_3 + \gamma_{13,1} + \gamma_{23,2}) \quad (3.23f)$$

$$\eta_{331} = \eta_{133} = \eta_{313} = \frac{1}{3}\gamma_{13,3} - \frac{1}{15}(\xi_1 + 2\varepsilon_{11,1} + \gamma_{12,2} + \gamma_{13,3}) \quad (3.23g)$$

$$\eta_{332} = \eta_{233} = \eta_{323} = \frac{1}{3}\gamma_{23,3} - \frac{1}{15}(\xi_2 + \gamma_{12,1} + 2\varepsilon_{22,2} + \gamma_{23,3}) \quad (3.23h)$$

$$\eta_{123} = \eta_{231} = \eta_{312} = \eta_{132} = \eta_{321} = \eta_{213} = \frac{1}{6}(\gamma_{23,1} + \gamma_{13,2} + \gamma_{12,3}) \quad (3.23j)$$

Substituting the strains in Eqs. (3.19) and (3.21) into Eq. (3.23), and Eq. (3.17c) into Eq. (3.14) leads to the expressions of deviatoric stretch gradient and strain gradient components as follows:

$$\boldsymbol{\eta} = \boldsymbol{\eta}^{(0)} + \Phi_1 \boldsymbol{\eta}^{(1)} + \Phi_2 \boldsymbol{\eta}^{(2)} + \Phi_3 \boldsymbol{\eta}^{(3)} + \Phi_{1,3} \boldsymbol{\eta}^{(4)} + \Phi_{2,3} \boldsymbol{\eta}^{(5)} + \Phi_{3,3} \boldsymbol{\eta}^{(6)} \quad (3.24a)$$

$$\boldsymbol{\chi} = \boldsymbol{\chi}^{(0)} + \boldsymbol{\chi}^{(1)} \Phi_{1,3} + \boldsymbol{\chi}^{(2)} \Phi_{2,3} + \boldsymbol{\chi}^{(3)} \Phi_{1,33} + \boldsymbol{\chi}^{(4)} \Phi_{2,33} + \boldsymbol{\chi}^{(5)} \Phi_2 \quad (3.24b)$$

where $\boldsymbol{\eta}^T = [\eta_{111} \quad \eta_{222} \quad \eta_{333} \quad 3\eta_{331} \quad 3\eta_{332} \quad 3\eta_{221} \quad 3\eta_{112} \quad 3\eta_{113} \quad 3\eta_{223} \quad 6\eta_{123}]$,

$\boldsymbol{\chi}^T = [\chi_{11} \quad \chi_{22} \quad 2\chi_{12} \quad \chi_{33} \quad 2\chi_{13} \quad 2\chi_{23}]$, and

$$\boldsymbol{\eta}^{(0)} = \frac{1}{5} \begin{Bmatrix} 2u_{1,11}^0 - 2u_{2,12}^0 - u_{1,22}^0 \\ 2u_{2,22}^0 - 2u_{1,12}^0 - u_{2,11}^0 \\ 0 \\ -(3u_{1,11}^0 + 2u_{2,12}^0 + u_{1,22}^0) \\ -(3u_{2,22}^0 + 2u_{1,12}^0 + u_{2,11}^0) \\ 4u_{1,22}^0 + 8u_{2,12}^0 - 3u_{1,11}^0 \\ 4u_{2,11}^0 + 8u_{1,12}^0 - 3u_{2,22}^0 \\ 0 \\ 0 \\ 0 \end{Bmatrix}, \boldsymbol{\eta}^{(1)} = \frac{1}{5} \begin{Bmatrix} 2u_{3,111}^0 - 3u_{3,122}^0 \\ 2u_{3,222}^0 - 3u_{3,112}^0 \\ 0 \\ -3(u_{3,111}^0 + u_{3,122}^0) \\ -3(u_{3,112}^0 + u_{3,222}^0) \\ 3(4u_{3,122}^0 - u_{3,111}^0) \\ 3(4u_{3,112}^0 - u_{3,222}^0) \\ 0 \\ 0 \\ 0 \end{Bmatrix} \quad (3.25a)$$

$$\boldsymbol{\eta}^{(2)} = \frac{1}{5} \begin{Bmatrix} 2\varphi_{1,11} - 2\varphi_{2,12} - \varphi_{1,22} \\ 2\varphi_{2,22} - 2\varphi_{1,12} - \varphi_{2,11} \\ 0 \\ -(3\varphi_{1,11} + 2\varphi_{2,12} + \varphi_{1,22}) \\ -(3\varphi_{2,22} + 2\varphi_{1,12} + \varphi_{2,11}) \\ 4\varphi_{1,22} + 8\varphi_{2,12} - 3\varphi_{1,11} \\ 4\varphi_{2,11} + 8\varphi_{1,12} - 3\varphi_{2,22} \\ 0 \\ 0 \\ 0 \end{Bmatrix}, \boldsymbol{\eta}^{(3)} = \frac{1}{5} \begin{Bmatrix} 0 \\ 0 \\ -(u_{3,11}^0 + u_{3,22}^0 + \varphi_{1,1} + \varphi_{2,2}) \\ 0 \\ 0 \\ 0 \\ 0 \\ 4u_{3,11}^0 - u_{3,22}^0 + 4\varphi_{1,1} - \varphi_{2,2} \\ 4u_{3,22}^0 - u_{3,11}^0 + 4\varphi_{2,2} - \varphi_{1,1} \\ 5(\varphi_{1,2} + \varphi_{2,1} + 2u_{3,12}^0) \end{Bmatrix} \quad (3.25b)$$

$$\boldsymbol{\eta}^{(4)} = \frac{1}{5} \begin{Bmatrix} 0 \\ 0 \\ -(u_{3,11}^0 + u_{3,22}^0) \\ 0 \\ 0 \\ 0 \\ 0 \\ 4u_{3,11}^0 - u_{3,22}^0 \\ 4u_{3,22}^0 - u_{3,11}^0 \\ 10u_{3,12}^0 \end{Bmatrix}, \boldsymbol{\eta}^{(5)} = \frac{1}{5} \begin{Bmatrix} 0 \\ 0 \\ -(\varphi_{1,1} + \varphi_{2,2}) \\ 0 \\ 0 \\ 0 \\ 0 \\ 4\varphi_{1,1} - \varphi_{2,2} \\ 4\varphi_{2,2} - \varphi_{1,1} \\ 5(\varphi_{1,2} + \varphi_{2,1}) \end{Bmatrix}, \boldsymbol{\eta}^{(6)} = \frac{1}{5} \begin{Bmatrix} -(\varphi_1 + u_{3,1}^0) \\ -(\varphi_2 + u_{3,2}^0) \\ 0 \\ 4(\varphi_1 + u_{3,1}^0) \\ 4(\varphi_2 + u_{3,2}^0) \\ -(\varphi_1 + u_{3,1}^0) \\ -(\varphi_2 + u_{3,2}^0) \\ 0 \\ 0 \\ 0 \end{Bmatrix} \quad (3.25c)$$

$$\boldsymbol{\chi}^{(0)} = \frac{1}{2} \begin{Bmatrix} u_{3,12}^0 \\ -u_{3,12}^0 \\ u_{3,22}^0 - u_{3,11}^0 \\ 0 \\ u_{2,11}^0 - u_{1,12}^0 \\ u_{2,12}^0 - u_{1,22}^0 \end{Bmatrix}, \boldsymbol{\chi}^{(1)} = \frac{1}{2} \begin{Bmatrix} -u_{3,12}^0 \\ u_{3,12}^0 \\ u_{3,11}^0 - u_{3,22}^0 \\ 0 \\ 0 \\ 0 \end{Bmatrix}, \boldsymbol{\chi}^{(2)} = \frac{1}{2} \begin{Bmatrix} -\varphi_{2,1} \\ \varphi_{1,2} \\ \varphi_{1,1} - \varphi_{2,2} \\ \varphi_{2,1} - \varphi_{1,2} \\ 0 \\ 0 \end{Bmatrix} \quad (3.25d)$$

$$\boldsymbol{\chi}^{(3)} = \frac{1}{2} \begin{Bmatrix} 0 \\ 0 \\ 0 \\ 0 \\ -u_{3,2}^0 \\ u_{3,1}^0 \end{Bmatrix}, \boldsymbol{\chi}^{(4)} = \frac{1}{2} \begin{Bmatrix} 0 \\ 0 \\ 0 \\ 0 \\ -\varphi_2 \\ \varphi_1 \end{Bmatrix}, \boldsymbol{\chi}^{(5)} = \frac{1}{2} \begin{Bmatrix} 0 \\ 0 \\ 0 \\ 0 \\ \varphi_{2,11} - \varphi_{1,12} \\ \varphi_{2,12} - \varphi_{1,22} \end{Bmatrix} \quad (3.25e)$$

The stress-strain relationship of microplates is represented as follows:

$$\boldsymbol{\sigma}^{(i)} = \begin{Bmatrix} \sigma_{11} \\ \sigma_{22} \\ \sigma_{12} \end{Bmatrix} = \mathbf{Q}_{\varepsilon}^{(i)} \boldsymbol{\varepsilon}^{(i)} = \begin{bmatrix} Q_{11} & Q_{12} & 0 \\ Q_{12} & Q_{22} & 0 \\ 0 & 0 & Q_{66} \end{bmatrix} \begin{Bmatrix} \varepsilon_{11} \\ \varepsilon_{22} \\ \gamma_{12} \end{Bmatrix} \quad (3.26a)$$

$$\boldsymbol{\sigma}^{(o)} = \begin{Bmatrix} \sigma_{13} \\ \sigma_{23} \end{Bmatrix} = \mathbf{Q}_{\varepsilon}^{(o)} \boldsymbol{\varepsilon}^{(ss)} = \begin{bmatrix} Q_{55} & 0 \\ 0 & Q_{44} \end{bmatrix} \begin{Bmatrix} \gamma_{13} \\ \gamma_{23} \end{Bmatrix} \quad (3.26b)$$

$$\mathbf{m} = \begin{Bmatrix} m_{11} \\ m_{22} \\ m_{12} \\ m_{33} \\ m_{23} \\ m_{13} \end{Bmatrix} = \alpha_\chi \mathbf{I}_{6 \times 6} \boldsymbol{\chi} = 2\mu l_1^2 \begin{bmatrix} 1 & 0 & 0 & 0 & 0 & 0 \\ 0 & 1 & 0 & 0 & 0 & 0 \\ 0 & 0 & 1 & 0 & 0 & 0 \\ 0 & 0 & 0 & 1 & 0 & 0 \\ 0 & 0 & 0 & 0 & 1 & 0 \\ 0 & 0 & 0 & 0 & 0 & 1 \end{bmatrix} \begin{Bmatrix} \chi_{11} \\ \chi_{22} \\ \chi_{12} \\ \chi_{33} \\ \chi_{23} \\ \chi_{13} \end{Bmatrix} \quad (3.26c)$$

$$\mathbf{p} = \begin{Bmatrix} p_1 \\ p_2 \\ p_3 \end{Bmatrix} = \alpha_\xi \mathbf{I}_{3 \times 3} \boldsymbol{\xi} = 2\mu l_2^2 \begin{bmatrix} 1 & 0 & 0 \\ 0 & 1 & 0 \\ 0 & 0 & 1 \end{bmatrix} \begin{Bmatrix} \xi_1 \\ \xi_2 \\ \xi_3 \end{Bmatrix} \quad (3.26d)$$

$$\boldsymbol{\tau} = \begin{Bmatrix} \tau_{111} \\ \tau_{222} \\ \tau_{112} \\ \tau_{221} \\ \tau_{331} \\ \tau_{332} \\ \tau_{333} \\ \tau_{113} \\ \tau_{223} \\ \tau_{123} \end{Bmatrix} = \alpha_\eta \mathbf{I}_{10 \times 10} \boldsymbol{\eta} = 2\mu l_3^2 \begin{bmatrix} 1 & 0 & 0 & 0 & 0 & 0 & 0 & 0 & 0 & 0 \\ 0 & 1 & 0 & 0 & 0 & 0 & 0 & 0 & 0 & 0 \\ 0 & 0 & 1 & 0 & 0 & 0 & 0 & 0 & 0 & 0 \\ 0 & 0 & 0 & 1 & 0 & 0 & 0 & 0 & 0 & 0 \\ 0 & 0 & 0 & 0 & 1 & 0 & 0 & 0 & 0 & 0 \\ 0 & 0 & 0 & 0 & 0 & 1 & 0 & 0 & 0 & 0 \\ 0 & 0 & 0 & 0 & 0 & 0 & 1 & 0 & 0 & 0 \\ 0 & 0 & 0 & 0 & 0 & 0 & 0 & 1 & 0 & 0 \\ 0 & 0 & 0 & 0 & 0 & 0 & 0 & 0 & 1 & 0 \\ 0 & 0 & 0 & 0 & 0 & 0 & 0 & 0 & 0 & 1 \end{bmatrix} \begin{Bmatrix} \eta_{111} \\ \eta_{222} \\ \eta_{112} \\ \eta_{221} \\ \eta_{331} \\ \eta_{332} \\ \eta_{333} \\ \eta_{113} \\ \eta_{223} \\ \eta_{123} \end{Bmatrix} \quad (3.26e)$$

where $\alpha_\chi = 2\mu l_1^2$, $\alpha_\xi = 2\mu l_2^2$, $\alpha_\eta = 2\mu l_3^2$,

$$Q_{44} = Q_{55} = Q_{66} = \mu = \frac{E(x_3)}{2(1+\nu)}, Q_{12} = \frac{\nu E(x_3)}{1-\nu^2}, Q_{22} = \frac{E(x_3)}{1-\nu^2}, Q_{11} = \frac{E(x_3)}{1-\nu^2}.$$

The variation of the strain energy of microplates is hence derived from Eq. (3.16) as follows:

$$\begin{aligned} \delta \Pi_{UB} &= \int_A (\boldsymbol{\sigma} \delta \boldsymbol{\varepsilon} + \mathbf{p} \delta \boldsymbol{\xi} + \boldsymbol{\tau} \delta \boldsymbol{\eta} + \mathbf{m} \delta \boldsymbol{\chi}) dA \\ &= \int_A \left[\mathbf{P}_\varepsilon^{(3)} \delta \boldsymbol{\varepsilon}^{(3)} + \mathbf{P}_\varepsilon^{(2)} \delta \boldsymbol{\varepsilon}^{(2)} + \mathbf{P}_\varepsilon^{(1)} \delta \boldsymbol{\varepsilon}^{(1)} + \mathbf{P}_\varepsilon^{(0)} \delta \boldsymbol{\varepsilon}^{(0)} \right. \\ &\quad + \mathbf{P}_\xi^{(4)} \delta \boldsymbol{\xi}^{(4)} + \mathbf{P}_\xi^{(3)} \delta \boldsymbol{\xi}^{(3)} + \mathbf{P}_\xi^{(2)} \delta \boldsymbol{\xi}^{(2)} + \mathbf{P}_\xi^{(1)} \delta \boldsymbol{\xi}^{(1)} + \mathbf{P}_\xi^{(0)} \delta \boldsymbol{\xi}^{(0)} \\ &\quad + \mathbf{P}_\chi^{(5)} \delta \boldsymbol{\chi}^{(5)} + \mathbf{P}_\chi^{(4)} \delta \boldsymbol{\chi}^{(4)} + \mathbf{P}_\chi^{(3)} \delta \boldsymbol{\chi}^{(3)} + \mathbf{P}_\chi^{(2)} \delta \boldsymbol{\chi}^{(2)} + \mathbf{P}_\chi^{(1)} \delta \boldsymbol{\chi}^{(1)} + \mathbf{P}_\chi^{(0)} \delta \boldsymbol{\chi}^{(0)} \\ &\quad \left. + \mathbf{P}_\eta^{(6)} \delta \boldsymbol{\eta}^{(6)} + \mathbf{P}_\eta^{(5)} \delta \boldsymbol{\eta}^{(5)} + \mathbf{P}_\eta^{(4)} \delta \boldsymbol{\eta}^{(4)} + \mathbf{P}_\eta^{(3)} \delta \boldsymbol{\eta}^{(3)} + \mathbf{P}_\eta^{(2)} \delta \boldsymbol{\eta}^{(2)} + \mathbf{P}_\eta^{(1)} \delta \boldsymbol{\eta}^{(1)} + \mathbf{P}_\eta^{(0)} \delta \boldsymbol{\eta}^{(0)} \right] dA \end{aligned} \quad (3.27)$$

where the stress resultants are given by:

$$\left(\mathbf{P}_\varepsilon^{(0)}, \mathbf{P}_\varepsilon^{(1)}, \mathbf{P}_\varepsilon^{(2)}\right) = \int_{-h/2}^{h/2} (1, \Phi_1, \Phi_2) \boldsymbol{\sigma}^{(i)} dx_3; \mathbf{P}_\varepsilon^{(3)} = \int_{-h/2}^{h/2} \Phi_3 \boldsymbol{\sigma}^{(o)} dx_3 \quad (3.28a)$$

$$\left(\mathbf{P}_\xi^{(0)}, \mathbf{P}_\xi^{(1)}, \mathbf{P}_\xi^{(2)}, \mathbf{P}_\xi^{(3)}, \mathbf{P}_\xi^{(4)}\right) = \int_{-h/2}^{h/2} (1, \Phi_1, \Phi_2, \Phi_{1,3}, \Phi_{2,3}) \mathbf{p} dx_3 \quad (3.28b)$$

$$\left(\mathbf{P}_\chi^{(0)}, \mathbf{P}_\chi^{(1)}, \mathbf{P}_\chi^{(2)}, \mathbf{P}_\chi^{(3)}, \mathbf{P}_\chi^{(4)}, \mathbf{P}_\chi^{(5)}\right) = \int_{-h/2}^{h/2} (1, \Phi_{1,3}, \Phi_{2,3}, \Phi_{1,33}, \Phi_{2,33}, \Phi_2) \mathbf{m} dx_3 \quad (3.28c)$$

$$\left(\mathbf{P}_\eta^{(0)}, \mathbf{P}_\eta^{(1)}, \mathbf{P}_\eta^{(2)}, \mathbf{P}_\eta^{(3)}, \mathbf{P}_\eta^{(4)}, \mathbf{P}_\eta^{(5)}, \mathbf{P}_\eta^{(6)}\right) = \int_{-h/2}^{h/2} (1, \Phi_1, \Phi_2, \Phi_3, \Phi_{1,3}, \Phi_{2,3}, \Phi_{3,3}) \boldsymbol{\eta} dx_3 \quad (3.28d)$$

The following stress resultants could be derived in terms of gradients and strains:

$$\begin{Bmatrix} \mathbf{P}_\varepsilon^{(0)} \\ \mathbf{P}_\varepsilon^{(1)} \\ \mathbf{P}_\varepsilon^{(2)} \\ \mathbf{P}_\varepsilon^{(3)} \end{Bmatrix} = \begin{bmatrix} \mathbf{A}^\varepsilon & \mathbf{B}^\varepsilon & \mathbf{B}_s^\varepsilon & \mathbf{0} \\ \mathbf{B}^\varepsilon & \mathbf{D}^\varepsilon & \mathbf{D}_s^\varepsilon & \mathbf{0} \\ \mathbf{B}_s^\varepsilon & \mathbf{D}_s^\varepsilon & \mathbf{H}_s^\varepsilon & \mathbf{0} \\ \mathbf{0} & \mathbf{0} & \mathbf{0} & \mathbf{A}_s^\varepsilon \end{bmatrix} \begin{Bmatrix} \boldsymbol{\varepsilon}^{(0)} \\ \boldsymbol{\varepsilon}^{(1)} \\ \boldsymbol{\varepsilon}^{(2)} \\ \boldsymbol{\varepsilon}^{(3)} \end{Bmatrix} \quad (3.29a)$$

$$\begin{Bmatrix} \mathbf{P}_\xi^{(0)} \\ \mathbf{P}_\xi^{(1)} \\ \mathbf{P}_\xi^{(2)} \\ \mathbf{P}_\xi^{(3)} \\ \mathbf{P}_\xi^{(4)} \end{Bmatrix} = \begin{bmatrix} \mathbf{A}^\xi & \mathbf{B}^\xi & \mathbf{B}_s^\xi & \bar{\mathbf{B}}^\xi & \bar{\mathbf{B}}_s^\xi \\ \mathbf{B}^\xi & \mathbf{D}^\xi & \mathbf{D}_s^\xi & \bar{\mathbf{O}}^\xi & \bar{\mathbf{P}}_s^\xi \\ \mathbf{B}_s^\xi & \mathbf{D}_s^\xi & \mathbf{H}_s^\xi & \bar{\mathbf{F}}_s^\xi & \bar{\mathbf{J}}^\xi \\ \bar{\mathbf{B}}^\xi & \bar{\mathbf{O}}^\xi & \bar{\mathbf{F}}_s^\xi & \bar{\mathbf{D}}^\xi & \bar{\mathbf{D}}_s^\xi \\ \bar{\mathbf{B}}_s^\xi & \bar{\mathbf{P}}_s^\xi & \bar{\mathbf{J}}^\xi & \bar{\mathbf{D}}_s^\xi & \bar{\mathbf{H}}_s^\xi \end{bmatrix} \begin{Bmatrix} \boldsymbol{\xi}^{(0)} \\ \boldsymbol{\xi}^{(1)} \\ \boldsymbol{\xi}^{(2)} \\ \boldsymbol{\xi}^{(3)} \\ \boldsymbol{\xi}^{(4)} \end{Bmatrix} \quad (3.29b)$$

$$\begin{Bmatrix} \mathbf{P}_\chi^{(0)} \\ \mathbf{P}_\chi^{(1)} \\ \mathbf{P}_\chi^{(2)} \\ \mathbf{P}_\chi^{(3)} \\ \mathbf{P}_\chi^{(4)} \\ \mathbf{P}_\chi^{(5)} \end{Bmatrix} = \begin{bmatrix} \mathbf{A}^\chi & \bar{\mathbf{B}}^\chi & \bar{\mathbf{B}}_s^\chi & \bar{\bar{\mathbf{B}}}^\chi & \bar{\bar{\mathbf{B}}}_s^\chi & \mathbf{B}_s^\chi \\ \bar{\mathbf{B}}^\chi & \bar{\mathbf{D}}^\chi & \bar{\mathbf{D}}_s^\chi & \bar{\mathbf{E}}^\chi & \bar{\mathbf{E}}_s^\chi & \bar{\mathbf{F}}_s^\chi \\ \bar{\mathbf{B}}_s^\chi & \bar{\mathbf{D}}_s^\chi & \bar{\mathbf{H}}_s^\chi & \bar{\mathbf{G}}_s^\chi & \bar{\mathbf{I}}^\chi & \bar{\mathbf{J}}^\chi \\ \bar{\bar{\mathbf{B}}}^\chi & \bar{\mathbf{E}}^\chi & \bar{\mathbf{G}}_s^\chi & \bar{\bar{\mathbf{D}}}^\chi & \bar{\bar{\mathbf{D}}}_s^\chi & \bar{\mathbf{K}}_s^\chi \\ \bar{\bar{\mathbf{B}}}_s^\chi & \bar{\mathbf{E}}_s^\chi & \bar{\mathbf{I}}^\chi & \bar{\bar{\mathbf{D}}}_s^\chi & \bar{\bar{\mathbf{H}}}_s^\chi & \bar{\mathbf{L}} \\ \mathbf{B}_s^\chi & \bar{\mathbf{F}}_s^\chi & \bar{\mathbf{J}}^\chi & \bar{\mathbf{K}}_s^\chi & \bar{\mathbf{L}} & \mathbf{H}_s^\chi \end{bmatrix} \begin{Bmatrix} \boldsymbol{\chi}^{(0)} \\ \boldsymbol{\chi}^{(1)} \\ \boldsymbol{\chi}^{(2)} \\ \boldsymbol{\chi}^{(3)} \\ \boldsymbol{\chi}^{(4)} \\ \boldsymbol{\chi}^{(5)} \end{Bmatrix} \quad (3.29c)$$

$$\begin{Bmatrix} \mathbf{P}_\eta^{(0)} \\ \mathbf{P}_\eta^{(1)} \\ \mathbf{P}_\eta^{(2)} \\ \mathbf{P}_\eta^{(3)} \\ \mathbf{P}_\eta^{(4)} \\ \mathbf{P}_\eta^{(5)} \\ \mathbf{P}_\eta^{(6)} \end{Bmatrix} = \begin{bmatrix} \mathbf{A}^\eta & \mathbf{B}^\eta & \mathbf{B}_s^\eta & \mathbf{A}_s^\eta & \bar{\mathbf{B}}^\eta & \bar{\mathbf{B}}_s^\eta & \bar{\mathbf{A}}_s^\eta \\ \mathbf{B}^\eta & \mathbf{D}^\eta & \mathbf{D}_s^\eta & \mathbf{D}_{ts}^\eta & \bar{\mathbf{O}}^\eta & \bar{\mathbf{P}}_s^\eta & \bar{\mathbf{Q}}_s^\eta \\ \mathbf{B}_s^\eta & \mathbf{D}_s^\eta & \mathbf{H}_s^\eta & \mathbf{D}_{hs}^\eta & \bar{\mathbf{F}}_s^\eta & \bar{\mathbf{J}}^\eta & \bar{\mathbf{F}}_{hs}^\eta \\ \mathbf{A}_s^\eta & \mathbf{D}_{ts}^\eta & \mathbf{D}_{hs}^\eta & \mathbf{H}_{ts}^\eta & \bar{\mathbf{F}}_{ts}^\eta & \bar{\mathbf{J}}_{hs}^\eta & \bar{\mathbf{R}}^\eta \\ \bar{\mathbf{B}}^\eta & \bar{\mathbf{O}}^\eta & \bar{\mathbf{F}}_s^\eta & \bar{\mathbf{F}}_{ts}^\eta & \bar{\mathbf{D}}^\eta & \bar{\mathbf{D}}_s^\eta & \bar{\mathbf{D}}_{ts}^\eta \\ \bar{\mathbf{B}}_s^\eta & \bar{\mathbf{P}}_s^\eta & \bar{\mathbf{J}}^\eta & \bar{\mathbf{J}}_{hs}^\eta & \bar{\mathbf{D}}_s^\eta & \bar{\mathbf{H}}_s^\eta & \bar{\mathbf{D}}_{hs}^\eta \\ \bar{\mathbf{A}}_s^\eta & \bar{\mathbf{Q}}_s^\eta & \bar{\mathbf{F}}_{hs}^\eta & \bar{\mathbf{R}}^\eta & \bar{\mathbf{D}}_{ts}^\eta & \bar{\mathbf{D}}_{hs}^\eta & \bar{\mathbf{H}}_{ts}^\eta \end{bmatrix} \begin{Bmatrix} \boldsymbol{\eta}^{(0)} \\ \boldsymbol{\eta}^{(1)} \\ \boldsymbol{\eta}^{(2)} \\ \boldsymbol{\eta}^{(3)} \\ \boldsymbol{\eta}^{(4)} \\ \boldsymbol{\eta}^{(5)} \\ \boldsymbol{\eta}^{(6)} \end{Bmatrix} \quad (3.29d)$$

where the microplates stiffness components are described as follows:

$$\left(\mathbf{D}_s^\varepsilon, \mathbf{B}_s^\varepsilon, \mathbf{H}_s^\varepsilon, \mathbf{D}^\varepsilon, \mathbf{B}^\varepsilon, \mathbf{A}^\varepsilon \right) = \int_{-h/2}^{h/2} \left(\Phi_1 \Phi_2, \Phi_2, \Phi_2^2, \Phi_1^2, \Phi_1, 1 \right) \mathbf{Q}_\varepsilon^{(i)} dx_3 \quad (3.30a)$$

$$\mathbf{A}_s^\varepsilon = \int_{-h/2}^{h/2} \Phi_3^2 \mathbf{Q}_\varepsilon^{(o)} dx_3 \quad (3.30b)$$

$$\begin{aligned} \left(\mathbf{A}^\xi, \mathbf{B}^\xi, \mathbf{B}_s^\xi, \bar{\mathbf{B}}^\xi, \bar{\mathbf{B}}_s^\xi \right) &= \left(A^\xi, B^\xi, B_s^\xi, \bar{B}^\xi, \bar{B}_s^\xi \right) \mathbf{I}_{3 \times 3} \\ &= \int_{-h/2}^{h/2} \left(1, \Phi_1, \Phi_2, \Phi_{1,3}, \Phi_{2,3} \right) \boldsymbol{\alpha}_\xi \mathbf{I}_{3 \times 3} dx_3 \end{aligned} \quad (3.30c)$$

$$\begin{aligned} \left(\mathbf{D}^\xi, \mathbf{D}_s^\xi, \bar{\mathbf{O}}^\xi, \bar{\mathbf{P}}_s^\xi \right) &= \left(D^\xi, D_s^\xi, \bar{O}^\xi, \bar{P}_s^\xi \right) \mathbf{I}_{3 \times 3} \\ &= \int_{-h/2}^{h/2} \Phi_1 \left(\Phi_1, \Phi_2, \Phi_{1,3}, \Phi_{2,3} \right) \boldsymbol{\alpha}_\xi \mathbf{I}_{3 \times 3} dx_3 \end{aligned} \quad (3.30d)$$

$$\begin{aligned} \left(\mathbf{H}_s^\xi, \bar{\mathbf{F}}_s^\xi, \bar{\mathbf{J}}^\xi, \bar{\mathbf{D}}^\xi, \bar{\mathbf{D}}_s^\xi, \bar{\mathbf{H}}_s^\xi \right) &= \left(H_s^\xi, \bar{F}_s^\xi, \bar{J}^\xi, \bar{D}^\xi, \bar{D}_s^\xi, \bar{H}_s^\xi \right) \mathbf{I}_{3 \times 3} \\ &= \int_{-h/2}^{h/2} \left(\Phi_2^2, \Phi_2 \Phi_{1,3}, \Phi_2 \Phi_{2,3}, \Phi_{1,3}^2, \Phi_{1,3} \Phi_{2,3}, \Phi_{2,3}^2 \right) \boldsymbol{\alpha}_\xi \mathbf{I}_{3 \times 3} dx_3 \end{aligned} \quad (3.30e)$$

$$\begin{aligned} \left(\mathbf{A}^\eta, \mathbf{B}^\eta, \mathbf{B}_s^\eta, \mathbf{A}_s^\eta, \bar{\mathbf{B}}^\eta, \bar{\mathbf{B}}_s^\eta, \bar{\mathbf{A}}_s^\eta \right) &= \left(A^\eta, B^\eta, B_s^\eta, A_s^\eta, \bar{B}^\eta, \bar{B}_s^\eta, \bar{A}_s^\eta \right) \mathbf{I}_{10 \times 10} \\ &= \int_{-h/2}^{h/2} \left(1, \Phi_1, \Phi_2, \Phi_3, \Phi_{1,3}, \Phi_{2,3}, \Phi_{3,3} \right) \boldsymbol{\alpha}_\eta \mathbf{I}_{10 \times 10} dx_3 \end{aligned} \quad (3.30f)$$

$$\begin{aligned}
& \left(\mathbf{D}^\eta, \mathbf{D}_s^\eta, \mathbf{D}_{ts}^\eta, \overline{\mathbf{O}}^\eta, \overline{\mathbf{P}}_s^\eta, \overline{\mathbf{Q}}_s^\eta \right) = \left(D^\eta, D_s^\eta, D_{ts}^\eta, \overline{O}^\eta, \overline{P}_s^\eta, \overline{Q}_s^\eta \right) \mathbf{I}_{10 \times 10} \\
& = \int_{-h/2}^{h/2} \Phi_1 \left(\Phi_1, \Phi_2, \Phi_3, \Phi_{1,3}, \Phi_{2,3}, \Phi_{3,3} \right) \alpha_\eta \mathbf{I}_{10 \times 10} dx_3
\end{aligned} \tag{3.30g}$$

$$\begin{aligned}
& \left(\mathbf{H}_s^\eta, \overline{\mathbf{D}}_{hs}^\eta, \overline{\mathbf{F}}_s^\eta, \overline{\mathbf{J}}^\eta, \overline{\mathbf{F}}_{hs}^\eta \right) = \left(H_s^\eta, \overline{D}_{hs}^\eta, \overline{F}_s^\eta, \overline{J}^\eta, \overline{F}_{hs}^\eta \right) \mathbf{I}_{10 \times 10} \\
& = \int_{-h/2}^{h/2} \Phi_2 \left(\Phi_2, \Phi_3, \Phi_{1,3}, \Phi_{2,3}, \Phi_{3,3} \right) \alpha_\eta \mathbf{I}_{10 \times 10} dx_3
\end{aligned} \tag{3.30h}$$

$$\begin{aligned}
& \left(\mathbf{H}_{ts}^\eta, \overline{\mathbf{F}}_{ts}^\eta, \overline{\mathbf{J}}_{hs}^\eta, \overline{\mathbf{R}}^\eta \right) = \left(H_{ts}^\eta, \overline{F}_{ts}^\eta, \overline{J}_{hs}^\eta, \overline{R}^\eta \right) \mathbf{I}_{10 \times 10} = \\
& \int_{-h/2}^{h/2} \Phi_3 \left(\Phi_3, \Phi_{1,3}, \Phi_{2,3}, \Phi_{3,3} \right) \alpha_\eta \mathbf{I}_{10 \times 10} dx_3
\end{aligned} \tag{3.30i}$$

$$\begin{aligned}
& \left(\overline{\mathbf{D}}^\eta, \overline{\mathbf{D}}_s^\eta, \overline{\mathbf{D}}_{ts}^\eta, \overline{\mathbf{H}}_s^\eta, \overline{\mathbf{D}}_{hs}^\eta, \overline{\mathbf{H}}_{ts}^\eta \right) = \left(\overline{D}^\eta, \overline{D}_s^\eta, \overline{D}_{ts}^\eta, \overline{H}_s^\eta, \overline{D}_{hs}^\eta, \overline{H}_{ts}^\eta \right) \mathbf{I}_{10 \times 10} \\
& = \int_{-h/2}^{h/2} \left(\Phi_{1,3}^2, \Phi_{1,3} \Phi_{2,3}, \Phi_{1,3} \Phi_{3,3}, \Phi_{2,3}^2, \Phi_{2,3} \Phi_{3,3}, \Phi_{3,3}^2 \right) \alpha_\eta \mathbf{I}_{10 \times 10} dx_3
\end{aligned} \tag{3.30j}$$

$$\begin{aligned}
& \left(\mathbf{A}^\chi, \overline{\mathbf{B}}^\chi, \overline{\mathbf{B}}_s^\chi, \overline{\mathbf{B}}^\chi, \overline{\mathbf{B}}_s^\chi, \mathbf{B}_s^\chi \right) = \left(A^\chi, \overline{B}^\chi, \overline{B}_s^\chi, \overline{\overline{B}}^\chi, \overline{\overline{B}}_s^\chi, B_s^\chi \right) \mathbf{I}_{6 \times 6} \\
& = \int_{-h/2}^{h/2} \left(1, \Phi_{1,3}, \Phi_{2,3}, \Phi_{1,33}, \Phi_{2,33}, \Phi_2 \right) \alpha_\chi \mathbf{I}_{6 \times 6} dx_3
\end{aligned} \tag{3.30k}$$

$$\begin{aligned}
& \left(\overline{\mathbf{D}}^\chi, \overline{\mathbf{D}}_s^\chi, \overline{\mathbf{E}}^\chi, \overline{\mathbf{E}}_s^\chi, \overline{\mathbf{F}}_s^\chi \right) = \left(\overline{D}^\chi, \overline{D}_s^\chi, \overline{E}^\chi, \overline{E}_s^\chi, \overline{F}_s^\chi \right) \mathbf{I}_{6 \times 6} \\
& = \int_{-h/2}^{h/2} \left(\Phi_{1,3} \Phi_{1,3}, \Phi_{2,3} \Phi_{1,3}, \Phi_{1,33} \Phi_{1,3}, \Phi_{2,33} \Phi_{1,3}, \Phi_2 \Phi_{1,3} \right) \alpha_\chi \mathbf{I}_{6 \times 6} dx_3
\end{aligned} \tag{3.30l}$$

$$\begin{aligned}
& \left(\overline{\mathbf{H}}_s^\chi, \overline{\mathbf{G}}_s^\chi, \overline{\mathbf{I}}^\chi, \overline{\mathbf{J}}^\chi \right) = \left(\overline{H}_s^\chi, \overline{G}_s^\chi, \overline{I}^\chi, \overline{J}^\chi \right) \mathbf{I}_{6 \times 6} \\
& = \int_{-h/2}^{h/2} \left(\Phi_{2,3} \Phi_{2,3}, \Phi_{1,33} \Phi_{2,3}, \Phi_{2,33} \Phi_{2,3}, \Phi_2 \Phi_{2,3} \right) \alpha_\chi \mathbf{I}_{6 \times 6} dx_3
\end{aligned} \tag{3.30m}$$

$$\begin{aligned}
& \left(\overline{\overline{\mathbf{D}}}^\chi, \overline{\overline{\mathbf{D}}}_s^\chi, \overline{\mathbf{K}}_s^\chi, \overline{\overline{\mathbf{H}}}_s^\chi, \overline{\mathbf{L}}^\chi, \mathbf{H}_s^\chi \right) = \left(\overline{\overline{D}}^\chi, \overline{\overline{D}}_s^\chi, \overline{K}_s^\chi, \overline{\overline{H}}_s^\chi, \overline{L}^\chi, H_s^\chi \right) \mathbf{I}_{6 \times 6} \\
& = \int_{-h/2}^{h/2} \left(\Phi_{1,33}^2, \Phi_{1,33} \Phi_{2,33}, \Phi_{1,33} \Phi_2, \Phi_{2,33}^2, \Phi_{2,33} \Phi_2, \Phi_2^2 \right) \alpha_\chi \mathbf{I}_{6 \times 6} dx_3
\end{aligned} \tag{3.30n}$$

The variation of work done by membrane compressive loads in thermo-mechanical environments is determined by:

$$\begin{aligned} \delta\Pi_{VB} = & -\int_A N^{(tr)} \left(u_{3,1}^0 \delta u_{3,1}^0 + u_{3,2}^0 \delta u_{3,2}^0 \right) dA \\ & -\int_A \left(N_1^{(m)} u_{3,1}^0 \delta u_{3,1}^0 + N_2^{(m)} u_{3,2}^0 \delta u_{3,2}^0 \right) dA \end{aligned} \quad (3.31)$$

where $N_1^{(m)}$ and $N_2^{(m)}$ are in-plane edge loads, $N_{12}^{(m)} = 0$; $N_1^{(tr)} = N_2^{(tr)} = N^{(tr)}$, $N_{12}^{(tr)} = 0$ are the pre-buckling in-plane thermal loads given by:

$$N^{(tr)} = \int_{-h/2}^{h/2} (Q_{11} + Q_{12}) \alpha \Delta T dz \quad (3.32)$$

in which α is the coefficient of thermal expansion; $\Delta T = T(z) - T_o$ is the current temperature's deviation from the reference one T_o . The work done by a transverse load q of the microplates is given by:

$$\delta\Pi_{FB} = -\int_A q u_3^0 dA \quad (3.33)$$

The variation of kinetic energy $\delta\Pi_{KB}$ calculated by:

$$\begin{aligned} \delta\Pi_{KB} = & \frac{1}{2} \int_V \rho \left(\dot{u}_1 \delta \dot{u}_1 + \dot{u}_2 \delta \dot{u}_2 + \dot{u}_3 \delta \dot{u}_3 \right) dV \\ = & \frac{1}{2} \int_A \left[I_2 \left(\dot{u}_{3,1}^0 \delta \dot{u}_{3,1}^0 + \dot{u}_{3,2}^0 \delta \dot{u}_{3,2}^0 \right) + K_2 \left(\dot{\phi}_1 \delta \dot{\phi}_1 + \dot{\phi}_2 \delta \dot{\phi}_2 \right) \right. \\ & I_0 \left(\dot{u}_1^0 \delta \dot{u}_1^0 + \dot{u}_2^0 \delta \dot{u}_2^0 + \dot{u}_3^0 \delta \dot{u}_3^0 \right) + I_1 \left(\dot{u}_1^0 \delta \dot{u}_{3,1}^0 + \dot{u}_{3,1}^0 \delta \dot{u}_1^0 + \dot{u}_2^0 \delta \dot{u}_{3,2}^0 + \dot{u}_{3,2}^0 \delta \dot{u}_2^0 \right) \\ & + J_1 \left(\dot{u}_1^0 \delta \dot{\phi}_1 + \dot{\phi}_1 \delta \dot{u}_1^0 + \dot{u}_2^0 \delta \dot{\phi}_2 + \dot{\phi}_2 \delta \dot{u}_2^0 \right) \\ & \left. + J_2 \left(\dot{u}_{3,1}^0 \delta \dot{\phi}_1 + \dot{\phi}_1 \delta \dot{u}_{3,1}^0 + \dot{u}_{3,2}^0 \delta \dot{\phi}_2 + \dot{\phi}_2 \delta \dot{u}_{3,2}^0 \right) \right] dA \end{aligned} \quad (3.34)$$

where $I_0, I_1, I_2, J_1, J_2, K_2$ are mass components of the microplate which are defined as:

$$(K_2, J_2, J_1, I_2, I_1, I_0) = \int_{-h/2}^{h/2} (\Phi_2^2, \Phi_1 \Phi_2, \Phi_2, \Phi_1^2, \Phi_1, 1) \rho dx_3 \quad (3.35)$$

3.2.3 Ritz-type series solution

According to the Ritz approach, the following series of approximation functions and associated series values can be used to describe the membrane and transverse displacements $(u_1^0, u_2^0, u_3^0, \varphi_1, \varphi_2)$ of the microplates:

$$u_1^0(x_1, x_2) = \sum_{i=1}^{n_1} \sum_{j=1}^{n_2} u_{1ij} R_{i,1}(x_1) P_j(x_2); u_2^0(x_1, x_2) = \sum_{i=1}^{n_1} \sum_{j=1}^{n_2} u_{2ij} R_i(x_1) P_{j,2}(x_2) \quad (3.36a)$$

$$u_3^0(x_1, x_2) = \sum_{i=1}^{n_1} \sum_{j=1}^{n_2} u_{3ij} R_i(x_1) P_j(x_2); \varphi_2(x_1, x_2) = \sum_{i=1}^{n_1} \sum_{j=1}^{n_2} y_{ij} R_i(x_1) P_{j,2}(x_2) \quad (3.36b)$$

$$\varphi_1(x_1, x_2) = \sum_{i=1}^{n_1} \sum_{j=1}^{n_2} x_{ij} R_{i,1}(x_1) P_j(x_2) \quad (3.36c)$$

where $u_{1ij}, u_{2ij}, u_{3ij}, x_{ij}, y_{ij}$ are represent unknown variables need to determined; the shape functions in x_1 -, x_2 - direction are $R_i(x_1), P_j(x_2)$, respectively. As a consequence, only two shape functions affect the five unknowns of the microplates. As mentioned in the introduction section, the accuracy and efficiency of the Ritz method strongly depend on the construction of the approximation functions. In general, these shape functions should be complete, continuous and independently linear. In this study, the Hermite polynomial, Laguerre polynomial, exponential function and orthogonal polynomials made from Gram Schmidt method which are defined by this recursion formula, are used to develop novel Ritz method's shape functions.

Hermite polynomial:

Hermite polynomial are characterized by the following recursion formula:

$$\begin{cases} He_0(x) = 1, & He_1(x) = 2x, \\ He_n(x) = 2xHe_{n-1}(x) - 2(n-1)He_{n-2}(x) \end{cases} \quad (3.37)$$

Hermite polynomials satisfy normalization as follows:

$$\int_{-\infty}^{\infty} (He(x))^2 e^{-x^2} dx = 2^n \sqrt{\pi} n! \quad (3.38)$$

Laguerre polynomial:

Hypergeometric functions define the generalized Laguerre function:

$$L(n, a, x) = \binom{n+a}{a} {}_1F_1(-n; a+1; x) \quad (3.39)$$

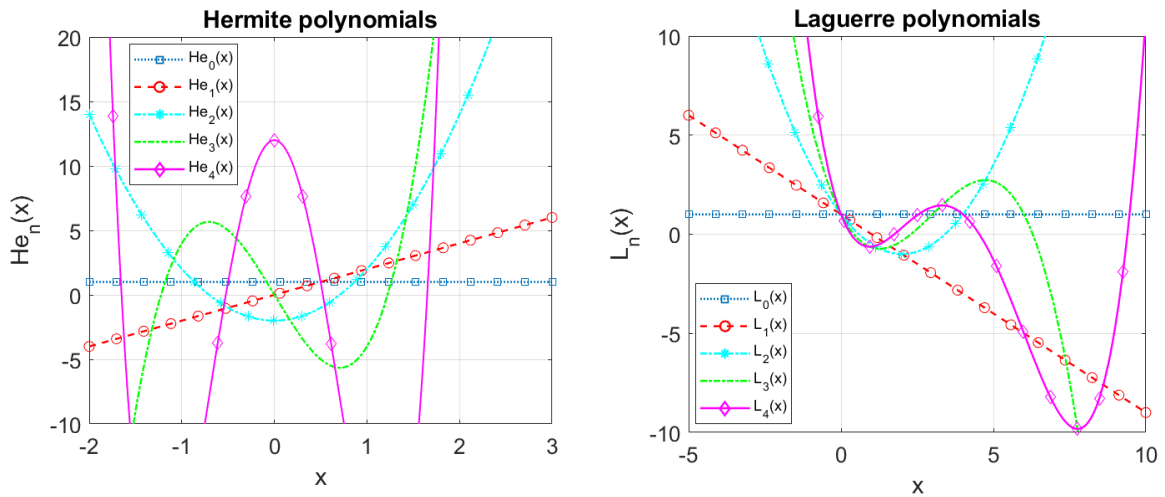
The function returns orthogonal generalized Laguerre polynomials for nonnegative integer values of n :

$$\langle f_1, f_2 \rangle = \int_0^\infty e^{-x} x^a f_1(x) f_2(x) dx \quad (3.40)$$

Furthermore, generalized Laguerre polynomials fulfill this normalization:

$$\langle L(n, a, x), L(m, a, x) \rangle = \begin{cases} 0 & \text{if } n \neq m \\ \frac{\Gamma(a+n+1)}{n!} & \text{if } n = m \end{cases} \quad (3.41)$$

The first five Hermite polynomials and Laguerre polynomials are displayed in Fig. 3.1



(a) The first five Hermite polynomials

(b) The first five Laguerre polynomials

Figure 3.1: The first five algorithm polynomials for series type solution

Gram-Schmidt-based orthogonal polynomials:

Next, the admissible functions known as orthogonal polynomials (OP) proposed by Bhat [136] are discussed, which are constructed using the GS method [137]. These

functions exhibit a rapid convergence rate, although they encounter challenges in determining the initial function. Using the GS approach is defined as follows:

$$\phi_1(x) = (x - A_1)\phi_0(x), \quad \phi_k(x) = (x - A_k)\phi_{k-1}(x) - D_k\phi_{k-2}(x) \quad (3.42a)$$

$$A_k = \frac{\int_c^d xw(x)\phi_{k-1}^2(x)dx}{\int_c^d w(x)\phi_{k-1}^2(x)dx}; \quad D_k = \frac{\int_c^d xw(x)\phi_{k-1}(x)\phi_{k-2}(x)dx}{\int_c^d w(x)\phi_{k-2}^2(x)dx} \quad (3.42b)$$

where $w(x)$ being the weighting function. The orthogonality is satisfied by the polynomials $\phi_k(x)$ as below:

$$\int_c^d w(x)\phi_k(x)\phi_l(x)dx = \begin{cases} 0 & \text{if } k \neq l \\ a_{kl} & \text{if } k = l \end{cases} \quad (3.43)$$

with $w(x) = 1$; $\phi_0(x) = 2x + 1$, and $[c, d] \in [-1, 1]$. The first five orthogonal polynomials are shown in Fig. 3.2.

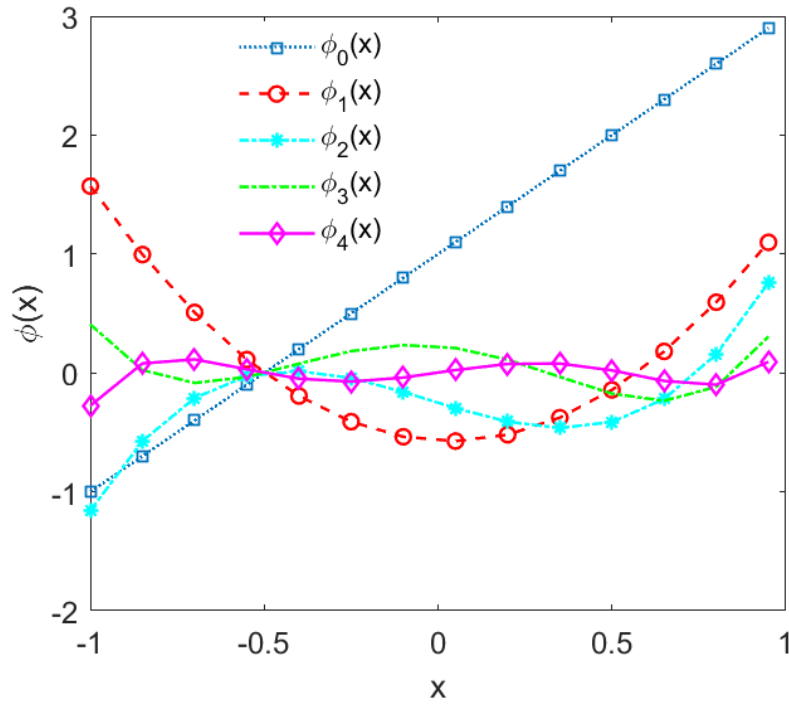
The functions $R_i(x_1)$ and $P_j(x_2)$ are generated to satisfy the boundary conditions (BCs) at the microplate edges as follows:

- Clamped (C): $\varphi_2 = \varphi_1 = u_3^0 = u_2^0 = u_1^0 = 0$ at $x_2 = 0, b$ and $x_1 = 0, a$
- Simply supported (S): $\varphi_2 = u_3^0 = u_2^0 = 0$ at $x_1 = 0, a$ and $\varphi_1 = u_3^0 = u_1^0 = 0$ at $x_2 = 0, b$

The combination of clamped and simply-supported BCs on the edges of the microplates leads to the various ones as follows: SSSS, SCSC, CSCS, CCCC which will be taken into account in the numerical examples as follows in the Table 3.1:

Table 3.1: Approximation functions of series solutions with different BCs

Boundary conditions		Approximation functions	
		$R_j(x_1)$	$P_j(x_2)$
SSSS	Ritz-Hermite	$x_1(a-x_1)He_j$	$x_2(b-x_2)He_j$
	Ritz-Laguerre	$x_1(a-x_1)L_j$	$x_2(b-x_2)L_j$
	Ritz-OP	$x_1(a-x_1)\phi_j$	$x_2(b-x_2)\phi_j$
SCSC	Ritz-Hermite	$x_1(a-x_1)^2He_j$	$x_2(b-x_2)^2He_j$
	Ritz-Laguerre	$x_1(a-x_1)^2L_j$	$x_2(b-x_2)^2L_j$
	Ritz-OP	$x_1(a-x_1)^2\phi_j$	$x_2(b-x_2)^2\phi_j$
CSCS	Ritz-Hermite	$x_1^2(a-x_1)He_j$	$x_2^2(b-x_2)He_j$
	Ritz-Laguerre	$x_1^2(a-x_1)L_j$	$x_2^2(b-x_2)L_j$
	Ritz-OP	$x_1^2(a-x_1)\phi_j$	$x_2^2(b-x_2)\phi_j$
CCCC	Ritz-Hermite	$x_1^2(a-x_1)^2He_j$	$x_2^2(b-x_2)^2He_j$
	Ritz-Laguerre	$x_1^2(a-x_1)^2L_j$	$x_2^2(b-x_2)^2L_j$
	Ritz-OP	$x_1^2(a-x_1)^2\phi_j$	$x_2^2(b-x_2)^2\phi_j$

**Figure 3.2:** The first five orthogonal polynomials based on GS process

Additionally, in order to construct characteristic equations of motion for the microplates, substituting the approximations in Eq. (3.36) into Eq. (3.34), Eq. (3.33), Eq. (3.31) and Eq. (3.16) by accounting for Eq. (3.15) leads to:

$$(\mathbf{K} - N^0 \mathbf{K}^g) \mathbf{d} + \mathbf{M} \ddot{\mathbf{d}} = \mathbf{F} \quad (3.44)$$

where $\mathbf{d}(t) = [\mathbf{u}_1 \quad \mathbf{u}_2 \quad \mathbf{u}_3 \quad \mathbf{x} \quad \mathbf{y}]^T$ is the displacement vector to be determined; $\mathbf{K} = \mathbf{K}^\varepsilon + \mathbf{K}^\chi + \mathbf{K}^\xi + \mathbf{K}^\eta$ [182, 183] is the stiffness matrix which is composed of those of the strains \mathbf{K}^ε , symmetric rotation gradients \mathbf{K}^χ , dilatation gradient \mathbf{K}^ξ , deviation stretch gradient \mathbf{K}^η , and \mathbf{F} is the force vector; \mathbf{K}^g is the geometric stiffness matrix; \mathbf{M} is the mass matrix. These components are given more details as follows:

$$\mathbf{K}^\kappa = \begin{bmatrix} \mathbf{K}^{\kappa 11} & \mathbf{K}^{\kappa 12} & \mathbf{K}^{\kappa 13} & \mathbf{K}^{\kappa 14} & \mathbf{K}^{\kappa 15} \\ {}^T \mathbf{K}^{\kappa 12} & \mathbf{K}^{\kappa 22} & \mathbf{K}^{\kappa 23} & \mathbf{K}^{\kappa 24} & \mathbf{K}^{\kappa 25} \\ {}^T \mathbf{K}^{\kappa 13} & {}^T \mathbf{K}^{\kappa 23} & \mathbf{K}^{\kappa 33} & \mathbf{K}^{\kappa 34} & \mathbf{K}^{\kappa 35} \\ {}^T \mathbf{K}^{\kappa 14} & {}^T \mathbf{K}^{\kappa 24} & {}^T \mathbf{K}^{\kappa 34} & \mathbf{K}^{\kappa 44} & \mathbf{K}^{\kappa 45} \\ {}^T \mathbf{K}^{\kappa 15} & {}^T \mathbf{K}^{\kappa 25} & {}^T \mathbf{K}^{\kappa 35} & {}^T \mathbf{K}^{\kappa 45} & \mathbf{K}^{\kappa 55} \end{bmatrix} \quad \text{with } \kappa = \{\varepsilon, \xi, \chi, \eta\} \quad (3.45a)$$

$$\mathbf{M} = \begin{bmatrix} \mathbf{M}^{11} & 0 & \mathbf{M}^{13} & \mathbf{M}^{14} & 0 \\ 0 & \mathbf{M}^{22} & \mathbf{M}^{23} & 0 & \mathbf{M}^{25} \\ {}^T \mathbf{M}^{13} & {}^T \mathbf{M}^{23} & \mathbf{M}^{33} & \mathbf{M}^{34} & \mathbf{M}^{35} \\ {}^T \mathbf{M}^{14} & 0 & {}^T \mathbf{M}^{34} & \mathbf{M}^{44} & \mathbf{M}^{45} \\ 0 & {}^T \mathbf{M}^{25} & {}^T \mathbf{M}^{35} & {}^T \mathbf{M}^{45} & \mathbf{M}^{55} \end{bmatrix} \quad (3.45b)$$

$$\mathbf{F} = [\mathbf{0} \quad \mathbf{0} \quad \mathbf{f} \quad \mathbf{0} \quad \mathbf{0}]^T \quad (3.45c)$$

$$\mathbf{K}^g = \begin{bmatrix} \mathbf{0} & \mathbf{0} & \mathbf{0} & \mathbf{0} & \mathbf{0} \\ \mathbf{0} & \mathbf{0} & \mathbf{0} & \mathbf{0} & \mathbf{0} \\ \mathbf{0} & \mathbf{0} & \mathbf{K}^{g33} & \mathbf{0} & \mathbf{0} \\ \mathbf{0} & \mathbf{0} & \mathbf{0} & \mathbf{0} & \mathbf{0} \\ \mathbf{0} & \mathbf{0} & \mathbf{0} & \mathbf{0} & \mathbf{0} \end{bmatrix} \quad \text{with } K_{ijkl}^{g33} = H_{ik}^{11} S_{jl}^{00} + H_{ik}^{00} S_{jl}^{11} \quad (3.45d)$$

where the components of stiffness matrix \mathbf{K}^ε are defined as follows:

$$K_{ijkl}^{\varepsilon 11} = A_{11}^\varepsilon T_{ik}^{22} S_{jl}^{00} + A_{66}^\varepsilon T_{ik}^{11} S_{jl}^{11}, K_{ijkl}^{\varepsilon 12} = A_{12}^\varepsilon T_{ik}^{02} S_{jl}^{20} + A_{66}^\varepsilon T_{ik}^{11} S_{jl}^{11}$$

$$K_{ijkl}^{\varepsilon 13} = B_{11}^\varepsilon T_{ik}^{22} S_{jl}^{00} + B_{12}^\varepsilon T_{ik}^{02} S_{jl}^{20} + 2B_{66}^\varepsilon T_{ik}^{11} S_{jl}^{11}$$

$$\begin{aligned}
K_{ijkl}^{\varepsilon 14} &= B_{s11}^{\varepsilon} T_{ik}^{22} S_{jl}^{00} + B_{s66}^{\varepsilon} T_{ik}^{11} S_{jl}^{11}, K_{ijkl}^{\varepsilon 15} = B_{s12}^{\varepsilon} T_{ik}^{02} S_{jl}^{20} + B_{s66}^{\varepsilon} T_{ik}^{11} S_{jl}^{11} \\
K_{ijkl}^{\varepsilon 22} &= A_{22}^{\varepsilon} T_{ik}^{00} S_{jl}^{22} + A_{66}^{\varepsilon} T_{ik}^{11} S_{jl}^{11}, K_{ijkl}^{\varepsilon 23} = B_{12}^{\varepsilon} T_{ik}^{20} S_{jl}^{02} + B_{22}^{\varepsilon} T_{ik}^{00} S_{jl}^{22} + 2B_{66}^{\varepsilon} T_{ik}^{11} S_{jl}^{11} \\
K_{ijkl}^{\varepsilon 24} &= B_{s12}^{\varepsilon} T_{ik}^{20} S_{jl}^{02} + B_{s66}^{\varepsilon} T_{ik}^{11} S_{jl}^{11}, K_{ijkl}^{\varepsilon 25} = B_{s22}^{\varepsilon} T_{ik}^{00} S_{jl}^{22} + B_{s66}^{\varepsilon} T_{ik}^{11} S_{jl}^{11} \\
K_{ijkl}^{\varepsilon 33} &= D_{11}^{\varepsilon} T_{ik}^{22} S_{jl}^{00} + D_{12}^{\varepsilon} (T_{ik}^{02} S_{jl}^{20} + T_{ik}^{20} S_{jl}^{02}) + D_{22}^{\varepsilon} T_{ik}^{00} S_{jl}^{22} + 4D_{66}^{\varepsilon} T_{ik}^{11} S_{jl}^{11} \\
&+ A_{s44}^{\varepsilon} T_{ik}^{00} S_{jl}^{11} + A_{s55}^{\varepsilon} T_{ik}^{11} S_{jl}^{00} - N^0 (T_{ik}^{11} S_{jl}^{00} + T_{ik}^{00} S_{jl}^{11}) \\
K_{ijkl}^{\varepsilon 34} &= D_{s11}^{\varepsilon} T_{ik}^{22} S_{jl}^{00} + D_{s12}^{\varepsilon} T_{ik}^{20} S_{jl}^{02} + 2D_{s66}^{\varepsilon} T_{ik}^{11} S_{jl}^{11} + A_{s55}^{\varepsilon} T_{ik}^{11} S_{jl}^{00} \\
K_{ijkl}^{\varepsilon 35} &= D_{s12}^{\varepsilon} T_{ik}^{02} S_{jl}^{20} + D_{s22}^{\varepsilon} T_{ik}^{00} S_{jl}^{22} + 2D_{s66}^{\varepsilon} T_{ik}^{11} S_{jl}^{11} + A_{s44}^{\varepsilon} T_{ik}^{00} S_{jl}^{11} \\
K_{ijkl}^{\varepsilon 44} &= H_{s11}^{\varepsilon} T_{ik}^{22} S_{jl}^{00} + H_{s66}^{\varepsilon} T_{ik}^{11} S_{jl}^{11} + A_{s55}^{\varepsilon} T_{ik}^{11} S_{jl}^{00} \\
K_{ijkl}^{\varepsilon 45} &= H_{s12}^{\varepsilon} T_{ik}^{02} S_{jl}^{20} + H_{s66}^{\varepsilon} T_{ik}^{11} S_{jl}^{11} \\
K_{ijkl}^{\varepsilon 55} &= H_{s22}^{\varepsilon} T_{ik}^{00} S_{jl}^{22} + H_{s66}^{\varepsilon} T_{ik}^{11} S_{jl}^{11} + A_{s44}^{\varepsilon} T_{ik}^{00} S_{jl}^{11}
\end{aligned} \tag{3.46}$$

The components of stiffness matrix \mathbf{K}^{χ} are defined as follows:

$$\begin{aligned}
K_{ijkl}^{\chi 11} &= \frac{A^{\chi}}{4} (T_{ik}^{22} S_{jl}^{11} + T_{ik}^{11} S_{jl}^{22}), K_{ijkl}^{\chi 12} = -\frac{A^{\chi}}{4} (T_{ik}^{22} S_{jl}^{11} + T_{ik}^{11} S_{jl}^{22}) \\
K_{ijkl}^{\chi 13} &= \frac{\overline{\overline{B}}^{\chi}}{4} (T_{ik}^{02} S_{jl}^{11} - T_{ik}^{11} S_{jl}^{02}), K_{ijkl}^{\chi 14} = \frac{1}{4} \left(B_s^{\chi} T_{ik}^{22} S_{jl}^{11} + B_s^{\chi} T_{ik}^{11} S_{jl}^{22} - \overline{\overline{B}}_s^{\chi} T_{ik}^{11} S_{jl}^{02} \right) \\
K_{ijkl}^{\chi 15} &= \frac{1}{4} \left(\overline{\overline{B}}_s^{\chi} T_{ik}^{02} S_{jl}^{11} - B_s^{\chi} T_{ik}^{22} S_{jl}^{11} - B_s^{\chi} T_{ik}^{11} S_{jl}^{22} \right), K_{ijkl}^{\chi 22} = \frac{A^{\chi}}{4} (T_{ik}^{22} S_{jl}^{11} + T_{ik}^{11} S_{jl}^{22}) \\
K_{ijkl}^{\chi 23} &= \frac{\overline{\overline{B}}^{\chi}}{4} (T_{ik}^{11} S_{jl}^{02} - T_{ik}^{02} S_{jl}^{11}), K_{ijkl}^{\chi 24} = \frac{1}{4} \left(\overline{\overline{B}}_s^{\chi} T_{ik}^{11} S_{jl}^{02} - B_s^{\chi} T_{ik}^{22} S_{jl}^{11} - B_s^{\chi} T_{ik}^{11} S_{jl}^{22} \right) \\
K_{ijkl}^{\chi 25} &= \frac{1}{4} \left(B_s^{\chi} T_{ik}^{22} S_{jl}^{11} + B_s^{\chi} T_{ik}^{11} S_{jl}^{22} - \overline{\overline{B}}_s^{\chi} T_{ik}^{02} S_{jl}^{11} \right)
\end{aligned}$$

$$\begin{aligned}
K_{ijkl}^{\chi 33} &= \frac{1}{4} \left(A^\chi - 2\bar{B}^\chi + \bar{D}^\chi \right) \left(T_{ik}^{00} S_{jl}^{22} - T_{ik}^{20} S_{jl}^{02} - T_{ik}^{02} S_{jl}^{20} + T_{ik}^{22} S_{jl}^{00} + 2T_{ik}^{11} S_{jl}^{11} \right) \\
&+ \frac{1}{4} \bar{\bar{D}}^\chi \left(T_{ik}^{00} S_{jl}^{11} + T_{ik}^{11} S_{jl}^{00} \right) \\
K_{ijkl}^{\chi 34} &= \frac{1}{4} \left[\left(\bar{B}_s^\chi - \bar{D}_s^\chi \right) \left(T_{ik}^{20} S_{jl}^{02} - T_{ik}^{22} S_{jl}^{00} - T_{ik}^{11} S_{jl}^{11} \right) \right. \\
&\left. + \bar{K}_s^\chi \left(T_{ik}^{20} S_{jl}^{11} - T_{ik}^{11} S_{jl}^{20} \right) + \bar{\bar{D}}_s^\chi T_{ik}^{11} S_{jl}^{00} \right] \\
K_{ijkl}^{\chi 35} &= \frac{1}{4} \left[\left(\bar{B}_s^\chi - \bar{D}_s^\chi \right) \left(-T_{ik}^{00} S_{jl}^{22} + T_{ik}^{02} S_{jl}^{20} - T_{ik}^{11} S_{jl}^{11} \right) \right. \\
&\left. + \bar{\bar{D}}_s^\chi T_{ik}^{00} S_{jl}^{11} + \bar{K}_s^\chi \left(T_{ik}^{11} S_{jl}^{20} - T_{ik}^{20} S_{jl}^{11} \right) \right] \\
K_{ijkl}^{\chi 44} &= \frac{1}{4} \left[\bar{H}_s^\chi \left(T_{ik}^{22} S_{jl}^{00} + 2T_{ik}^{11} S_{jl}^{11} \right) + \bar{\bar{H}}_s^\chi T_{ik}^{11} S_{jl}^{00} \right. \\
&\left. - \bar{L}^\chi \left(T_{ik}^{11} S_{jl}^{20} + T_{ik}^{11} S_{jl}^{02} \right) + H_s^\chi \left(T_{ik}^{22} S_{jl}^{11} + T_{ik}^{11} S_{jl}^{22} \right) \right] \\
K_{ijkl}^{\chi 45} &= \frac{1}{4} \left[\bar{L}^\chi \left(T_{ik}^{11} S_{jl}^{20} + T_{ik}^{02} S_{jl}^{11} \right) - \bar{H}_s^\chi \left(T_{ik}^{02} S_{jl}^{20} + T_{ik}^{11} S_{jl}^{11} \right) - H_s^\chi \left(T_{ik}^{11} S_{jl}^{22} + T_{ik}^{22} S_{jl}^{11} \right) \right] \\
K_{ijkl}^{\chi 55} &= \frac{1}{4} \left[\bar{H}_s^\chi \left(2T_{ik}^{11} S_{jl}^{11} + T_{ik}^{00} S_{jl}^{22} \right) + \bar{\bar{H}}_s^\chi T_{ik}^{00} S_{jl}^{11} \right. \\
&\left. - \bar{L}^\chi \left(T_{ik}^{20} S_{jl}^{11} + T_{ik}^{02} S_{jl}^{11} \right) + H_s^\chi \left(T_{ik}^{11} S_{jl}^{22} + T_{ik}^{22} S_{jl}^{11} \right) \right]
\end{aligned} \tag{3.47}$$

The components of stiffness matrix \mathbf{K}^ξ :

$$\begin{aligned}
K_{ijkl}^{\xi 11} &= A^\xi \left(T_{ik}^{33} S_{jl}^{00} + T_{ik}^{22} S_{jl}^{11} \right), K_{ijkl}^{\xi 12} = A^\xi \left(T_{ik}^{13} S_{jl}^{20} + T_{ik}^{02} S_{jl}^{31} \right) \\
K_{ijkl}^{\xi 13} &= B^\xi \left(T_{ik}^{33} S_{jl}^{00} + T_{ik}^{13} S_{jl}^{20} + T_{ik}^{02} S_{jl}^{31} + T_{ik}^{22} S_{jl}^{11} \right) \\
K_{ijkl}^{\xi 14} &= B_s^\xi \left(T_{ik}^{33} S_{jl}^{00} + T_{ik}^{22} S_{jl}^{11} \right), K_{ijkl}^{\xi 15} = B_s^\xi \left(T_{ik}^{13} S_{jl}^{20} + T_{ik}^{02} S_{jl}^{31} \right) \\
K_{ijkl}^{\xi 22} &= A^\xi \left(T_{ik}^{11} S_{jl}^{22} + T_{ik}^{00} S_{jl}^{33} \right), K_{ijkl}^{\xi 23} = B^\xi \left(T_{ik}^{31} S_{jl}^{02} + T_{ik}^{11} S_{jl}^{22} + T_{ik}^{20} S_{jl}^{13} + T_{ik}^{00} S_{jl}^{33} \right) \\
K_{ijkl}^{\xi 24} &= B_s^\xi \left(T_{ik}^{31} S_{jl}^{02} + T_{ik}^{20} S_{jl}^{13} \right), K_{ijkl}^{\xi 25} = B_s^\xi \left(T_{ik}^{11} S_{jl}^{22} + T_{ik}^{00} S_{jl}^{33} \right)
\end{aligned}$$

$$\begin{aligned}
K_{ijkl}^{\xi 33} &= D_s^\xi \left(T_{ik}^{33} S_{jl}^{00} + T_{ik}^{00} S_{jl}^{33} + T_{ik}^{31} S_{jl}^{02} + T_{ik}^{02} S_{jl}^{31} \right) \\
&+ D_s^\xi \left(T_{ik}^{13} S_{jl}^{20} + T_{ik}^{20} S_{jl}^{13} + T_{ik}^{11} S_{jl}^{22} + T_{ik}^{22} S_{jl}^{11} \right) \\
&+ \overline{D}_s^\xi \left(T_{ik}^{22} S_{jl}^{00} + T_{ik}^{20} S_{jl}^{02} + T_{ik}^{02} S_{jl}^{20} + T_{ik}^{00} S_{jl}^{22} \right) \\
K_{ijkl}^{\xi 34} &= D_s^\xi \left(T_{ik}^{33} S_{jl}^{00} + T_{ik}^{31} S_{jl}^{02} + T_{ik}^{22} S_{jl}^{11} + T_{ik}^{20} S_{jl}^{13} \right) + \overline{D}_s^\xi \left(T_{ik}^{22} S_{jl}^{00} + T_{ik}^{20} S_{jl}^{02} \right) \\
K_{ijkl}^{\xi 35} &= D_s^\xi \left(T_{ik}^{13} S_{jl}^{20} + T_{ik}^{11} S_{jl}^{22} + T_{ik}^{02} S_{jl}^{31} + T_{ik}^{00} S_{jl}^{33} \right) + \overline{D}_s^\xi \left(T_{ik}^{02} S_{jl}^{20} + T_{ik}^{00} S_{jl}^{22} \right) \\
K_{ijkl}^{\xi 44} &= H_s^\xi T_{ik}^{33} S_{jl}^{00} + H_s^\xi T_{ik}^{22} S_{jl}^{11} + \overline{H}_s^\xi T_{ik}^{22} S_{jl}^{00} \\
K_{ijkl}^{\xi 45} &= H_s^\xi T_{ik}^{13} S_{jl}^{20} + H_s^\xi T_{ik}^{02} S_{jl}^{31} + \overline{H}_s^\xi T_{ik}^{02} S_{jl}^{20} \\
K_{ijkl}^{\xi 55} &= H_s^\xi T_{ik}^{00} S_{jl}^{33} + H_s^\xi T_{ik}^{11} S_{jl}^{22} + \overline{H}_s^\xi T_{ik}^{00} S_{jl}^{22}
\end{aligned} \tag{3.48}$$

The components of stiffness matrix \mathbf{K}^η are defined as follows:

$$\begin{aligned}
K_{ijkl}^{\eta 11} &= \frac{A^\eta}{25} \left(22T_{ik}^{33} S_{jl}^{00} - 11T_{ik}^{31} S_{jl}^{02} - 11T_{ik}^{13} S_{jl}^{20} + 18T_{ik}^{11} S_{jl}^{22} + 72T_{ik}^{22} S_{jl}^{11} \right) \\
K_{ijkl}^{\eta 12} &= \frac{2A^\eta}{25} \left(-11T_{ik}^{13} S_{jl}^{20} - 11T_{ik}^{02} S_{jl}^{31} + 18T_{ik}^{11} S_{jl}^{22} + 18T_{ik}^{22} S_{jl}^{11} \right) \\
K_{ijkl}^{\eta 13} &= B^\eta \left(22T_{ik}^{33} S_{jl}^{00} - 11T_{ik}^{31} S_{jl}^{02} - 33T_{ik}^{13} S_{jl}^{20} \right) / 25 \\
&- \overline{A}_s^\eta \left(11T_{ik}^{13} S_{jl}^{00} + 7T_{ik}^{11} S_{jl}^{02} + 14T_{ik}^{02} S_{jl}^{11} \right) / 25 \\
&+ B^\eta \left(54T_{ik}^{11} S_{jl}^{22} - 22T_{ik}^{02} S_{jl}^{31} + 108T_{ik}^{22} S_{jl}^{11} \right) / 25 \\
K_{ijkl}^{\eta 14} &= B_s^\eta \left(22T_{ik}^{33} S_{jl}^{00} - 11T_{ik}^{31} S_{jl}^{02} - 11T_{ik}^{13} S_{jl}^{20} + 18T_{ik}^{11} S_{jl}^{22} + 72T_{ik}^{22} S_{jl}^{11} \right) / 25 \\
&- \overline{A}_s^\eta \left(11T_{ik}^{13} S_{jl}^{00} + 7T_{ik}^{11} S_{jl}^{02} \right) / 25 \\
K_{ijkl}^{\eta 15} &= \left[2B_s^\eta \left(18T_{ik}^{11} S_{jl}^{22} - 11T_{ik}^{13} S_{jl}^{20} + 18T_{ik}^{22} S_{jl}^{11} - 11T_{ik}^{02} S_{jl}^{31} \right) - 14\overline{A}_s^\eta T_{ik}^{02} S_{jl}^{11} \right] / 25 \\
K_{ijkl}^{\eta 22} &= A^\eta \left(72T_{ik}^{11} S_{jl}^{22} + 22T_{ik}^{00} S_{jl}^{33} - 11T_{ik}^{02} S_{jl}^{31} - 11T_{ik}^{20} S_{jl}^{13} + 18T_{ik}^{22} S_{jl}^{11} \right) / 25
\end{aligned}$$

$$\begin{aligned}
K_{ijkl}^{\eta 23} &= B^\eta \left(22T_{ik}^{00} S_{jl}^{33} - 22T_{ik}^{31} S_{jl}^{02} + 108T_{ik}^{11} S_{jl}^{22} \right) / 25 \\
&+ B^\eta \left(-11T_{ik}^{02} S_{jl}^{31} - 33T_{ik}^{20} S_{jl}^{13} + 54T_{ik}^{22} S_{jl}^{11} \right) / 25 \\
&- \bar{A}_s^\eta \left(14T_{ik}^{11} S_{jl}^{02} + 7T_{ik}^{02} S_{jl}^{11} + 11T_{ik}^{00} S_{jl}^{13} \right) / 25
\end{aligned}$$

$$K_{ijkl}^{\eta 24} = \frac{2B_s^\eta}{25} \left(-11T_{ik}^{31} S_{jl}^{02} + 18T_{ik}^{11} S_{jl}^{22} + 18T_{ik}^{22} S_{jl}^{11} - 11T_{ik}^{20} S_{jl}^{13} \right) - \frac{14\bar{A}_s^\eta}{25} T_{ik}^{11} S_{jl}^{02}$$

$$\begin{aligned}
K_{ijkl}^{\eta 25} &= \frac{B_s^\eta}{25} \left(72T_{ik}^{11} S_{jl}^{22} + 22T_{ik}^{00} S_{jl}^{33} - 11T_{ik}^{02} S_{jl}^{31} - 11T_{ik}^{20} S_{jl}^{13} + 18T_{ik}^{22} S_{jl}^{11} \right) \\
&- \frac{\bar{A}_s^\eta}{25} \left(7T_{ik}^{02} S_{jl}^{11} + 11T_{ik}^{00} S_{jl}^{13} \right)
\end{aligned}$$

$$\begin{aligned}
K_{ijkl}^{\eta 33} &= \frac{D^\eta}{25} \left(22T_{ik}^{33} S_{jl}^{00} - 33T_{ik}^{31} S_{jl}^{02} - 33T_{ik}^{13} S_{jl}^{20} + 162T_{ik}^{11} S_{jl}^{22} \right) \\
&+ \frac{D^\eta}{25} \left(+162T_{ik}^{22} S_{jl}^{11} + 22T_{ik}^{00} S_{jl}^{33} - 33T_{ik}^{02} S_{jl}^{31} - 33T_{ik}^{20} S_{jl}^{13} \right) \\
&- \frac{\bar{Q}_s^\eta}{25} \left(11T_{ik}^{00} S_{jl}^{13} + 11T_{ik}^{13} S_{jl}^{00} + 11T_{ik}^{31} S_{jl}^{00} + 11T_{ik}^{00} S_{jl}^{31} \right) \\
&- \frac{\bar{Q}_s^\eta}{25} \left(21T_{ik}^{02} S_{jl}^{11} + 21T_{ik}^{11} S_{jl}^{02} + 21T_{ik}^{11} S_{jl}^{20} + 21T_{ik}^{20} S_{jl}^{11} \right) \\
&+ \frac{H_{ts}^\eta + 2\bar{F}_{ts}^\eta + \bar{D}^\eta}{25} \left(18T_{ik}^{22} S_{jl}^{00} - 7T_{ik}^{20} S_{jl}^{02} - 7T_{ik}^{02} S_{jl}^{20} + 18T_{ik}^{00} S_{jl}^{22} + 100T_{ik}^{11} S_{jl}^{11} \right) \\
&+ \frac{18\bar{H}_{ts}^\eta}{25} \left(T_{ik}^{11} S_{jl}^{00} + T_{ik}^{00} S_{jl}^{11} \right)
\end{aligned}$$

$$\begin{aligned}
K_{ijkl}^{\eta 34} &= \frac{D_s^\eta}{25} \left(22T_{ik}^{33} S_{jl}^{00} - 33T_{ik}^{31} S_{jl}^{02} - 11T_{ik}^{13} S_{jl}^{20} \right) \\
&+ \frac{D_s^\eta}{25} \left(54T_{ik}^{11} S_{jl}^{22} - 22T_{ik}^{20} S_{jl}^{13} + 108T_{ik}^{22} S_{jl}^{11} \right) - \frac{\bar{Q}_s^\eta}{25} \left(11T_{ik}^{13} S_{jl}^{00} + 21T_{ik}^{11} S_{jl}^{02} \right) \\
&+ \frac{H_{ts}^\eta + \bar{J}_{hs}^\eta + \bar{F}_{ts}^\eta + \bar{D}_s^\eta}{25} \left(18T_{ik}^{22} S_{jl}^{00} - 7T_{ik}^{20} S_{jl}^{02} + 50T_{ik}^{11} S_{jl}^{11} \right) \\
&- \frac{\bar{F}_{hs}^\eta}{25} \left(14T_{ik}^{20} S_{jl}^{11} + 11T_{ik}^{31} S_{jl}^{00} + 7T_{ik}^{11} S_{jl}^{20} \right) + \frac{18\bar{H}_{ts}^\eta}{25} T_{ik}^{11} S_{jl}^{00}
\end{aligned}$$

$$\begin{aligned}
K_{ijkl}^{\eta 35} &= \frac{D_s^\eta}{25} (108T_{ik}^{11}S_{jl}^{22} + 54T_{ik}^{22}S_{jl}^{11} + 22T_{ik}^{00}S_{jl}^{33}) - \frac{\bar{Q}_s^\eta}{25} (21T_{ik}^{02}S_{jl}^{11} + 11T_{ik}^{00}S_{jl}^{13}) \\
&+ \frac{D_s^\eta}{25} (-33T_{ik}^{02}S_{jl}^{31} - 11T_{ik}^{20}S_{jl}^{13} - 22T_{ik}^{13}S_{jl}^{20}) + \frac{18\bar{H}_{ts}^\eta}{25} T_{ik}^{00}S_{jl}^{11} \\
&+ \frac{H_{ts}^\eta + \bar{J}_{hs}^\eta + \bar{F}_{ts}^\eta + \bar{D}_s^\eta}{25} (18T_{ik}^{00}S_{jl}^{22} - 7T_{ik}^{02}S_{jl}^{20} + 50T_{ik}^{11}S_{jl}^{11}) \\
&- \frac{\bar{F}_{hs}^\eta}{25} (14T_{ik}^{11}S_{jl}^{20} + 11T_{ik}^{00}S_{jl}^{31} + 7T_{ik}^{20}S_{jl}^{11}) \\
\\
K_{ijkl}^{\eta 44} &= \frac{H_s^\eta}{25} (22T_{ik}^{33}S_{jl}^{00} - 11T_{ik}^{31}S_{jl}^{02} - 11T_{ik}^{13}S_{jl}^{20} + 18T_{ik}^{11}S_{jl}^{22} + 72T_{ik}^{22}S_{jl}^{11}) \\
&+ \frac{H_{ts}^\eta + 2\bar{J}_{hs}^\eta + \bar{H}_s^\eta}{25} (18T_{ik}^{22}S_{jl}^{00} + 25T_{ik}^{11}S_{jl}^{11}) + \frac{18\bar{H}_{ts}^\eta}{25} T_{ik}^{11}S_{jl}^{00} \\
&- \frac{\bar{F}_{hs}^\eta}{25} (11T_{ik}^{31}S_{jl}^{00} + 7T_{ik}^{11}S_{jl}^{20} + 11T_{ik}^{13}S_{jl}^{00} + 7T_{ik}^{11}S_{jl}^{02}) \\
\\
K_{ijkl}^{\eta 45} &= \frac{H_s^\eta}{25} (36T_{ik}^{11}S_{jl}^{22} + 36T_{ik}^{22}S_{jl}^{11} - 22T_{ik}^{13}S_{jl}^{20} - 22T_{ik}^{02}S_{jl}^{31}) \\
&- \frac{14\bar{F}_{hs}^\eta}{25} (T_{ik}^{02}S_{jl}^{11} + T_{ik}^{11}S_{jl}^{20}) + \frac{H_{ts}^\eta + 2\bar{J}_{hs}^\eta + \bar{H}_s^\eta}{25} (25T_{ik}^{11}S_{jl}^{11} - 7T_{ik}^{02}S_{jl}^{20}) \\
\\
K_{ijkl}^{\eta 55} &= \frac{H_s^\eta}{25} (72T_{ik}^{11}S_{jl}^{22} + 22T_{ik}^{00}S_{jl}^{33} - 11T_{ik}^{02}S_{jl}^{31} - 11T_{ik}^{20}S_{jl}^{13} + 18T_{ik}^{22}S_{jl}^{11}) \\
&+ \frac{H_{ts}^\eta + 2\bar{J}_{hs}^\eta + \bar{H}_s^\eta}{25} (18T_{ik}^{00}S_{jl}^{22} + 25T_{ik}^{11}S_{jl}^{11}) + \frac{18\bar{H}_{ts}^\eta}{25} T_{ik}^{00}S_{jl}^{11} \\
&- \frac{\bar{F}_{hs}^\eta}{25} (11T_{ik}^{00}S_{jl}^{13} + 7T_{ik}^{02}S_{jl}^{11} + 11T_{ik}^{00}S_{jl}^{31} + 7T_{ik}^{20}S_{jl}^{11})
\end{aligned} \tag{3.49}$$

The components of mass matrix \mathbf{M} are given by:

$$\begin{aligned}
M_{ijkl}^{11} &= I_0 T_{ik}^{11} S_{jl}^{00}, M_{ijkl}^{13} = I_1 T_{ik}^{11} S_{jl}^{00}, M_{ijkl}^{14} = J_1 T_{ik}^{11} S_{jl}^{00} \\
M_{ijkl}^{22} &= I_0 T_{ik}^{00} S_{jl}^{11}, M_{ijkl}^{23} = I_1 T_{ik}^{00} S_{jl}^{11}, M_{ijkl}^{25} = J_1 T_{ik}^{00} S_{jl}^{11} \\
M_{ijkl}^{33} &= I_0 T_{ik}^{00} S_{jl}^{00} + I_2 (T_{ik}^{11} S_{jl}^{00} + T_{ik}^{00} S_{jl}^{11}), M_{ijkl}^{34} = J_2 T_{ik}^{11} S_{jl}^{00}, M_{ijkl}^{35} = J_2 T_{ik}^{00} S_{jl}^{11} \\
M_{ijkl}^{44} &= K_2 T_{ik}^{11} S_{jl}^{00}, M_{ijkl}^{55} = K_2 T_{ik}^{00} S_{jl}^{11}
\end{aligned} \tag{3.50}$$

$$\text{with } T_{ik}^{rs} = \int_0^a \frac{\partial^r R_i}{\partial x_1^r} \frac{\partial^s R_k}{\partial x_1^s} dx_1, S_{jl}^{rs} = \int_0^b \frac{\partial^r P_j}{\partial x_2^r} \frac{\partial^s P_l}{\partial x_2^s} dx_2, f_{ij} = \int_0^a \int_0^b q R_i P_j dx_1 dx_2$$

Furthermore, based on Eq. (3.44), the critical buckling loads N^{cr} of the microplate can be obtained by disregarding the mass inertia components, and solving the characteristic equation $(\mathbf{K} - N^0 \mathbf{K}^g) \mathbf{d} = \mathbf{0}$. For free vibration analysis, it is supposed that $N^0 = 0$ and $\mathbf{d}(t) = \mathbf{d} e^{i\omega t}$, where $i^2 = -1$ represents the imaginary unit, and ω denotes the natural frequency of the microplate. By solving the equation $(\mathbf{K} - \omega^2 \mathbf{M}) \mathbf{d} = \mathbf{0}$, the natural frequencies will be determined. It is worth to notice that for static analysis, the static responses of the microplates can be obtained from the equation $\mathbf{Kd} = \mathbf{F}$.

3.3 Numerical results

3.3.1 Convergence study of solution

The PMF microplates are designed to be made of metal foam materials whose characteristics are followed: $E_{\max} = 200 \text{ GPa}$, $\rho_{\max} = 7850 \text{ kg/m}^3$, $\nu_{\max} = 0.33$ [174]. For simplicity purpose, the numerical examples utilize the following normalized response parameters $\bar{\omega} = 100\omega h \sqrt{\rho_{\max} / E_{\max}}$. To evaluate the convergence and efficiency of the current computational method, this example will compare the convergence speed and stability of the proposed Hermite-Ritz and Laguerre-Ritz, Exponential-Ritz, OP-Ritz solutions with those of the Ritz solution obtained from other shape functions. The following approximation functions will be used in Eq. (3.36) for the computations:

Static Beam Functions (SBF) [129]:

$$F_j(x_2) = A_j + B_j x_2 + C_j x_2^2 + D_j x_2^3 + \sin\left(\frac{jx_2}{b}\right) \quad (3.47)$$

$$\text{with } A_j = 0; B_j = -\frac{j\pi}{b}; C_j = \frac{j\pi((-1)^j + 2)}{b^2}; D_j = -\frac{j\pi((-1)^j + 1)}{b^3}.$$

Non-Orthogonal Polynomials (NOP) [140]:

$$F_j(x_2) = (b - x_2)^2 x_2^{j+1} \quad (3.48)$$

Product of Trigonometric Functions (PTF) [41]:

$$F_j(x_2) = \sin\left(\frac{\pi x_2}{b}\right) \sin\left(\frac{j\pi x_2}{b}\right) \quad (3.49)$$

Characteristic Functions (CF) [131]:

$$F_j(x_2) = \sin \alpha_j x_2 - \sinh \alpha_j x_2 - \phi_j (\cos \alpha_j x_2 - \cosh \alpha_j x_2) \quad (3.50)$$

with $\phi_j = \frac{\sin \alpha_j b - \sinh \alpha_j b}{\cos \alpha_j b - \cosh \alpha_j b}$; $\alpha_j = \frac{(j+0.5)\pi}{b}$. It is noted that the functions $T_j(x_1)$

are defined in a similar way by replacing the variable x_2 for x_1 , the length b for the width a in the previous equations. For the purpose of investigating the convergence of approximation functions, the reference distance is defined as follows:

$$d_f = \omega_{i+1} - \omega_i \quad (3.51)$$

where ω_i and ω_{i+1} are results of fundamental frequency of porous metal foam at n_i and n_{i+1} , respectively. In order to evaluate the convergence of the proposed Ritz solutions, Table 3.2 and Figs. 3.3-3.4 compare the convergence speed of fundamental frequencies of the PMF CCCC plates with side-to-thickness ratio $a/h = 10$ and porous parameter $\beta = 0.3$. It is worthy to noticing that the results are computed with six types of shape functions (Hermite-Ritz and Laguerre-Ritz, Exponential-Ritz, OP-Ritz, SBF, NOP, CF and PTF), the number of series in x_2 - and x_1 - direction are supposed to be similar, i.e. $n_1 = n_2 = n$. The tabular data and graph illustrate that the overall trend of solutions is to decrease with an increase in the number of series until reaching a converged value, after which the graphs stabilize. In comparing the stabilization of solutions based on the number of series,

it's noted that the responses derived from the SBF function require the largest number of series $n=15$, while the proposed Hermite and Laguerre orthogonal polynomials record the lowest number of series $n=3$. The responses from OP_GS and Exponential polynomials have converged at $n=5$ and $n=6$, respectively. The responses from NOP and PTF and CF functions are obviously converged at $n=8$ and $n=9$, respectively. The current Hermite-Ritz and Laguerre-Ritz, Exponential-Ritz, OP-Ritz solutions exhibit efficiency in terms of convergence when compared to solutions using earlier shape functions ([41, 129, 140, 184]).

Table 3.2: Comparison with convergence speed of the series solution ($n = n_1 = n_2$) of porous metal foam PMF microplates with full clamped boundary condition for ($a/h=10$, $\beta=0.3$, $h/l=\infty$)

Solution	Number of series $n = n_1 = n_2$									
	2	3	5	6	8	9	10	15	16	17
SBF	11.765	11.27	10.681	10.125	9.905	9.858	9.772	9.4444	9.444	9.444
NOP	9.455	9.44	9.382	9.373	9.362	9.363	9.362	9.364	9.362	9.362
PTF	9.784	9.486	9.401	9.400	9.362	9.364	9.362	9.364	9.363	9.362
CF	9.560	9.545	9.503	9.467	9.402	9.388	9.388	9.388	9.388	9.388
Hermite	9.649	9.382	9.382	9.382	9.381	9.383	9.384	9.381	9.382	9.382
Laguerre	9.5341	9.364	9.364	9.364	9.364	9.364	9.364	9.364	9.364	9.364
OP_GS	9.5571	9.381	9.373	9.373	9.373	9.373	9.373	9.373	9.373	9.373
Exponential	9.5730	9.406	9.357	9.355	9.355	9.355	9.355	9.355	9.355	9.355
IGA [174]	9.5202									

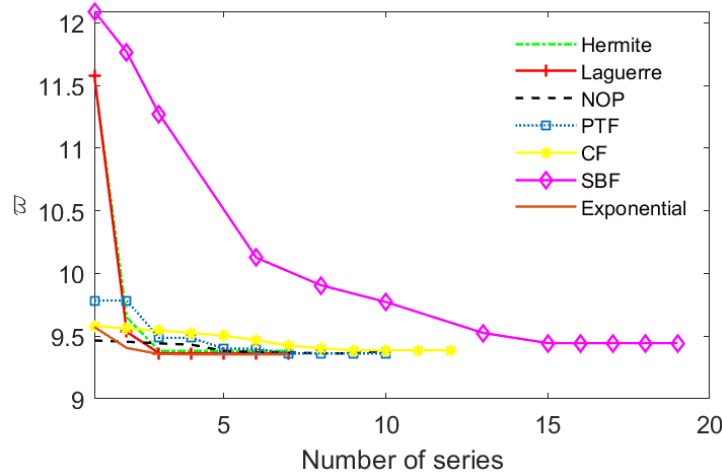


Figure 3.3: Comparison with both convergence speed of number of series of porous metal foam PMF microplates with full clamped boundary condition for normalized fundamental frequency ($a/h=10$, $\beta=0.3$, $h/l=\infty$)

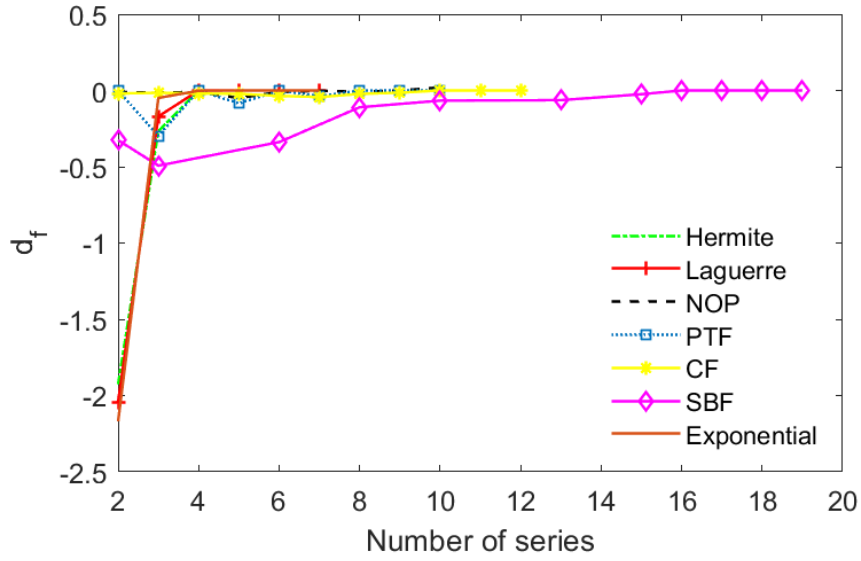


Figure 3.4: Distance of normalized fundamental frequency of porous metal foam PMF microplates with full clamped boundary condition ($a/h = 10$, $\beta = 0.3$, $h/l = \infty$)

3.3.2 Analysis of PMF microplates

3.3.2.1 Size dependent analysis of PMF microplates using modified couple stress

3.3.2.1.1 Free vibration analysis

In this example, free vibration $\bar{\omega} = 100\omega h \sqrt{\rho_{\max} / E_{\max}}$ behaviors of the square PMF microplates with various BCs such as SSSS, CCCC and SCSC are analysed. The PMF microplates are designed to be made of metal foam materials whose characteristics are followed: $E_{\max} = 200$ GPa, $\rho_{\max} = 7850 \text{ kg/m}^3$, $\nu_{\max} = 0.33$. In order to examine the convergence of buckling and free vibration responses of PMF microplates with different BCs, Table 3.3 presents the results of square microplates with $a/h = 10$, $\beta = 0.1$ and $h/l = 1$ using the Hermite and Laguerre polynomials. The results obtained demonstrate a rapid convergence of the proposed solution for all cases, with a convergence point observed at a number of series of $n=3$ serves as a convergence point.

Table 3.3: Convergence study of the series solution of porous metal foam PMF microplates with different boundary conditions ($a/h=10$, $\beta=0.1$, $h/l=1$) under uniform distribution and Hermite polynomial

BCs	Solution	Number of series $n = n_1 = n_2$						
		1	2	3	4	5	6	7
Normalized fundamental frequency								
SSSS	Hermite	15.6713	13.6135	13.6004	13.6005	13.6016	13.6008	13.6005
	Laguerre	15.6197	13.5862	13.5604	13.5603	13.5604	13.5605	13.5604
SCSC	Hermite	22.2541	20.2237	20.2040	20.2040	20.2042	20.2043	20.2041
	Laguerre	22.1756	20.0831	20.0677	20.0679	20.0677	20.0678	20.0677
CCCC	Hermite	29.6893	28.9057	28.6386	28.6385	28.6388	28.6387	28.6386
	Laguerre	29.6589	28.8648	28.6135	28.6137	28.6136	28.6135	28.6135
Normalized critical buckling load for biaxial compression								
SSSS	Hermite	12.5538	10.7729	9.1169	9.1170	9.1169	9.1171	9.1170
	Laguerre	12.5497	10.7654	9.1132	9.1133	9.1131	9.1132	9.1132
SCSC	Hermite	19.9021	18.2037	17.3403	17.3426	17.3412	17.3408	17.3404
	Laguerre	19.7828	18.1026	17.2474	17.2426	27.2424	27.2425	17.2424
CCCC	Hermite	32.9265	31.8104	31.7498	31.7498	31.7499	31.7499	31.7498
	Laguerre	32.9873	31.8926	31.8486	31.8487	31.8488	31.8486	31.8486

Their normalized fundamental frequencies are reported in Tables 3.4-3.6 with $\beta = 0.1, 0.2, 0.3$, and 0.4 , $h/l = \infty, 10, 5, 2, 1$, $a/h = 10$, and three porosity distributions (UD, AD, SD).

Table 3.4: Normalized fundamental frequencies of PMF rectangular microplates for simply supported boundary condition with $a / h = 10$

Type distribution	β	Theory	h / l				
			∞	10	5	2	1
Uniform	0.1	Ritz-Hermite	5.7950	5.9242	6.2959	8.4518	13.6004
		Ritz-Laguerre	5.7850	5.9136	6.2836	8.4305	13.5604
		IGA [174]	5.7276	-	-	-	-
	0.2	Ritz-Hermite	5.6551	5.7849	6.1579	8.3123	13.4323
		Ritz-Laguerre	5.6453	5.7745	6.1458	8.2914	13.3928
		IGA [174]	5.6244	-	-	-	-
	0.3	Ritz-Hermite	5.5103	5.6404	6.0140	8.1634	13.2463
		Ritz-Laguerre	5.5007	5.6302	6.0021	8.1428	13.2073
		IGA [174]	5.5125	-	-	-	-
	0.4	Ritz-Hermite	5.3583	5.4886	5.8620	8.0019	13.0374
		Ritz-Laguerre	5.3490	5.4786	5.8504	7.9815	12.9990
Symmetric	0.1	Ritz-Hermite	5.8931	6.0203	6.3864	8.5195	13.6430
		Ritz-Laguerre	5.8830	6.0095	6.3740	8.4983	13.6031
		IGA [174]	5.8052	-	-	-	-
	0.2	Ritz-Hermite	5.8614	5.9868	6.3482	8.4562	13.5258
		Ritz-Laguerre	5.8513	5.9761	6.3359	8.4351	13.4864
		IGA [174]	5.7905	-	-	-	-
	0.3	Ritz-Hermite	5.8373	5.9607	6.3164	8.3945	13.4030
		Ritz-Laguerre	5.8273	5.9501	6.3042	8.3737	13.3641
		IGA [174]	5.7806	-	-	-	-
	0.4	Ritz-Hermite	5.8227	5.9437	6.2927	8.3360	13.2752
		Ritz-Laguerre	5.8127	5.9332	6.2806	8.3154	13.2369
Asymmetric	0.1	Ritz-Hermite	5.8142	5.9431	6.3138	8.4655	13.6100
		Ritz-Laguerre	5.8042	5.9324	6.3014	8.4443	13.5701
		IGA [174]	5.7422	-	-	-	-
	0.2	Ritz-Hermite	5.6935	5.8226	6.1937	8.3414	13.4558
		Ritz-Laguerre	5.6836	5.8121	6.1816	8.3204	13.4163
		IGA [174]	5.6527	-	-	-	-
	0.3	Ritz-Hermite	5.5665	5.6958	6.0673	8.2097	13.2901
		Ritz-Laguerre	5.5568	5.6856	6.0554	8.1890	13.2511
		IGA [174]	5.5529	-	-	-	-
	0.4	Ritz-Hermite	5.4297	5.5594	5.9313	8.0680	13.1114
		Ritz-Laguerre	5.4203	5.5493	5.9195	8.0475	13.0729

Table 3.5: Normalized fundamental frequencies of PMF rectangular microplates for full clamped boundary condition with $a / h = 10$

Type distribution	β	Theory	h / l				
			∞	10	5	2	1
Uniform	0.1	Ritz-Hermite	9.8398	10.2084	11.2347	16.6898	28.6386
		Ritz-Laguerre	9.8202	10.1891	11.2161	16.6711	28.6135
		IGA [174]	9.8918	-	-	-	-
	0.2	Ritz-Hermite	9.7059	9.9853	11.0126	16.4507	28.2951
		Ritz-Laguerre	9.6968	9.9666	10.9945	16.4325	28.2804
		IGA [174]	9.7136	-	-	-	-
	0.3	Ritz-Hermite	9.3824	9.7521	10.7786	16.1909	27.4022
		Ritz-Laguerre	9.3639	9.7339	10.7610	16.1731	27.4001
		IGA [174]	9.5202	-	-	-	-
	0.4	Ritz-Hermite	9.2358	9.5050	10.5287	15.9042	26.9741
		Ritz-Laguerre	9.2178	9.4874	10.5117	15.8868	26.9688
Symmetric	0.1	Ritz-Hermite	9.9853	10.3490	11.3634	16.7781	28.6911
		Ritz-Laguerre	9.9653	10.3293	11.3444	16.7591	28.6658
		IGA [174]	10.0044	-	-	-	-
	0.2	Ritz-Hermite	9.9215	10.2809	11.2836	16.6400	28.4350
		Ritz-Laguerre	9.9015	10.2612	11.2647	16.6211	28.4099
		IGA [174]	9.9537	-	-	-	-
	0.3	Ritz-Hermite	9.8661	10.2205	11.2095	16.4985	28.1614
		Ritz-Laguerre	9.8462	10.2009	11.1906	16.4797	28.1365
		IGA [174]	9.9063	-	-	-	-
	0.4	Ritz-Hermite	9.8213	10.1698	11.1428	16.3549	27.8712
		Ritz-Laguerre	9.8013	10.1501	11.1238	16.3361	27.8465
Asymmetric	0.1	Ritz-Hermite	9.8687	10.2363	11.2605	16.7085	28.6519
		Ritz-Laguerre	9.8524	10.2195	11.2422	16.6814	28.6226
		IGA [174]	9.9133	-	-	-	-
	0.2	Ritz-Hermite	9.7140	10.0418	11.0654	16.4925	28.3518
		Ritz-Laguerre	9.7080	10.0253	11.0474	16.4660	28.3035
		IGA [174]	9.7558	-	-	-	-
	0.3	Ritz-Hermite	9.4686	9.8365	10.8590	16.2617	27.9877
		Ritz-Laguerre	9.4531	9.8205	10.8415	16.2358	27.9804
		IGA [174]	9.5816	-	-	-	-
	0.4	Ritz-Hermite	9.2470	9.6151	10.6365	16.0129	27.6375
		Ritz-Laguerre	9.2319	9.5994	10.6195	15.9877	27.6314

Table 3.6: Normalized fundamental frequencies of rectangular porous metal foam microplates with $a/h = 10$ and SCSC boundary condition

Type distribution	β	Theory	h/l				
			∞	10	5	2	1
Uniform	0.1	Ritz-Hermite	7.6602	7.8896	8.5375	12.1058	20.2040
		Ritz-Laguerre	7.6430	7.8683	8.5058	12.0348	20.0677
	0.2	Ritz-Hermite	7.4797	7.7099	8.3591	11.9203	19.9663
		Ritz-Laguerre	7.4625	7.6886	8.3275	11.8498	19.8314
	0.3	Ritz-Hermite	7.2922	7.5229	8.1724	11.7204	19.7014
		Ritz-Laguerre	7.2751	7.5016	8.1409	11.6506	19.5679
	0.4	Ritz-Hermite	7.0950	7.3256	7.9741	11.5015	19.4016
		Ritz-Laguerre	7.0779	7.3045	7.9429	11.4326	19.2700
Symmetric	0.1	Ritz-Hermite	7.7830	8.0090	8.6483	12.1852	20.2524
		Ritz-Laguerre	7.7662	7.9881	8.6170	12.1143	20.1162
	0.2	Ritz-Hermite	7.7377	7.9609	8.5924	12.0894	20.0745
		Ritz-Laguerre	7.7213	7.9404	8.5615	12.0193	19.9396
	0.3	Ritz-Hermite	7.7011	7.9209	8.5430	11.9935	19.8859
		Ritz-Laguerre	7.6852	7.9010	8.5128	11.9242	19.7525
	0.4	Ritz-Hermite	7.6752	7.8911	8.5022	11.8989	19.6876
		Ritz-Laguerre	7.6601	7.8718	8.4727	11.8306	19.5557
Asymmetric	0.1	Ritz-Hermite	7.6843	7.9132	8.5594	12.1223	20.2155
		Ritz-Laguerre	7.6767	7.9007	8.5350	12.0520	20.0710
	0.2	Ritz-Hermite	7.5280	7.7572	8.4037	11.9558	19.9961
		Ritz-Laguerre	7.5201	7.7445	8.3791	11.8861	19.8530
	0.3	Ritz-Hermite	7.3635	7.5929	8.2393	11.7786	19.7597
		Ritz-Laguerre	7.3554	7.5800	8.2147	11.7094	19.6182
	0.4	Ritz-Hermite	7.1861	7.4158	8.0622	11.5877	19.5045
		Ritz-Laguerre	7.1778	7.4028	8.0376	11.5192	19.3646

Since no data of free vibration responses of PMF microplates using the MCT and HSDT is available, the obtained results are compared with those from the earlier

work of Pham et al. [174] for PMF macroplates without the size effects, i.e. $h/l = \infty$. It can be seen from Tables 3.4 and 3.5 that there are good agreements between the two models for all cases. It is also observed from these tables that the results vary with the porosity distribution in which the largest and smallest frequencies correspond to SD and UD. Some new results for microplates are given in Tables 3.4-3.6 can be used for the benchmark in future research.

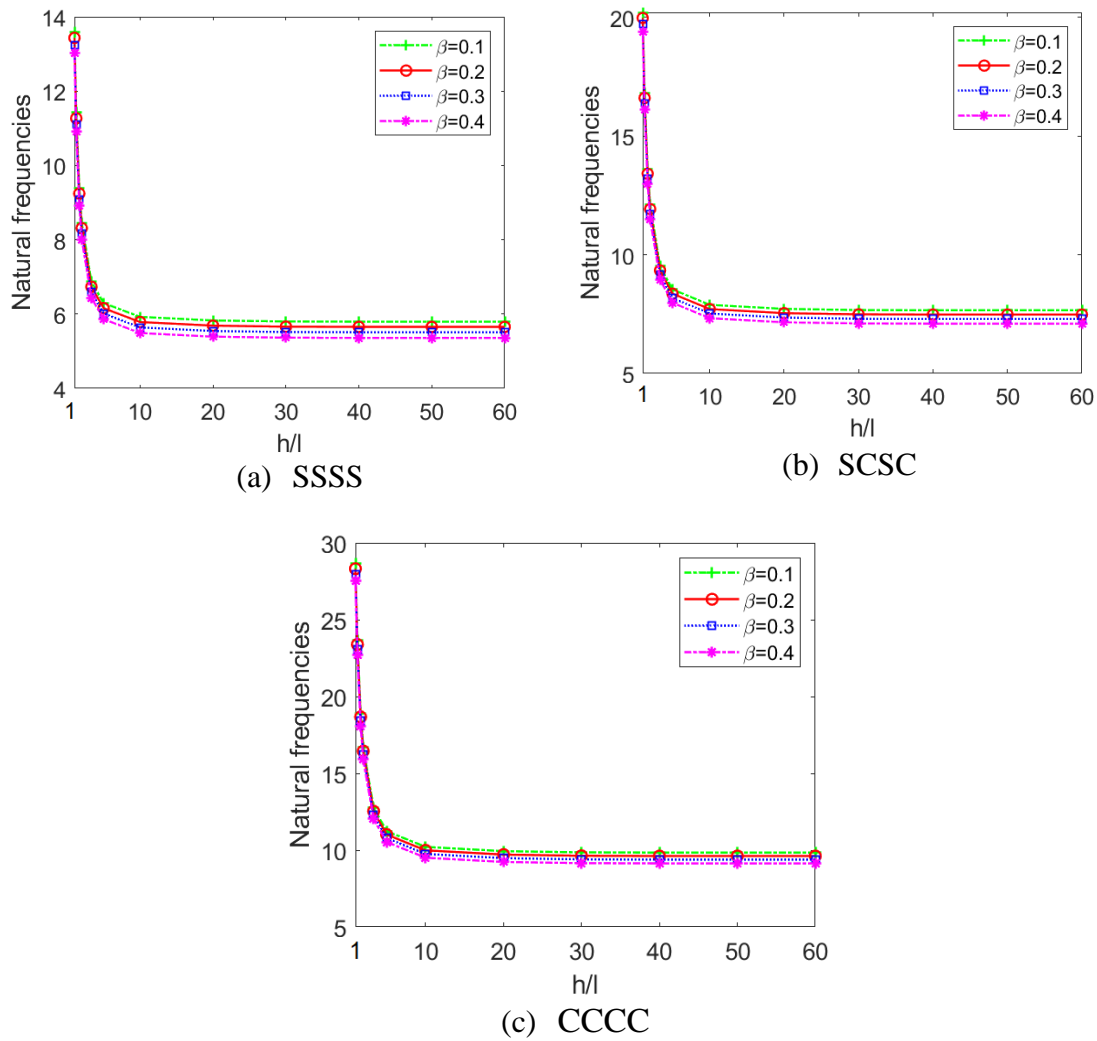


Figure 3.5: Variation of normalized fundamental frequencies with respect the length scale-to-thickness ratio h/l and $a/h = 10$ under uniform distribution
Figs. 3.5 and 3.6 illustrate the effect of the porosity coefficients, porosity distribution, size effects and boundary conditions on the normalized fundamental

frequencies of square PMF microplates. Accordingly, their fundamental frequencies decrease as the porosity coefficient and thickness-to-MLSP ratio increase for both various boundary conditions and porosity contributions. The curves are observed to become flat when the ratio of h/l reaches to 20 from which the size effects appear insignificantly. It is also seen that the size effect is most prominent at the ratio of $h/l = 1$ and decreases sharply from $h/l = 1$ to $h/l = 10$.

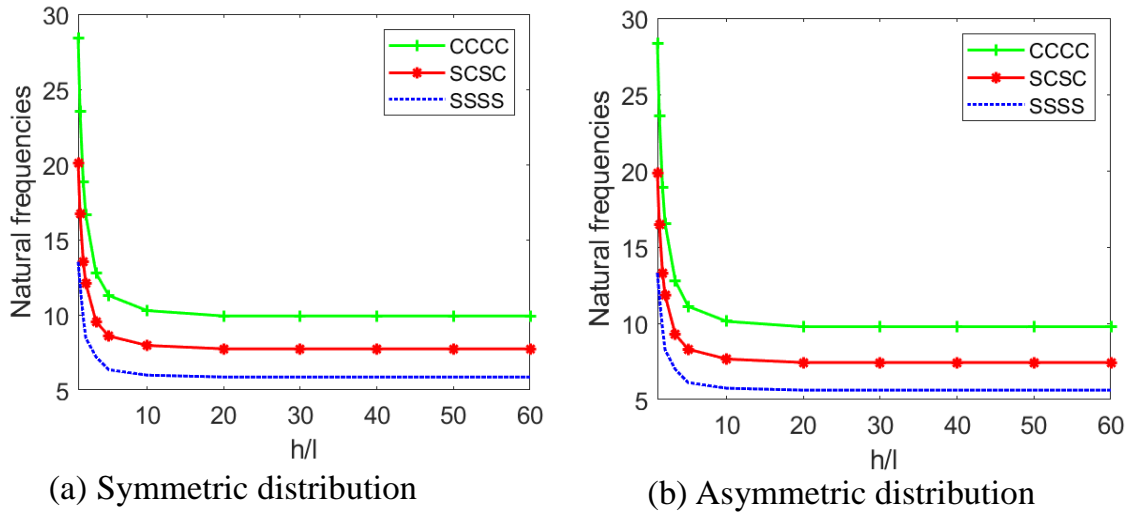


Figure 3.6: Variation of normalized fundamental frequencies with respect to the length scale-to-thickness ratio h/l and $a/h = 10$, $\beta = 0.2$

3.3.2.1.2 Critical buckling analysis

In this example, buckling $\bar{N}_{cr} = N_{cr} a^2 / (h^3 E_{\max})$ behaviors of the square PMF microplates with various configurations are considered. Their normalized critical buckling loads with various configurations are given in Tables 3.7-3.10. It is noted that the obtained results in Tables 3.7 and 3.8 for PMF SSSS microplates under biaxial compression $(N_1^{(0)}, N_2^{(0)}, N_{12}^{(0)} = 1, 1, 0)$ and uniaxial compression $(N_1^{(0)}, N_2^{(0)}, N_{12}^{(0)} = 1, 0, 0)$ are benchmarked with those derived from Hung et al. ([20]) without the size effects ($h/l = \infty$). It is observed that two models are in good agreements for different cases. New results with different thickness-to-MLSP's ratios and boundary conditions are provided in Tables 3.7- 3.10 for future benchmarks.

Table 3.7: The normalized critical buckling load of the SSSS metal foam square microplate under uniaxial compression $a/h = 10$

Type distribution	β	Theory	h/l				
			∞	10	5	2	1
Uniform	0.1	Ritz-Hermite	3.2565	3.4002	3.8312	6.8477	17.6179
		Ritz-Laguerre	3.2576	3.4013	3.8324	6.8499	17.6228
		IGA [20]	3.2625	-	-	-	-
	0.2	Ritz-Hermite	2.9905	3.1263	3.5339	6.3864	16.5708
		Ritz-Laguerre	2.9915	3.1274	3.5351	6.3884	16.5753
		IGA [20]	3.0337	-	-	-	-
	0.3	Ritz-Hermite	2.7274	2.8549	3.2376	5.9161	15.4791
		Ritz-Laguerre	2.7282	2.8559	3.2387	5.9179	15.4833
		IGA [20]	2.7992	-	-	-	-
	0.4	Ritz-Hermite	2.6027	2.7348	3.1309	5.6331	14.9277
		Ritz-Laguerre	2.6079	2.7400	3.1363	5.6478	14.9290
		IGA [20]	2.5578	-	-	-	-
	0.5	Ritz-Hermite	2.3250	2.4465	2.8109	5.3608	14.4634
		Ritz-Laguerre	2.3297	2.4512	2.8157	5.3651	14.4632
		IGA [20]	2.3076	-	-	-	-
	0.6	Ritz-Hermite	2.0427	2.1526	2.4824	4.7904	13.0289
		Ritz-Laguerre	2.0468	2.1568	2.4867	4.7941	13.0286
		IGA [20]	2.0459	-	-	-	-
	0.7	Ritz-Hermite	1.7507	1.8478	2.1393	4.1788	11.4591
		Ritz-Laguerre	1.7542	1.8515	2.1430	4.1820	11.4588
		IGA [20]	1.7679	-	-	-	-
Symmetric	0.1	Ritz-Hermite	3.3825	3.5275	3.9626	7.0081	17.8820
		Ritz-Laguerre	3.3891	3.5345	3.9706	7.0230	17.9206
		IGA [20]	3.3520	-	-	-	-
	0.2	Ritz-Hermite	3.2272	3.3645	3.7764	6.6593	16.9527
		Ritz-Laguerre	3.2335	3.3712	3.7841	6.6736	16.9900
		IGA [20]	3.2164	-	-	-	-
	0.3	Ritz-Hermite	3.0753	3.2046	3.5923	6.3057	15.9944
		Ritz-Laguerre	3.0814	3.2109	3.5996	6.3194	16.0303
		IGA [20]	3.0796	-	-	-	-
	0.4	Ritz-Hermite	2.9259	3.0467	3.4092	5.9459	15.0038
		Ritz-Laguerre	2.9315	3.0526	3.4160	5.9588	15.0384
		IGA [20]	2.9410	-	-	-	-
	0.5	Ritz-Hermite	2.7781	2.8901	3.2262	5.5785	13.9779
		Ritz-Laguerre	2.7833	2.8957	3.2326	5.5908	14.0113
		IGA [20]	2.8000	-	-	-	-
	0.6	Ritz-Hermite	2.6304	2.7332	3.0418	5.2012	12.9126
		Ritz-Laguerre	2.6354	2.7385	3.0479	5.2132	12.9452
		IGA [20]	2.6555	-	-	-	-
	0.7	Ritz-Hermite	2.4808	2.5741	2.8538	4.8117	11.8035
		Ritz-Laguerre	2.4854	2.5789	2.8595	4.8232	11.8355
		IGA [20]	2.5054	-	-	-	-

Table 3.8: The normalized critical buckling load of the SSSS metal foam square microplate under biaxial compression $a/h = 10$

Type distribution	β	Theory	h/l				
			∞	10	5	2	1
Uniform	0.1	Ritz-Hermite	1.6598	1.7344	1.9582	3.5245	9.1169
		Ritz-Laguerre	1.6617	1.7362	1.9599	3.5252	9.1132
		IGA [20]	1.6313	-	-	-	-
	0.2	Ritz-Hermite	1.5242	1.5948	1.8064	3.2876	8.5757
		Ritz-Laguerre	1.5260	1.5965	1.8080	3.2881	8.5722
		IGA [20]	1.5169	-	-	-	-
	0.3	Ritz-Hermite	1.3901	1.4564	1.6551	3.0459	8.0114
		Ritz-Laguerre	1.3917	1.4580	1.6566	3.0464	8.0081
		IGA [20]	1.3996	-	-	-	-
	0.4	Ritz-Hermite	1.2566	1.3182	1.5032	2.7976	7.4187
		Ritz-Laguerre	1.2581	1.3197	1.5045	2.7980	7.4157
		IGA [20]	1.2789	-	-	-	-
	0.5	Ritz-Hermite	1.1284	1.1791	1.3492	2.5398	6.7905
		Ritz-Laguerre	1.1298	1.1804	1.3505	2.5403	6.7876
		IGA [20]	1.1538	-	-	-	-
Symmetric	0.1	Ritz-Hermite	1.6919	1.7645	1.9821	3.5052	8.9437
		Ritz-Laguerre	1.6958	1.7685	1.9866	3.5134	8.9647
		IGA [20]	1.6760	-	-	-	-
	0.2	Ritz-Hermite	1.6143	1.6830	1.8890	3.3308	8.4789
		Ritz-Laguerre	1.6179	1.6868	1.8933	3.3386	8.4991
		IGA [20]	1.6082	-	-	-	-
	0.3	Ritz-Hermite	1.5383	1.6029	1.7968	3.1539	7.9996
		Ritz-Laguerre	1.5418	1.6066	1.8010	3.1614	8.0191
		IGA [20]	1.5398	-	-	-	-
	0.4	Ritz-Hermite	1.4636	1.5240	1.7053	2.9740	7.5042
		Ritz-Laguerre	1.4668	1.5274	1.7091	2.9811	7.5229
		IGA [20]	1.4705	-	-	-	-
	0.5	Ritz-Hermite	1.3896	1.4457	1.6138	2.7902	6.9911
		Ritz-Laguerre	1.3927	1.4489	1.6174	2.7970	7.0091
		IGA [20]	1.4000	-	-	-	-

New results for two kinds of critical buckling load of PMF microplates using MCT theory with two kinds of boundary conditions (CCCC and SCSC) are found in Tables 3.9 and 3.10 under uniform distribution and symmetric distribution. Besides, the results obtained from the two approaches of the Ritz method are also compared with each other.

Table 3.9: The normalized critical buckling load of the metal foam square microplates under biaxial compression with many boundary conditions, $a/h = 10$

BCs	Type distribution	β	Theory	h/l				
				∞	10	5	2	1
SCSC	Uniform	0.1	Ritz-Hermite	2.5725	2.7218	3.1684	6.2766	17.3403
			Ritz-Laguerre	2.5757	2.7225	3.1620	6.2673	17.2474
		0.2	Ritz-Hermite	2.3649	2.5061	2.9284	5.8675	16.3300
			Ritz-Laguerre	2.3678	2.5066	2.9223	5.8509	16.2477
		0.3	Ritz-Hermite	2.1591	2.2916	2.6882	5.4480	15.2726
			Ritz-Laguerre	2.1616	2.2920	2.6823	5.4343	15.1917
		0.4	Ritz-Hermite	1.9536	2.0770	2.4460	5.0145	14.0583
			Ritz-Laguerre	1.9559	2.0772	2.4405	4.9939	13.9994
		0.5	Ritz-Hermite	1.7467	1.8602	2.1996	4.5622	12.9731
			Ritz-Laguerre	1.7487	1.8603	2.1945	4.5549	12.8973
	Symmetric	0.1	Ritz-Hermite	2.6373	2.7851	3.2271	6.3035	17.3159
			Ritz-Laguerre	2.6396	2.7852	3.2212	6.2610	17.1914
		0.2	Ritz-Hermite	2.5144	2.6542	3.0727	5.9848	16.3127
			Ritz-Laguerre	2.5166	2.6545	3.0672	5.9450	16.1989
		0.3	Ritz-Hermite	2.3934	2.5250	2.9189	5.6599	15.4188
			Ritz-Laguerre	2.3956	2.5253	2.9138	5.6229	15.2963
		0.4	Ritz-Hermite	2.2735	2.3966	2.7648	5.3274	14.4510
			Ritz-Laguerre	2.2757	2.3971	2.7603	5.2934	14.3806
		0.5	Ritz-Hermite	2.1539	2.2680	2.6095	4.9858	13.4462
			Ritz-Laguerre	2.1561	2.2686	2.6055	4.9551	13.3688
CCCC	Uniform	0.1	Ritz-Hermite	3.8964	4.1769	5.0167	10.8758	31.7498
			Ritz-Laguerre	3.8916	4.1732	5.0160	10.8953	31.8486
		0.2	Ritz-Hermite	3.5870	3.8523	4.6465	10.1878	29.9295
			Ritz-Laguerre	3.5828	3.8490	4.6460	10.2061	30.0218
		0.3	Ritz-Hermite	3.2794	3.5285	4.2743	9.4783	28.0183
			Ritz-Laguerre	3.2755	3.5254	4.2739	9.4952	28.1040
		0.4	Ritz-Hermite	2.9713	3.2031	3.8974	8.7412	25.9982
			Ritz-Laguerre	2.9678	3.2004	3.8970	8.7567	26.0769
		0.5	Ritz-Hermite	2.6601	2.8734	3.5121	7.9681	23.8437
			Ritz-Laguerre	2.6569	2.8709	3.5117	7.9821	23.9152
	Symmetric	0.1	Ritz-Hermite	4.0128	4.2937	5.1346	11.0014	31.9071
			Ritz-Laguerre	4.0101	4.2911	5.1323	11.0004	31.9084
		0.2	Ritz-Hermite	3.8218	4.0876	4.8836	10.4371	30.2273
			Ritz-Laguerre	3.8192	4.0851	4.8815	10.4361	30.2285
		0.3	Ritz-Hermite	3.6324	3.8826	4.6318	9.8587	28.4864
			Ritz-Laguerre	3.6299	3.8802	4.6298	9.8578	28.4875
		0.4	Ritz-Hermite	3.4431	3.6771	4.3775	9.2638	26.6787
			Ritz-Laguerre	3.4407	3.6748	4.3755	9.2628	26.6797
		0.5	Ritz-Hermite	3.2524	3.4693	4.1187	8.6494	24.7981
			Ritz-Laguerre	3.2501	3.4672	4.1169	8.6485	24.7990

Table 3.10: The normalized critical buckling load of the metal foam square microplates under uniaxial compression with many boundary conditions, $a/h = 10$

BCs	Type distribution	β	Theory	h/l				
				∞	10	5	2	1
SCSC	Uniform	0.1	Ritz-Hermite	4.7816	5.0648	5.9094	11.7613	32.5557
			Ritz-Laguerre	4.7944	5.0757	5.9164	11.7602	32.5554
		0.2	Ritz-Hermite	4.3975	4.6651	5.4635	10.9965	30.6609
			Ritz-Laguerre	4.4087	4.6747	5.4694	10.9948	30.6594
		0.3	Ritz-Hermite	4.0162	4.2675	5.0169	10.2118	28.6774
			Ritz-Laguerre	4.0261	4.2757	5.0218	10.2096	28.6749
		0.4	Ritz-Hermite	3.6353	3.8691	4.5663	9.4006	26.5867
			Ritz-Laguerre	3.6439	3.8761	4.5703	9.3980	26.5831
		0.5	Ritz-Hermite	3.2515	3.4664	4.1075	8.5539	24.3627
			Ritz-Laguerre	3.2587	3.4723	4.1106	8.5508	24.3584
	Symmetric	0.1	Ritz-Hermite	4.9348	5.2183	6.0637	11.9181	32.7184
			Ritz-Laguerre	4.9488	5.2303	6.0716	11.9175	32.7172
		0.2	Ritz-Hermite	4.7033	4.9718	5.7723	11.3150	31.0072
			Ritz-Laguerre	4.7171	4.9837	5.7802	11.3142	31.0035
		0.3	Ritz-Hermite	4.4751	4.7279	5.4817	10.6997	29.2375
			Ritz-Laguerre	4.4885	4.7395	5.4895	10.6987	29.2309
		0.4	Ritz-Hermite	4.2482	4.4848	5.1900	10.0696	27.4035
			Ritz-Laguerre	4.2617	4.4966	5.1979	10.0685	27.3939
		0.5	Ritz-Hermite	4.0211	4.2408	4.8954	9.4221	25.4996
			Ritz-Laguerre	4.0348	4.2528	4.9036	9.4207	25.4861
CCCC	Uniform	0.1	Ritz-Hermite	7.2066	7.7529	9.3772	20.5925	60.5079
			Ritz-Laguerre	7.2087	7.7607	9.3998	20.6066	60.5522
		0.2	Ritz-Hermite	6.6402	7.1564	8.6914	19.2962	56.1332
			Ritz-Laguerre	6.6424	7.1637	8.7125	19.3026	56.1381
		0.3	Ritz-Hermite	6.0758	6.5601	8.0006	17.9581	51.9046
			Ritz-Laguerre	6.0778	6.5668	8.0200	18.0165	51.9990
		0.4	Ritz-Hermite	5.5495	5.9598	7.2997	16.5666	48.0675
			Ritz-Laguerre	5.5513	5.9660	7.3175	16.6068	48.0901
	Symmetric	0.1	Ritz-Hermite	7.4160	7.9634	9.5899	20.8101	60.6146
			Ritz-Laguerre	7.4182	7.9713	9.6128	20.9251	61.0770
		0.2	Ritz-Hermite	7.0582	7.5769	9.1175	19.7408	57.4269
			Ritz-Laguerre	7.0605	7.5846	9.1394	19.8490	57.8579
		0.3	Ritz-Hermite	6.7020	7.1909	8.6423	18.6441	54.1228
			Ritz-Laguerre	6.7040	7.1980	8.6627	18.7448	54.5204
		0.4	Ritz-Hermite	6.3440	6.8020	8.1607	17.5149	50.6915
			Ritz-Laguerre	6.3462	6.8089	8.1800	17.6081	51.0542

Moreover, Fig. 3.7 displays the normalized critical buckling loads of PMF SD microplates with respect to the thickness-to-MLSP's ratio. It is interesting to observe that the porosity does not significantly impact on the size effect, when the thickness-to-MLSP's ratio increases, the curves of critical buckling loads decrease

suddenly from $h/l \leq 10$ and then become stable from $h/l \geq 20$. As expected, the normalized critical buckling loads slightly decreases with an increase of the porous parameter due to the reduction of the stiffness. In comparison of the porosity distribution types (UD and SD), similar to the free vibration responses, it is observed that the uniform arrangement of porosity requires a critical buckling load smaller than the symmetric distribution. It affirms that the symmetric distribution of porosity demonstrates more advantage in stiffness than the uniform one.

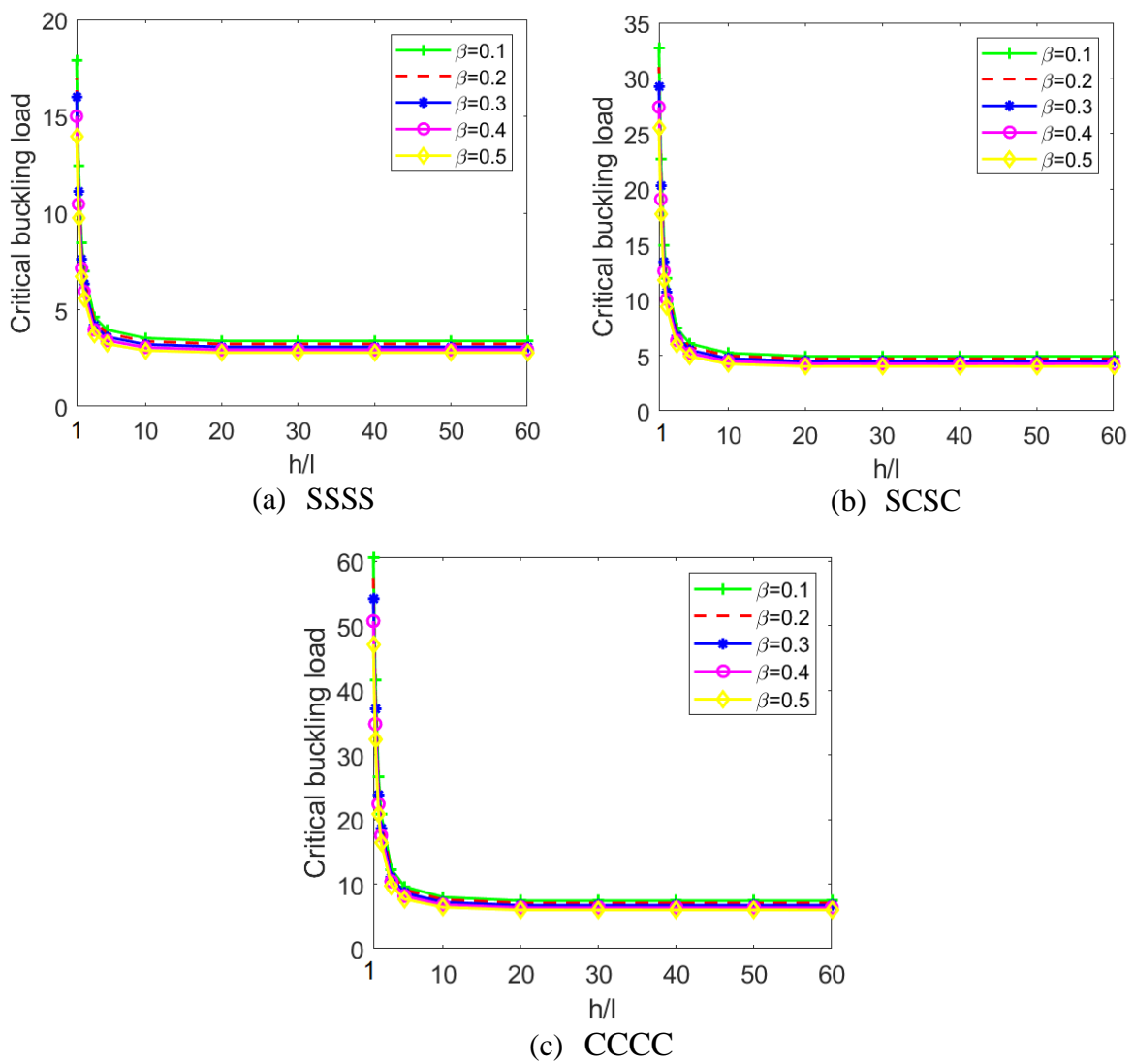


Figure 3.7: Variation of normalized critical buckling load for uniaxial compression with respect to the length scale-to-thickness ratio h/l and $a/h = 10$ under symmetric distribution

3.3.2.2 The size dependent analysis of PMF microplates using modified strain gradient

In this example, free vibration $\bar{\omega} = \omega h \sqrt{\rho_{\max} / E_{\max}}$ and buckling loads (uniaxial compression and biaxial compression) $\bar{N}_{cr} = N_{cr} a^2 / (h^3 E_{\max})$ behaviors of the square PMF microplates with simply supported (SSSS) are analysed. The PMF microplates are designed to be made of metal foam materials whose characteristics are followed: $E_{\max} = 200$ GPa, $\rho_{\max} = 7850 \text{ kg/m}^3$, $\nu_{\max} = 0.33$.

Table 3.11: Normalized fundamental frequencies of PMF rectangular microplates for simply supported boundary condition with $a / h = 10$

Type distribution	β	Theory	h / l			
			10	5	2	1
Uniform	0.1	Ritz-Hermite	0.0606	0.0715	0.1234	0.2264
		Ritz-Laguerre	0.0606	0.0715	0.1233	0.2262
	0.2	Ritz-Hermite	0.0592	0.0702	0.1218	0.2240
		Ritz-Laguerre	0.0592	0.0702	0.1218	0.2239
		IGA [20]	0.0601	0.0706	0.1203	0.2196
	0.3	Ritz-Hermite	0.0578	0.0688	0.1201	0.2212
		Ritz-Laguerre	0.0578	0.0688	0.1200	0.2211
		IGA [20]	0.0590	0.0692	0.1179	0.2153
Symmetric	0.1	Ritz-Hermite	0.0615	0.0723	0.1238	0.2267
		Ritz-Laguerre	0.0615	0.0723	0.1238	0.2265
	0.2	Ritz-Hermite	0.0611	0.0718	0.1228	0.2247
		Ritz-Laguerre	0.0611	0.0718	0.1228	0.2246
		IGA [20]	0.0617	0.0720	0.1215	0.2212
	0.3	Ritz-Hermite	0.0608	0.0714	0.1218	0.2225
		Ritz-Laguerre	0.0608	0.0713	0.1217	0.2224
		IGA [20]	0.0615	0.0715	0.1200	0.2180
Asymmetric	0.1	Ritz-Hermite	0.0608	0.0717	0.1235	0.2264
		Ritz-Laguerre	0.0607	0.0717	0.1234	0.2263
	0.2	Ritz-Hermite	0.0596	0.0705	0.1221	0.2242
		Ritz-Laguerre	0.0596	0.0705	0.1220	0.2241
		IGA [20]	0.0604	0.0708	0.1206	0.2202
	0.3	Ritz-Hermite	0.0584	0.0693	0.1205	0.2218
		Ritz-Laguerre	0.0583	0.0692	0.1205	0.2217
		IGA [20]	0.0594	0.0696	0.1185	0.2164

Their normalized fundamental frequencies are reported in Tables 3.11-3.13 with $\beta = 0.1, 0.2$, and 0.3 , $h/l = 10, 5, 2, 1$, $a/h = 10$, and three porosity distributions (UD, AD, SD) are benchmarked with those derived from Hung et al. [20] with various material length scale parameters.

Table 3.12: Normalized critical buckling load under uniaxial compression of PMF rectangular microplates for simply supported boundary condition with $a/h = 10$

Type distribution	β	Theory	h/l			
			10	5	2	1
Uniform	0.1	Ritz-Hermite	3.6690	5.0792	14.9412	50.0314
		Ritz-Laguerre	3.6665	5.0754	14.9287	49.9844
		IGA [20]	3.7311	5.1334	14.9043	49.7140
	0.2	Ritz-Hermite	3.3772	4.7119	14.0463	47.2574
		Ritz-Laguerre	3.3748	4.7084	14.0345	47.2129
		IGA [20]	3.4694	4.7734	13.8590	46.2271
Symmetric	0.1	Ritz-Hermite	3.7821	5.1928	15.0594	50.1759
		Ritz-Laguerre	3.7795	5.1890	15.0467	50.1283
		IGA [20]	3.8216	5.2281	15.0408	50.0280
	0.2	Ritz-Hermite	3.6027	4.9396	14.2906	47.5816
		Ritz-Laguerre	3.6002	4.9359	14.2785	47.5360
		IGA [20]	3.6551	4.9697	14.1530	46.9191
Asymmetric	0.1	Ritz-Hermite	3.6912	5.1018	14.9670	50.0702
		Ritz-Laguerre	3.6887	5.0981	14.9544	50.0230
		IGA [20]	3.7482	5.1521	14.9364	49.7997
	0.2	Ritz-Hermite	3.4194	4.7560	14.1038	47.3657
		Ritz-Laguerre	3.4171	4.7525	14.0919	47.3211
		IGA [20]	3.5018	4.8109	13.9370	46.4604

Table 3.13: Normalized critical buckling load under biaxial compression of PMF rectangular microplates for simply supported boundary condition with $a/h = 10$

Type distribution	β	Theory	h/l			
			10	5	2	1
Uniform	0.1	Ritz-Hermite	1.8345	2.5395	7.4701	25.0148
		Ritz-Laguerre	1.8332	2.5376	7.4640	24.9916
		IGA [20]	1.8655	2.5667	7.4522	24.8570
	0.2	Ritz-Hermite	1.6886	2.3558	7.0226	23.6278
		Ritz-Laguerre	1.6874	2.3541	7.0169	23.6059
		IGA [20]	1.7347	2.3867	6.9295	23.1136
Symmetric	0.1	Ritz-Hermite	1.8910	2.5963	7.5291	25.0870
		Ritz-Laguerre	1.8897	2.5944	7.5229	25.0635
		IGA [20]	1.9108	2.6140	7.5204	25.0140
	0.2	Ritz-Hermite	1.8013	2.4697	7.1447	23.7899
		Ritz-Laguerre	1.8001	2.4679	7.1388	23.7674
		IGA [20]	1.8276	2.4849	7.0765	23.4596
Asymmetric	0.1	Ritz-Hermite	1.8456	2.5508	7.4829	25.0342
		Ritz-Laguerre	1.8443	2.5490	7.4768	25.0109
		IGA [20]	1.8741	2.5761	7.4682	24.8999
	0.2	Ritz-Hermite	1.7097	2.3779	7.0513	23.6820
		Ritz-Laguerre	1.7085	2.3762	7.0456	23.6599
		IGA [20]	1.7509	2.4054	6.9685	23.2302

3.3.3 Analysis of FG sandwich microplates

3.3.3.1 Analysis of FG sandwich microplates using MCT

3.3.3.1.1 Material properties of FG sandwich microplates

They are made from a ceramic and metal whose mean material properties are given by:

- MAT 1: ZrO_2 ($E_c = 244.27 \text{ GPa}$, $\alpha_c = 12.766 \times 10^{-6} 1/\text{C}$, $\nu_c = 0.3$),
 $\text{Ti} - \text{Al6} - 4\text{V}$ ($E_m = 66.2 \text{ GPa}$, $\alpha_m = 10.3 \times 10^{-6} 1/\text{C}$, $\nu_m = 0.3$).
- MAT 2: Al_2O_3 ($E_c = 380 \text{ GPa}$, $\rho_c = 3800 \text{ kg/m}^3$, $\alpha_c = 7.4 \times 10^{-6} 1/\text{C}$, $\nu_c = 0.3$),
 Al ($E_m = 70 \text{ GPa}$, $\rho_m = 2702 \text{ kg/m}^3$, $\alpha_m = 23 \times 10^{-6} 1/\text{C}$, $\nu_m = 0.3$).

The following normalized parameters are used:

$$\bar{\omega} = \frac{\omega a^2}{h} \sqrt{\frac{\rho_0}{E_0}}; (E_0 = 1 \text{ GPa}, \rho_0 = 1 \text{ kg/m}^3) \quad (3.52a)$$

$$\bar{N}_{cr} = \frac{N_{cr} a^2}{100 h^3 E_0}; \bar{T}_{cr} = \Delta T_{cr} \times 10^{-3} \quad (3.52b)$$

3.3.3.1.2 Vibration analysis

Non-dimensional deterministic fundamental frequencies of SSSS $\text{Al}/\text{Al}_2\text{O}_3$ sandwich microplates (MAT 2) are shown in Table 3.14 to demonstrate the correctness of the current theory for vibration analysis. It is noted that the results are computed without temperature effects and validated with those from Thai et al. [185].

Table 3.14: Comparison of non-dimensional fundamental frequency $\bar{\omega}$ of square SSSS FG sandwich microplates (MAT 2, $a/h = 10$)

P	h/l	Theory	1-0-1	2-1-2	2-1-1	1-1-1	2-2-1	1-2-1
0.5	∞	Present	1.4414	1.4814	1.5044	1.5182	1.5448	1.5728
		MCT [185]	1.4462	1.4861	1.5084	1.5213	1.5492	1.5766
	5	Present	1.5978	1.6412	1.6639	1.6793	1.7059	1.7345
		MCT [185]	1.5987	1.6423	1.6643	1.6788	1.7064	1.7345
	5/3	Present	2.5192	2.5876	2.6090	2.6353	2.6650	2.6996
		MCT [185]	2.5006	2.5667	2.5900	2.6142	2.6437	2.6787
	1	Present	3.7337	3.8305	3.8583	3.8965	3.9337	3.9800
		MCT [185]	3.6872	3.7836	3.8126	3.8488	3.8885	3.9325
1	∞	Present	1.2428	1.3002	1.3330	1.3536	1.3951	1.4398
		MCT [185]	1.2449	1.3019	1.3352	1.3552	1.3975	1.4413
	5	Present	1.3972	1.4622	1.4948	1.5189	1.5610	1.6054
		MCT [185]	1.3963	1.4612	1.4941	1.4941	1.5590	1.6038
	5/3	Present	2.2831	2.3940	2.4305	2.4687	2.5162	2.5745
		MCT [185]	2.2638	2.3729	2.4092	2.4492	2.4950	2.5512
	1	Present	3.4251	3.5941	3.6398	3.7004	3.7575	3.8367
		MCT [185]	3.3769	3.5413	3.5882	3.6486	3.7072	3.7830
5	∞	Present	0.9468	0.9822	1.0308	1.0442	1.1094	1.1739
		MCT [185]	0.9473	0.9832	1.0320	1.0461	1.1105	1.1756
	5	Present	1.0994	1.1394	1.1886	1.2156	1.2796	1.3500
		MCT [185]	1.1083	1.1379	1.1882	1.2136	1.2785	1.3480
	5/3	Present	1.7689	1.9910	2.0574	2.1321	2.2139	2.3144
		MCT [185]	1.7540	1.9730	2.0398	2.1137	2.1944	2.2944
	1	Present	2.6648	3.0474	3.1405	3.2691	3.3784	3.5261
		MCT [185]	2.6261	2.9984	3.0933	3.2160	3.3274	3.4702
10	∞	Present	0.9284	0.9430	0.9922	0.9960	1.0605	1.1229
		MCT [185]	0.9296	0.9443	0.9935	0.9969	1.0625	1.1247
	5	Present	1.0338	1.0924	1.1448	1.1626	1.2313	1.2991
		MCT [185]	1.0326	1.0912	1.1434	1.1619	1.2294	1.2982
	5/3	Present	1.6480	1.9024	1.9786	2.0600	2.1486	2.2601
		MCT [185]	1.6350	1.8863	1.9614	2.0420	2.1309	2.2392
	1	Present	2.4530	2.9105	3.0198	3.1652	3.2897	3.4536
		MCT [185]	2.4205	2.8645	2.9739	3.1138	3.2394	3.3986

3.3.3.1.3 Mechanical buckling and thermal bucking analysis

The biaxial of non-dimensional deterministic critical buckling loads of SSSS Al/Al_2O_3 microplates (MAT 2) are shown in Table 3.15 for various values of $a/h = 10$, p and h/l , and compared with those published by Thai et al. [186]. An excellent agreement with earlier ones can be observed.

Table 3.15: Non-dimensional critical buckling loads of square SSSS FG sandwich microplates (MAT 2) ($a/h = 10$) with biaxial compression

p	h/l	Theory	1-0-1	2-1-2	2-1-1	1-1-1	2-2-1	1-2-1
0	∞	Present	6.5028	6.5028	6.5028	6.5028	6.5028	6.5028
		MCT [186]	6.5244	6.5244	6.5244	6.5244	6.5244	6.5244
	5	Present	7.6525	7.6525	7.6525	7.6525	7.6525	7.6525
		MCT [186]	7.6507	7.6507	7.6507	7.6507	7.6507	7.6507
	5/3	Present	16.8490	16.8490	16.8490	16.8490	16.8490	16.8490
		MCT [186]	16.6536	16.6536	16.6536	16.6536	16.6536	16.6536
1	1	Present	35.2385	35.2385	35.2385	35.2385	35.2385	35.2385
		MCT [186]	34.6404	34.6404	34.6404	34.6404	34.6404	34.6404
	∞	Present	2.5838	2.9203	3.0972	3.2326	3.4749	3.7534
		MCT [186]	2.5925	2.9301	3.1077	3.2435	3.4867	3.7662
	5	Present	3.2653	3.6956	3.8959	4.0704	4.3440	4.6693
		MCT [186]	3.2609	3.6906	3.8908	4.0649	4.3383	4.6632
	5/3	Present	8.7161	9.8974	10.2848	10.7723	11.2954	11.9955
		MCT [186]	8.5680	9.7282	10.1120	10.5884	11.1065	11.7939
	1	Present	19.6139	22.2967	23.0585	24.1715	25.1938	26.6433
		MCT [186]	19.0532	21.6545	22.4164	23.4849	24.5068	25.9187
5	∞	Present	1.3294	1.5215	1.7020	1.7900	2.0562	2.3675
		MCT [186]	1.3337	1.5266	1.7077	1.7960	2.0632	2.3756
	5	Present	1.6980	2.0469	2.2664	2.4197	2.7380	3.1275
		MCT [186]	1.6960	2.0445	2.2636	2.4168	2.7346	3.1231
	5/3	Present	4.6463	6.2490	6.7810	7.4568	8.1917	9.2066
		MCT [186]	4.5696	6.1430	6.6668	7.3276	8.0512	9.0429
	1	Present	10.5408	14.6501	15.8069	17.5270	19.0950	21.3603
		MCT [186]	10.2367	14.1766	15.3203	16.9495	18.4979	20.6714
10	∞	Present	1.2439	1.3734	1.5461	1.5976	1.8540	2.1401
		MCT [186]	1.2479	1.3779	1.5514	1.6029	1.8603	2.1474
	5	Present	1.4413	1.7118	1.9372	2.0199	2.3532	2.6647
		MCT [186]	1.4115	1.6816	1.8885	1.9710	2.2723	2.6059
	5/3	Present	3.9196	5.5886	6.1450	6.8379	7.6059	8.6601
		MCT [186]	3.8578	5.4951	6.0425	6.7211	7.4766	8.5067
	1	Present	8.6748	13.0792	14.3174	16.1503	17.8273	20.2462
		MCT [186]	8.4504	12.6622	13.8814	15.6153	17.2662	19.5807

The deterministic critical buckling temperature of SSSS FG sandwich microplates with MAT 1 under biaxial compression is also estimated in order to further validate the proposed technique with uniform and linear distribution. The outcomes are compared with those obtained by Zenkour et al. [66] and Daikh et al. [187]. As seen in Tables 3.16 and 3.17, the present solutions match well with those from earlier ones. Tables 3.18 and 3.19 provide some new results of the thermal buckling of CSCS and CCCC FG sandwich microplates.

Table 3.16: Non-dimensional critical buckling temperature \bar{T}_{cr} of square SSSS FG sandwich microplates (MAT 1) under uniform distribution with biaxial compression

a/h	p	h/l	Theory	1-0-1	2-1-2	2-2-1	1-1-1	1-2-1
5	0.5	∞	Present	2.8652	2.8237	2.8582	2.8263	2.8652
			HPT [66]	-	-	2.8632	2.8322	2.8697
			HPT[187]	2.8707	2.8302	-	2.8322	2.8697
		10	Present	3.0391	2.9952	3.0275	2.9963	3.0336
		5	Present	3.5609	3.5097	3.5356	3.5064	3.5387
		2	Present	7.2172	7.1128	7.0927	7.0784	7.0753
		1	Present	20.2608	19.9707	19.7861	19.8241	19.6944
		2	Present	2.6301	2.3961	2.4177	2.3595	2.4279
			HPT [66]	-	-	2.4183	2.3599	2.4287
			HPT[187]	2.6345	2.3963	-	2.3599	2.4287
	2	10	Present	2.8142	2.5734	2.5903	2.5336	2.5987
		5	Present	3.3664	3.1055	3.1083	3.0558	3.1111
		2	Present	7.2302	6.8289	6.7329	6.7105	6.6972
		1	Present	21.0124	20.1094	19.6617	19.7458	19.4885
	10	0.5	Present	0.8006	0.7895	0.8036	0.7920	0.8072
			HPT [66]	-	-	0.8059	0.7945	0.8092
			HPT[187]	0.8031	0.7922	-	0.7945	0.8092
		10	Present	0.8445	0.8327	0.8464	0.8349	0.8496
		5	Present	0.9761	0.9625	0.9745	0.9636	0.9771
		2	Present	1.8983	1.8713	1.8719	1.8646	1.8694
		1	Present	5.1908	5.1170	5.0767	5.0822	5.0556
		2	Present	0.7169	0.6498	0.6612	0.6414	0.6656
			HPT [66]	-	-	0.6621	0.6423	0.6668
			HPT[187]	0.7178	0.6507	-	0.6423	0.6668
	2	10	Present	0.7633	0.6945	0.7047	0.6853	0.7089
		5	Present	0.9024	0.8285	0.8351	0.8168	0.8381
		2	Present	1.8758	1.7663	1.7484	1.7374	1.7418
		1	Present	5.1513	5.1143	5.0090	5.0241	4.9683

Table 3.17: Non-dimensional critical buckling temperature \bar{T}_{cr} of square SSSS FG sandwich microplates (MAT 1) under linear distribution with biaxial compression, $T_b = 25^\circ C$

a/h	p	h/l	Theory	1-0-1	2-1-2	2-2-1	1-1-1	1-2-1
5	0.5	∞	Present	5.6189	5.5292	5.3622	5.5293	5.5998
			HPT [66]	-	-	5.4417	5.6144	5.6894
			HPT[187]	5.6914	5.6105	-	5.6144	5.6894
		10	Present	5.9600	5.8650	5.6798	5.8620	5.9289
		5	Present	6.9831	6.8723	6.6328	6.8598	6.9160
		2	Present	14.1524	13.9264	13.3052	13.8469	13.8268
		1	Present	39.7280	39.0998	37.1151	38.7782	38.4860
	2	∞	Present	5.1581	4.6895	4.3583	4.6133	4.7424
			HPT [66]	-	-	4.4071	4.6699	4.8074
			HPT[187]	5.2103	4.7427	-	4.6699	4.8074
		10	Present	5.5190	5.0366	4.6695	4.9536	5.0760
		5	Present	6.6017	6.0777	5.6031	5.9745	6.0768
		2	Present	14.1778	13.3634	12.1359	13.1187	13.0802
		1	Present	41.2017	39.3500	35.4382	38.6005	38.0611
10	0.5	∞	Present	1.5708	1.5466	1.5167	1.5502	1.5782
			HPT [66]	-	-	1.4972	1.5391	1.5685
			HPT[187]	1.5562	1.5344	-	1.5391	1.5685
		10	Present	1.6569	1.6313	1.5885	1.6341	1.6613
		5	Present	1.9149	1.8853	1.8289	1.8857	1.9101
		2	Present	3.7231	3.6646	3.5122	3.6483	3.6539
		1	Present	10.1790	10.0190	9.5235	9.9421	9.8801
	2	∞	Present	1.4067	1.2725	1.1925	1.2549	1.3014
			HPT [66]	-	-	1.1731	1.2347	1.2837
			HPT[187]	1.3856	1.2515	-	1.2347	1.2837
		10	Present	1.4976	1.3599	1.2708	1.3406	1.3855
		5	Present	1.7703	1.6221	1.5060	1.5977	1.6376
		2	Present	3.6790	3.4571	3.1521	3.3973	3.4026
		1	Present	10.4936	10.0084	9.0288	9.8221	9.7038

Table 3.18: Non-dimensional critical buckling temperature \bar{T}_{cr} of square FG sandwich microplates (MAT 1) under uniform distribution with biaxial compression

BCs	p	h/l	Theory	1-0-1	2-1-2	2-2-1	1-1-1	1-2-1
$a/h=5$								
CSCS	0.5	∞	Present	4.2188	4.1548	4.1877	4.1550	4.1920
		10	Present	4.5793	4.5102	4.5388	4.5036	4.5412
		5	Present	5.6498	5.5657	5.5812	5.5502	5.5776
		2	Present	13.0949	12.9023	12.8237	12.8234	12.7779
		1	Present	39.5812	39.0115	38.5968	38.7035	38.3992
	2	∞	Present	3.9457	3.6089	3.6173	3.5456	3.6242
		10	Present	4.3266	3.9758	3.9747	3.9069	3.9778
		5	Present	5.4591	5.0670	5.0370	4.9780	5.0287
		2	Present	13.3304	12.6528	12.4203	12.4232	12.3328
		1	Present	41.3300	39.6361	38.6845	38.9069	38.3152
CCCC	0.5	∞	Present	6.0403	5.9696	5.9703	5.9712	5.9830
		10	Present	6.7604	6.6550	6.6614	6.6319	6.6559
		5	Present	8.8280	8.6919	8.6757	8.6523	8.6555
		2	Present	23.2428	22.8973	22.6967	22.7331	22.5951
		1	Present	74.4843	73.4092	72.5563	72.8005	72.1597
	2	∞	Present	5.8827	5.3268	5.2999	5.2335	5.2793
		10	Present	6.5364	6.0414	5.9914	5.9246	5.9784
		5	Present	8.7276	8.1530	8.0464	7.9963	8.0113
		2	Present	23.9800	22.8551	22.3528	22.4250	22.1628
		1	Present	78.1686	75.0826	73.1813	73.6825	72.4412
$a/h=10$								
CSCS	0.5	∞	Present	1.2629	1.2447	1.2646	1.2478	1.2698
		10	Present	1.3546	1.3340	1.3533	1.3364	1.3576
		5	Present	1.6242	1.6010	1.6170	1.6011	1.6198
		2	Present	3.5111	3.4605	3.4532	3.4448	3.4456
		1	Present	10.2315	10.0853	9.9942	10.0122	9.9487
	2	∞	Present	1.1380	1.0329	1.0486	1.0189	1.0553
		10	Present	1.2337	1.1251	1.1384	1.1094	1.1441
		5	Present	1.5198	1.4006	1.4067	1.3799	1.4097
		2	Present	3.5114	3.3192	3.2751	3.2633	3.2585
		1	Present	10.6067	10.1548	9.9316	9.9733	9.8451
CCCC	0.5	∞	Present	1.9793	1.9499	1.9779	1.9508	1.9854
		10	Present	2.1554	2.1239	2.1499	2.1253	2.1541
		5	Present	2.6817	2.6424	2.6614	2.6319	2.6636
		2	Present	6.3550	6.2624	6.2357	6.2286	6.2173
		1	Present	19.4421	19.1633	18.9723	19.0172	18.8798
	2	∞	Present	1.7995	1.6372	1.6558	1.6148	1.6632
		10	Present	1.9849	1.8154	1.8306	1.7888	1.8377
		5	Present	2.5416	2.3515	2.3524	2.3146	2.3540
		2	Present	6.4214	6.0892	5.9919	5.9838	5.9545
		1	Present	20.2446	19.4079	18.9595	19.0571	18.7855

Table 3.19: Non-dimensional critical buckling temperature \bar{T}_{cr} of square FG sandwich microplates (MAT 1) under linear distribution with biaxial compression, $T_b = 25^\circ C$

BCs	\bar{p}	h/l	Theory	1-0-1	2-1-2	2-2-1	1-1-1	1-2-1	
$a/h=5$									
CSCS	0.5	∞	Present	8.2731	8.1351	7.8562	8.1208	8.1926	
		10	Present	8.9800	8.8310	8.5147	8.8104	8.8749	
		5	Present	11.0790	10.8976	10.4700	10.8576	10.9002	
		2	Present	25.6773	25.2613	24.0553	25.0843	24.9704	
		1	Present	77.6111	76.3782	72.3996	75.7077	75.0373	
	2	∞	Present	7.7376	7.0658	6.5206	6.9356	7.0788	
		10	Present	8.4844	7.7805	7.1646	7.6383	7.7694	
		5	Present	10.7051	9.9158	9.0793	9.7320	9.8218	
		2	Present	26.1390	24.7593	22.3865	24.2862	24.0863	
		1	Present	81.0401	77.5589	69.7241	76.0570	74.8287	
	CCCC	0.5	∞	Present	11.3498	11.6886	11.0893	11.5192	11.6801
			10	Present	13.2567	13.0291	12.4996	12.9769	13.0029
			5	Present	17.3110	17.0191	16.2743	16.9250	16.9179
			2	Present	45.5751	44.8296	42.5747	44.4686	44.1542
			1	Present	146.048	143.722	140.099	142.404	141.009
2		∞	Present	11.3820	10.4687	9.5652	10.4857	10.3737	
		10	Present	12.8190	11.8248	10.8069	11.5793	11.6859	
		5	Present	17.1112	15.9533	14.5040	15.6295	15.6496	
		2	Present	47.0206	44.7227	40.2883	43.8378	43.2838	
		1	Present	153.272	146.918	139.899	143.037	141.475	
$a/h=10$									
CSCS	0.5	∞	Present	2.4771	2.4377	2.3737	2.4416	2.4823	
		10	Present	2.6548	2.6122	2.5393	2.6150	2.6538	
		5	Present	3.1858	3.1354	2.0526	3.1329	3.1664	
		2	Present	6.8856	6.7759	6.4783	6.7391	6.7339	
		1	Present	20.0628	19.7461	18.7476	19.5854	19.4417	
	2	∞	Present	2.2323	2.0222	1.8907	1.9928	2.0618	
		10	Present	2.4200	2.2026	2.0526	2.1697	2.2354	
		5	Present	2.9809	2.7417	2.5362	2.6985	2.7540	
		2	Present	6.8860	6.4958	5.9037	6.3800	6.3647	
		1	Present	20.7985	19.8714	17.9010	19.4970	19.2279	
	CCCC	0.5	∞	Present	3.8819	3.8270	3.4247	3.8245	3.8766
			10	Present	4.2267	4.1577	4.0323	4.1589	4.2104
			5	Present	5.2592	5.1741	4.9934	5.1644	5.2064
			2	Present	12.4618	12.2613	11.6975	12.1844	12.1503
			1	Present	38.1228	37.5191	35.5885	37.1999	36.8942
2		∞	Present	3.5242	3.2014	2.9860	3.1533	3.2524	
		10	Present	3.8936	3.5540	3.3005	3.4976	3.5894	
		5	Present	4.9846	4.6020	4.2407	4.5257	4.5983	
		2	Present	12.5920	11.9164	10.8003	11.6984	11.6310	
		1	Present	39.6963	37.9774	34.1725	37.2542	36.6881	

3.3.3.2 Analysis of FG sandwich microplates using MST

The deterministic critical buckling temperature $\bar{T}_{cr} = \Delta T_{cr} \times 10^{-3}$ of (SSSS, CSCS, CCCC) FG sandwich microplates with MAT 1 under biaxial compression is also estimated in order to further validate the proposed technique with uniform and linear distribution using modified strain gradient theory with three material length scale parameters. Tables 3.20 and 3.21 provide some new results of the thermal buckling of SSSS, CSCS and CCCC FG sandwich microplates.

Table 3.20: Non-dimensional critical buckling temperature \bar{T}_{cr} of square FG sandwich microplates (MAT 1) under uniform distribution with biaxial compression, $a/h = 10$

BCs	p	h/l	1-0-1	2-1-2	2-2-1	1-1-1	1-2-1
SSSS	0.5	10	0.9532	0.9399	0.9523	0.9412	0.9550
		5	1.4081	1.3884	1.3955	1.3860	1.3957
		2	4.5928	4.5269	4.4962	4.4983	4.4791
		1	15.9077	15.6816	15.5202	15.5599	15.4420
	2	10	0.8779	0.8049	0.8122	0.7937	0.8154
		5	1.3580	1.2672	1.2626	1.2475	1.2611
		2	4.7128	4.4969	4.4093	4.4180	4.3751
		1	16.6085	15.9421	15.5673	15.6539	15.4170
	CCCC	10	2.3827	2.3476	2.3704	2.3477	2.3746
		5	3.5907	3.5386	3.5477	3.5284	3.5449
		2	12.0173	11.8423	11.7536	11.7636	11.7058
		1	41.6999	41.1039	40.6891	40.7874	40.4832
	2	10	2.2247	2.0459	2.0551	2.0147	2.0593
		5	3.4980	3.2717	3.2480	3.2177	3.2412
		2	12.3656	11.8038	11.5624	11.5926	11.4674
		1	43.4969	41.7230	40.7455	40.9630	40.3455
CSCS	0.5	10	1.5094	1.4878	1.5052	1.4889	1.5087
		5	2.2481	2.2162	2.2249	2.2113	2.2245
		2	7.4110	7.3039	7.2515	7.2565	7.2231
		1	25.6694	25.2969	25.0420	25.1062	24.9150
	2	10	1.3981	1.2834	1.2925	1.2648	1.2967
		5	2.1777	2.0339	2.0236	2.0015	2.0201
		2	7.6157	7.2685	7.1232	7.1397	7.0664
		1	26.8012	25.7212	25.1128	25.2531	24.8685

Table 3.21: Non-dimensional critical buckling temperature \bar{T}_{cr} of square FG sandwich microplates (MAT 1) under linear distribution with biaxial compression, $T_b = 25^\circ C$, $a/h = 10$

BCs	p	h/l	1-0-1	2-1-2	2-2-1	1-1-1	1-2-1
SSSS	0.5	10	1.8690	1.8401	1.7863	1.8410	1.8661
		5	2.7610	2.7183	2.6175	2.7112	2.7273
		2	9.0055	8.8629	8.4338	8.7990	8.7528
		1	31.1916	30.7010	29.1123	30.4362	30.1754
	2	10	1.7214	1.5750	1.4639	1.5515	1.5925
		5	2.6628	2.4796	2.2756	2.4387	2.4628
		2	9.2407	8.7993	7.9472	8.6364	8.5443
		1	32.5657	31.1950	28.0579	30.6006	30.1099
	CCCC	10	4.6738	4.5976	4.4475	4.5932	4.6412
		5	7.0411	6.9288	6.6582	6.9031	6.9287
		2	23.5612	23.1860	22.0473	23.0116	22.8747
		1	81.7677	80.4775	76.3244	79.7851	79.1105
	CSCS	10	4.3623	4.0038	3.7047	3.9389	4.0264
		5	6.8615	6.4023	5.8555	6.2908	6.3334
		2	24.2464	23.0982	20.8402	22.6626	22.3976
		1	85.2892	81.6442	73.4378	80.0766	78.7964
CSCS	0.5	10	2.9606	2.9138	2.8242	2.9133	2.9492
		5	4.4091	4.3398	4.1743	4.3264	4.3478
		2	14.5322	14.3006	13.6031	14.1953	14.1156
		1	50.3330	49.5395	46.9738	49.1105	48.6876
	2	10	2.7424	2.5122	2.3304	2.4736	2.5334
		5	4.2710	3.9809	3.6481	3.9136	3.9462
		2	14.9337	14.2237	12.8394	13.9579	13.8016
		1	52.5524	50.3312	45.2630	49.3662	48.5680

3.3.4 Analysis of FGP microplates

3.3.4.1 Analysis of FG microplates using MCT

In order to verify the accuracy of the present theory for vibration analysis

$\bar{\omega} = (\omega a^2 / h) \sqrt{\rho_c / E_c}$, Table 3.22 displays non-dimensional deterministic fundamental frequencies of Al / Al_2O_3 : Al_2O_3 ($E_c = 380$ GPa, $\rho_c = 3800$ kg/m³, $\nu_c = 0.3$), Al ($E_m = 70$ GPa, $\rho_m = 2702$ kg/m³, $\nu_m = 0.3$) microplates with SSSS and CCCC BCs. Various values of p , h/l and a/h are considered.

Table 3.22: Non-dimensional natural frequency of the FG square microplates

BCs	a/h	p	Theory	h/l				
				∞	5	2.5	1.25	1
SSSS	20	1	Present	4.5218	4.9612	6.0813	9.3027	11.1206
			RPT [188]	4.5228	4.9568	6.0756	9.2887	11.1042
			RPT [189]	4.5228	4.9556	6.0714	9.2768	11.0882
		2	Present	4.1098	4.4980	5.5114	8.4121	10.0595
			RPT [188]	4.1100	4.5006	5.5082	8.4062	10.0450
		5	Present	3.8921	4.2000	5.0188	7.4385	8.8270
			RPT [188]	3.8884	4.2005	5.0199	7.4397	8.8286
		10	Present	3.7631	4.0302	4.7433	6.9005	8.1468
			RPT [188]	3.7622	4.0323	4.7488	6.9013	8.1494
	10	1	Present	4.4209	4.8572	5.9865	9.1997	11.0105
			RPT [188]	4.4192	4.8526	5.9664	9.1537	10.9511
		2	Present	4.0104	4.4022	5.4165	8.3166	9.9495
			RPT [188]	4.0090	4.4006	5.4071	8.2863	9.9101
		5	Present	3.7681	4.0828	4.9083	7.3331	8.7203
			RPT [188]	3.7682	4.0876	4.9169	7.3338	8.7135
		10	Present	3.6387	3.9112	4.6331	6.7911	8.0442
			RPT [188]	3.6368	3.9162	4.6464	6.8030	8.0448
CCCC	5	1	Present	6.4417	7.9096	11.0832	19.0090	23.2057
			IGA [190]	6.3868	-	-	-	-
		2	Present	5.7789	7.1127	9.9861	17.1343	20.8920
			IGA [190]	5.7292	-	-	-	-
		5	Present	5.1524	6.2984	8.7539	14.9050	18.1416
			IGA [190]	5.1082	-	-	-	-
		10	Present	4.8661	5.8924	8.1005	13.6879	16.6596
			IGA [190]	4.8214	-	-	-	-
	10	1	Present	7.6557	8.9348	11.9381	19.7962	24.0526
			IGA [190]	7.6251	-	-	-	-
		2	Present	6.9136	8.0861	10.7890	17.8776	21.7236
			IGA [190]	6.8944	-	-	-	-
		5	Present	6.3989	7.3509	9.6103	15.6233	18.9125
			IGA [190]	6.3722	-	-	-	-
		10	Present	6.1521	6.9730	8.9756	14.3803	17.3596
			IGA [190]	6.1039	-	-	-	-

The obtained solutions are compared with those reported by refined plate theory (RPT) by Thai and Kim [188] using Navier solution and Nguyen et al. [189] based on isogeometric analysis (IGA-RPT), and by Thai et al. [190] using IGA-TSDT. It can be seen that there are good agreements among the models.

Table 3.23 illustrates the non-dimensional deterministic critical buckling loads $\bar{N}_{cr} = N_{cr} a^2 / (h^3 E_m)$ of Al / Al₂O₃ plates with SSSS and CCCC BCs for various p and a / h . The obtained results are validated with those reported by Thai et al. [190] and Thai et al. [191]. An excellent agreement with previous ones can be observed.

Table 3.23: Non-dimensional critical buckling loads of the FG square plates

BCs	a/h	Theory	p			
			1	2	5	10
Axial compression $\left(N_1^0, N_2^0, N_{12}^0 = 1, 0, 0\right)$						
SSSS	5	Present	8.2250	6.3433	5.0517	4.4807
		IGA [190]	8.2245	6.3432	5.0531	4.4807
		IGA-TSDT [191]	8.2245	6.3432	5.0531	4.4807
	10	Present	9.3395	7.2635	6.0352	5.4537
		IGA [190]	9.3391	7.2631	6.0353	5.4528
		IGA-TSDT [191]	9.3391	7.2631	6.0353	5.4529
CCCC	10	Present	21.0950	16.2860	13.0276	11.5736
		IGA [190]	20.9471	16.1682	12.9218	11.4711
Biaxial compression $\left(N_1^0, N_2^0, N_{12}^0 = 1, 1, 0\right)$						
SSSS	5	Present	4.1125	3.1717	2.5259	2.2404
		IGA [190]	4.1122	3.1716	2.5265	2.2403
		IGA-TSDT [191]	4.1123	3.1716	2.5265	2.2403
	10	Present	4.6697	3.6317	3.0176	2.7268
		IGA [190]	4.6696	3.6315	3.0177	2.7264
		IGA-TSDT [191]	4.6696	3.6315	3.0177	2.7264
CCCC	10	Present	11.4214	8.8376	7.1420	6.3759
		IGA [190]	11.3805	8.8028	7.1165	6.3518

In order to further verify the proposed method, the deterministic critical buckling loads of SSSS FG microplates with material properties: $E_c = 14.4$ GPa, $\nu_c = 0.38$,

$E_m = 1.44 \text{ GPa}$, $\nu_m = 0.38$ under biaxial loads are also calculated. The results are compared with those from Thai et al. [190] (IGA-TSDT) and by Nguyen et al. [189] (IGA-RPT). It can be seen in Table 3.24 that the results predicted by proposed model are in good agreement with those from previous ones.

Table 3.24: Non-dimensional critical buckling loads of SSSS FG square microplates with biaxial compression

a/h	p	Theory	h/l				
			∞	5	2.5	1.25	1
10	0	Present	18.0854	20.9253	29.4718	63.6538	88.2866
		IGA [190]	18.0754	20.9026	29.3735	63.1958	88.5417
		RPT [189]	18.0756	20.8497	29.1700	62.4358	87.3775
	1	Present	7.8281	9.3962	14.1003	32.9144	47.0226
		IGA- [190]	7.8276	9.3767	14.0232	32.6037	46.5372
		RPT [189]	7.8277	9.3581	13.9459	32.2693	45.9981
	10	Present	3.4988	4.0175	5.5737	11.7984	16.4669
		IGA- [190]	3.4969	4.0513	5.6631	11.9349	16.6033
		RPT [189]	3.4982	4.0246	5.5925	11.8036	16.4431
20	0	Present	18.9254	21.7833	30.3569	64.6505	90.3698
		IGA [190]	18.9243	21.7771	30.3324	64.5348	90.1804
		RPT [189]	18.9244	21.7628	30.2773	64.3321	89.8715
	1	Present	8.1147	9.6868	14.4033	33.2685	47.4168
		IGA [190]	8.1142	9.6815	14.3832	33.1882	47.2914
		RPT [189]	8.1143	9.6766	14.3626	33.0999	47.1494
	10	Present	3.7475	4.2674	5.8270	12.0655	16.7444
		IGA [190]	3.7450	4.2752	5.8505	12.1011	16.7793
		RPT [189]	3.7454	4.2677	5.8312	12.0666	16.7376

3.3.4.2 Analysis of FGP microplates using MCT

In this section [192], numerical examples are performed to investigate vibration and buckling responses of FGP microplates with three kinds of boundary conditions (SSSS, CSCS, CCCC), in which the shear function $\Psi(x_3) = \cot^{-1}(h/x_3) - 16x_3^3/15h^3$ ([141])) is used. The FGP microplates are

supposed to be composed of a mixture of ceramic and metal materials whose mean properties are: Al_2O_3 ($E_c = 380 \text{ GPa}$, $\rho_c = 3800 \text{ kg/m}^3$, $\nu_c = 0.3$), Al ($E_m = 70 \text{ GPa}$, $\rho_m = 2702 \text{ kg/m}^3$, $\nu_m = 0.3$). For simplicity, the following normalized response parameters are used in the numerical examples:

$$\bar{\omega} = (\omega a^2 / h) \sqrt{\rho_c / E_c} ; \bar{N}_{cr} = N_{cr} a^2 / h^3 E_m \quad (3.53)$$

Table 3.25: Convergence study of the series solution of Al/Al₂O₃ FGP microplates with different boundary conditions ($a/h = 10$, $p = 10$, $\beta = 0.1$, $h/l = 1$)

Solution	Number of series $n = n_1 = n_2$					
	2	4	6	8	10	12
Normalized fundamental frequency						
SSSS	7.6675	7.5748	7.5508	7.5531	7.5523	7.5529
CSCS	11.8257	11.4713	11.4652	11.4652	11.4652	11.4652
CCCC	16.4080	16.3353	16.3332	16.3281	16.3285	16.3283
Normalized critical buckling load with axial compression ($N_1^0, N_2^0, N_{12}^0 = 1, 0, 0$)						
SSSS	21.3756	21.1557	20.9383	20.8252	20.8263	20.8258
CSCS	42.7373	40.1757	39.0022	38.8722	38.8720	38.8721
CCCC	75.9027	74.8932	72.6642	72.4134	72.4140	72.4135

In order to study the convergence of present solutions, Table 3.25 shows non-dimensional deterministic critical buckling loads \bar{N}_{cr} and fundamental frequencies $\bar{\omega}$ of the Al/Al₂O₃ square FGP microplates with $a/h = 10$, $p = 10$, $h/l = 1$ and $\beta = 0.1$. The results are calculated for three types of BCs (SSSS, CSCS and CCCC) and the same number of series type-solution in x_1 - and x_2 -direction ($n_1 = n_2 = n$). The responses show a rapid convergence for a number of series $n = 8$, hence this number will be used for the numerical examples.

3.3.4.2.1 Vibration analysis

In order to verify the accuracy of the present theory in predicting vibration behaviors, Table 3.26 displays normalized deterministic fundamental frequencies of Al/Al₂O₃ FGP microplates with simply supported boundary condition in which the

results are computed with side-to-thickness ratio $a/h = 20$, power-law index $p = 1, 2, 5, 10$, porosity parameter $\beta = 0, 0.2$, and material length scale $h/l = \infty, 10, 5, 2, 1$. The obtained solutions are compared with those from Farzam et al. [48] using a refined HSDT (RPT) and isogeometric approach (IGA). It can be observed that there are good agreements between the two models for all cases. Therefore, the present model shows to be reliable to predict the dynamic behaviors of FGP microplates.

Table 3.26: Normalized fundamental frequencies of simply supported FGP microplates with $a/h = 20$

β	h/l	Theory	p			
			1	2	5	10
0	∞	Present	4.5218	4.1098	3.8921	3.7631
		IGA [48]	4.5228	4.1101	3.8884	3.7622
	10	Present	4.6387	4.2122	3.9707	3.8305
		IGA [48]	4.6351	4.2111	3.9688	3.8316
	5	Present	4.9612	4.4980	4.2000	4.0302
		IGA [48]	4.9568	4.5006	4.2005	4.0324
	2	Present	6.7964	6.1561	5.5531	5.2202
		IGA [48]	6.7948	6.1565	5.5551	5.2212
	1	Present	11.1206	10.0595	8.8270	8.1468
		IGA [48]	11.1043	10.0451	8.8287	8.1496
0.2	∞	Present	4.2063	3.4877	3.0203	2.9228
		IGA [48]	4.2068	3.4871	3.0179	2.9184
	10	Present	4.3259	3.6089	3.1042	2.9862
		IGA [48]	4.3331	3.6038	3.1056	2.9849
	5	Present	4.6960	3.9324	3.3551	3.1733
		IGA [48]	4.6914	3.9330	3.3550	3.1752
	2	Present	6.6954	5.7322	4.7415	4.2613
		IGA [48]	6.6819	5.7303	4.7440	4.2686
	1	Present	11.2241	9.7475	7.9145	6.8643
		IGA [48]	11.2026	9.7395	7.9132	6.8669

3.3.4.2.2 Buckling analysis

The accuracy study of present theory in predicting buckling behaviors is carried out in Table 3.27, which illustrates non-dimensional deterministic critical buckling loads with biaxial compression of Al/Al₂O₃ FGP microplates with clamped

boundary conditions on its edges. The results are reported with the side-to-thickness ratio $a/h = 20$, various values of the power-law index $p = 1, 2, 5, 10$, two porous parameters $\beta = 0$ and 0.2 , and compared to those derived from Farzam et al. [48]. It is observed that there are no significant differences between the models, it shows that the present theory is reliable in predicting buckling behaviors of FGP microplates.

Table 3.27: Normalized critical buckling loads of FGP plates with biaxial compression, $a/h = 20$ and CCCC boundary condition

β	Theory	p			
		1	2	5	10
0	Present	12.5415	9.7627	8.1499	7.3803
	IGA [48]	12.5747	9.7903	8.1821	7.4115
0.2	Present	8.7149	5.5752	3.8308	3.4123
	IGA [48]	8.7341	5.5870	3.8437	3.4270

3.3.4.3 Analysis of FGP microplates using MST

In this section [193], numerical examples with the shear function $f(x_3) = x_3 - 4x_3^3/3h^2$ ([194]) are performed to explore the deterministic and stochastic responses of FGP microplates with various BCs. The FGP microplates are expected to be made of a combination of ceramic and metal materials with mean properties as follows: Al_2O_3 ($E_c = 380 \text{ GPa}$, $\rho_c = 3800 \text{ kg/m}^3$, $\alpha_c = 7.4 \times 10^{-6} \text{ 1/C}$, $\nu_c = 0.3$), Al ($E_m = 70 \text{ GPa}$, $\rho_m = 2702 \text{ kg/m}^3$, $\alpha_m = 23 \times 10^{-6} \text{ 1/C}$, $\nu_m = 0.3$). For simplification purpose, all three length scale parameters are considered to have the same value, i.e. $l_1 = l_2 = l_3 = l$. In practice, these material length scale values should be derived mainly via experimental data. Unless special mention, square FGP microplates with three BCs (SSSS, SCSC, CCCC) are considered in numerical examples, and for convenience, the following normalized parameters are used in the computations:

$$\bar{T}_{cr} = T_{cr} \times 10^{-3} ; \bar{w} = \frac{10E_c h^3}{qa^4} u_3 \left(\frac{a}{2}, \frac{b}{2} \right); \bar{\omega} = \frac{\omega a^2}{h} \sqrt{\frac{\rho_c}{E_c}} \quad (3.54)$$

For convergence study of the present solution, Fig. 3.8 shows the normalized critical buckling temperatures \bar{T}_{cr} of Al/Al₂O₃ FGP microplates under biaxial compression with $a/h = 20$, $p = 5$, $\beta = 0.1$ and $h/l = 5$. The results are calculated with three types of BCs (SSSS, SCSC, CCCC) and the same number of series in x_1 - and x_2 -direction ($n_1 = n_2 = n$). It is observed from Fig. 3.8 that the results converge quickly for a small number of series in which the CCCC and SCSC boundary conditions having more kinematic constraints converge lower than the SSSS one. Obviously, the number of series $n = 8$ can ensure the stability and convergence of the present solution, hence this value will be used for following numerical computations.

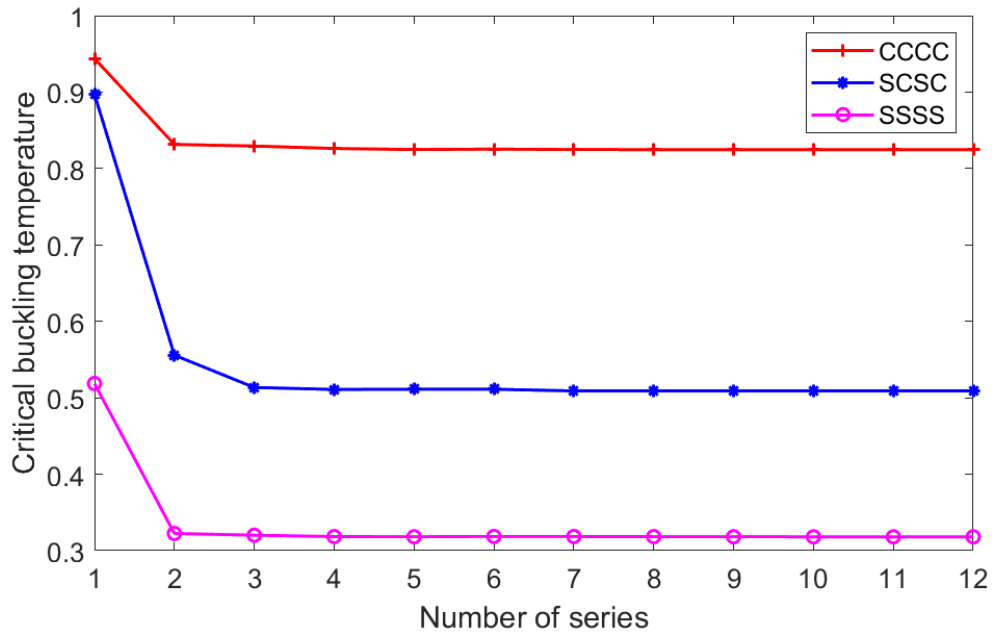


Figure 3.8: Convergence study of series solution of Al/Al₂O₃ FGP microplates with different BCs ($a/h = 20$, $p = 5$, $\beta = 0.1$, $h/l = 5$)

3.4.2.2.1 Static analysis

In order to verify the accuracy of the present FGP microplate model in predicting static behaviors, the first example is performed on the simply supported FG square

microplates subjected to sinusoidally distributed loads without porosity effect ($\beta = 0$).

Table 3.28: Normalized transverse center displacements of FGP microplates under sinusoidal load ($\beta = 0$, SSSS)

a/h	p	Theory	h/l					
			0	20	10	5	2	1
5	0.5	Present	0.5177	0.4957	0.4411	0.3065	0.1011	0.0292
		MST [191]	0.5176	0.4965	0.4426	0.3098	0.1018	0.0303
		RPT [195]	0.5198	0.4983	0.4435	0.3086	0.0997	0.0293
		IGA [190]	0.5177	0.4975	0.4457	0.3153	0.1045	0.0310
	1	Present	0.6688	0.6387	0.5625	0.3860	0.1226	0.0353
		MST [191]	0.6688	0.6399	0.5670	0.3908	0.1252	0.0369
		RPT[195]	0.6688	0.6396	0.5658	0.3879	0.1223	0.0357
		IGA[190]	0.6688	0.6412	0.5709	0.3977	0.1286	0.0378
	2	Present	0.8672	0.8261	0.7256	0.5021	0.1521	0.0442
		MST [191]	0.8671	0.8292	0.7332	0.5021	0.1580	0.0460
		RPT [195]	0.8671	0.8286	0.7313	0.4980	0.1544	0.0447
		IGA[190]	0.8671	0.8307	0.7379	0.5107	0.1627	0.0475
	4	Present	1.0411	0.9899	0.8681	0.6024	0.1898	0.0552
		MST [191]	1.0409	0.9977	0.8875	0.6159	0.1964	0.0573
		RPT[195]	1.0408	0.9967	0.8843	0.6095	0.1921	0.0558
		IGA[190]	1.0409	0.9994	0.8927	0.6263	0.2034	0.0597
	10	Present	1.2279	1.1681	1.0282	0.7443	0.2455	0.0728
		MST [191]	1.2276	1.1811	1.0609	0.7548	0.2510	0.0743
		RPT[195]	1.2269	1.1790	1.0557	0.7455	0.2454	0.0724
		IGA[190]	1.2276	1.1829	1.0668	0.7678	0.2614	0.0781
10	0.5	Present	0.4538	0.4361	0.3884	0.2747	0.0895	0.0263
		MST[191]	0.4537	0.4355	0.3887	0.2723	0.0884	0.0260
	1	Present	0.5890	0.5646	0.5003	0.3479	0.1106	0.0322
		MST[191]	0.5890	0.5640	0.5004	0.3453	0.1095	0.0320
	2	Present	0.7572	0.7258	0.6426	0.4463	0.1418	0.0412
		MST[191]	0.7573	0.7253	0.6439	0.4446	0.1407	0.0409
	4	Present	0.8814	0.8475	0.7588	0.5404	0.1797	0.0531
		MST[191]	0.8815	0.8480	0.7614	0.5405	0.1784	0.0526
	10	Present	1.0086	0.9739	0.8808	0.6497	0.2325	0.0707
		MST [191]	1.0087	0.9755	0.8879	0.6535	0.2298	0.0694

Various values of the power-law index p , length-to-thickness ratio a/h , and thickness-to-MLSP ratio h/l are considered for static responses of Al/Al₂O₃ FG microplates. The obtained results are reported in Tables 3.28 and 3.29, and compared with those derived from Thai et al. [191], Thai et al. [190] using the

MST, isogeometric approach and HSDT, Zhang et al. [195] using the MST, Navier method and HSDT. It can be seen that there are good agreement between the models for different BCs, material distribution and size effects, which shows the accuracy of present approach for static behaviors.

Table 3.29: Normalized transverse center displacements of FGP microplates under sinusoidal load with $a/h = 10$ $\beta = 0$ and different boundary conditions

BCs	p	Theory	h/l					
			0	20	10	5	2	1
CCCC	0.5	Present	0.1755	0.1677	0.1488	0.1032	0.0331	0.0099
		MST [191]	0.1747	0.1675	0.1492	0.1042	0.0340	0.0100
		IGA [190]	0.1773	-	0.1521	0.1068	0.0349	0.0103
	1	Present	0.2271	0.2165	0.1909	0.1306	0.0412	0.0121
		MST [191]	0.2261	0.2163	0.1951	0.1349	0.0419	0.0123
		IGA [190]	0.2295	-	0.1915	0.1318	0.0430	0.0126
	2	Present	0.2936	0.2794	0.2456	0.1673	0.0529	0.0158
		MST[191]	0.2922	0.2794	0.2472	0.1694	0.0532	0.0155
		IGA [190]	0.2967	-	0.2517	0.1733	0.0547	0.0159
	5	Present	0.3631	0.3452	0.3047	0.2124	0.0706	0.0211
		MST [191]	0.3609	0.3466	0.3100	0.2182	0.0712	0.0209
		IGA [190]	0.3676	-	0.3161	0.2233	0.0734	0.0216
	10	Present	0.4068	0.3873	0.3436	0.2437	0.0838	0.0252
		MST [191]	0.4041	0.3893	0.3582	0.2523	0.0854	0.0254
		IGA[190]	0.4121	-	0.3510	0.2584	0.0884	0.0265
SCSC	0.5	Present	0.2585	0.2477	0.2198	0.1514	0.0477	0.0139
		IGA [190]	0.2472	-	0.2122	0.1492	0.0488	0.0144
	1	Present	0.3349	0.3200	0.2823	0.1917	0.0591	0.0171
		IGA [190]	0.3201	-	0.2724	0.1886	0.0602	0.0176
	2	Present	0.4318	0.4126	0.3643	0.2480	0.0769	0.0221
		IGA [190]	0.4133	-	0.3513	0.2425	0.0768	0.0223
	5	Present	0.5256	0.5055	0.4540	0.3218	0.1059	0.0311
		IGA [190]	0.5086	-	0.4389	0.3118	0.1035	0.0306
	10	Present	0.5849	0.5646	0.5118	0.3720	0.1280	0.0382
		IGA [190]	0.5685	-	0.4961	0.3604	0.1246	0.0375

Table 3.30: Normalized transverse center displacements of FGP square microplates under sinusoidal load with different boundary conditions

BCs	a/h	β	p	h/l				
				∞	10	5	2	1
SSSS	10	0.1	0.5	0.5111	0.4342	0.3025	0.0962	0.0280
			1	0.6947	0.5831	0.3964	0.1218	0.0351
			2	0.9578	0.7987	0.5365	0.1622	0.0464
			5	1.2183	1.0372	0.7244	0.2345	0.0687
			10	1.3565	1.1739	0.8523	0.2968	0.0891
		0.2	0.5	0.5822	0.4903	0.3356	0.1043	0.0301
			1	0.8456	0.6983	0.4610	0.1361	0.0387
			2	1.3214	1.0690	0.6800	0.1909	0.0536
			5	1.9318	1.5884	1.0391	0.3052	0.0870
			10	2.1828	1.8440	1.2843	0.4187	0.1231
		0.1	0.5	0.2906	0.2449	0.1662	0.0512	0.0149
			1	0.3939	0.3278	0.2177	0.0653	0.0187
			2	0.5436	0.4503	0.2971	0.0882	0.0249
			5	0.7016	0.5956	0.4110	0.1301	0.0373
			10	0.7870	0.6844	0.4904	0.1641	0.0483
SCSC	10	0.2	0.5	0.3305	0.2758	0.1841	0.0552	0.0159
			1	0.4781	0.3909	0.2525	0.0729	0.0206
			2	0.7462	0.5979	0.3749	0.1033	0.0288
			5	1.1042	0.9064	0.5905	0.1675	0.0476
			10	1.2676	1.0785	0.7459	0.2348	0.0674
		0.1	0.5	0.1969	0.1640	0.1100	0.0335	0.0101
			1	0.2663	0.2191	0.1439	0.0426	0.0128
			2	0.3682	0.3012	0.1962	0.0573	0.0164
			5	0.4827	0.4036	0.2735	0.0844	0.0244
			10	0.5480	0.4671	0.3281	0.1070	0.0315
		0.2	0.5	0.2233	0.1842	0.1216	0.0362	0.0104
			1	0.3219	0.2603	0.1664	0.0475	0.0135
			2	0.5018	0.3975	0.2462	0.0676	0.0210
			5	0.7550	0.6090	0.3888	0.1106	0.0313
			10	0.8832	0.7357	0.4969	0.1526	0.0440
CCCC	10	0.1	0.5	0.1969	0.1640	0.1100	0.0335	0.0101
			1	0.2663	0.2191	0.1439	0.0426	0.0128
			2	0.3682	0.3012	0.1962	0.0573	0.0164
			5	0.4827	0.4036	0.2735	0.0844	0.0244
			10	0.5480	0.4671	0.3281	0.1070	0.0315
		0.2	0.5	0.2233	0.1842	0.1216	0.0362	0.0104
			1	0.3219	0.2603	0.1664	0.0475	0.0135
			2	0.5018	0.3975	0.2462	0.0676	0.0210
			5	0.7550	0.6090	0.3888	0.1106	0.0313
			10	0.8832	0.7357	0.4969	0.1526	0.0440

Moreover, in order to investigate effects of porosity β , material parameter p , side-to-thickness ratio a/h , size effects h/l and boundary conditions on the static responses of FGP microplates, Table 3.30 present their center transverse displacements with various configurations. The variations of center deflections with respect to a/h and h/l are also plotted in Fig. 3.9. It can be seen that the transverse displacements increase with increase of the p and h/l . The graph in Fig.

3.9b reveals that the deflections vary gradually for $h/l \leq 10$ and from $h/l = 25$ the curves become flatter and the results tend to be closed to those obtained from the classical theory ($h/l = \infty$), which explains that the size effects on deflections of FGP microplates are not significant from $h/l > 25$.

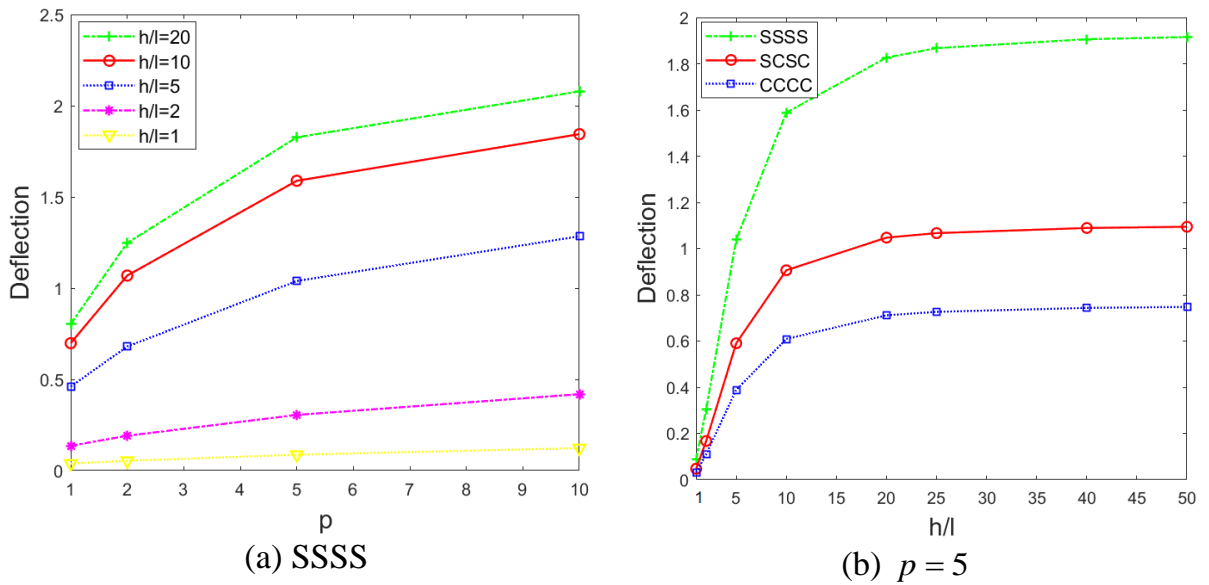


Figure 3.9: Variation of normalized center deflection with respect to the power index p and thickness-to-length scale h/l of FGP microplates ($\beta = 0.2$, $a/h = 10$)

3.4.2.2.2 Free vibration analysis

In order to study the accuracy of present solutions in predicting vibration responses, Tables 3.31-3.33 provide the fundamental frequencies of Al/Al₂O₃ FGP microplates without porosity effects ($\beta = 0$) in which the solutions are computed for various configurations. The obtained results are compared with those derived from Thai et al. [191] and Thai et al. [190] based on the MST, IGA and HSDT, Zhang et al. [195] based on the MST and Navier procedure and a refined HSDT. It can be seen that there is no discrepancy between models. The fundamental frequencies decrease with the increase of p as expected. The effect of p on the natural frequencies of Al/Al₂O₃ FGP microplates is also plotted in Fig. 3.10a for $h/l = 1, 2, 5, 10, 20$, $a/h = 10$ and $\beta = 0.2$. There exist large deviations of these curves, which indicate

significant size effects. Moreover, the variations of fundamental frequencies with respect to h/l are displayed in Fig. 3.10b. It is observed that the results decrease with the increase of h/l up to $h/l=10$ and then the curves become flatter which indicates the size effects can be neglected.

Table 3.31: Normalized fundamental frequencies $\bar{\omega} = \omega h \sqrt{\rho_c / E_c}$ of Al/Al₂O₃ FGP square microplates ($\beta = 0, a/h = 10$, SSSS)

p	Theory	h/l				
		∞	10	5	2	1
0	Present	0.0577	0.0615	0.0726	0.1250	0.2283
	MST [191]	0.0577	0.0619	0.0729	0.1254	0.2297
	RPT [195]	0.0577	0.0619	0.0730	0.1258	0.2309
	IGA[190]	0.0577	0.0617	0.0725	0.1240	0.2268
0.5	Present	0.0490	0.0529	0.0626	0.1099	0.2035
	MST [191]	0.0490	0.0529	0.0633	0.1110	0.2047
	RPT [195]	0.0489	0.0529	0.0632	0.1113	0.2057
	IGA[190]	0.0490	0.0528	0.0629	0.1098	0.2023
1	Present	0.0441	0.0475	0.0574	0.1014	0.1884
	MST [191]	0.0442	0.0479	0.0577	0.1024	0.1896
	RPT [195]	0.0442	0.0480	0.0578	0.1028	0.1907
	IGA[190]	0.0442	0.0478	0.0573	0.1013	0.1873
2	Present	0.0401	0.0431	0.0520	0.0926	0.1722
	MST [191]	0.0401	0.0435	0.0523	0.0930	0.1722
	RPT [195]	0.0401	0.0435	0.0524	0.0933	0.1731
	IGA[190]	0.0401	0.0434	0.0520	0.0918	0.1698
5	Present	0.0377	0.0403	0.0476	0.0809	0.1489
	MST [191]	0.0377	0.0404	0.0477	0.0822	0.1508
	RPT [195]	0.0377	0.0405	0.0478	0.0825	0.1514
	IGA[190]	0.0377	0.0403	0.0474	0.0810	0.1482
10	Present	0.0364	0.0388	0.0452	0.0757	0.1360
	MST [191]	0.0363	0.0387	0.0451	0.0761	0.1384
	RPT [195]	0.0364	0.0388	0.0453	0.0764	0.1390
	IGA[190]	0.0364	0.0387	0.0449	0.0750	0.1359

Table 3.32: Normalized fundamental frequencies of Al/Al₂O₃ FGP square microplates ($\beta = 0, a/h = 10$, CCCC and SCSC)

BCs	p	Theory	h/l					
			∞	20	10	5	2	1
CCCC	0.5	Present	8.4735	8.6614	9.1920	11.0307	18.9020	35.1640
		IGA [190]	8.4405	-	9.1227	10.8954	19.0701	35.1215
	1	Present	7.6782	7.8132	8.3908	10.0530	17.6636	32.3192
		IGA [190]	7.6251	-	8.2766	9.9597	17.6422	32.6292
	2	Present	6.9176	7.1106	7.5746	9.0783	15.9206	28.8231
		IGA [190]	6.8944	-	7.4923	9.0367	16.0977	29.8609
	5	Present	6.4231	6.5519	6.9710	8.3300	13.9971	25.9460
		IGA [190]	6.3722	-	6.8823	8.2026	14.3324	26.4157
	10	Present	6.1199	6.2784	6.6505	7.8617	13.0441	23.9971
		IGA [190]	6.1039	-	6.5602	7.7407	13.2706	24.2754
SCSC	0.5	Present	6.7197	6.8676	7.2931	8.7900	15.6599	29.0008
		IGA[190]	6.9031	-	7.4556	8.8961	15.5600	28.6567
	1	Present	6.0650	6.2057	6.6094	8.0210	14.4368	26.8247
		IGA[190]	6.2329	-	6.7605	8.1283	14.3915	26.6161
	2	Present	5.4955	5.6222	5.9858	7.2578	13.0467	24.2396
		IGA[190]	5.6405	-	6.1230	7.3744	13.1146	24.3082
	5	Present	5.1361	5.2381	5.5323	6.5758	11.4606	21.0871
		IGA[190]	5.2361	-	5.6429	6.7021	11.6480	21.4179
	10	Present	4.9452	5.0338	5.2903	6.2080	10.5865	19.3316
		IGA[190]	5.0254	-	5.3868	6.3288	10.7777	19.6645

In order to study further the size effects of vibration problems, Fig. 3.11 illustrates the ratio of fundamental frequencies computed from the MST over the MCT, which is expressed with respect to h/l , $p = 5$, $\beta = 0.2$, $a/h = 10$ and different boundary conditions. It can be observed that the MST with three MLSPs produces frequencies larger than the MCT with one MLSP, especially when the microplate thickness is close to the MLSP. It emphasizes the importance of the consideration of three components e.g. the dilatation, deviatoric stretch and symmetric part of rotation

gradient tensor in the MST rather than only the symmetric part of rotation gradient tensor in the MCT when dealing with microplates. As expected, by increasing the size scale, the difference between the theories is decreased.

Table 3.33: Normalized fundamental frequencies of Al/Al₂O₃ FGP square microplates

BCs	a/h	β	p	h/l				
				∞	10	5	2	1
SSSS	10	0.1	0.5	4.8469	5.2465	6.2753	11.1444	20.5884
			1	4.2815	4.6668	5.6497	10.2161	19.0334
			2	3.7640	4.1238	4.9947	9.1029	16.9999
			5	3.4574	3.6783	4.4653	7.8075	14.4907
			10	3.3327	3.5350	4.1840	7.0993	12.8651
		0.2	0.5	4.7972	5.2009	6.1126	11.1001	20.1158
			1	4.1121	4.5268	5.5541	10.0543	19.0057
			2	3.4064	3.7713	4.7471	8.9419	16.8823
			5	2.9323	3.2158	3.9832	7.3159	13.7288
			10	2.8148	3.0352	3.6550	6.4101	11.7388
		0.1	0.5	6.6598	7.2591	8.7147	15.3799	28.4118
			1	5.8920	6.4631	7.9308	14.1016	26.1753
			2	5.1741	5.6891	7.0084	12.5850	23.7134
			5	4.7171	5.1198	6.1693	10.9865	20.3606
			10	4.5305	4.8659	5.7523	9.9342	18.2235
SCSC	10	0.2	0.5	6.5990	7.1277	8.5988	15.1299	28.1844
			1	5.6709	6.2750	7.7094	14.0535	26.0222
			2	4.6990	5.2527	6.6405	12.5620	23.6336
			5	4.0124	4.4345	5.5079	10.2385	19.2228
			10	3.8229	4.1489	4.9977	8.8931	16.4769
		0.1	0.5	8.3865	9.1064	11.0009	18.7157	35.0700
			1	7.4713	8.1995	9.9376	17.5254	32.1417
			2	6.5451	7.2033	8.8372	15.7657	28.6778
			5	5.8837	6.1920	7.8150	13.3725	23.7300
			10	5.6264	6.1831	7.3008	12.0451	21.4739
		0.2	0.5	8.3202	9.1037	11.0001	18.6797	34.9638
			1	7.1684	7.9717	9.7343	17.3071	32.1207
			2	5.9501	6.6362	8.3403	15.2109	28.4556
			5	5.0257	5.6144	6.9379	11.9968	20.3562
			10	4.7414	5.2673	6.3223	10.5215	19.6228
CCCC	10	0.1	0.5	8.3865	9.1064	11.0009	18.7157	35.0700
			1	7.4713	8.1995	9.9376	17.5254	32.1417
			2	6.5451	7.2033	8.8372	15.7657	28.6778
			5	5.8837	6.1920	7.8150	13.3725	23.7300
			10	5.6264	6.1831	7.3008	12.0451	21.4739
		0.2	0.5	8.3202	9.1037	11.0001	18.6797	34.9638
			1	7.1684	7.9717	9.7343	17.3071	32.1207
			2	5.9501	6.6362	8.3403	15.2109	28.4556
			5	5.0257	5.6144	6.9379	11.9968	20.3562
			10	4.7414	5.2673	6.3223	10.5215	19.6228

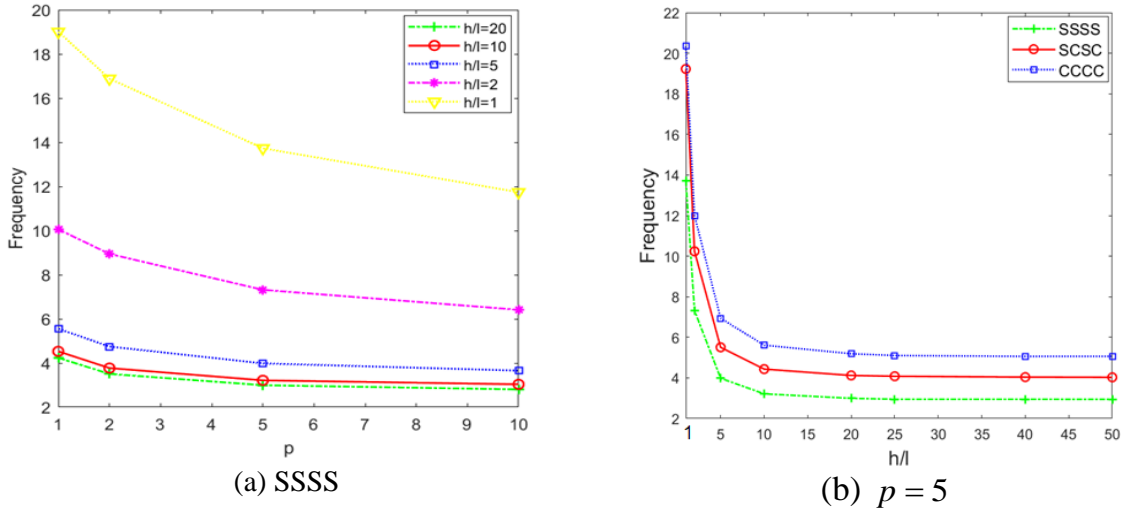


Figure 3.10: Variation of normalized fundamental frequencies with respect to the power index p and thickness-to-MLSP ratio h/l ($a/h = 10$, $\beta = 0.2$)

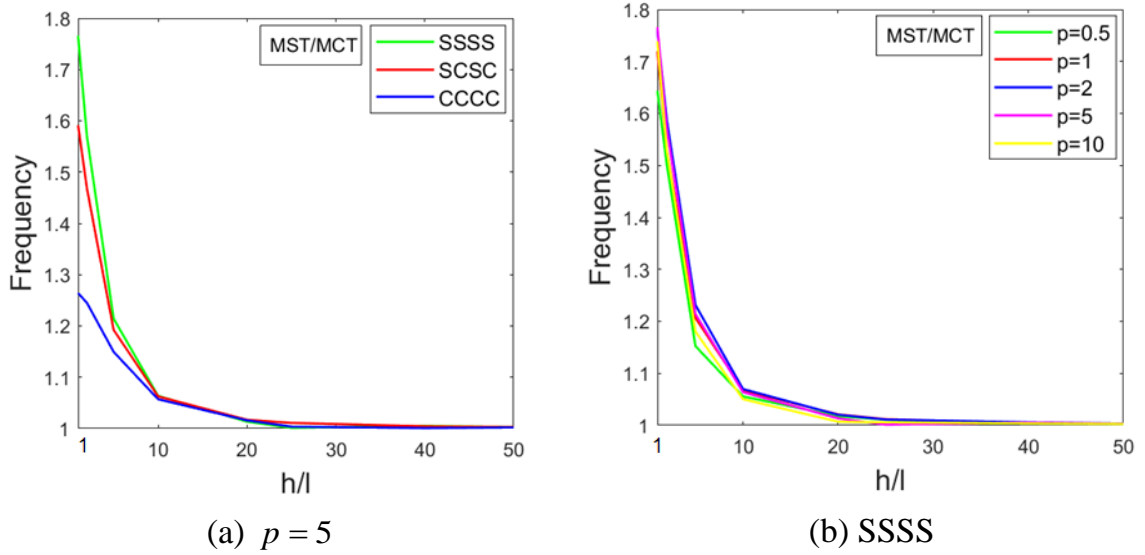


Figure 3.11: Size effect of the MCT and MST for the normalized fundamental frequencies with respect to the length scale-to-thickness ratio h/l ($\beta = 0.2$, $p = 5$, $a/h = 10$)

3.4.2.2.3 Buckling analysis

In order to verify the accuracy of present theory in predicting buckling behaviors with deterministic material properties, Table 3.34 presents normalized critical buckling loads of simply supported FGM microplates under mechanical loads in which the responses are calculated with both axial compression

$(N_1^{(m)}, N_2^{(m)}, N_{12}^{(m)} = 1, 0, 0)$ and biaxial compression $(N_1^{(m)}, N_2^{(m)}, N_{12}^{(m)} = 1, 1, 0)$,

different values of $h/l = \infty, 10, 5, 2, 1$, and no porosity effect is accounted ($\beta = 0$).

Table 3.34: Normalized critical buckling load $\bar{N}_{cr} = (N_{cr}^m a^2 / h^3 E_m)$ of Al/Al₂O₃ FGP square microplates ($\beta = 0, a/h = 10, \text{SSSS}$)

P	Theory	h/l				
		∞	10	5	2	1
Axial compression $\left(N_1^{(m)}, N_2^{(m)}, N_{12}^{(m)} = 1, 0, 0\right)$						
0.5	Present	12.1593	14.1562	20.1595	62.2324	212.5038
	MST [191]	12.1236	14.1490	20.1999	62.1669	211.1461
	RPT [195]	12.1213	14.1543	20.2387	62.6144	213.5682
	IGA [190]	12.1230	14.0850	19.9551	60.8187	206.3342
1	Present	9.3724	11.0035	15.9002	50.1979	172.6696
	MST [191]	9.3391	10.9906	15.9260	50.1870	171.9637
	RPT [195]	9.3391	10.9968	15.9590	50.5419	173.7865
	IGA [190]	9.3391	10.9375	15.7204	49.0315	167.6943
2	Present	7.2889	8.5648	12.3864	39.0974	134.4300
	MST [191]	7.2631	8.5419	12.3708	39.0731	134.2383
	RPT [195]	7.2631	8.5479	12.4000	39.3331	135.4673
	IGA [190]	7.2631	8.5479	12.4000	39.3331	135.4673
5	Present	6.0563	7.0017	9.7751	28.8861	96.9485
	MST [191]	6.0353	6.9468	9.6789	28.7840	96.9802
	RPT [195]	6.0353	6.9549	9.7100	28.9617	97.6728
	IGA [190]	6.0353	6.9131	9.5425	27.9155	93.4952
10	Present	5.4723	6.2570	8.5295	24.0504	79.2548
	MST [191]	5.4529	6.1945	8.4150	23.9178	79.2302
	RPT [195]	5.4528	6.2026	8.4445	24.0660	79.7717
	IGA [190]	5.4528	6.1674	8.3032	23.1847	76.2541
Biaxial compression $\left(N_1^{(m)}, N_2^{(m)}, N_{12}^{(m)} = 1, 1, 0\right)$						
0.5	Present	6.0800	7.0780	10.0781	31.1022	106.1940
	MST[191]	6.0618	7.0745	10.1000	31.0834	105.6232
	RPT[195]	6.0606	7.0772	10.1193	31.3072	106.7841
	IGA[190]	6.0615	7.0425	9.9775	30.4094	103.1673
1	Present	4.6865	5.5017	7.9490	25.0897	86.2975
	MST[191]	4.6696	5.4953	7.9630	25.0935	85.9820
	RPT[195]	4.6695	5.4984	7.9795	25.2710	86.8932
	IGA[190]	4.6696	5.4688	7.8602	24.5158	83.8473
2	Present	3.6447	4.2824	6.1925	19.5433	67.1946
	MST[191]	3.6315	4.2710	6.1854	19.5365	67.1192
	RPT[195]	3.6315	4.2740	6.2000	19.6665	67.7337
	IGA[190]	3.6315	4.2740	6.2000	19.6665	67.7337
10	Present	2.7363	3.1284	4.2640	12.0217	39.6153
	MST[191]	2.7264	3.0972	4.2075	11.9589	39.6151
	RPT[195]	2.7264	3.1013	4.2222	12.0330	39.8858
	IGA[190]	2.7264	3.0837	4.1516	11.5924	38.1271

These results are then compared with those reported by Thai et al. [191], Thai et al. [190], and Zhang et al. [195]. It can be seen from Table 1 that there are good agreements among models, the effects of thickness-to-MLSP ratio impacted importantly on critical buckling loads of FGM microplates. Similarly, the accuracy of the present model in predicting buckling behaviors is also verified as expected in Table 3.35 for SCSC and CCCC boundary conditions of FGM microplates.

Table 3.35: Normalized critical buckling load $\bar{N}_{cr} = (N_{cr}^m a^2 / h^3 E_m)$ of Al/Al₂O₃ FGP square microplates with axial compression $(N_1^{(m)}, N_2^{(m)}, N_{12}^{(m)} = 1, 0, 0)$, $\beta = 0$, $a/h = 10$, SCSC and CCCC boundary conditions

p	Theory	h/l				
		∞	10	5	2	1
SCSC						
0.5	Present	20.4079	23.9355	34.5293	106.2774	360.4446
	IGA [190]	20.7870	24.2336	34.4511	104.9240	355.0073
1	Present	15.7470	18.6220	27.2586	87.4220	300.6437
	IGA [190]	16.0781	18.9077	27.2924	85.1205	290.3734
2	Present	12.2120	14.4381	21.1388	68.0160	234.9042
	IGA [190]	12.4183	14.6427	21.2445	67.0440	230.0893
5	Present	10.0014	11.5889	16.3775	50.0462	170.4489
	IGA [190]	9.9661	11.6057	16.4530	50.0703	169.7890
10	Present	8.9785	10.2705	14.1665	41.5532	139.4981
	IGA [190]	8.8672	10.2203	14.1983	41.6312	139.1741
CCCC						
0.5	Present	27.2737	31.9314	45.8300	140.3232	477.7048
	IGA[190]	27.0706	31.6036	45.0313	137.6734	466.5827
1	Present	21.0949	24.8790	36.1457	114.3872	391.8628
	IGA [190]	20.9471	24.6676	35.6870	111.7391	381.8401
2	Present	16.2844	19.2023	27.8882	88.3252	302.6476
	IGA [190]	16.1682	19.0964	27.7817	88.0910	302.9154
5	Present	13.0268	15.1511	21.4006	64.5835	219.5999
	IGA [190]	12.9218	15.0971	21.5034	65.8642	223.8079
10	Present	11.5736	13.3378	18.4901	53.8684	179.6851
	IGA [190]	11.4711	13.2770	18.5512	54.7761	183.4780

Moreover, in order to investigate the effects of porosity, material distribution and boundary conditions, and size effects in mechanical buckling responses further, Table 3.36 introduces new numerical results of critical buckling loads for the FGP microplates under uniaxial compression with porous parameter $\beta = 0.1$ and 0.2 , side-to-thickness ratio $a/h = 10$, different power indices $p = 0.5, 1, 2, 5, 10$, various

values of $h/l = \infty, 10, 5, 2, 1$, and three boundary conditions (SSSS, SCSC, CCCC).

Table 3.36: Normalized critical buckling load $\bar{N}_{cr} = (N_{cr}^m a^2 / h^3 E_m)$ of Al/Al₂O₃ FGP square microplates ($a/h = 10$, SSSS), $(N_1^{(m)}, N_2^{(m)}, N_{12}^{(m)}) = (1, 0, 0)$

β	p	Theory	h/l				
			∞	10	5	2	1
SSSS							
0.1	0.5	Present	10.7948	12.6701	18.3088	57.8304	198.9871
	1	Present	7.9448	9.4448	13.9488	45.4984	158.1497
	2	Present	5.7630	6.8953	10.2914	34.0529	118.8672
	5	Present	4.5302	5.3182	7.6301	23.5858	80.4325
	10	Present	4.0691	4.6990	6.5045	18.7935	62.4979
0.2	0.5	Present	9.4762	11.2247	16.4823	53.3286	184.9203
	1	Present	6.5272	7.8908	11.9841	40.6488	142.9793
	2	Present	4.1773	5.1601	8.1107	28.7696	102.5064
	5	Present	2.8570	3.4750	5.2956	17.9166	62.9178
	10	Present	2.5287	2.9923	4.2978	13.1640	44.7111
SCSC							
0.1	0.5	Present	18.1615	21.4830	31.4557	100.8126	346.1531
	1	Present	13.3906	16.0431	24.0094	79.4346	275.5905
	2	Present	9.6990	11.6851	17.6630	59.4432	208.0289
	5	Present	7.5049	8.8335	12.8445	41.0540	141.9227
	10	Present	6.6698	7.6989	10.8027	32.6080	110.5416
0.2	0.5	Present	15.9821	19.0868	28.4059	93.1467	321.8675
	1	Present	11.0405	13.4593	20.7214	71.1660	249.3802
	2	Present	7.0742	8.8085	14.0286	50.4483	179.7521
	5	Present	4.7670	5.8212	9.0096	31.4459	111.6549
	10	Present	4.1405	4.8922	7.1593	23.0534	79.7902
CCCC							
0.1	0.5	Present	24.3601	28.7527	41.8178	132.4741	453.8002
	1	Present	18.0333	21.5132	31.8839	103.7666	358.2498
	2	Present	13.0317	15.6155	23.3124	76.7932	264.9759
	5	Present	9.8266	11.5830	16.7471	52.3538	179.5735
	10	Present	8.5850	9.9884	14.0572	41.8132	123.2950
0.2	0.5	Present	21.5197	25.6169	37.8204	122.3423	421.5245
	1	Present	14.9569	18.1229	27.5534	92.7331	322.8644
	2	Present	9.6040	11.8409	18.4980	64.5556	221.4257
	5	Present	6.3170	7.6725	11.6563	38.6637	132.2340
	10	Present	5.3232	6.3350	9.2270	26.8966	92.8254

The variation of normalized critical buckling loads with respect to p and h/l is also plotted in Figs. 3.12 and 3.13. It is observed that the critical buckling loads

decrease with an increase of the power-law index p , porosity parameter β and thickness-to-MLSP ratio h/l . This phenomena can be explained by the fact that the increase of p , β and h/l leads to the decrease of stiffness of the FGP microplates. It is interesting to see that the size effects of FGP microplates are importantly significant from $h/l < 20$ for both FGM microplates ($\beta = 0$) and FGP microplates ($\beta = 0.1, 0.2$). Fig. 3.13 also shows that the porosity effect does not impact significantly on the size effects of FGP microplates.

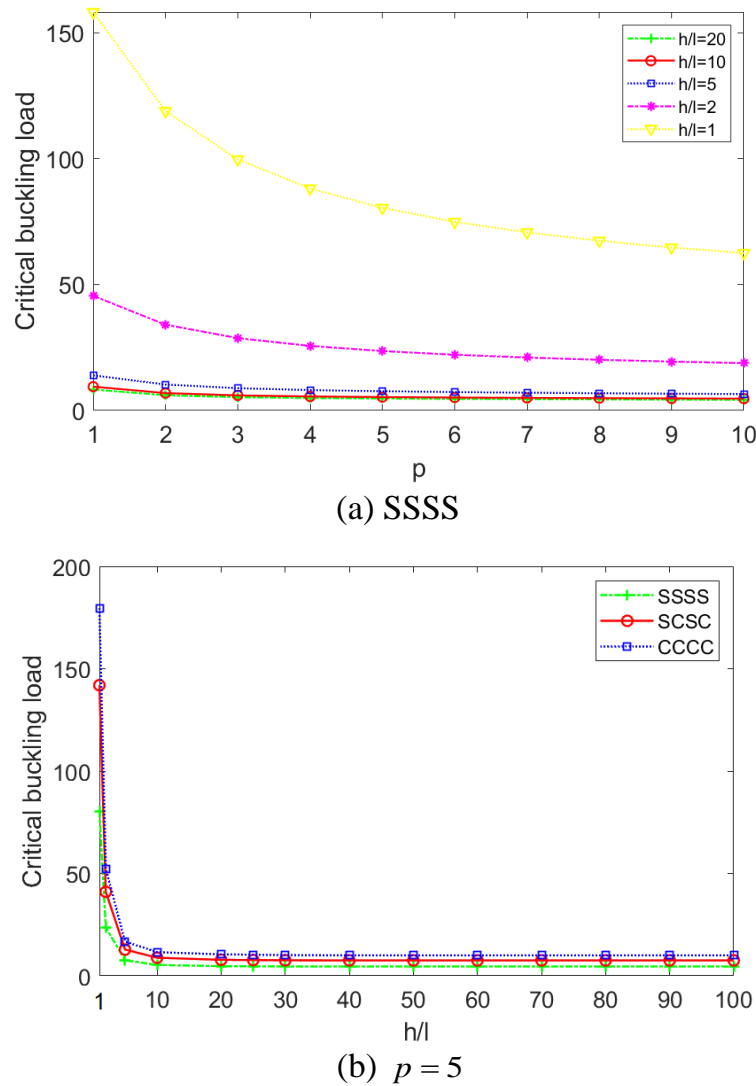


Figure 3.12: Variation of normalized critical buckling load for axial compression with respect the power index p and length scale-to-thickness ratio h/l ($a/h=10$, $\beta=0.1$)

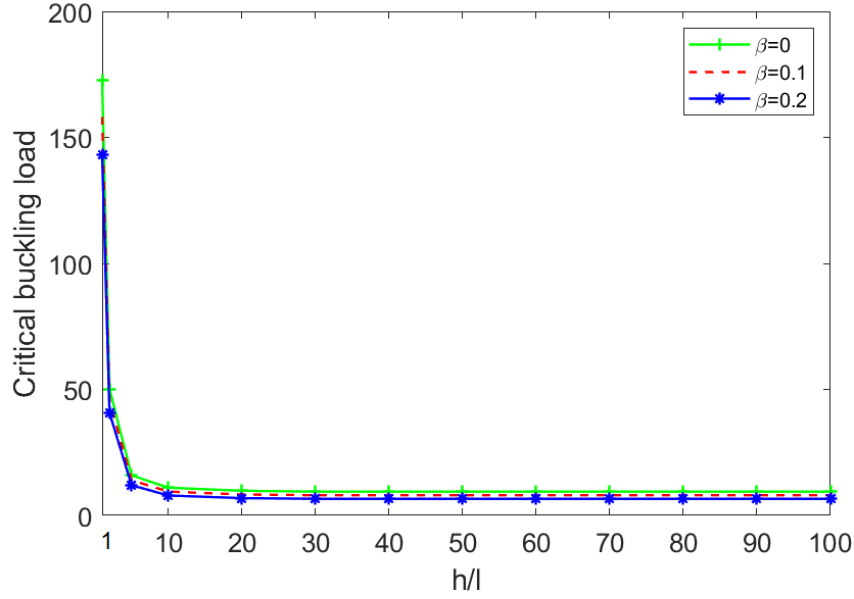
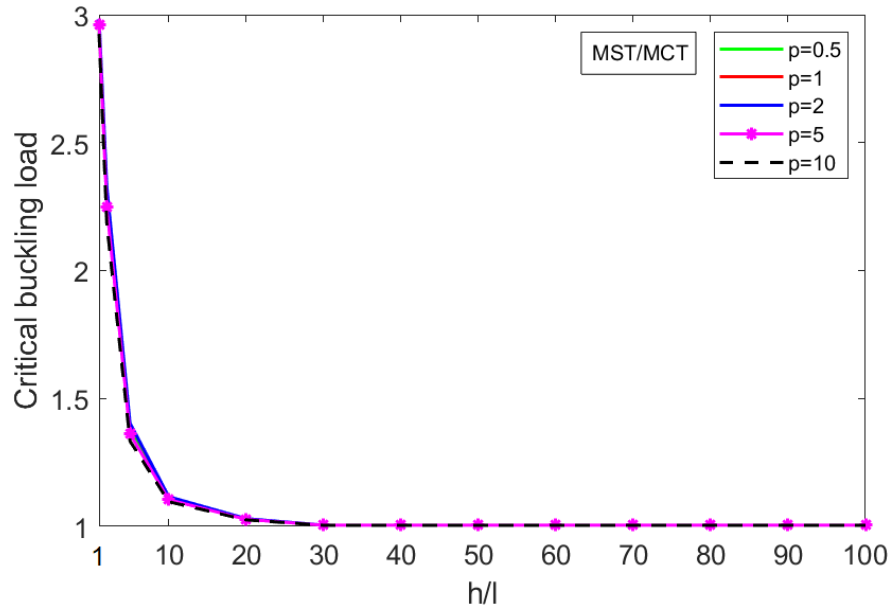
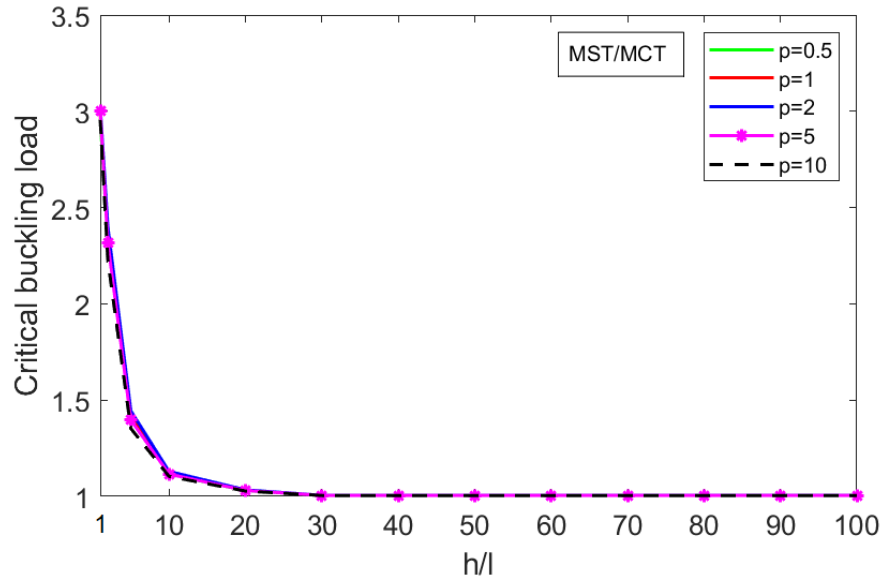


Figure 3.13: Size effect of the MST for the normalized critical buckling load with respect to the length scale-to-thickness ratio h/l under simply supported and axial compression, $a/h=10$, and power – law index $p=1$

In order to examine the size effects of FGP microplates further, Figs. 3.14 and 3.15 provide the variation of the proportion of critical buckling loads derived from the MST and MCT with respect to h/l . The results are computed for FGP microplates with $a/h=10$, $\beta=0.2$, $p=1$ and different boundary conditions. Three curves are observed in which the highest and lowest curves correspond to the SSSS and CCCC boundary conditions, respectively. It is clear from these graphs that the MST with three MLSPs generates the critical buckling loads much larger than the MCT with one MLSP, especially when the MLSP is close to the microplate thickness. As seen in Figs 3.14 and 3.15, for $h/l=1$ and SSSS boundary condition, the critical buckling loads obtained from the MST is greater three times than those from the MCT. The difference between these theories are sharply decreased up to $h/l=20$ from which the size effects can be neglected. It underlines how crucial it is to take into account three MLSPs while dealing with microplate problems.



(a) $\beta = 0$



(b) $\beta = 0.2$

Figure 3.14: Size effect of the MCT and MST for the normalised critical buckling load with respect to the length scale-to-thickness ratio h/l under simply supported and axial compression, $a/h=10$

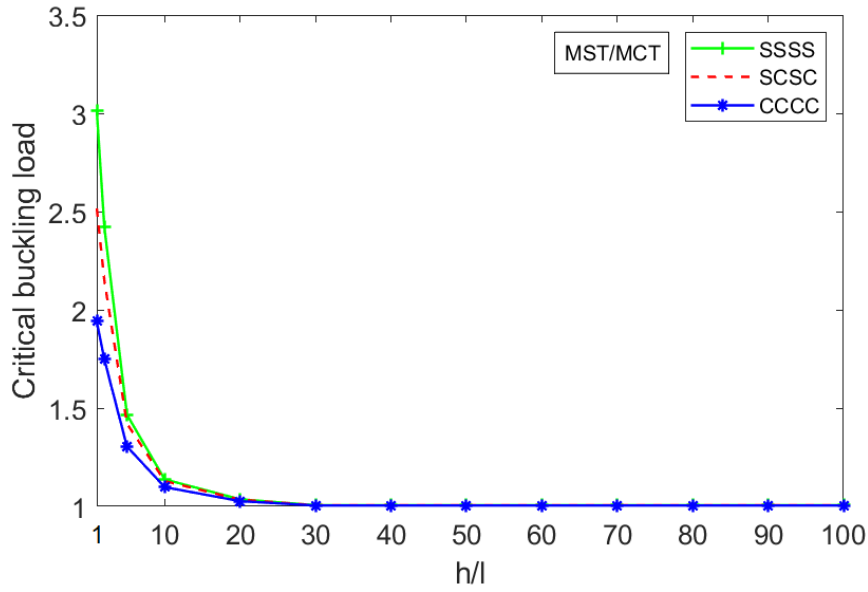


Figure 3.15: The normalized critical buckling under impacting size effect of the MST and MCT with axial compression, $a/h=10$, $\beta=0.2$, $p=1$

The next example is to consider deterministic critical buckling temperatures. Tables 3.37 - 3.39 present normalized critical buckling temperatures of FGP microplates with three types of temperature distribution (UTR, LTR, NLTR), $a/h=20$, $p=0,1,5,10$ and $h/l=\infty, 10, 5, 2, 1$. For verification purpose, the obtained critical buckling temperatures for FGM plates without porous parameters ($\beta=0$) and size effect are compared to those provided by Zenkour et al. ([196]), Yaghoobi et al. [197]. It is seen that there are good agreements among the models. The porosity and size effects on critical buckling temperatures reporting new numerical results are presented in Tables 3.37 – 3.39 and will be used as benchmarks for future researches. Figs. 3.16- 3.18 also display the variation of the critical buckling temperature with respect to the power-law index p , porosity parameter β , different temperature distributions (UTR, LTR, NLTR) and boundary conditions. It is interesting to observe from these graphs that the critical buckling temperatures increase with the porosity parameter β , this can be explained by the fact that an increase of the porous parameter led to the increase of the thermal conductivity coefficient and therefore it requires a higher critical buckling load.

Table 3.37: Normalized thermal critical buckling load \bar{T}_{cr} of Al/Al₂O₃ FGP square microplates with biaxial compression $(N_1^{(tr)}, N_2^{(tr)}, N_{12}^{(tr)} = 1, 1, 0)$ and $a/h = 20$ under uniform distribution

BCs		p	Theory	h/l				
				∞	10	5	2	1
SSSS								
$\beta = 0$	0	Present	0.4218	0.4835	0.6691	1.9704	6.6189	
		HSDT [196]	0.4215	-	-	-	-	
	1	Present	0.1964	0.2303	0.3324	1.0482	3.6054	
		HSDT [196]	0.1962	-	-	-	-	
	5	Present	0.1786	0.2046	0.2823	0.8242	2.7581	
		HSDT [196]	0.1785	-	-	-	-	
$\beta = 0.1$	10	Present	0.1834	0.2073	0.2784	0.7736	2.5401	
		HSDT [196]	0.1831	-	-	-	-	
	0	Present	0.5437	0.6265	0.8758	2.6239	8.8690	
		Present	0.2206	0.2622	0.3871	1.2629	4.3917	
	5	Present	0.1930	0.2244	0.3182	0.9728	3.3096	
		Present	0.2067	0.2354	0.3207	0.9130	3.0261	
$\beta = 0.2$	10	Present	0.2067	0.2354	0.3207	0.9130	3.0261	
		Present	0.7513	0.8705	1.2289	3.7427	12.7232	
	1	Present	0.2494	0.3015	0.4583	1.5576	5.4844	
		Present	0.1924	0.2318	0.3496	1.1726	4.1113	
	5	Present	0.1924	0.2318	0.3496	1.1726	4.1113	
		Present	0.2235	0.2596	0.3663	1.1071	3.7505	
SCSC								
$\beta = 0$	0	Present	0.6778	0.7785	1.0805	3.1951	10.7448	
	1	Present	0.3161	0.3716	0.5381	1.7036	5.8633	
	5	Present	0.2865	0.3282	0.4532	1.3291	4.4592	
	10	Present	0.2936	0.3317	0.4458	1.2450	4.1022	
$\beta = 0.1$	0	Present	0.8743	1.0093	1.4151	4.2562	14.4002	
	1	Present	0.3554	0.4233	0.6271	2.0541	7.1462	
	5	Present	0.3098	0.3601	0.5112	1.5695	5.3516	
	10	Present	0.3310	0.3764	0.5129	1.4686	4.8856	
$\beta = 0.2$	0	Present	1.2081	1.4029	1.9864	6.0725	20.6616	
	1	Present	0.4020	0.4873	0.7434	2.5356	8.9306	
	5	Present	0.3092	0.3726	0.5627	1.8936	6.6505	
	10	Present	0.3577	0.4146	0.5853	1.7804	6.0543	
CCCC								
$\beta = 0.0$	0	Present	1.0893	1.2534	1.7454	5.1862	17.4462	
	1	Present	0.5092	0.5997	0.8710	2.7683	9.5260	
	5	Present	0.4587	0.5266	0.7303	2.1551	7.2379	
	10	Present	0.4691	0.5310	0.7169	2.0168	6.6553	
$\beta = 0.1$	0	Present	1.4057	1.6260	2.2871	6.9105	23.3840	
	1	Present	0.5731	0.6839	1.0162	3.3393	11.6128	
	5	Present	0.4965	0.5786	0.8248	2.5465	8.6892	
	10	Present	0.5285	0.6026	0.8249	2.3793	7.9270	
$\beta = 0.2$	0	Present	1.9443	2.2614	3.2123	9.8621	33.5549	
	1	Present	0.6491	0.7883	1.2057	4.1243	14.5162	
	5	Present	0.4969	0.6002	0.9100	3.0767	10.8067	
	10	Present	0.5710	0.6638	0.9419	2.8862	9.8272	

Table 3.38: Normalized thermal critical buckling load \bar{T}_{cr} of Al/Al₂O₃ FGP square microplates with biaxial compression ($N_1^{(tr)}, N_2^{(tr)}, N_{12}^{(tr)} = 1, 1, 0$) and $a/h = 20$ under linear temperature distribution

BCs		p	Theory	h/l					
				∞	10	5	2	1	
SSSS									
$\beta = 0$	0	Present	0.8325	0.9543	1.3206	3.8889	13.0637		
		HSDT [196]	0.8330	-	-	-	-		
	1	Present	0.3638	0.4266	0.6157	1.9416	6.6783		
		HSDT [196]	0.3587	-	-	-	-		
	5	Present	0.3040	0.3483	0.4804	1.4026	4.6940		
		HSDT [196]	0.2987	-	-	-	-		
$\beta = 0.1$	10	Present	0.3213	0.3632	0.4879	1.3556	4.4515		
		HSDT [196]	0.3156	-	-	-	-		
	0	Present	1.0730	1.2366	1.7286	5.1788	17.5047		
		Present	0.4050	0.4813	0.7106	2.3183	8.0619		
	5	Present	0.3141	0.3652	0.5178	1.5831	5.3857		
		Present	0.3468	0.3949	0.5379	1.5314	5.0761		
$\beta = 0.2$	10	Present	1.4829	1.7181	2.4255	7.3868	25.1115		
		Present	0.4521	0.5467	0.8310	2.8240	9.9438		
	5	Present	0.3095	0.3488	0.5261	1.7647	6.1874		
		Present	0.3436	0.3992	0.5633	1.7023	5.7669		
	SCSC								
	$\beta = 0$	0	Present	1.3378	1.5366	2.1325	6.3061	21.2068	
Present			0.5856	0.6883	0.9967	3.1556	10.8606		
5		Present	0.4876	0.5585	0.7713	2.2619	7.5890		
		Present	0.5146	0.5812	0.7812	2.1818	7.1888		
$\beta = 0.1$		10	Present	1.7258	1.9921	2.7929	8.4005	28.4214	
			Present	0.6524	0.7771	1.1513	3.7707	13.1183	
	5	Present	0.5041	0.5860	0.8319	2.5540	8.7086		
		Present	0.5552	0.6315	0.8604	2.4634	8.1952		
	$\beta = 0.2$	10	Present	2.3846	2.7688	3.9205	11.9852	40.7795	
			Present	0.7289	0.8836	1.3478	4.5974	16.1921	
5		Present	0.4953	0.5607	0.8468	2.8499	10.0089		
		Present	0.5501	0.6375	0.9000	2.7376	9.3093		
CCCC									
$\beta = 0.0$		0	Present	2.1500	2.4738	3.4449	10.2358	34.4334	
	Present		0.9432	1.1108	1.6134	5.1277	17.6450		
	5	Present	0.7806	0.8962	1.2429	3.6677	12.3179		
		Present	0.8220	0.9306	1.2564	3.5343	11.6630		
	$\beta = 0.1$	10	Present	2.7744	3.2092	4.5141	13.6392	46.1527	
			Present	1.0521	1.2554	1.8654	6.1301	21.3176	
5		Present	0.8079	0.9416	1.3422	4.1440	14.1401		
		Present	0.8865	1.0109	1.3838	3.9911	13.2970		
$\beta = 0.2$		10	Present	3.8373	4.4632	6.3400	19.4646	66.2268	
			Present	1.1769	1.4292	2.1860	7.4777	26.3194	
	5	Present	0.7878	0.9033	1.3695	4.6303	16.2639		
		Present	0.8779	1.0207	1.4484	4.4380	15.1107		

Table 3.39: Normalized thermal critical buckling load \bar{T}_{cr} of Al/Al₂O₃ FGP square microplates with biaxial compression $(N_1^{(tr)}, N_2^{(tr)}, N_{12}^{(tr)} = 1, 1, 0)$ and $a/h = 20$ under nonlinear temperature distribution

BCs	p	Theory	h/l				
			∞	10	5	2	1
SSSS							
$\beta = 0$	0	Present	0.8436	0.9670	1.3382	3.9407	13.2379
		FSDT [197]	0.8330	-	-	-	-
	1	Present	0.6554	0.7687	1.1094	3.4982	12.0321
		FSDT [197]	0.3746	-	-	-	-
	5	Present	0.4326	0.4955	0.6836	1.9956	6.6784
		FSDT [197]	0.3746	-	-	-	-
$\beta = 0.1$	0	Present	0.4042	0.4569	0.6137	1.7051	5.5989
		FSDT [197]	0.3660	-	-	-	-
	1	Present	1.0873	1.2531	1.7517	5.2479	17.7381
		FSDT [197]	0.7327	0.8706	1.2855	4.1939	14.5842
	5	Present	0.4449	0.5173	0.7335	2.2425	7.6292
		FSDT [197]	0.4347	0.4951	0.6744	1.9199	6.3640
$\beta = 0.2$	0	Present	0.4347	0.4951	0.6744	1.9199	6.3640
		FSDT [197]	0.4042	0.4569	0.6137	1.7051	5.5989
	1	Present	1.5027	1.7410	2.4579	7.4853	25.4463
		FSDT [197]	0.8232	0.9954	1.5131	5.1421	18.1060
	5	Present	0.8232	0.9954	1.5131	5.1421	18.1060
		FSDT [197]	0.4372	0.4907	0.7401	2.4824	8.7039
SCSC							
$\beta = 0$	0	Present	0.4283	0.4976	0.7020	2.1216	7.1875
		FSDT [197]	0.4283	0.4976	0.7020	2.1216	7.1875
	1	Present	1.3557	1.5569	2.1610	6.3902	21.4896
		FSDT [197]	1.0550	1.2402	1.7957	5.6854	19.5674
	5	Present	0.6937	0.7946	1.0974	3.2182	10.7974
		FSDT [197]	0.6473	0.7311	0.9826	2.7443	9.0419
$\beta = 0.1$	0	Present	0.6473	0.7311	0.9826	2.7443	9.0419
		FSDT [197]	1.7486	2.0186	2.8301	8.5125	28.8004
	1	Present	1.7486	2.0186	2.8301	8.5125	28.8004
		FSDT [197]	1.1802	1.4058	2.0827	6.8214	23.7315
	5	Present	1.1802	1.4058	2.0827	6.8214	23.7315
		FSDT [197]	0.7141	0.8301	1.1785	3.6179	12.3362
$\beta = 0.2$	0	Present	0.6960	0.7917	1.0787	3.0884	10.2745
		FSDT [197]	0.6960	0.7917	1.0787	3.0884	10.2745
	1	Present	2.4162	2.8058	3.9728	12.1451	41.3232
		FSDT [197]	1.3272	1.6089	2.4541	8.3710	29.4832
	5	Present	1.3272	1.6089	2.4541	8.3710	29.4832
		FSDT [197]	0.6976	0.7987	1.1912	4.0090	14.0796
CCCC							
$\beta = 0.0$	0	Present	0.6856	0.7946	1.1217	3.4120	11.6025
		FSDT [197]	0.6856	0.7946	1.1217	3.4120	11.6025
	1	Present	2.1787	2.5067	3.4908	10.3723	34.8925
		FSDT [197]	1.6994	2.0013	2.9068	9.2386	31.7907
	5	Present	1.1107	1.2751	1.7684	5.2183	17.5254
		FSDT [197]	1.0341	1.1705	1.5802	4.4453	14.6694
$\beta = 0.1$	0	Present	1.0341	1.1705	1.5802	4.4453	14.6694
		FSDT [197]	2.8114	3.2520	4.5743	13.8211	46.7680
	1	Present	2.8114	3.2520	4.5743	13.8211	46.7680
		FSDT [197]	1.9033	2.2712	3.3745	11.0895	38.5645
	5	Present	1.9033	2.2712	3.3745	11.0895	38.5645
		FSDT [197]	1.1445	1.3338	1.9013	5.8702	20.0301
$\beta = 0.2$	0	Present	1.1114	1.2674	1.7348	5.0036	16.6705
		FSDT [197]	1.1114	1.2674	1.7348	5.0036	16.6705
	1	Present	3.8886	4.5227	6.4246	19.7241	67.1098
		FSDT [197]	1.2290	2.6023	3.9804	13.6157	47.9233
	5	Present	1.2290	2.6023	3.9804	13.6157	47.9233
		FSDT [197]	1.1218	1.2907	1.9265	6.5135	22.8785
CCCC							
$\beta = 0.0$	0	Present	1.0944	1.2722	1.8052	5.5312	18.8330
		FSDT [197]	1.0944	1.2722	1.8052	5.5312	18.8330
	1	Present	2.1787	2.5067	3.4908	10.3723	34.8925
		FSDT [197]	1.6994	2.0013	2.9068	9.2386	31.7907
	5	Present	1.1107	1.2751	1.7684	5.2183	17.5254
		FSDT [197]	1.0341	1.1705	1.5802	4.4453	14.6694
$\beta = 0.1$	0	Present	1.0341	1.1705	1.5802	4.4453	14.6694
		FSDT [197]	2.8114	3.2520	4.5743	13.8211	46.7680
	1	Present	2.8114	3.2520	4.5743	13.8211	46.7680
		FSDT [197]	1.9033	2.2712	3.3745	11.0895	38.5645
	5	Present	1.9033	2.2712	3.3745	11.0895	38.5645
		FSDT [197]	1.1445	1.3338	1.9013	5.8702	20.0301
$\beta = 0.2$	0	Present	1.1114	1.2674	1.7348	5.0036	16.6705
		FSDT [197]	1.1114	1.2674	1.7348	5.0036	16.6705
	1	Present	3.8886	4.5227	6.4246	19.7241	67.1098
		FSDT [197]	1.2290	2.6023	3.9804	13.6157	47.9233
	5	Present	1.2290	2.6023	3.9804	13.6157	47.9233
		FSDT [197]	1.1218	1.2907	1.9265	6.5135	22.8785
CCCC							
$\beta = 0.0$	0	Present	1.0944	1.2722	1.8052	5.5312	18.8330
		FSDT [197]	1.0944	1.2722	1.8052	5.5312	18.8330
	1	Present	2.1787	2.5067	3.4908	10.3723	34.8925
		FSDT [197]	1.6994	2.0013	2.9068	9.2386	31.7907
	5	Present	1.1107	1.2751	1.7684	5.2183	17.5254
		FSDT [197]	1.0341	1.1705	1.5802	4.4453	14.6694
$\beta = 0.1$	0	Present	1.0341	1.1705	1.5802	4.4453	14.6694
		FSDT [197]	2.8114	3.2520	4.5743	13.8211	46.7680
	1	Present	2.8114	3.2520	4.5743	13.8211	46.7680
		FSDT [197]	1.9033	2.2712	3.3745	11.0895	38.5645
	5	Present	1.9033	2.2712	3.3745	11.0895	38.5645
		FSDT [197]	1.1445	1.3338	1.9013	5.8702	20.0301
$\beta = 0.2$	0	Present	1.1114	1.2674	1.7348	5.0036	16.6705
		FSDT [197]	1.1114	1.2674	1.7348	5.0036	16.6705
	1	Present	3.8886	4.5227	6.4246	19.7241	67.1098
		FSDT [197]	1.2290	2.6023	3.9804	13.6157	47.9233
	5	Present	1.2290	2.6023	3.9804	13.6157	47.9233
		FSDT [197]	1.1218	1.2907	1.9265	6.5135	22.8785
CCCC							
$\beta = 0.0$	0	Present	1.0944	1.2722	1.8052	5.5312	18.8330
		FSDT [197]	1.0944	1.2722	1.8052	5.5312	18.8330
	1	Present	2.1787	2.5067	3.4908	10.3723	34.8925
		FSDT [197]	1.6994	2.0013	2.9068	9.2386	31.7907
	5	Present	1.1107	1.2751	1.7684	5.2183	17.5254
		FSDT [197]	1.0341	1.1705	1.5802	4.4453	14.6694
$\beta = 0.1$	0	Present	1.0341	1.1705	1.5802	4.4453	14.6694
		FSDT [197]	2.8114	3.2520	4.5743	13.8211	46.7680
	1	Present	2.8114	3.2520	4.5743	13.8211	46.7680
		FSDT [197]	1.9033	2.2712	3.3745	11.0895	38.5645
	5	Present	1.9033	2.2712	3.3745	11.0895	38.5645
		FSDT [197]	1.1445	1.3338	1.9013	5.8702	20.0301
$\beta = 0.2$	0	Present	1.1114	1.2674	1.7348	5.0036	16.6705
		FSDT [197]	1.1114	1.2674	1.7348	5.0036	16.6705
	1	Present	3.8886	4.5227	6.4246	19.7241	67.1098
		FSDT [197]	1.2290	2.6023	3.9804	13.6157	47.9233
	5	Present	1.2290	2.6023	3.9804	13.6157	47.9233
		FSDT [197]	1.1218	1.2907	1.9265	6.5135	22.8785
CCCC							
$\beta = 0.0$	0	Present	1.0944	1.2722	1.8052	5.5312	18.8330
		FSDT [197]	1.0944	1.2722	1.8052	5.5312	18.8330
	1	Present	2.1787	2.5067	3.4908	10.3723	34.8925
		FSDT [197]	1.6994	2.0013	2.9068	9.2386	31.7907
	5	Present	1.1107	1.2751	1.7684	5.2183	17.5254
		FSDT [197]	1.0341	1.1705	1.5802	4.4453	14.6694
$\beta = 0.1$	0	Present	1.0341	1.1705	1.5802	4.4453	14.6694
		FSDT [197]	2.8114	3.2520	4.5743	13.8211	46.7680
	1	Present	2.8114	3.2520	4.5743	13.8211	46.7680
		FSDT [197]	1.9033	2.2712	3.3745	11.0895	38.5645
	5	Present	1.9033	2.2712	3.3745	11.0895	38.5645
		FSDT [197]	1.1445	1.3338	1.9013	5.8702	20.0301
$\beta = 0.2$	0	Present	1.1114	1.2674	1.7348	5.0036	16.6705
		FSDT [197]	1.1114	1.2674	1.7348	5.0036	16.6705
	1	Present	3.8886	4.5227	6.4246	19.7241	67.1098
		FSDT [197]	1.2290	2.6023	3.9804	13.6157	47.9233
	5	Present	1.2290	2.6023	3.9804	13.6157	47.9233
		FSDT [197]	1.1218	1.2907	1.9265	6.5135	22.8785
CCCC							
$\beta = 0.0$	0	Present	1.0944	1.2722	1.8052	5.5312	18.8330
		FSDT [197]	1.0944	1.2722	1.8052	5.5312	18.8330
	1	Present	2.1787	2.5067	3.4908	10.3723	34.8925
		FSDT [197]	1.6994	2.0013	2.9068	9.2386	31.7907
	5	Present	1.1107	1.2751	1.7684	5.2183	17.5254
		FSDT [197]	1.0341	1.1705	1.5802	4.4453	14.6694
$\beta = 0.1$	0	Present	1.0341	1.1705	1.5802	4.4453	14.6694
		FSDT [197]	2.8114	3.2520	4.5743	13.8211	46.7680
	1	Present	2.8114	3.2520	4.5743	13.8211	46.7680
		FSDT [197]	1.9033	2.2712	3.3745	11.0895	38.5645
	5	Present	1.9033	2.2712	3.3745	11.0895	38.5645
		FSDT [197]	1.1445	1.3338	1.9013	5.8702	20.0301
$\beta = 0.2$	0	Present	1.1114	1.2674	1.7348	5.0036	16.6705
		FSDT [197]	1.1114	1.2674	1.7348	5.0036	16.6705
	1	Present	3.8886	4.5227	6.4246	19.7241	67.1098
		FSDT [197]	1.2290	2.6023	3.9804	13.6157	47.9233
	5	Present	1.2290	2.6023	3.9804	13.6157	47.9233
		FSDT [197]	1.1218	1.2907	1.9265	6.5135	22.8785
CCCC							
$\beta = 0.0$	0	Present	1.0944	1.2722	1.8052	5.5312	18.8330
		FSDT [197]	1.0944	1.2722	1.8052	5.5312	18.8330
	1	Present	2.1787	2.5067	3.4908	10.3723	34.8925
		FSDT [197]	1.6994	2.0013	2.9068	9.2386	31.7907
	5	Present	1.1107	1.2751	1.7684	5.2183	17.5254
		FSDT [197]	1.0341	1.1705	1.5802	4.4453	14.6694
$\beta = 0.1$	0	Present	1.0341	1.1705	1.5802	4.4453	14.6694
		FSDT [197]	2.8114	3.2520	4.5743	13.8211	46.7680
	1	Present	2.8114	3.2520	4.5743	13.8211	46.7680
		FSDT [197]	1.9033	2.2712	3.3745	11.0895	38.5645
	5	Present	1.9033	2.2712	3.3745	11.0895	38.5645
		FSDT [197]	1.1445	1.3338	1.9013	5.8702	20.0301
$\beta = 0.2$	0	Present	1.1114	1.2674	1.7348	5.0036	16.6705
		FSDT [197]	1.1114	1.2674	1.7348	5.0036	16.6705
	1	Present	3.8886	4.5227	6.4246	19.7241	67.1098
		FSDT [197]	1.2290	2.6023	3.9804	13.6157	47.9233
	5	Present	1.2290	2.6023	3.9804	13.6157	47.

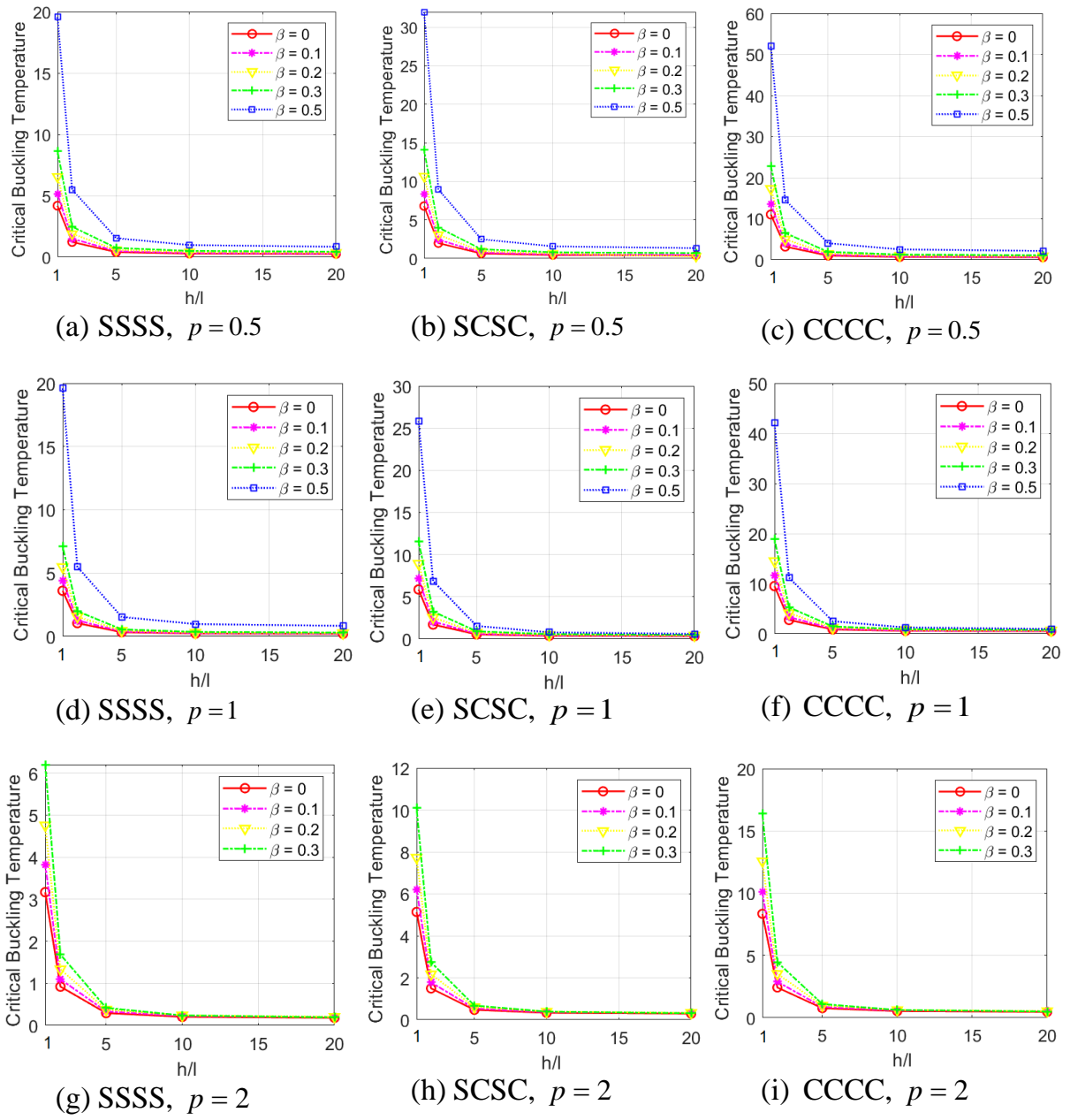


Figure 3.16: Variation of normalized thermal buckling load with respect to the length scale-to-thickness ratio h/l ($a/h = 20$) with biaxial compression under uniform distribution

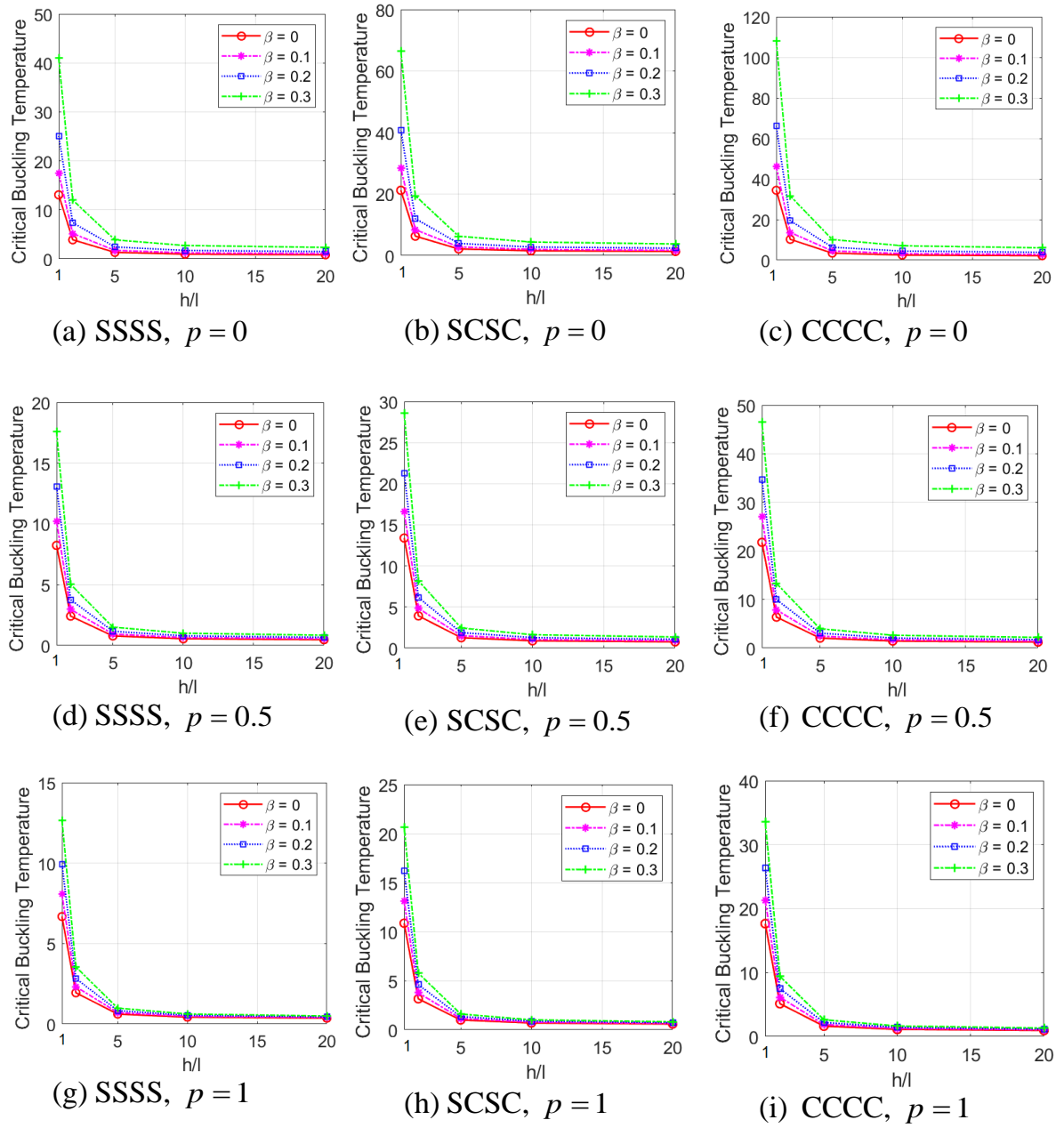


Figure 3.17: Variation of normalized thermal buckling load with respect the length scale-to-thickness ratio h/l ($a/h = 20$) with biaxial compression under linear distribution

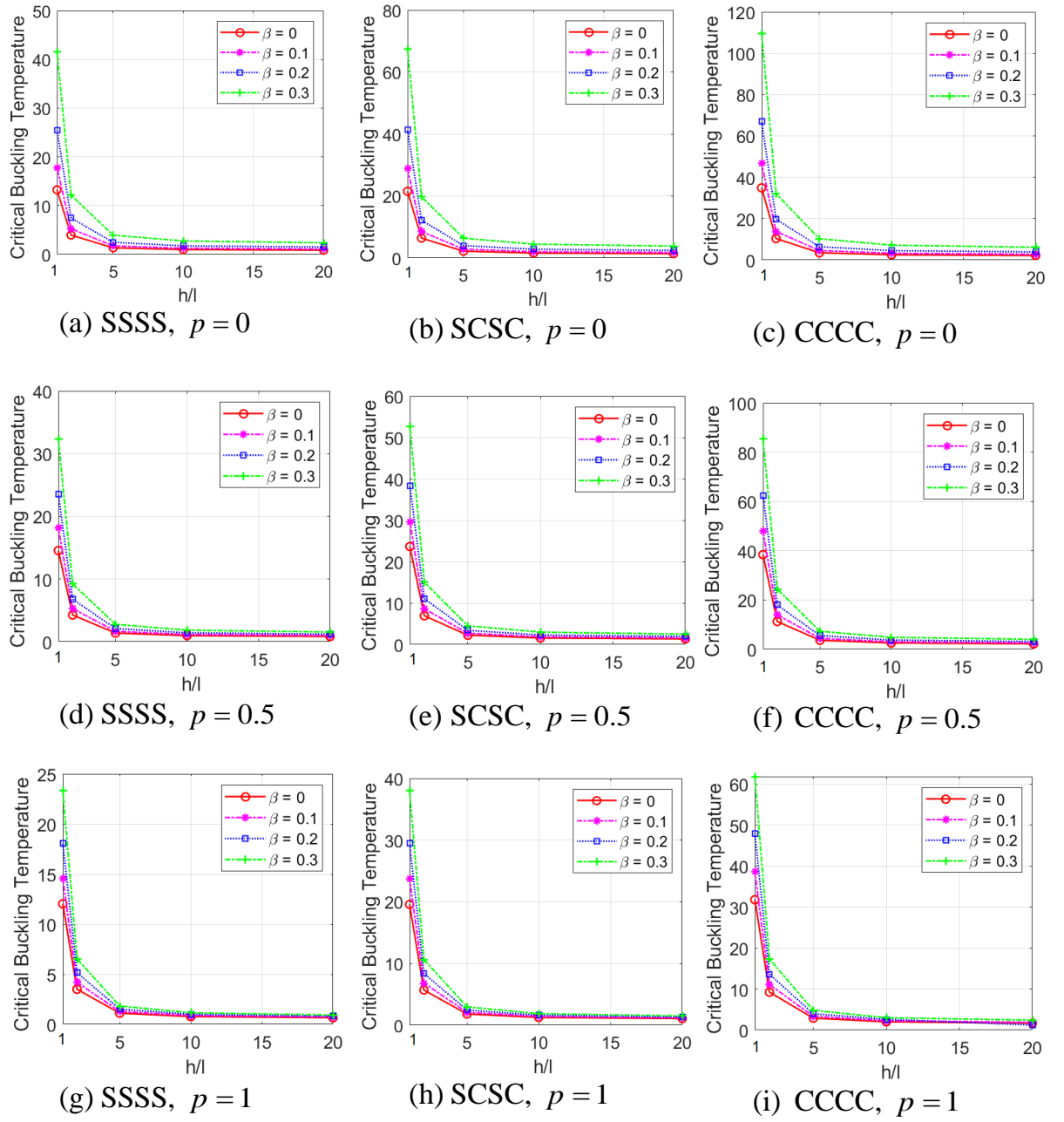


Figure 3.18: Variation of normalized thermal buckling load with respect to the length scale-to-thickness ratio h/l ($a/h = 20$) with biaxial compression under nonlinear distribution

3.4 Conclusions

This chapter introduces novel approximation functions for the Ritz method to analyze the behaviors of FG, FG sandwich, FGP, and PMF microplates. A unified higher-order shear deformation theory (HSDT) is formulated to approximate the

displacement field accurately. To capture size-dependent effects in microplates, the modified strain gradient theory (MST) is employed. The governing equations of motion are derived using Hamilton's principle. Convergence and validation studies are performed to verify the accuracy and reliability of the proposed solutions. The influence of the porosity parameters, shape functions, and boundary conditions on the microplates' frequency, buckling, and static responses have been examined. Some findings are followed:

- The chapter proposed new computational algorithms, which combined the Ritz method with novels OP, unified HSDT, MCT, and MST theory for analysis of microplates. Based on the findings of this study, the OP-Ritz shape functions proposed in this chapter are suitable for the behaviors analysis of microplates.
- The increase of the porosity coefficient and thickness-to-MLSP ratio leads to the reduction of the stiffness, natural frequencies and critical buckling loads of the porous microplates.
- The size effects are significant when the thickness-to-MLSP ratio is smaller than 20, the porosity does not impact importantly on the size effects of porous microplates.

Moreover, the theoretical formulation and novel hybrid shape functions of the computational method proposed in this chapter will be used in the subsequent chapters.

CHAPTER 4

INTELLIGENT COMPUTATIONAL ALGORITHMS FOR STOCHASTIC ANALYSIS OF FUNCTIONALLY GRADED MICROPLATES WITH UNCERTAINTIES OF MATERIAL PROPERTIES

This chapter use the theoretical formulation of chapter three for stochastic behaviors analysis of the microplates. The governing equations of motions are derived from Hamilton's principle. The solutions are approximated by bi-directional series in which hybrid shape functions are proposed, then the stiffness and mass matrix are explicitly derived. In order to investigate the stochastic responses of the microplates by using the polynomial chaos expansion (PCE), stochastic collocation method (SC) and Monte Carlo method under uncertainty of material properties. Besides, this chapter also proposes intelligent computational methods using the neural network systems (ANN, DNN) integrated with a balance composite motion optimization (BCMO) algorithm and an improved BCMO algorithm (iBCMO) to formulate a so-called BCMO-ANN and iBCMO-DNN for stochastic responses of microplates. The DNN with the long short-term memory model is used as a surrogate method to replace the time-consuming computational model, while the iBCMO is used to search the set of optimal solutions. The obtained numerical results for various configurations of boundary conditions, uncertainty parameters, three types of temperature distribution indicated that the model presents its accuracy and effectiveness in predicting stochastic free vibration, critical buckling, and thermal buckling of the microplates.

4.1 Introduction

In practice, the material properties of microplates could be uncertain due to manufacture processing or other unexpected phenomena, it led to changes of behaviors of the microplates and therefore required advanced computational methods to quantify the solution field. Literature review [198] shows that majority studies of the microplates focused on deterministic analysis, which provides only mean responses and neglects the deviation caused by the random their material properties.

Practically, in order to predict stochastic responses of structures, Monte Carlo Simulation (MCS) method is the simplest one to solve this complicated problem. Nonetheless, this approach is infeasible in different cases due to its expensive computational cost, especially when a complicated physical model is considered. Another approach is to use polynomial chaos expansion (PCE) which speeds up the computing process while still maintains the accuracy. Stochastic collocation (SC) is known as one of stochastic expansion method similar to the popular PCE. It method allows for the efficient and accurate computation of statistics and solutions of mathematical models that involve stochastic input parameters. It is particularly useful in the field of uncertainty quantification, where it can be used to estimate the propagation of uncertainties in physical systems or to quantify the sensitivity of system response to uncertain parameters. It derives the Lagrange interpolation polynomials for a set of collocation points and reproduces the model responses at these collocation points as of expansion coefficients.

In addition, there has been significant scholarly interest in the optimal design of plates. Optimization algorithms can be classified into two primary categories: gradient-based methods such as sequential quadratic programming, optimality criterion, force method, and non-gradient-based methods. Algorithms in the first group quickly find the best solutions. However, a common limitation of these algorithms is their tendency to become stuck at local optimal solutions. Furthermore, it is imperative to conduct sensitivity analyses on both the fitness and

constraint functions, as they play a crucial role in the optimization process. However, it is worth noting that performing these analyses can be intricate and resource-intensive. In order to mitigate these limitations, a variety of by natural phenomena simulation algorithms have been devised. Owing to its advantages, these optimization algorithms have been applied for the optimization of structures ([199-201]), In practice, the algorithms require dependent parameters and high computational costs. In order to overcome this adverse, the Balancing Composite Motion Optimization algorithm (BCMO) [107] has been recently developed, in which no dependent parameters are required. This method is inspired by the fact that the solution space is assumed to be in Cartesian coordinates and the searching movements of candidate solutions are compositely equalized in both global and local ones. In fact, a candidate solution can move closer to better ones to exploit the local regions, and move further to explore the search space. Thus, the best-ranked individual in each generation can jump immediately from space to space or intensify its current local space. Furthermore, the machine learning, which involves an artificial neural network (ANN), has been used to predict the behaviors of materials ([202-204]). Besides, the combination between the BCMO algorithm and ANN (BCMO-ANN) to determine optimal responses for microplates with uncertainties of material properties has not been developed yet, this interesting topic needs to be investigated. Moreover, size effects of microplates have been a challenging topic which needs to be studied further. Moreover, a novel intelligent computation algorithm iBCMO-DNN for solving the stochastic thermal buckling problems of microplates will propose with the aims of reducing the computational time in dealing with stochastic problems.

The main objective of this chapter is to develop a stochastic model for behaviors analysis of the microplates using various advanced algorithms such as Monte Carlo simulation with 10,000 samples, polynomial chaos expansion, stochastic collocation, BCMO-ANN and iBCMO-DNN algorithms. The governing equations of motions are derived from Hamilton's principle and then bi-directional series-type

solutions with hybrid shape functions. The deterministic responses of microplates are derived from Ritz-based solver based on a general HSDT and modified couple stress (MCT) and modified strain gradient (MST). Numerical results are displaced for various configurations of boundary conditions, uncertainty parameters, bending, free vibration, buckling load, and temperature distribution on the critical buckling temperature of microplates.

4.2 Polynomial chaos expansion

The key idea of this approach is to approximate the stochastic outputs as a series in an orthogonal space including the basis functions and their appropriate coefficients. The PCE of real value random variables is investigated by starting from a univariate case and passing to a multivariate one. The first step of PCE is to approximate the responses, \hat{u} , which is a quantity of interest (QoI). In this study, \hat{u} is fundamental frequency or critical buckling load of the FG microplates in terms of a truncated orthogonal series as follows ([148, 149]):

$$\hat{u} \approx \hat{u}_{PCE}(\mathbf{x}) = \sum_{i=0}^{P-1} c_i He_i(\mathbf{q}) + r \quad (4.1)$$

where \hat{u}_{PCE} is the response of interest obtained from the PCE; \mathbf{q} is a vector of independent random variables in PCE space mapped to physical random parameters \mathbf{x} ; He_i are multivariate orthogonal basis functions; c_i are coefficients to be determined so that the residual r is minimized; P is the permutation of the qualified order of the polynomial n , and the number of random variable d , which is given by Askey's scheme ([148]):

$$P = \frac{(n+d)!}{n!d!} \quad (4.2)$$

The second step is to estimate all associated coefficients. This task can be easily obtained by forcing the residual minimum resulting in the inner product of the residual and each basis function He_i becomes zero. By taking the inner product of both sides of Eq. (4.1) with respect to He_j :

$$\langle \hat{u}, He_j \rangle = \sum_{i=0}^{P-1} c_i \langle He_i, He_j \rangle \quad (4.3)$$

then enforcing the orthogonality of He_j , Eq. (4.3) becomes:

$$c_i = \frac{\langle \hat{u}, He_i \rangle}{\langle He_i, He_i \rangle} = \frac{1}{\langle He_i, He_i \rangle} \int \hat{u} He_i \rho_Q(\mathbf{q}) d\mathbf{q} \quad (4.4)$$

where He_i is Hermite polynomial, and the “truth” response \hat{u} is unknown, thus Gauss-Hermite quadrature approach is implemented for computing c_i as follows:

$$c_i = \frac{1}{\gamma_i} \sum_{j_1=1}^{N_{gp}^1} \dots \sum_{j_d=1}^{N_{gp}^d} (w_{j_1}^1 \times \dots \times w_{j_d}^d) \times \hat{u}(q_{j_1}^1, \dots, q_{j_d}^d) \times He_i(q_{j_1}^1, \dots, q_{j_d}^d) \quad (4.5)$$

where $\gamma_i = \langle He_i, He_i \rangle$ can be analytically computed; N_{gp}^i is the number of quadrature point; q_j^i and w_j^i are the set of quadrature points and their weights, respectively for the random variable i^{th} . For convenience, N_{gp}^i for each variable is chosen equally such that:

$$N_{gp}^1 = N_{gp}^2 = \dots = N_{gp}^d = N_{gp} \quad (4.6)$$

where $N_{gp} = n + 1$ and the total number of Gauss points is at least $(n + 1)^d$. Note that in Eq. (4.6), $\hat{u}(q_{j_1}^1, \dots, q_{j_d}^d)$ is the “exact” response obtained from the “truth” computational model by solving characteristic equations of motion microplates. It means that in order to estimate all polynomial coefficients c_i , $(n + 1)^d$ microplate models need to be run for \hat{u} . For the third-order PCE model of four random variables, for instance, $(3 + 1)^4 = 256$ “truth” samples which is considered as the total computational cost of deriving PCE model, are needed.

Another advantage of PCE is that the mean and variance of the response can be analytical estimated from its coefficients as:

$$\mu_{\hat{u}} = E[\hat{u}_{PCE}] = c_0; \quad \bar{\sigma}_{\hat{u}}^2 = E[(\hat{u}_{PCE} - \mu_{\hat{u}})^2] = \sum_{i=1}^{P-1} c_i^2 \langle He_i, He_i \rangle = \sum_{i=1}^{P-1} c_i^2 \gamma_i \quad (4.7)$$

Moreover, Sobol' sensitivity indices can be also estimated directly from the PCE coefficients in which S_k is the first-order main effect, S_k^T is the total sensitivity index of a random variable X_k defined as follows ([205]):

$$S_k = \frac{D_k}{\sigma_u^2}; S_k^T = \frac{D_k^T}{\sigma_u^2} \quad (4.8)$$

where $D_k = \sum_{j \in \Gamma_k} c_j^2 \langle He_j(\mathbf{q}), He_j(\mathbf{q}) \rangle$ and $D_k^T = \sum_{j \in \Gamma_k^T} c_j^2 \langle He_j(\mathbf{q}), He_j(\mathbf{q}) \rangle$; Γ_k

includes all j such that the multivariate function $He_j(\mathbf{q})$ only includes the variable q_k (i.e, $He_j(\mathbf{q}) = He_j(q_k)$), while Γ_k^T includes all j such that $He_j(\mathbf{q})$ must include the variable q_k (i.e, $He_j(\mathbf{q}) = He_j(q_1 \dots q_k \dots q_d)$).

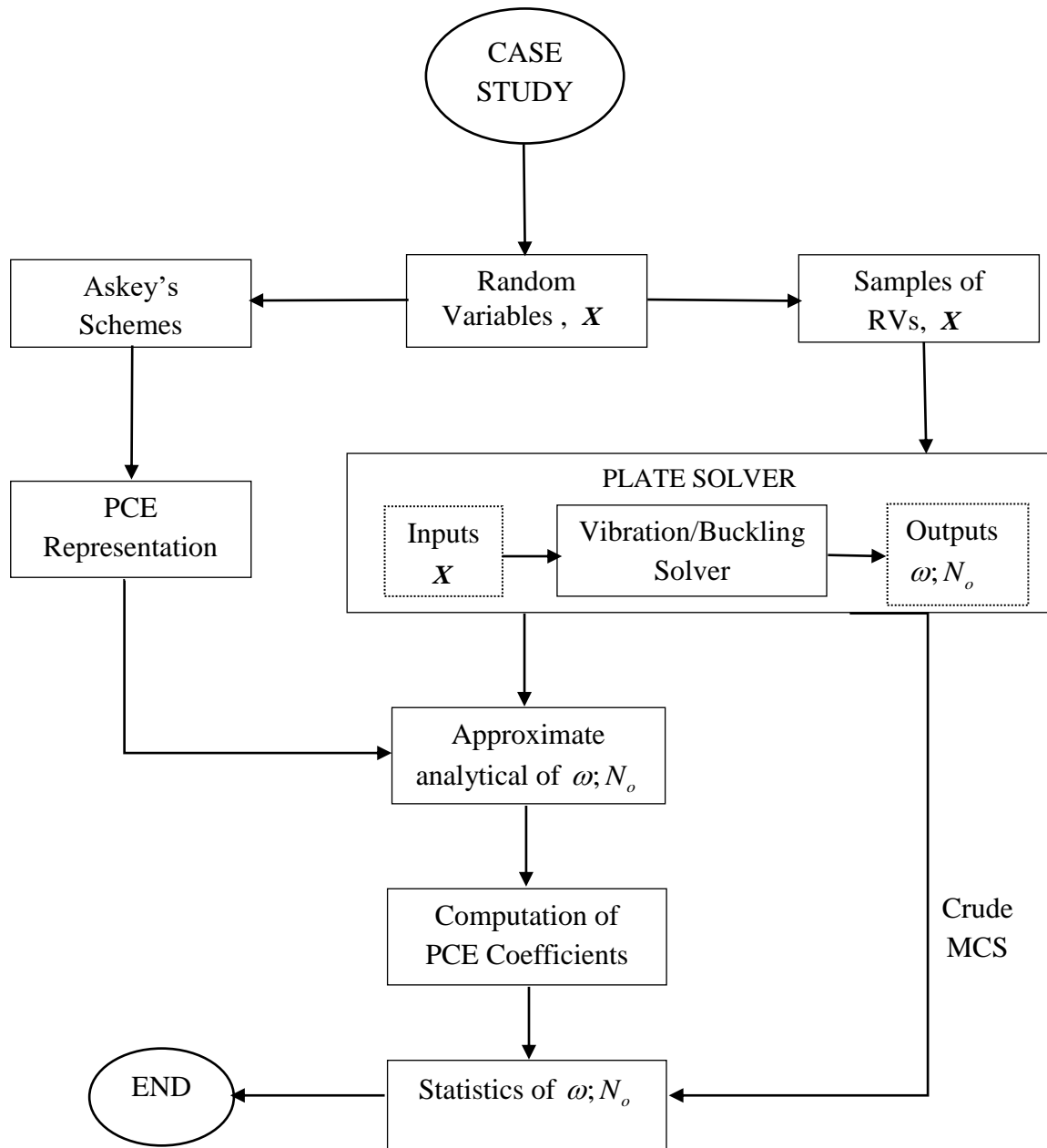


Figure 4.1: Flowchart of stochastic free vibration and buckling analysis of the microplates using PCE and MCS

4.3 Stochastic collocation

For 1-D problem (i.e., one random input X) and n_i interpolation points, it approximates the stochastic response u by forming the Lagrange functions and estimating the model response at interpolation points $u(q_i)$ as follows ([150, 151]):

$$u(X) \approx \hat{u}(X) = \sum_{i=1}^{n_i} u(q_i) L_i(q) \quad (4.9)$$

where q is a standard variable mapping to the physical variable X and for maximizing performance of this approach q_i are defined as appropriate Gauss quadrature points corresponding to the distribution of q . More specifically, q could be normal, uniform or exponential variable, and q_i are probabilistic Gauss-Hermite, Gauss-Legendre or Gauss-Laguerre quadrature points, respectively. The 1-D Lagrange interpolation $L_i(q)$ is defined as:

$$L_i(q) = \prod_{\substack{j=1 \\ j \neq i}}^{n_i} \frac{q - q_j}{q_i - q_j} \quad (4.10)$$

A tensor product of 1-D functions is applied to expand the SC approximation to the multi-dimensional space. Particularly, the expansion of d -variable and n_k collocation points for the k^{th} variable can be expressed as:

$$\hat{u}(\mathbf{q}) = \sum_{j_1=1}^{n_1} \dots \sum_{j_d=1}^{n_d} u(q_{j_1}^1, \dots, q_{j_d}^d) \times (L_{j_1}^1 \otimes \dots \otimes L_{j_d}^d) \quad (4.11)$$

where $\mathbf{q} = [q^1, q^2, \dots, q^d]^T$ is a vector of random inputs and $L_{j_k}^k = \prod_{\substack{s=1 \\ s \neq j_k}}^{n_k} \frac{q^k - q_s^k}{q_{j_k}^k - q_s^k}$ in

which q_s^k is a collocation point of the variable q^k . Note that in this paper, q^k is the standard normal variable and q_s^k is Gauss-Hermite quadrature point. For convenience, the number of quadrature points for each variable is chosen equally such that:

$$n_1 = n_2 = \dots = n_d = N_{gp} \quad (4.12)$$

The total number of Gauss point for the full tensor product is $(N_{gp})^d$. Note that in Eq. (4.11), $u(q_{j_1}^1, \dots, q_{j_d}^d)$ is the “correct” response achieved from the “right” model by solving characteristic equations of motion microplates. When the SC model is constructed, MCS can perform directly from Eq. (4.11) to facilitate the probabilistic characteristics of the output, \mathbf{u} . The cost for evaluating the approximate \mathbf{u} using Eq. (4.11) is considerably lower than that for the original model in characteristic equations of motion microplates ; hence, the total cost when using the SC model may be thought of as simply the cost of $(N_{gp})^d$ truth model runs. To assess the accuracy of the proposed SC model, 10,000 samples of MCS drawn from the original computational model represented in characteristic equations of motion are also generated. To distinguish between MCS carried out on the SC model (Eq. (4.11)) and MCS performed with the model in characteristic equations of motion of microplates, the former is referred to simply as the SC method. It is demonstrated in the following section that to achieve sufficient accuracy, the computational cost of the SC model is much lower than that of MCS (i.e., $N_{gp}^d \ll 10,000$). It is also noted that for high-dimensional problems (i.e., the number of random variable, d is large), SC method is also expensive compared to MCS, then alternative surrogate models with or without dimension reduction techniques should be adopted.

4.4 Intelligent stochastic computational algorithms based on optimization and machine learning methods

4.4.1 Balancing composite motion optimization: BCMO

The balancing composite motion optimization is a meta-heuristic algorithm technique was initially developed by Le-Duc et al. [107] in which the key idea of this approach is to balance the individual composite motion features within the global optimum. Balancing global and local search via a probabilistic decision model creates a mechanism of mobility for each individual.

Initialization: As follows, a random initialization is used to create the population distribution:

$$x_i = x_j^L + rand(1, d) \times (x_i^U - x_j^L) \quad (4.13)$$

where x_i^L is the lower bound and x_i^U is the upper bound of the i^{th} – individual; number of items is d . Based on the input in Eq. (4.13), the population objective function values $f(x)$ are then evaluated, and all individuals are sorted based on the sorting $f(x)$ as follows:

$$x = \arg sort \{f(x)\} \quad (4.14)$$

Best individual and instant global point: The instant global point x_{Oin}^t is determined as the prior best of x_1^{t-1} with regard to a trial u_1^t , where u_1^t is calculated using population information from the current generation as follows:

$$u_1^t = (LB + UB) / 2 + v_{k1/k2}^t + v_{k2/1}^t \quad (4.15)$$

where $v_{k1/k2}^t$ is the relative motions of the individual k_1^{th} with respect to the individual k_2^{th} ; $v_{k2/1}^t$ is the relative motions of the individual k_2^{th} with respect to the previous best one. $v_{k1/k2}^t$ and $v_{k2/1}^t$ are determined as follows:

$$v_{i/j} = dv_{ij} (x_j - x_i) \quad (4.16)$$

where dv_{ij} is a vector that could be computed using the trial number TV_j :

$$dv_{ij} = \begin{cases} rand(1, d) & \text{if } TV_j > \zeta \\ -rand(1, d) & \text{otherwise} \end{cases} \quad (4.17)$$

where ζ is the probability threshold in selecting the mutation and crossover phases. The value of $\zeta = 0.5$ has been chosen for balance of global and local search phases as well as mutation and crossover mechanisms for solving general optimization problems ([107]).

Instant global point is defined:

$$x_{Oin}^t = \begin{cases} u_1^t & \text{if } f(u_1^t) < f(x_1^{t-1}) \\ x_1^{t-1} & \text{otherwise} \end{cases} \quad (4.18)$$

Individuals' composite mobility in the solution space: In BCMO, v_j represents the global search motion, which is governed by:

$$v_j = L_{GS} \times dv_j \times (x_{Oin} - x_j) \quad (4.19)$$

where

$$L_{GS} = \begin{cases} e^{-\frac{1}{d} \frac{j}{NP} r_j^2} & \text{if } TV_j > \zeta \\ e^{-\frac{1}{d} \left(1 - \frac{j}{NP}\right)^2 r_j^2} & \text{otherwise} \end{cases} ; \quad dv_{ij} = \begin{cases} rand(1, d) & \text{if } TV_j > \zeta \\ -rand(1, d) & \text{otherwise} \end{cases} \quad (4.20)$$

where NP is the population size.

The distance from the j^{th} individual to O_{in} call r_j is calculated by:

$$r_j = \|x_j - x_{Oin}\| \quad (4.21)$$

These v_{ik} instances have equal probability and can be calculated as follows:

$$P(v_{ik}) = P(v_{i/j}) \times P(v_j) = \zeta^2 \quad \text{with } k = 1, \dots, 4 \quad (4.22)$$

The i^{th} individual's position is updated as follows:

$$x_i^{t+1} = x_i^t + v_{i/j} + v_j \quad (4.23)$$

It is noted that in the original BCMO, the function *rand* is a random number which is uniformly distributed in the range $[0,1]$, the present iBCMO tries to enhance convergence speed while guarantees the solution accuracy by defining a subset $[a_1, b_1] \in [0,1]$ which gives the most optimal values. Moreover, it is worthy to noticing that the probabilistic threshold ζ for choosing its mutation and crossover phases might be changed with different problems, therefore which will be selected throughout numerical simulations.

4.4.2 Artificial neural network (ANN) and BMCO algorithm: BCMO-ANN

The Artificial Neural Network (ANN) system shown in Fig. 4.2 contains three kinds of layers, namely, input layer, hidden layer, output layer in which each layer consists of neurons that are connected to each other in the previous layer.

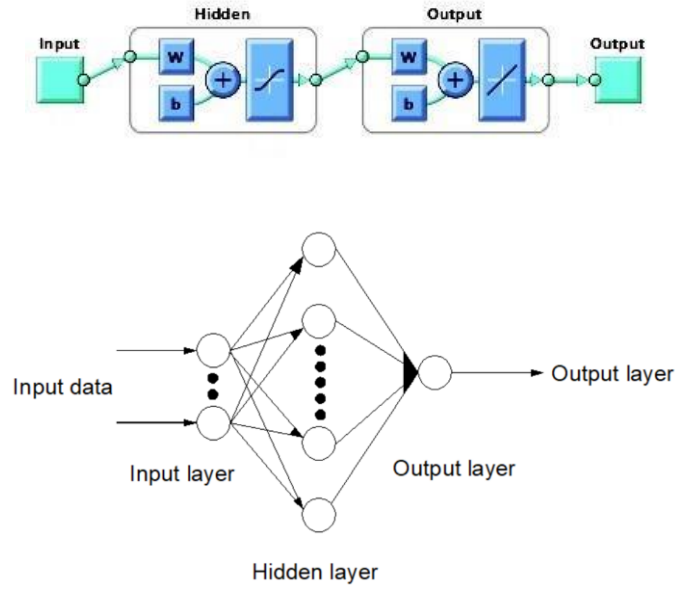


Figure 4.2: An artificial neural network structure

The input data from the outside are multiplied by the weights before they reach the nodes. Each node in the next layer will get a sum of the output values of the previous nodes multiplied with respective weights. The output data of the activation function for the sum is expressed as follows:

$$y_i^n = \varphi(x_i^n) = \varphi\left(\sum_{j=1}^{lm_{n-1}} w_{ij}^{n-1} \times y_j^{n-1} + b_i^n\right) \quad (4.24)$$

where y_i^n and x_i^n are data pair output and input of activation function of node i , respectively; w_{ij}^{n-1} is the weight between the output node i and input node j ; b_i^n is the bias of node j ; φ is the activation function. Moreover, it is known that the activation function plays an important role in defining the output signal of each neuron in each layer of a neural network. Different activation functions have been, therefore, developed in the literature ([156]). For the present study, the activation function used to update weight and bias values is based on the Levenberg - Marquardt optimization ([206, 207]).

Furthermore, a loss function is required to evaluate the performance of the prediction model. The objective of loss function is to measure the difference between target values and predicted ones, from which during the training process, the difference between the model outputs and the target values are converged to zeros. The loss functions are hence constructed to deal with different kinds of optimization problems. In practice, the mean square error (MSE) [158] is commonly used to evaluate the accuracy of the prediction model. It is also considered as a loss function during training process of the ANN. The statement of MSE is illustrated as follows:

$$MSE = \frac{1}{lm} \sum_i^{lm} (y_i - \hat{y}_i)^2 \quad (4.25)$$

where lm is the number of training samples; y_i is the actual output data; \hat{y}_i is the predicted value of the i^{th} – sample.

4.4.3 Deep neural network (DNN) and improved BMCO algorithm: iBCMO-DNN

The present section proposes a novel intelligent computational iBCMO-DNN algorithm which enables to capture uncertain responses of the FGP microplates. A deep feedforward neural network is shown in Fig. 4.3 in which the input data of the neural network is passed through the input layer, hidden layers and output layer.

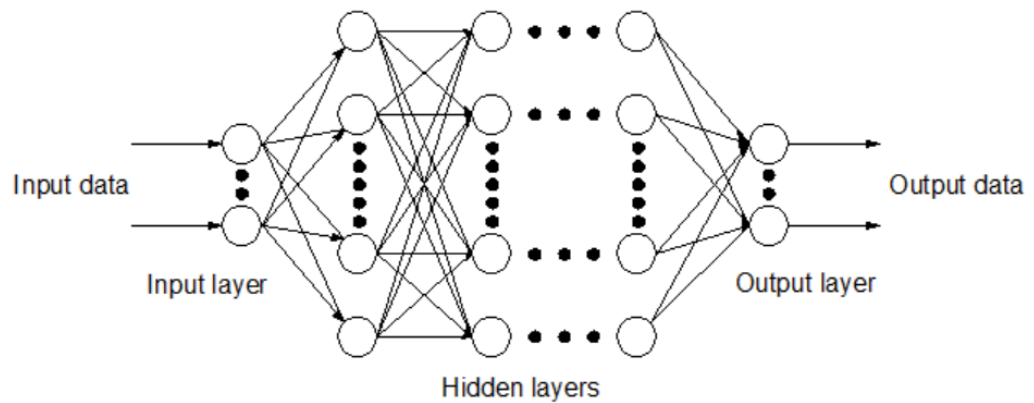


Figure 4.3: Deep neural network

Before reaching the nodes, the input data from the outside is multiplied by the weights. Each node in the succeeding layers will get the total of the preceding nodes' output values multiplied by their respective weights, and the activation function's output data for the sum is supplied as follows ([155]):

$$y_i^n = \varphi(x_i^n) = \varphi\left(\sum_{j=1}^{L_{n-1}} w_{ij}^{n-1} \times y_j^{n-1} + b_i^n\right) \quad (4.26)$$

where a data pair with output and input of activation function of node i which are y_i^n and x_i^n , respectively; b_i^n is the bias of node j ; w_{ij}^{n-1} is the weight between the output node i and input node j ; φ is the activation function. Many kinds of activation functions are available in the literature ([208]), in the present manuscript, the long short-term memory network (LSTM) [209] will be applied in which the tanh activation function is used for nodes of the input layer and hidden layers, and the sigmoid activation function for the output nodes.

The flowchart of iBCMO-DNN algorithm is presented in Fig. 4.4. It is noted that the input and associated output of a data pair is namely a training data. A goal value will be estimated from the corresponding input data in the training data, this goal value is compared with the corresponding output one in order to estimate the error value of the loss function. Moreover, in the present study, the mean square error (MSE) [158] will be used for the process of training as follows:

$$MSE = \frac{1}{L} \sum_i^L (y_i - \hat{y}_i)^2 \quad (4.27)$$

where L is number of samples; y_i is output data; \hat{y}_i is goal data to be predicted. Furthermore, the adaptive moment estimation (Adam) [162] to adjust weights and bias for minimizing the cost function is determined by the gradient of the loss function. The batch gradient descent (BGD) calculates gradients using the whole data set in the dataset and updates them only after all training data has been assessed. As a result, various deficiencies in memory, training speed, and stability

appear. Hence, in the current task, mini-batch gradient descent (mBGD) ([163]) was used.

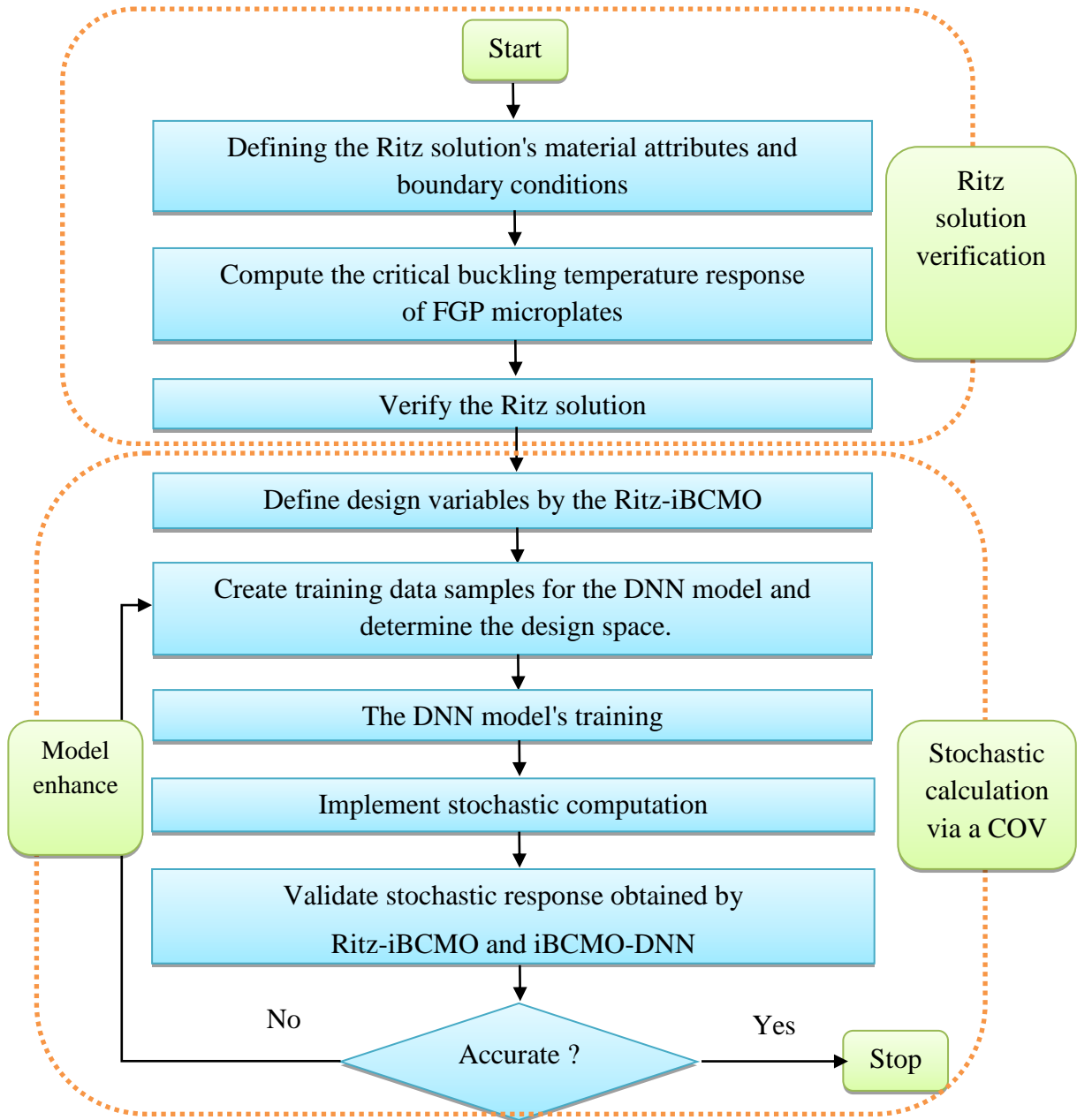


Figure 4.4: The flowchart of the stochastic response of FGP microplates

4.5 Numerical results

4.5.1 Stochastic vibration analysis of FG microplates using polynomial chaos expansion

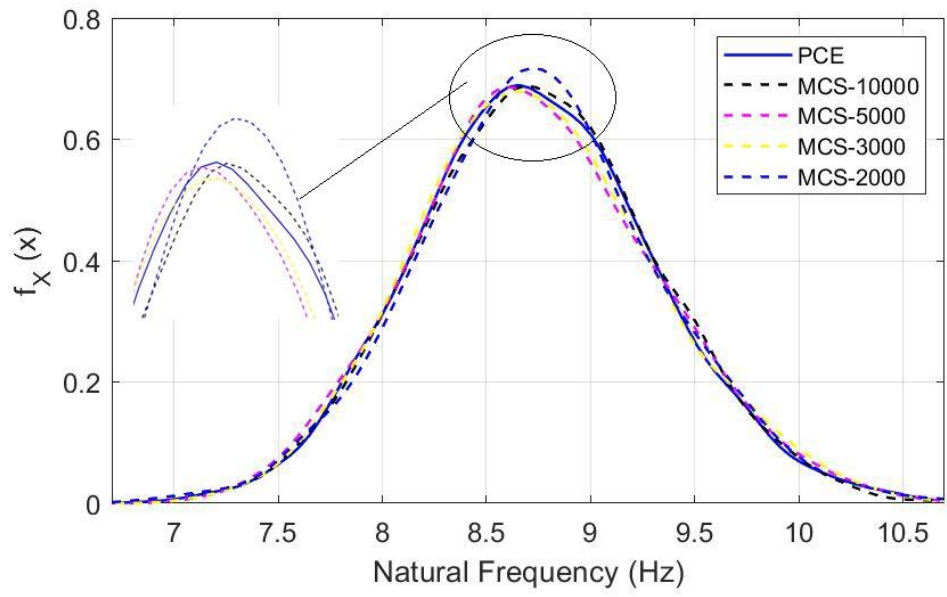
The FG microplates are supposed to be made of a mixture of ceramic and metal whose mean material properties are given as follows:

- MAT 1: Al_2O_3 ($E_c = 380 \text{ GPa}$, $\rho_c = 3800 \text{ kg/m}^3$, $\nu_c = 0.3$), Al ($E_m = 70 \text{ GPa}$, $\rho_m = 2702 \text{ kg/m}^3$, $\nu_m = 0.3$).

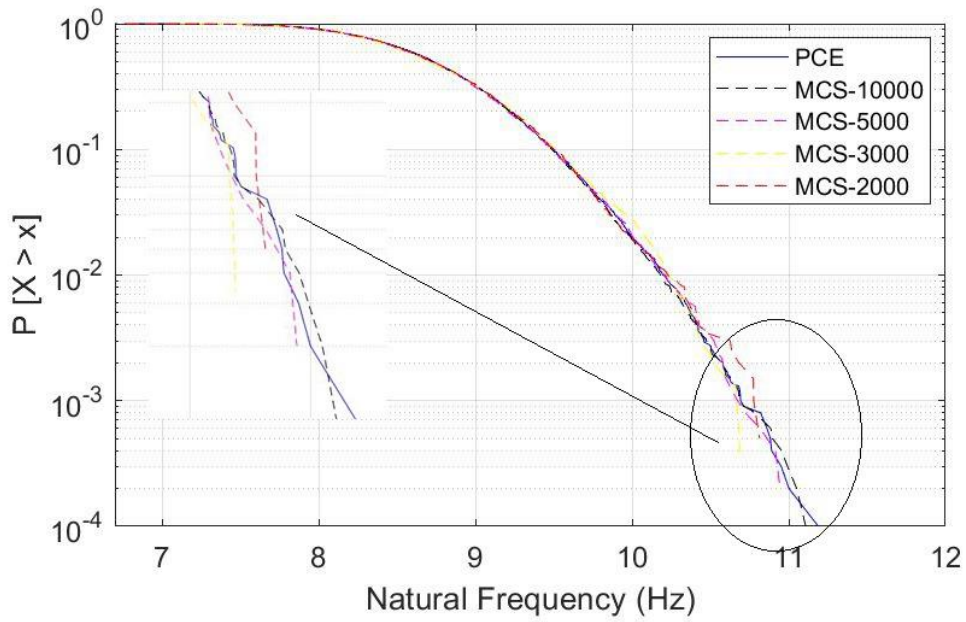
In order to investigate of the stochastic responses of the FG microplates, the material properties (E_c , E_m , and ρ_c , ρ_m) are assumed to be randomly distributed via the lognormal distributions and the coefficient of variation (COV) for all random variables is set to equal 10%. The MCS with 10,000 samples is considered as the exact solutions for comparison purpose. For convenience, the following non-dimensional parameters are used in the numerical examples:

$$\bar{\omega} = (\omega a^2 / h) \sqrt{\rho_c / E_c} \quad (4.28)$$

Next, stochastic vibration analysis employs four random variables (E_m , E_c , ρ_m , ρ_c) with the mean values of MAT 1. The MCS with 10,000 samples is analyzed for comparison purpose and used to investigate the performance of the proposed PCE model. It should be noted that only 256 samples are needed for third-order PCE model. The first four statistical moments of the fundamental frequency, namely the mean, standard deviation (SD), skewness and kurtosis obtained from the MCS and PCE models, for various values of p and a/h are compared in Tables 4.1 and 4.2.



(a) Probability density function (PDF)



(b) Probability of exceedance (PoE)

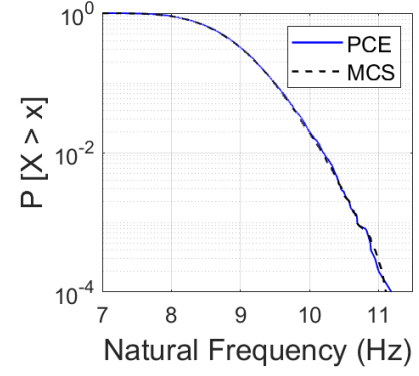
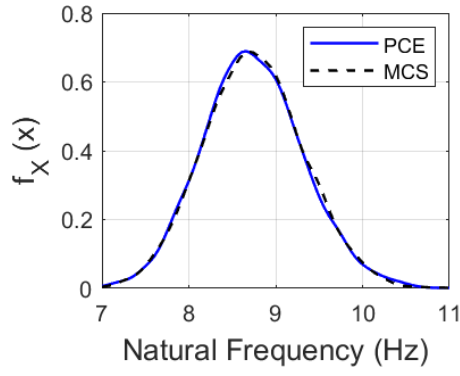
Figure 4.5: PDF and PoE of MCS and PCE methods for the fundamental frequency (Hz) of the FG microplates with SSSS BC ($p = 5$, $h/l = 1$, $a/h = 10$)

Table 4.1: Comparison study between MCS (10.000 samples) and PCE (256 samples) for the mean, standard deviation (SD), Kurtosis and Skewness for the fundamental frequency of the FG plates ($a / h = 5$, MAT 1)

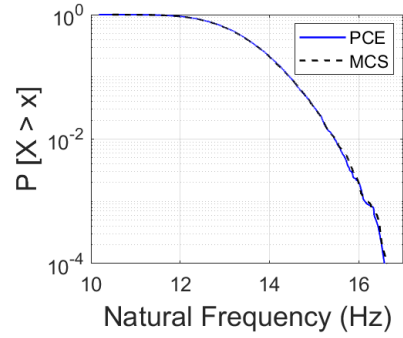
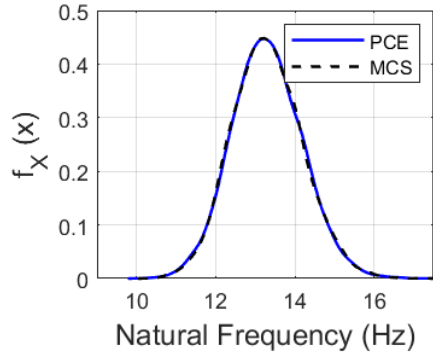
BCs	p	Theory	mean	SD	Kurtosis	Skewness	COV(%)	Time(s)	Determined
SSSS	1	PCE	4.0790	0.2114	2.5845	0.0262	5.2	14.06	4.0782
		MCS	4.0787	0.2114	2.5844	0.0264	5.2	536.56	
	2	PCE	3.6839	0.2875	2.6374	0.1295	7.8	12.32	3.6811
		MCS	3.6849	0.2870	2.6377	0.1299	7.8	568.27	
	5	PCE	3.3997	0.3535	2.6737	0.2114	10.4	13.14	3.3950
		MCS	3.3988	0.3537	2.6734	0.2117	10.4	526.38	
	10	PCE	3.2601	0.3738	2.6984	0.2509	11.5	13.65	3.2511
		MCS	3.2577	0.3734	2.6983	0.2512	11.5	525.58	
CSCS	1	PCE	5.2247	0.2664	2.5709	0.0156	5.1	15	5.2238
		MCS	5.2272	0.2664	2.5707	0.0151	5.1	523.46	
	2	PCE	4.7038	0.3599	2.6277	0.1248	7.7	25	4.6999
		MCS	4.7045	0.3596	2.6278	0.1249	7.7	549.55	
	5	PCE	4.2712	0.4427	2.6774	0.2147	10.4	16	4.2627
		MCS	4.2687	0.4429	2.6775	0.2146	10.4	580.37	
	10	PCE	4.0666	0.4718	2.7066	0.2578	11.6	31	4.0550
		MCS	4.0656	0.4720	2.7064	0.2577	11.6	592.43	
CCCC	1	PCE	6.4425	0.3222	2.5557	0.0034	5.0	16.00	6.4417
		MCS	6.4429	0.3218	2.5550	0.0039	5.0	533.16	
	2	PCE	5.7829	0.4327	2.6171	0.1170	7.5	14.87	5.7789
		MCS	5.7815	0.4324	2.6179	0.1164	7.5	529.85	
	5	PCE	5.1638	0.5327	2.6805	0.2195	10.3	15.28	5.1524
		MCS	5.1649	0.5332	2.6811	0.2189	10.3	574.46	
	10	PCE	4.8807	0.5726	2.7155	0.2652	11.7	15.57	4.8661
		MCS	4.8811	0.5727	2.7150	0.2659	11.7	581.27	

Table 4.2: Comparison study between MCS (10.000 samples) and PCE (256 samples) for the mean, standard deviation (SD), Kurtosis and Skewness for the fundamental frequency of the FG microplates ($a/h = 10$, MAT 1)

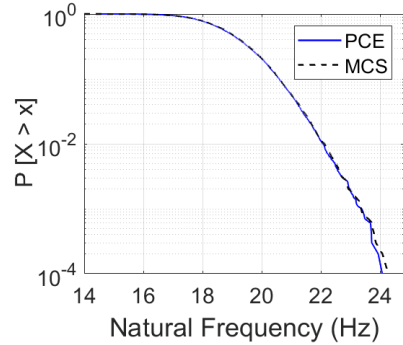
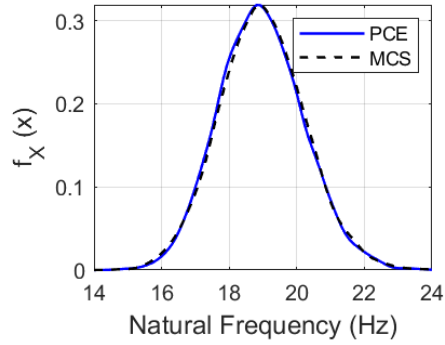
BCs	p	Theory	Mean	SD	Kurtosis	Skewness	COV (%)	Time(s)	Present
$h/l=1$									
SSSS	1	PCE	11.0107	0.5087	2.4628	-0.0532	4.6	17.02	11.0105
		MCS	11.0100	0.5087	2.4633	-0.0531	4.6	814.11	
	5	PCE	8.7431	0.8313	2.6301	0.1966	9.5	18.12	8.7203
		MCS	8.7456	0.8317	2.6308	0.1962	9.5	815.30	
	10	PCE	8.0719	0.8990	2.6953	0.2624	11.1	18.47	8.0442
		MCS	8.0747	0.8986	2.6949	0.2629	11.1	817.04	
CCCC	1	PCE	24.0519	1.1046	2.4451	-0.0594	4.6	17.68	24.0526
		MCS	24.0482	1.1041	2.4547	-0.0596	4.6	818.84	
	5	PCE	18.9599	1.7906	2.6265	0.1961	9.4	17.82	18.9125
		MCS	18.9631	1.7912	2.6260	0.1962	9.4	817.73	
	10	PCE	17.4222	1.9411	2.7025	0.2651	11.1	18.44	17.3596
		MCS	17.4209	1.9406	2.7031	0.2645	11.1	818.42	
$h/l=5$									
SSSS	1	PCE	4.8590	0.2458	2.5788	0.0199	5.1	17.65	4.8572
		MCS	4.8565	0.2453	2.5779	0.0197	5.1	811.69	
	5	PCE	4.0912	0.4163	2.6649	0.2053	10.2	18.20	4.0828
		MCS	4.0913	0.4164	2.6648	0.2049	10.2	815.24	
	10	PCE	3.9210	0.4402	2.6852	0.2476	11.2	17.95	3.9112
		MCS	3.9213	0.4406	2.6855	0.2480	11.2	817.51	
CCCC	1	PCE	8.9385	0.4421	2.5478	0.0197	4.9	17.10	8.9348
		MCS	8.9356	0.4426	2.5481	0.0199	4.9	816.86	
	5	PCE	7.3712	0.7425	2.6682	0.2108	10.1	17.66	7.3509
		MCS	7.3723	0.7429	2.6675	0.2106	10.1	820.08	
	10	PCE	6.9934	0.7913	2.6981	0.2564	11.3	17.90	6.9730
		MCS	6.9955	0.7917	2.6987	0.2568	11.3	818.79	
$h/l=10$									
SSSS	1	PCE	4.5341	0.2337	2.5998	0.0357	5.2	17.82	4.5338
		MCS	4.5330	0.2339	2.5995	0.0352	5.2	819.66	
	5	PCE	3.8564	0.3966	2.6671	0.2078	10.3	18.05	3.8502
		MCS	3.8580	0.3970	2.6675	0.2877	10.3	817.34	
	10	PCE	3.7169	0.4179	2.6889	0.2474	11.2	18.25	3.7072
		MCS	3.7199	0.4183	2.6891	0.2476	11.2	818.59	
CCCC	1	PCE	8.0048	0.4076	2.5525	0.0165	5.1	17.30	8.0090
		MCS	8.0032	0.4071	2.5520	0.0164	5.1	816.72	
	5	PCE	6.6760	0.6844	2.6616	0.2069	10.3	17.53	6.6562
		MCS	6.6778	0.6849	2.6611	0.2071	10.3	819.33	
	10	PCE	6.3784	0.7261	2.6906	0.2524	11.4	17.87	6.3648
		MCS	6.3783	0.7261	2.6905	0.2525	11.4	817.85	



a) SSSS



b) CSCS



c) CCCC

Probability density function (PDF)

Probability of exceedance (PoE)

Figure 4.6: PDF and PoE of MCS and PCE methods for the fundamental frequency (Hz) of the FG microplates with SSSS, CSCS, CCCC BCs ($p = 5$, $h/l = 1$, $a/h = 10$)

It can be observed that all statistical moments obtained from MCS and PCE show good agreement in all cases. The required computational time of the present approach is about 1/47 compared with direct MCS method. The mean values of fundamental frequencies for both PCE and MCS are close to the deterministic ones

for all BCs and different values of p . Interestingly, although the COV of input random variables are kept the same, the COV of fundamental frequency increases with the increase of p .

Figs. 4.6-4.9 compare the probability density function (PDF) and probability of exceedance (PoE) of MCS and PCE for the vibration and buckling analysis of the FG plates and microplates with various BCs. It can be observed again that the results of MCS are in good agreement with PCE.

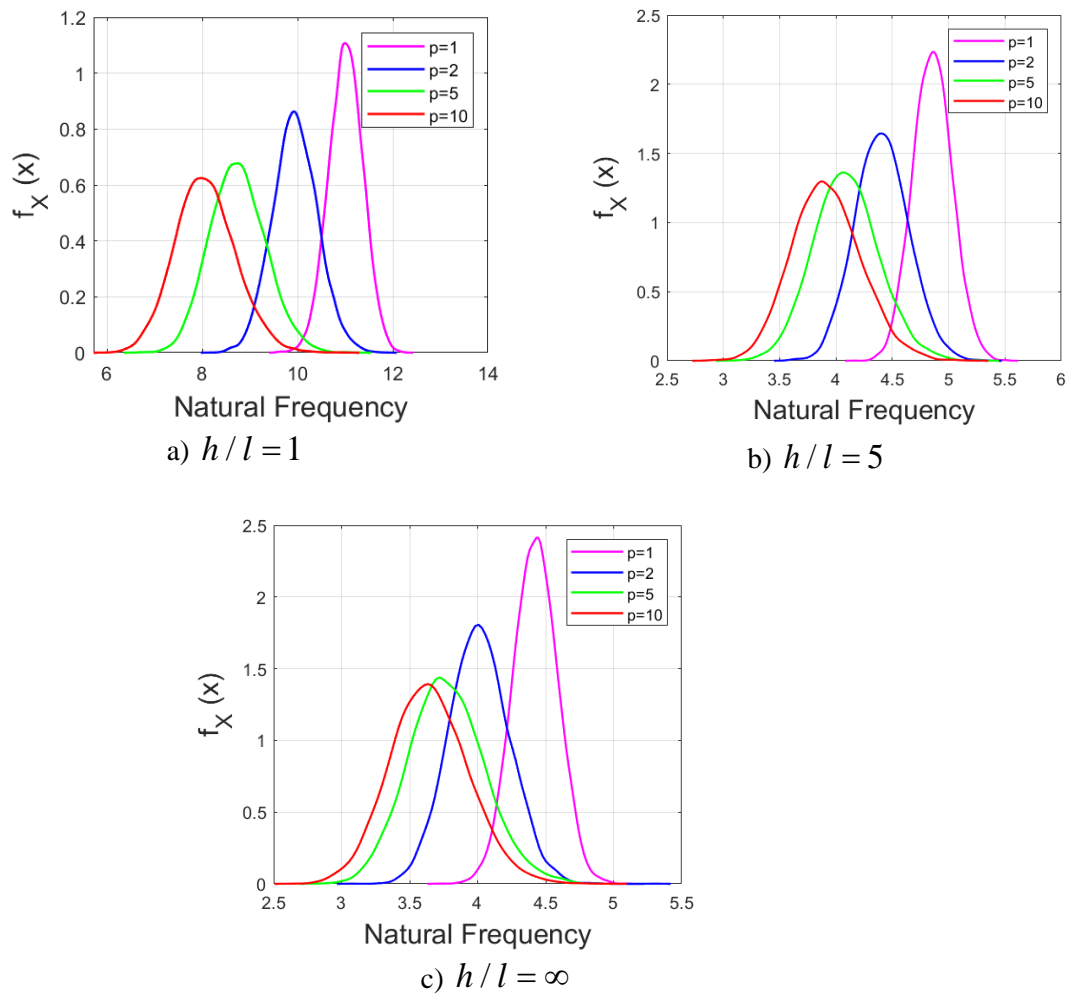
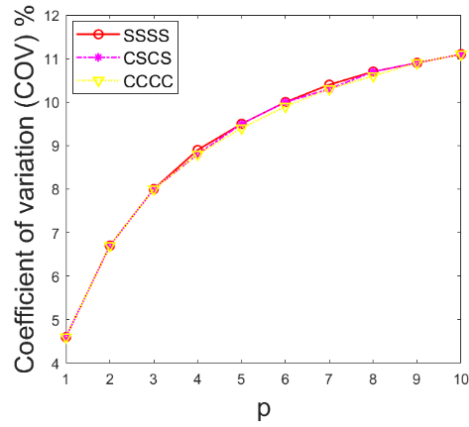
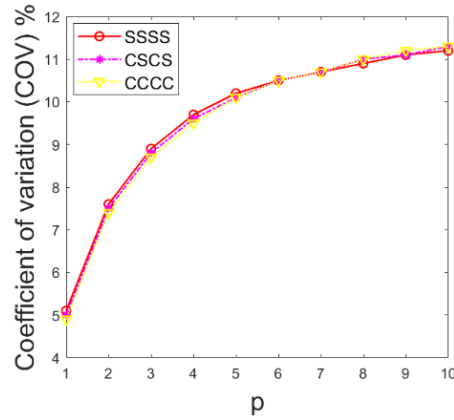


Figure 4.7: Probability density function (PDF) for the natural frequencies and critical buckling loads of SSSS FG microplates ($a/h = 10$) with various power-law index p (PCE order-3)

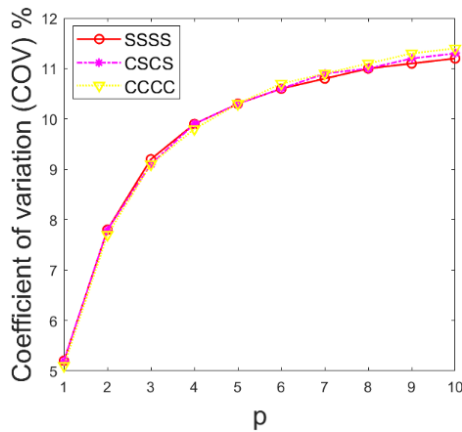
It is consistent with what is observed from the comparison of the COV of these stochastic responses shown in Fig. 4.11.



a) $h/l = 1$



b) $h/l = 5$



c) $h/l = \infty$

Figure 4.8: Coefficient of variation (COV) with respect the power-law index p of the FG microplates ($a/h = 10$) with various BCs and h/l

The linear quantile-quantile plots shown in Fig. 4.9 further confirm the matching statistical distribution of the fundamental frequencies computed from MCS and PCE. Thus, the PCE method gives an affordable alternative solution to predict the stochastic analysis of the FG microplates with multiple uncertain material properties.

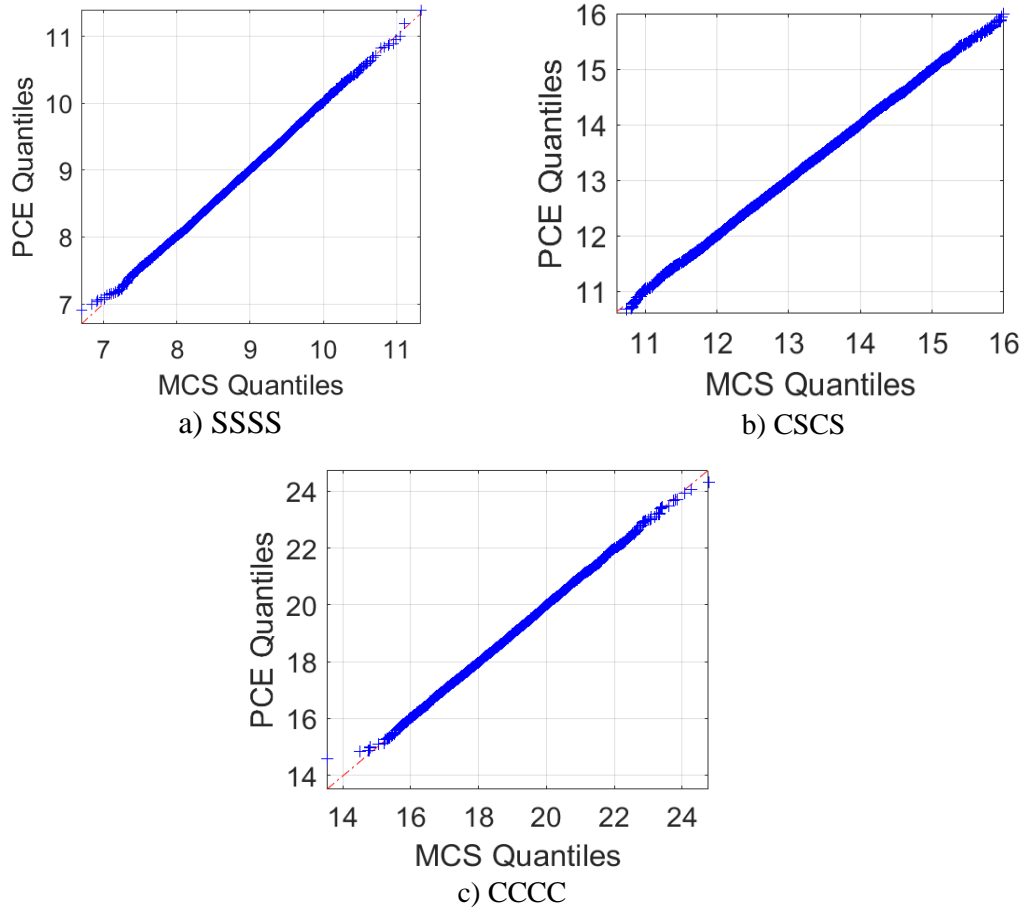


Figure 4.9: Quantile-quantile plot of PCE and MCS method for the fundamental frequencies of the FG microplates with various BCs ($p = 5$, $h/l = 1$, $a/h = 10$)

Figs. 4.10 and 4.11 compares the sensitivity indices based on the first-order and total Sobol indices for the vibration analysis using MCS and PCE. It is seen that the Sobol indices computed from the PCE are closely matched with those calculated from MCS. It is observed that the sensitivity indices of mass densities (ρ_c, ρ_m) are higher than those of Young's modulus (E_c, E_m) for all cases.

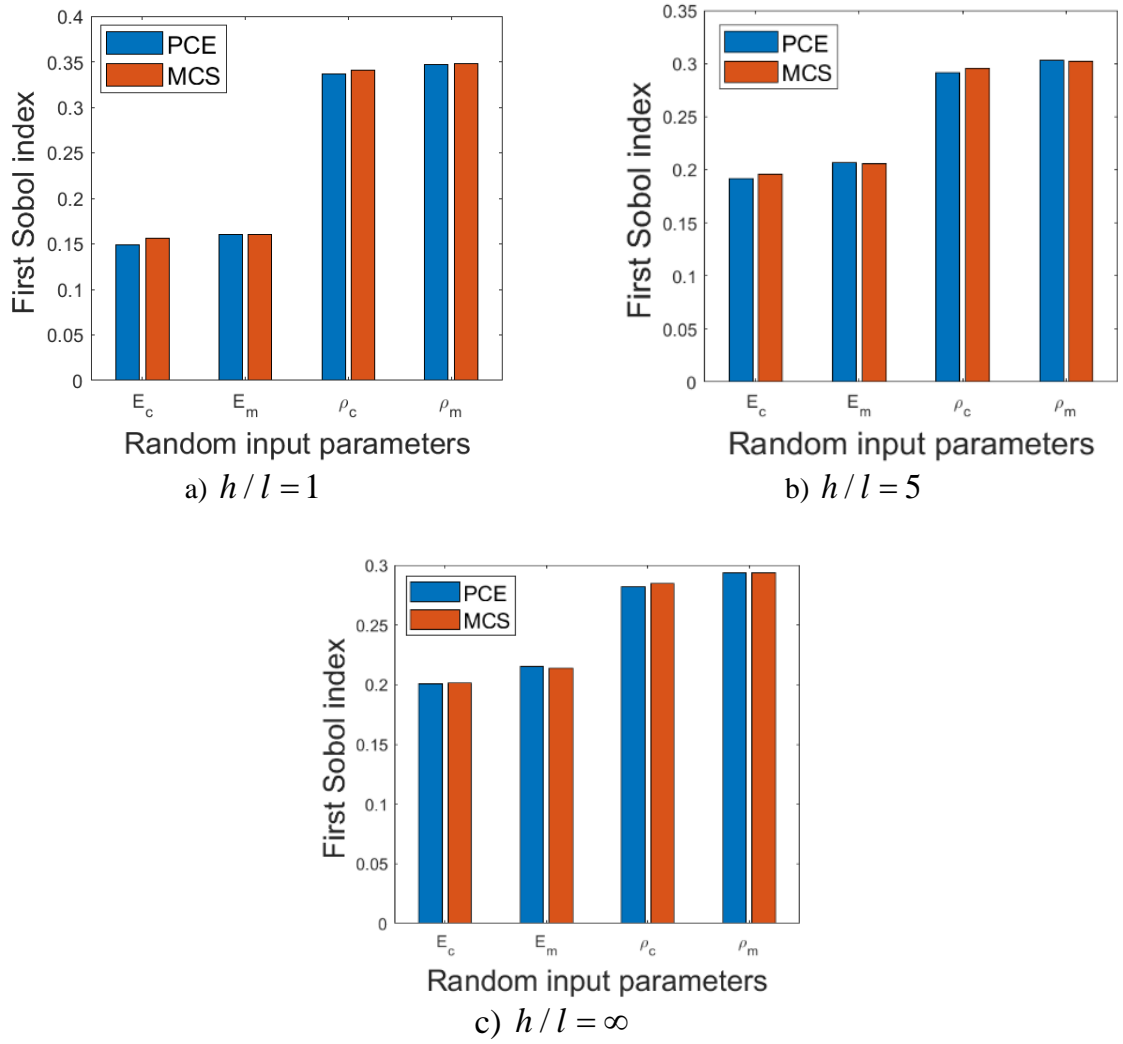


Figure 4.10: First Sobol index of the random input variables with respect to the fundamental frequencies of SSSS FG microplates ($p = 5, a/h = 10$)

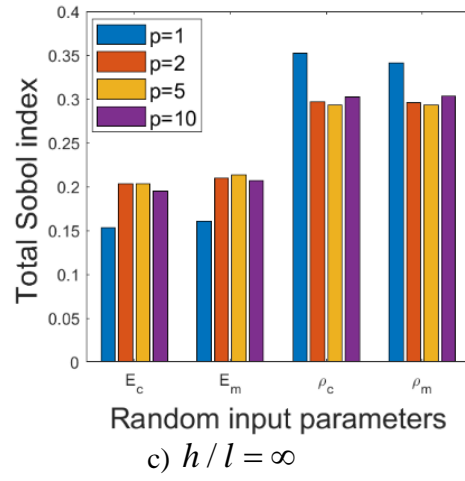
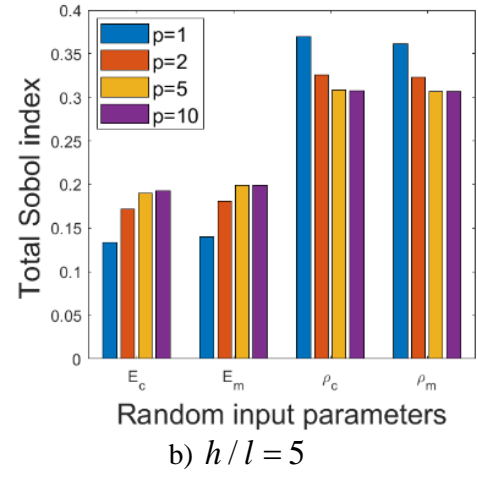
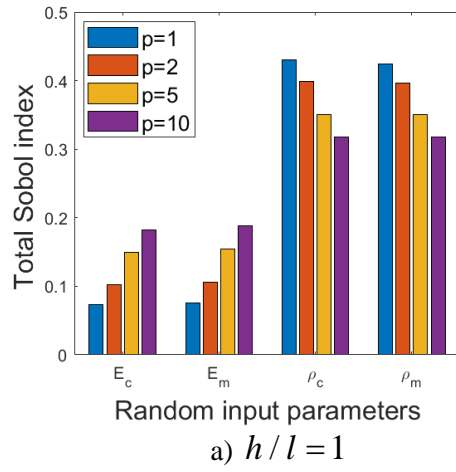


Figure 4.11: Total Sobol index of the random input variables with respect to the fundamental frequencies of the CCCC FG microplates ($a/h = 10$)

4.5.2 Stochastic thermal buckling analysis of FG sandwich microplates using stochastic collocation

They are made from a ceramic and metal whose mean material properties are given by:

- MAT 3: ZrO_2 ($E_c = 244.27 \text{ GPa}$, $\alpha_c = 12.766 \times 10^{-6} \text{ 1/C}$, $\nu_c = 0.3$),
 $\text{Ti} - \text{Al6} - 4\text{V}$ ($E_m = 66.2 \text{ GPa}$, $\alpha_m = 10.3 \times 10^{-6} \text{ 1/C}$, $\nu_m = 0.3$).
- MAT 4: Al_2O_3 ($E_c = 380 \text{ GPa}$, $\rho_c = 3800 \text{ kg/m}^3$, $\alpha_c = 7.4 \times 10^{-6} \text{ 1/C}$, $\nu_c = 0.3$),
 Al ($E_m = 70 \text{ GPa}$, $\rho_m = 2702 \text{ kg/m}^3$, $\alpha_m = 23 \times 10^{-6} \text{ 1/C}$, $\nu_m = 0.3$).

The following normalized parameters are used:

$$\bar{T}_{cr} = \Delta T_{cr} \times 10^{-3} \quad (4.30)$$

The material properties (E_c , E_m , and α_c , α_m) with MAT 3 mean values are taken to be used at random using the lognormal distributions with their coefficient of variation (COV) of 10% as a case-study. The proposed method can work for any continuous probability distributions with different values of COV. It should be mentioned that these distributions must be calibrated using experimental data for real application. The assumptions of lognormal distributions are appropriate for non-negative values. For comparison, 10,000 samples of the MCS are utilized.

For the SC model with the Gauss quadrature point $N_{gp} = 4$, only 256 samples are needed. Table 4.3 list the results of the FG sandwich microplates with $h/l = 1$ and $h/l = 5$ for two types of BCs, a/h and p . The statistical moments derived from SC and MCS exhibit strong concordance. It is noted that this case's computing time is around 1/10 of the time required by the direct MCS technique. Again, for both SC and MCS, the mean values of the critical buckling temperature are quite similar to the corresponding deterministic responses.

Table 4.3: The standard deviation (SD), mean, Skewness, Kurtosis for the biaxial thermal buckling of FG sandwich microplates (MAT 3, $a/h=10$) under linear distribution of SC (256 samples) and MCS (10.000 samples), $T_b = 25^\circ C$

BCs	p	Theory	Mean	SD	Kurtosis	Skewness	COV (%)	Time (s)	Present
1-1-1									
$h/l=1$									
SSSS	0.5	SC	10.0239	0.8972	3.7410	0.5955	8.9	30	9.9421
		MCS	10.0179	0.8962	3.7306	0.5927	8.9	325	
	2	SC	9.8862	0.8221	3.4865	0.5257	8.3	33	9.8221
		MCS	9.9028	0.8225	3.4923	0.5270	8.3	330	
CCCC	0.5	SC	37.4986	3.3337	3.4160	0.5005	9.0	40	37.1999
		MCS	37.4981	3.3363	3.4145	0.4994	9.0	342	
	2	SC	37.4604	3.1073	3.4426	0.4919	8.3	41	37.2542
		MCS	37.4520	3.1061	3.4461	0.4912	8.3	340	
$h/l=5$									
SSSS	0.5	SC	1.9025	0.1750	3.5750	0.5379	9.2	31	1.8857
		MCS	1.8990	0.1741	3.5568	0.5388	9.2	331	
	2	SC	1.6121	0.1451	3.4563	0.4883	9.0	32	1.5977
		MCS	1.6120	0.1459	3.4534	0.4870	9.0	343	
CCCC	0.5	SC	5.2057	0.4802	3.7467	0.5627	9.2	35	5.1644
		MCS	5.2083	0.4811	3.7479	0.5611	9.2	339	
	2	SC	4.5258	0.4083	3.5553	0.5651	9.0	33	4.5257
		MCS	4.5315	0.4093	3.5512	0.5664	9.0	342	
2-1-2									
$h/l=1$									
SSSS	0.5	SC	10.1009	0.8765	3.6702	0.5612	8.7	36	10.0190
		MCS	10.1144	0.8751	3.6789	0.5680	8.7	336	
	2	SC	10.0814	0.7879	3.6023	0.4996	7.8	32	10.0084
		MCS	10.0814	0.7875	3.6088	0.4978	7.8	340	
CCCC	0.5	SC	37.8308	3.2790	3.4421	0.4947	8.7	38	37.5191
		MCS	37.7803	3.2773	3.4489	0.4940	8.7	345	
	2	SC	38.1656	2.9707	3.3935	0.4623	7.8	35	37.9774
		MCS	38.0900	2.9685	3.3911	0.4637	7.8	339	
$h/l=5$									
SSSS	0.5	SC	1.9006	0.1756	3.6637	0.5696	9.2	32	1.8853
		MCS	1.8996	0.1749	3.6758	0.5677	9.2	330	
	2	SC	1.6355	0.1449	3.4050	0.4536	8.9	31	1.6221
		MCS	1.6344	0.1459	3.4225	0.4503	8.9	342	
CCCC	0.5	SC	5.2082	0.4516	3.6203	0.5790	8.7	37	5.1741
		MCS	5.2046	0.4527	3.6243	0.5781	8.7	336	
	2	SC	4.6453	0.3921	3.2125	0.3540	8.4	33	4.6020
		MCS	4.6464	0.3925	3.2137	0.3433	8.4	335	

Figs. 4.12–4.13 compare the linear quantile–quantile, probability of exceeding (PoE), and probability density function (PDF) of SC and MCS for the thermal buckling of the FG sandwich microplates with various BCs. It is clear that the SC method offers a feasible alternative approach for simulating the uncertainties of various material characteristics.

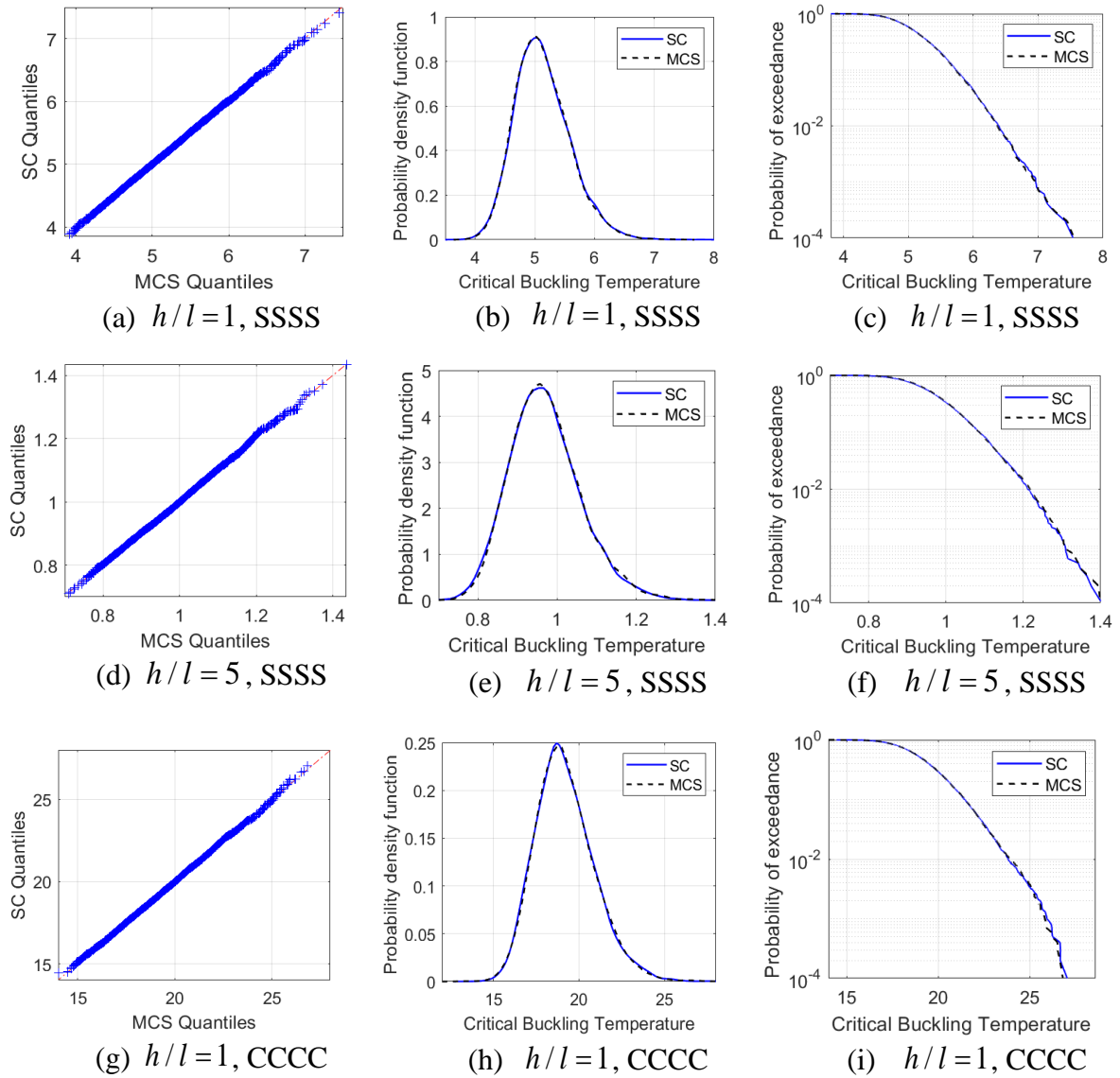


Figure 4.12: Quantile-quantile, PDF and PoE of MCS and SC for the critical buckling temperature of the (1-1-1) FG sandwich microplates under uniform distribution with SSSS, CCCC BCs (MAT 1, $p = 0.5$, $a/h = 10$)

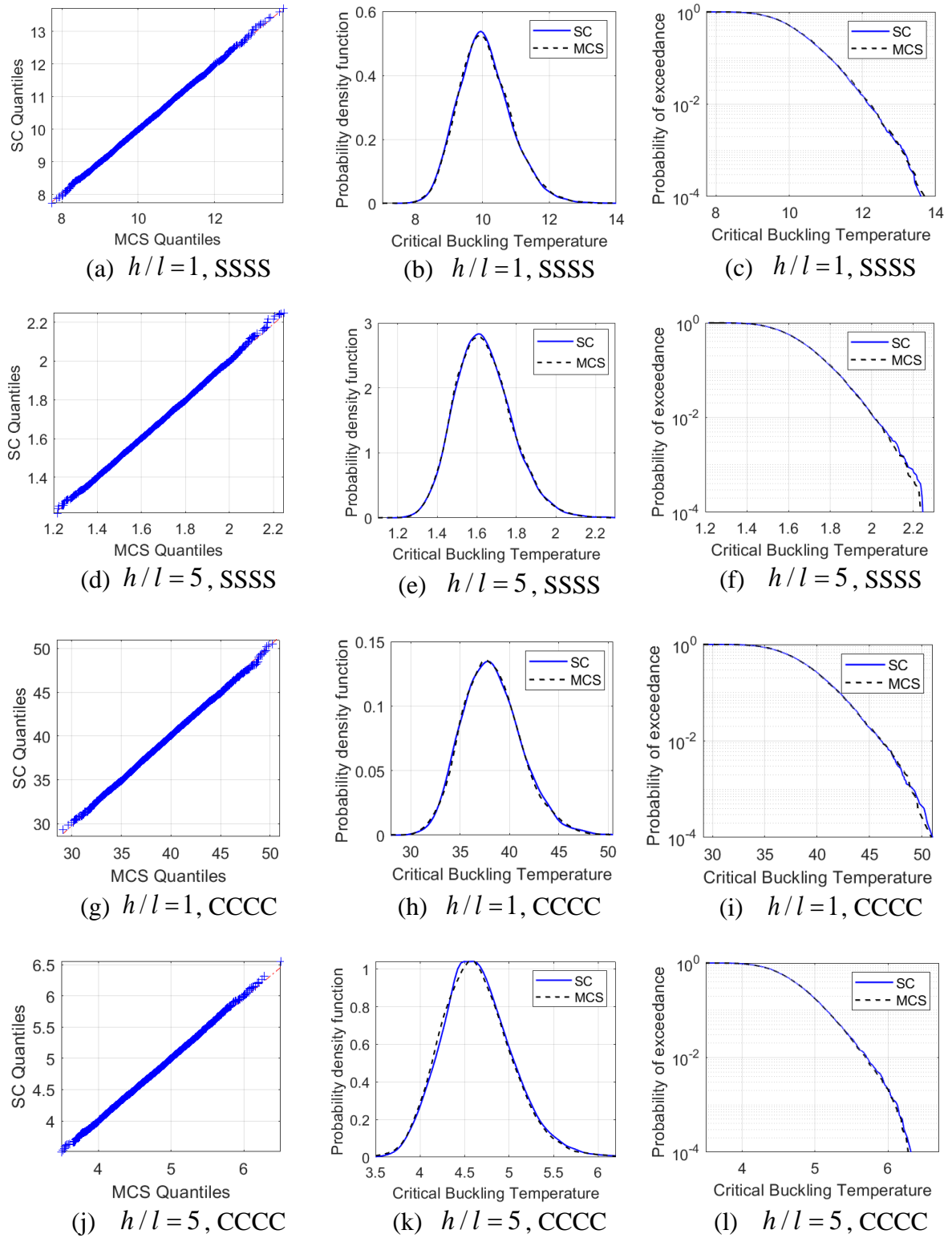


Figure 4.13: Quantile-quantile, PDF and PoE of MCS and SC for the critical buckling temperature of the (2-1-2) FG sandwich microplates under linear distribution with SSSS, CCCC BCs (MAT 1, $p = 2$, $a/h = 10$)

A decrease in critical buckling temperature is observed with an increase in the material length scale parameter with $h/l = \infty$ being the minimal value (Fig. 4.14).

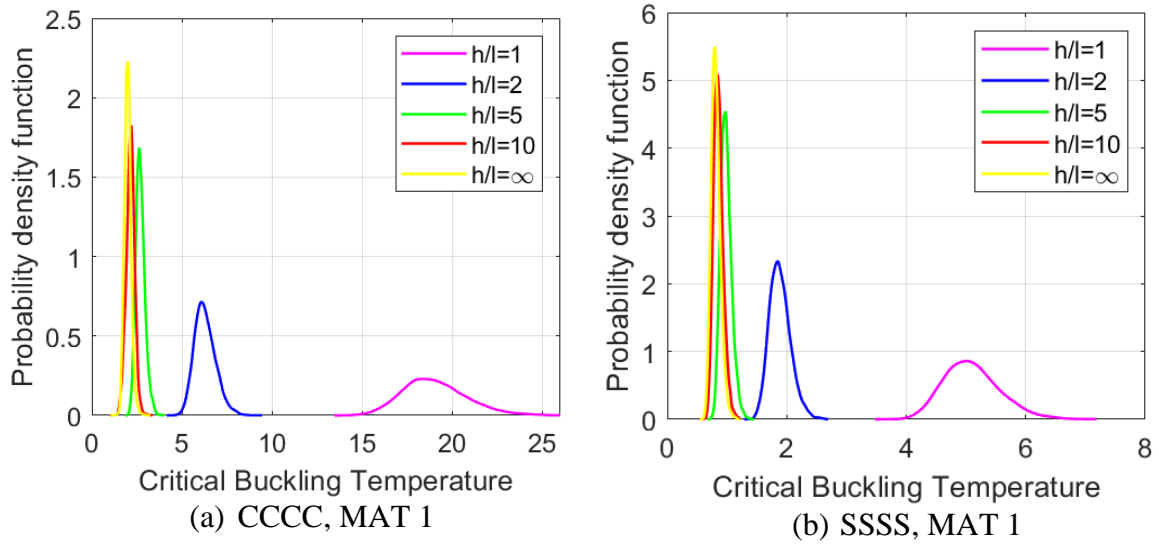


Figure 4.14: Probability density function (PDF) for the critical buckling temperature and free vibration of (1-2-1) FG sandwich microplates under uniform distribution with various ratio thickness to material h/l , ($a/h=10$, $p=0.5$)

Additionally, this graph interestingly shows that a decrease of h/l leads to the uncertainty expansion of the critical buckling temperature. It is interesting to see in Fig. 4.15 that when p decreases, the thermal buckling uncertainty appears to expand. It is similar when comparing the COV of these stochastic responses in Fig. 4.16. It is worth noting that even when maintaining a constant COV of the input random variables, the thermal buckling COV drops as p increases.

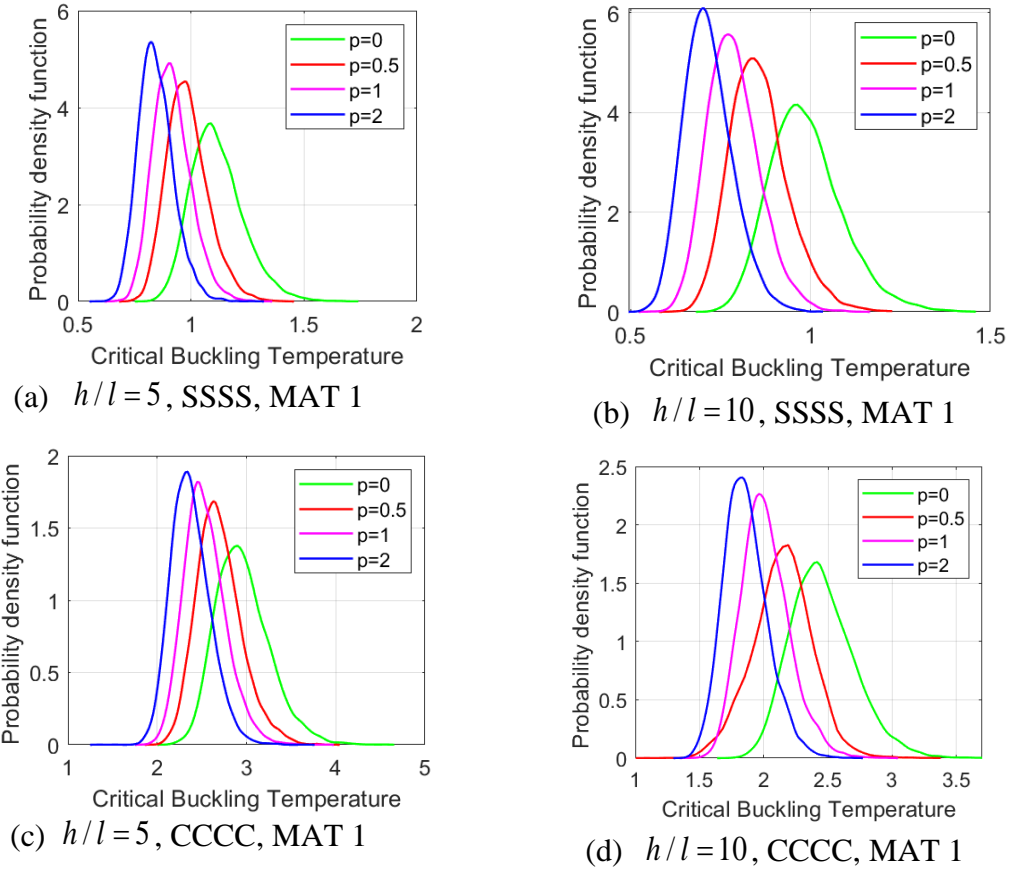


Figure 4.15: Probability density function (PDF) for the natural frequencies and critical buckling temperature of (1-2-1) FG sandwich microplates under uniform distribution with various power-law index p ($a/h=10$)

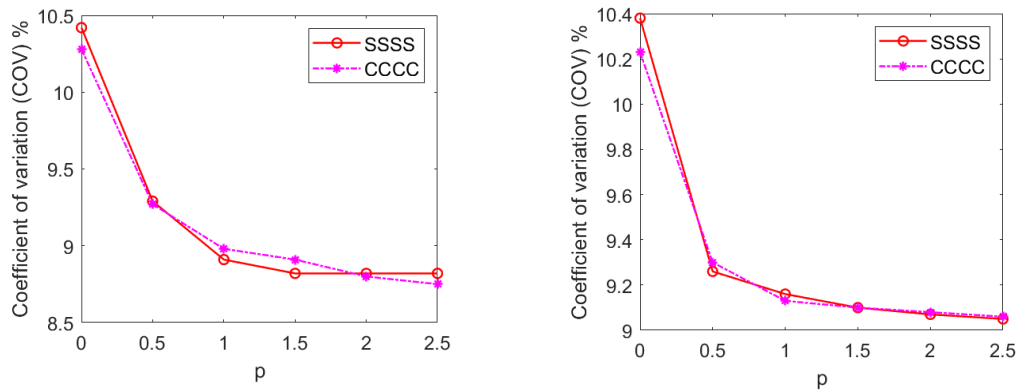


Figure 4.16: Coefficient of variation (COV) of critical buckling temperature (MAT 1) with respect to the power-law index p of the FG sandwich microplates (1-2-1) with various BCs and h/l , $a/h=10$ under uniform distribution

4.5.3 Stochastic vibration analysis of FGP microplates using BCMO-ANN algorithm

In this section [192], numerical examples are performed to investigate stochastic vibration and buckling responses of FGP microplates with three kinds of boundary conditions (SSSS, CSCS, CCCC), in which the shear function $\Psi(x_3) = \cot^{-1}(h/x_3) - 16x_3^3/15h^3$ ([141])) is used. The FGP microplates are supposed to be composed of a mixture of ceramic and metal materials whose mean properties are: Al_2O_3 ($E_c = 380$ GPa, $\rho_c = 3800$ kg/m³, $\nu_c = 0.3$), Al ($E_m = 70$ GPa, $\rho_m = 2702$ kg/m³, $\nu_m = 0.3$), whereas for stochastic analysis, Young's moduli and mass densities are assumed to be randomly distributed via a uniform distribution. For simplicity, the following normalized response parameters are used in the numerical examples:

$$\bar{\omega} = (\omega a^2 / h) \sqrt{\rho_c / E_c} \quad (4.31)$$

Moreover, in order to investigate stochastic behaviors of FGP microplates, four random variables of material properties ($E_{m,i}, E_{c,i}, \rho_{m,i}, \rho_{c,i}$) are employed with the population size $NP = 500$. It is noted that the weight and bias values are automatically updated according to Levenberg - Marquardt optimization, the number of nodes in each hidden layer is 21. The dataset, which consists of input-output pairs and training samples are randomly generated through iterations in the ANN training process. In addition, in the prediction process, training samples in the dataset are divided into two groups, in which 80% pairs in data is used for the training set and 20% for the test set. Tables 4.4-4.6 present the mean and standard deviation (SD) of normalized fundamental frequencies of Al/ Al_2O_3 FGP microplates with different boundary conditions for both Ritz-BCMO and BCMO-ANN models.

Table 4.4: Mean and standard deviation (SD) of normalized fundamental frequencies for FGP microplates with $a/h = 10$ and SSSS boundary condition

β	p	h/l	Theory	Mean	SD	Time(s)	Present
0.1	1	10	Ritz-BCMO	4.4049	0.0496	615	4.4073
			BCMO-ANN	4.4090	0.0491	10	
		1	Ritz-BCMO	11.0692	0.1051	617	11.0673
			BCMO-ANN	11.0745	0.1059	11	
		10	Ritz-BCMO	3.3994	0.0953	625	3.4012
			BCMO-ANN	3.4040	0.0961	10	
	10	5	Ritz-BCMO	3.5922	0.0997	623	3.6001
			BCMO-ANN	3.6037	0.0993	12	
		1	Ritz-BCMO	7.5662	0.1991	627	7.5531
			BCMO-ANN	7.5376	0.1983	10	
		10	Ritz-BCMO	2.8681	0.1277	631	2.8822
			BCMO-ANN	2.8645	0.1274	12	
0.2	1	10	Ritz-BCMO	4.2436	0.0509	630	4.2482
			BCMO-ANN	4.2456	0.0512	11	
		5	Ritz-BCMO	4.6082	0.0522	624	4.6121
			BCMO-ANN	4.6074	0.0530	11	
		1	Ritz-BCMO	11.1087	0.1075	628	11.1145
			BCMO-ANN	11.1292	0.1066	12	
	10	10	Ritz-BCMO	2.8681	0.1277	631	2.8822
			BCMO-ANN	2.8645	0.1274	12	
		5	Ritz-BCMO	3.0547	0.1323	630	3.0723
			BCMO-ANN	3.0676	0.1309	10	
		1	Ritz-BCMO	6.7642	0.2269	628	6.7687
			BCMO-ANN	6.7623	0.2270	11	

The solutions are computed with porous parameter $\beta = 0.1$ and 0.2 , side-to-thickness ratio $a/h = 10$, two values of the power-law index $p = 1$ and $p = 10$, length scale parameter $h/l = 10, 5, 1$. It can be seen that the statistical moments of normalized fundamental frequencies obtained from the Ritz-BCMO and BCMO-ANN show great agreements in all cases. The mean values of non-dimensional fundamental frequencies for both Ritz-BCMO and BCMO-ANN are close to the

deterministic result for all BCs, different power-law index p and porosity parameter β . As expected, the natural frequencies decrease with an increase of the porosity density, power-law index and length scale parameter. Regarding the computational cost, it can be observed that the computational time required by the present Ritz-BCMO method is about 55 times larger than that by the present BCMO-ANN method.

Table 4.5: Mean and standard deviation (SD) of normalized fundamental frequencies for FG microplates with $a/h = 10$ and CSCS boundary condition

BCs	β	p	h/l	Theory	mean	SD	Time(s)	Present
CSCS	0.1	1	10	Ritz-BCMO	5.9709	0.0661	629	5.9773
				BCMO-ANN	5.9776	0.0666	11	
			5	Ritz-BCMO	6.5932	0.0697	628	6.5935
				BCMO-ANN	6.6068	0.0703	12	
		10	1	Ritz-BCMO	16.9205	0.1596	630	16.9323
				BCMO-ANN	16.9302	0.1595	11	
			10	Ritz-BCMO	4.5456	0.1275	628	4.5427
				Ritz-MCS	4.5391	0.1287	11	
		5	1	Ritz-BCMO	4.8913	0.1382	631	4.9086
				BCMO-ANN	4.9023	0.1370	10	
	0.2	1	10	Ritz-BCMO	11.4432	0.3015	630	11.4652
				BCMO-ANN	11.4558	0.3012	11	
			5	Ritz-BCMO	5.7790	0.0689	620	5.7776
				BCMO-ANN	5.7884	0.0683	11	
			1	Ritz-BCMO	6.4178	0.0737	625	6.4255
				BCMO-ANN	6.4172	0.0736	10	
		10	1	Ritz-BCMO	17.0373	0.1633	623	17.0376
				BCMO-ANN	17.0405	0.1631	10	
			10	Ritz-BCMO	3.8388	0.1654	619	3.8509
				BCMO-ANN	3.8154	0.1669	10	
		5	1	Ritz-BCMO	4.2145	0.1769	621	4.2046
				BCMO-ANN	4.2134	0.1762	12	
			1	Ritz-BCMO	10.3099	0.3396	623	10.3087
				BCMO-ANN	10.2909	0.3409	11	

Table 4.6: Mean and standard deviation (SD) of normalized fundamental frequencies for FG microplates with $a/h = 10$ and CCCC boundary condition

BCs	β	p	h/l	Theory	Mean	SD	Time(s)	Present
CCCC	0.1	1	10	Ritz-BCMO	7.8171	0.0853	626	7.8053
				BCMO-ANN	7.8213	0.0848	11	
		5		Ritz-BCMO	8.7926	0.0918	628	8.7911
				BCMO-ANN	8.8009	0.0916	11	
		1		Ritz-BCMO	24.2602	0.2261	622	24.2394
				BCMO-ANN	24.2660	0.2246	10	
		10	10	Ritz-BCMO	5.8450	0.1658	629	5.8401
				Ritz-MCS	5.8386	0.1659	11	
			5	Ritz-BCMO	6.4137	0.1806	624	6.4284
				BCMO-ANN	6.4515	0.1806	12	
	0.2	1		Ritz-BCMO	16.3403	0.4260	630	16.3281
				BCMO-ANN	16.3219	0.4286	12	
			10	Ritz-BCMO	7.5722	0.0897	623	7.5793
				BCMO-ANN	7.5727	0.0884	10	
		5		Ritz-BCMO	8.5922	0.0947	625	8.6040
				BCMO-ANN	8.5938	0.0946	10	
		1		Ritz-BCMO	24.4008	0.2330	619	24.4211
				BCMO-ANN	24.3982	0.2328	12	
		10	10	Ritz-BCMO	4.9445	0.2153	631	4.9617
				BCMO-ANN	4.9350	0.2156	12	
			5	Ritz-BCMO	5.5006	0.2257	630	5.5266
				BCMO-ANN	5.4974	0.2265	12	
		1		Ritz-BCMO	14.6568	0.4808	628	14.7174
				BCMO-ANN	14.6502	0.4800	11	

In order to demonstrate the performance of present model further, Figs. 4.17 and 4.18 present the scatter plots and probability density function of the Ritz-BCMO model with BCMO-ANN one of the normalized fundamental frequencies for FG microplates with different boundary conditions, $p = 1$, $a/h = 10$, $h/l = 1$ and $h/l = 10$, respectively. These graphs indicates that the present BCMO-ANN model can effectively substitute the Ritz-BCMO for stochastic analysis with accuracy and significant saving of computational time. Additionally, Figs. 4.19 and 4.20 show the loss function and linear regression of normalized fundamental frequencies of FGP microplates with $p = 10$, $a/h = 10$, $\beta = 0.1$ and 0.2 . Obviously, MSE is smaller than 10^{-4} for both the training set and test set.

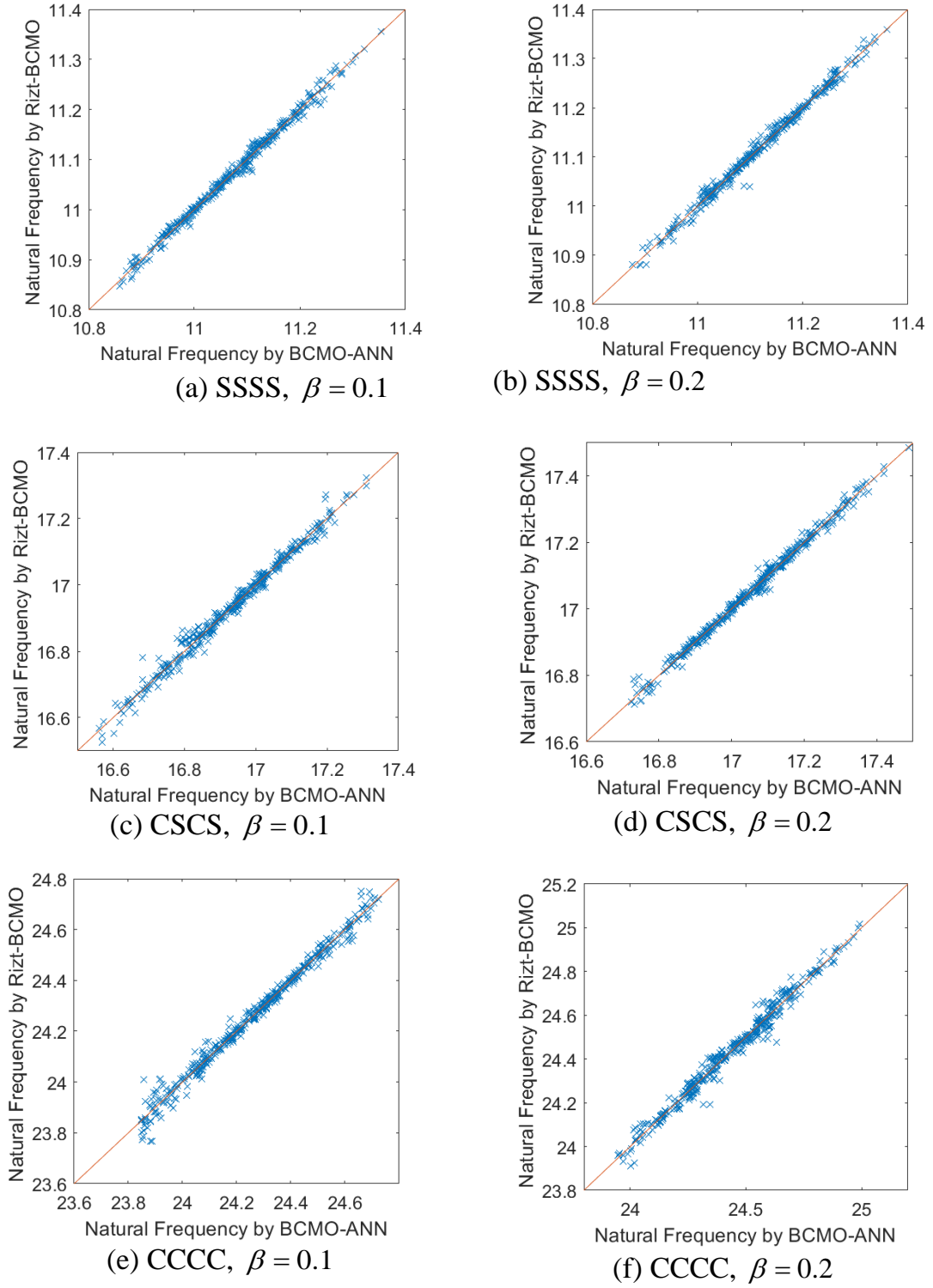
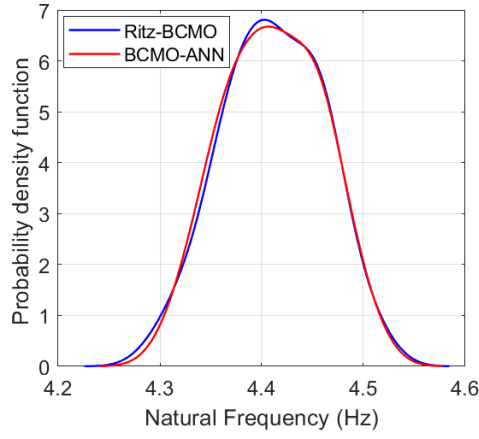
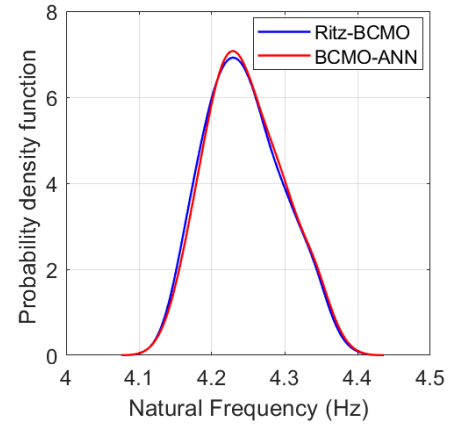


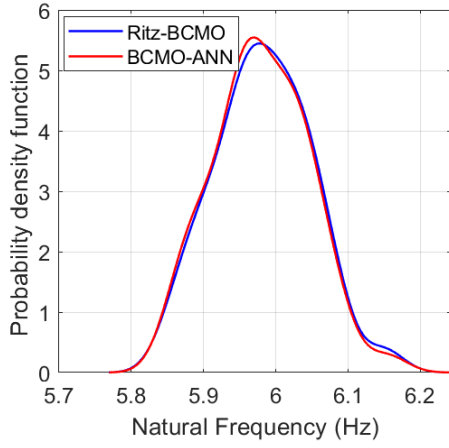
Figure 4.17: Scatter plot of the Ritz-BCMO model with ANN-BCMO one on the normalized fundamental frequencies for FGP microplates with different boundary conditions, $p = 1$, $a/h = 10$ and $h/l = 1$



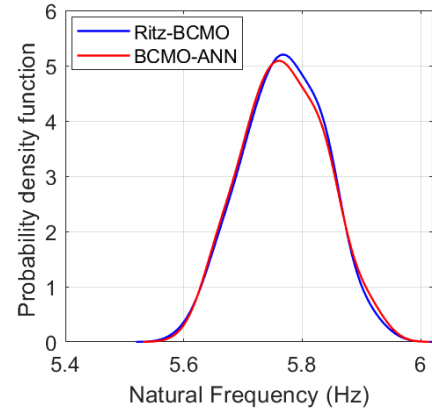
(a) SSSS, $\beta = 0.1$



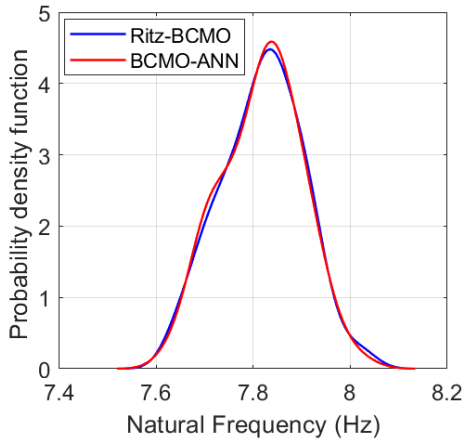
(b) SSSS, $\beta = 0.2$



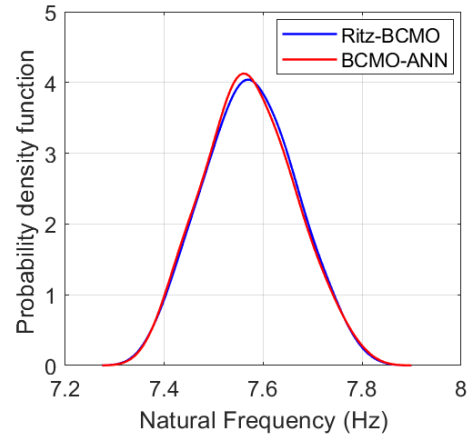
(c) CSCS, $\beta = 0.1$



(d) CSCS, $\beta = 0.2$

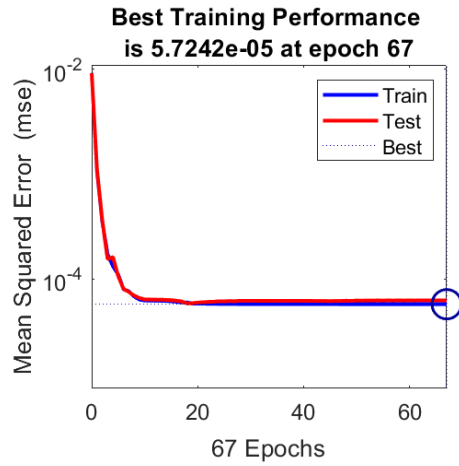


(e) CCCC, $\beta = 0.1$

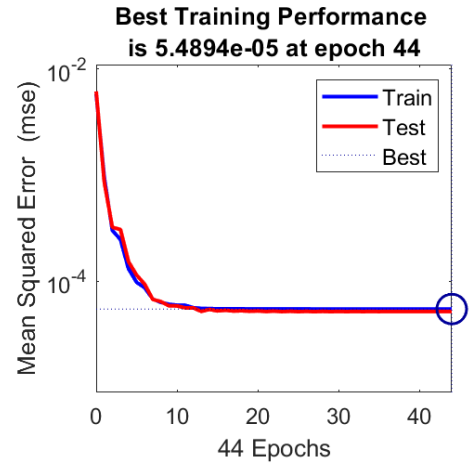


(f) CCCC, $\beta = 0.2$

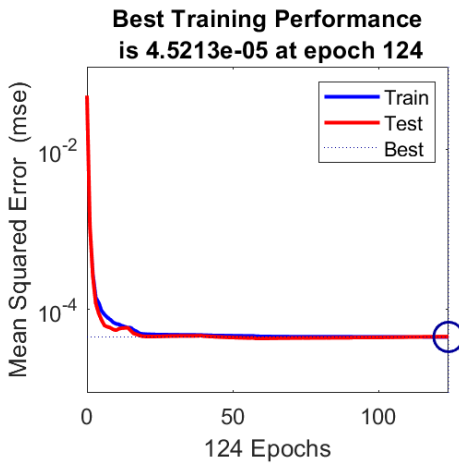
Figure 4.18: Probability density function (PDF) of Ritz-BCMO and BCMO-ANN methods for normalized fundamental frequencies of FGP microplates with different boundary conditions, $p = 1$, $a/h = 10$ and $h/l = 10$



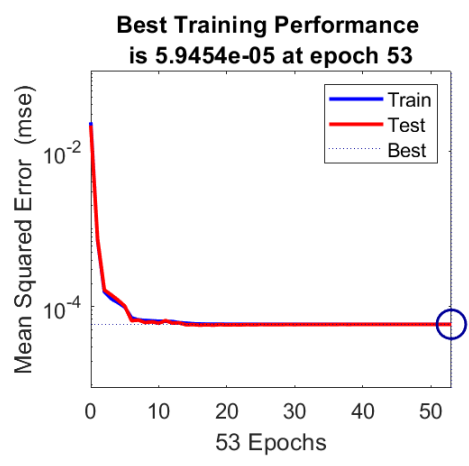
(a) SSSS, $\beta = 0.1$



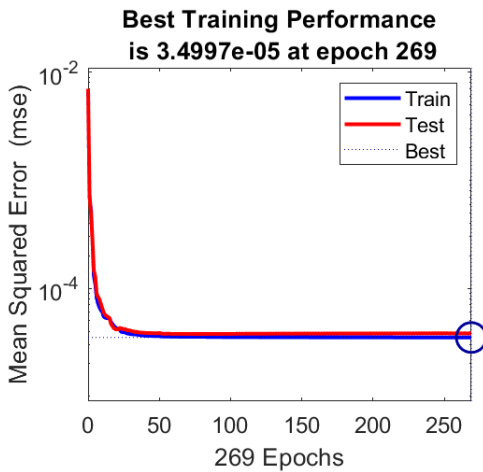
(b) SSSS, $\beta = 0.2$



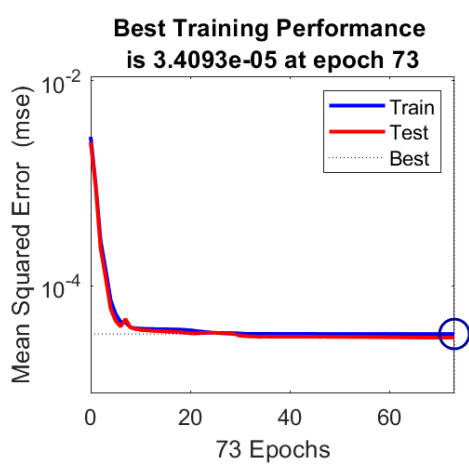
(c) CSCS, $\beta = 0.1$



(d) CSCS, $\beta = 0.2$



(e) CCCC, $\beta = 0.1$



(f) CCCC, $\beta = 0.2$

Figure 4.19: Loss function of the normalized fundamental frequencies for FGP microplates with different boundary conditions, $p = 10$, $a/h = 10$ and $h/l = 5$

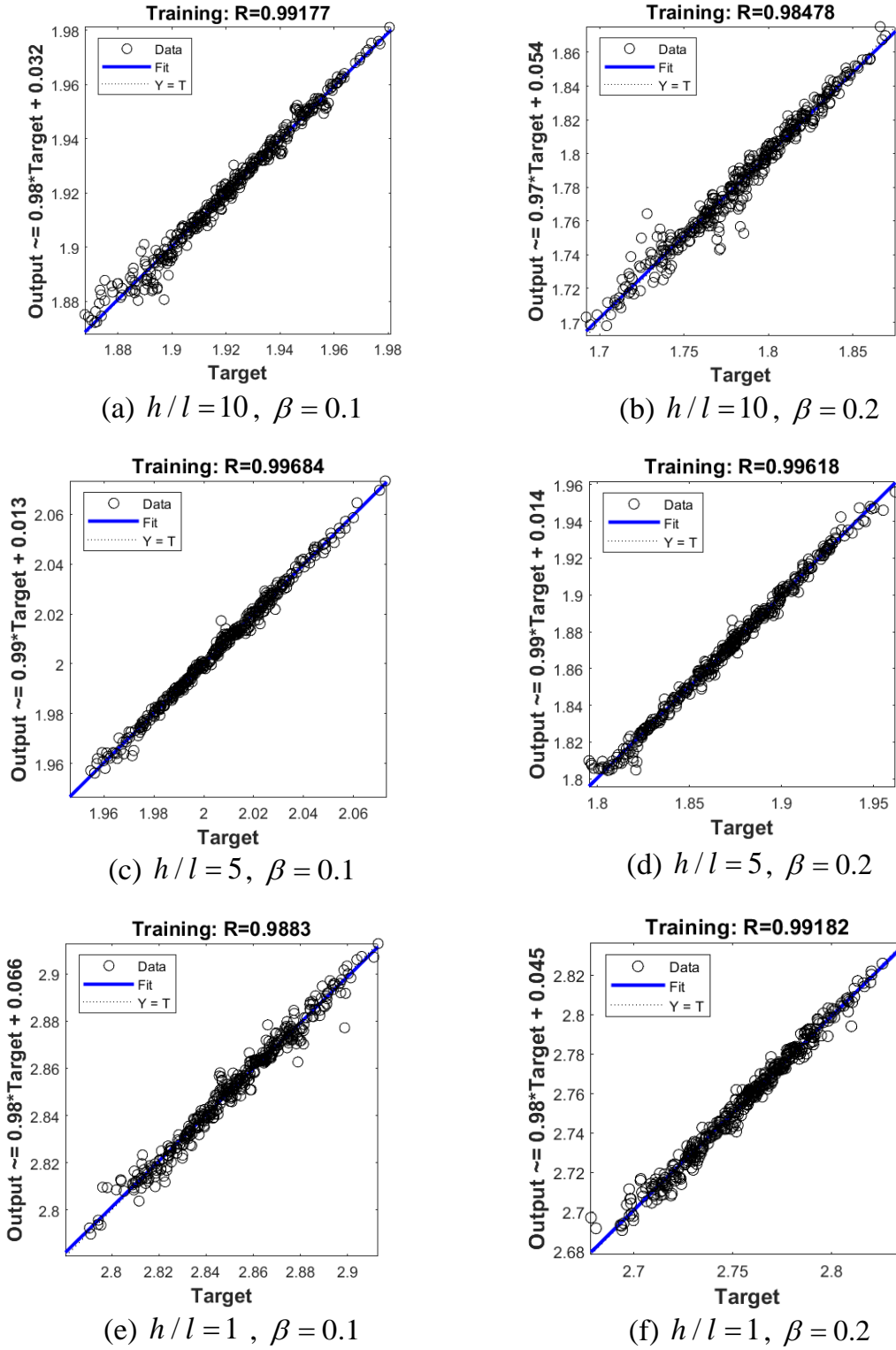


Figure 4.20: Regression of the normalized fundamental frequencies with log transfer function for FGP microplates with full clamped boundary condition, $p = 10$ and $a/h = 10$

4.5.4 Stochastic thermal buckling analysis of FGP microplates using iBCMO-DNN algorithm

In this section [193], numerical examples with the shear function $f(x_3) = x_3 - 4x_3^3 / 3h^2$ ([194]) are performed to explore the deterministic and stochastic responses of FGP microplates with various BCs. The FGP microplates are expected to be made of a combination of ceramic and metal materials with mean properties as follows: Al_2O_3 ($E_c = 380 \text{ GPa}$, $\rho_c = 3800 \text{ kg/m}^3$, $\alpha_c = 7.4 \times 10^{-6} \text{ 1/C}$, $\nu_c = 0.3$), Al ($E_m = 70 \text{ GPa}$, $\rho_m = 2702 \text{ kg/m}^3$, $\alpha_m = 23 \times 10^{-6} \text{ 1/C}$, $\nu_m = 0.3$). For simplification purpose, all three length scale parameters are considered to have the same value, i.e. $l_1 = l_2 = l_3 = l$. In practice, these material length scale values should be derived mainly via experimental data. Unless special mention, square FGP microplates with three BCs (SSSS, SCSC, CCCC) are considered in numerical examples, and for convenience, the following normalized parameters are used in the computations:

$$\bar{T}_{cr} = T_{cr} \times 10^{-3} \quad (4.32)$$

For stochastic analysis, the material characteristics ($E_m, E_c, \alpha_c, \alpha_m, p$) are assumed to be distributed randomly using uniform distributions, and the coefficient of variation (COV) is set at 10% for all random variables.

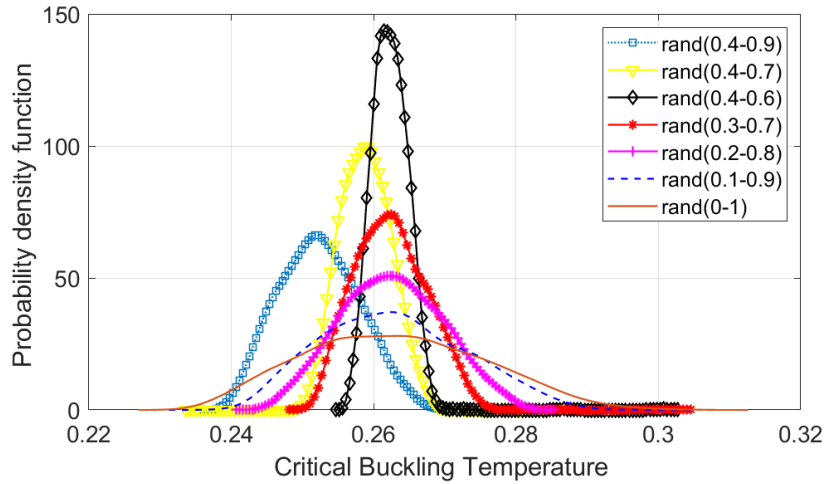
The objective of this example is to examine the optimal random range $[a_1, b_1]$ and probability threshold ζ serving for studying stochastic critical buckling temperatures of FGP microplates. As explained in the introduction section, the BCMO is a meta-heuristic algorithm which enables to optimize responses and save the computational costs ([107]). However, in practice, the original BCMO algorithm will take a long time to tackle complicated problems such as stochastic size effects. Alternatively, by narrowing the random range in $[a_1, b_1] \in [0, 1]$ and changing the probabilistic threshold ζ in the optimization process of solution field,

and using the DNN for learning behaviors, the present iBCMO-DNN provides a novel intelligent computational algorithm for solving stochastic problems. In order to determine the optimal random range $[a_1, b_1]$, Table 4.7 presents the comparison of the normalized critical buckling temperature \bar{T}_{cr} of simply supported Al/Al₂O₃ FGP square microplates under uniform temperature distribution.

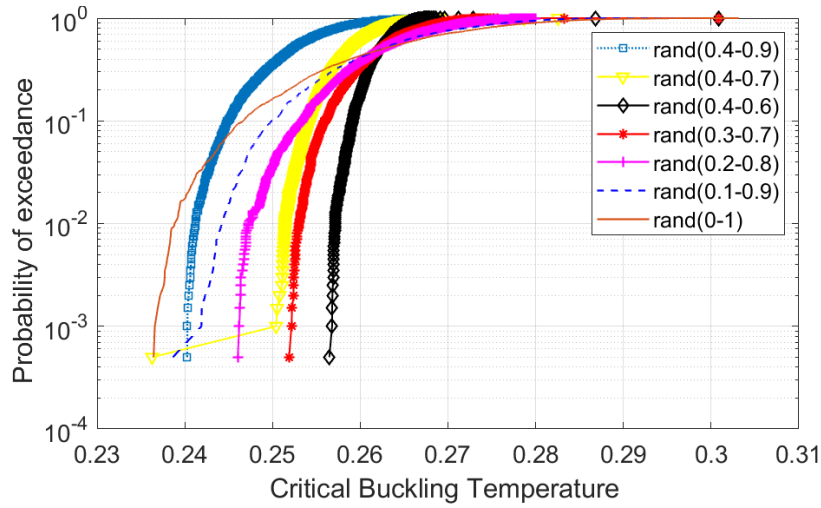
Table 4.7: Comparison of the *rand* coefficient of the Ritz-iBCMO algorithm for the normalized critical buckling temperature \bar{T}_{cr} of Al/Al₂O₃ FGP square microplates with $a/h = 20$, $\beta = 0.1$, $p = 1$, $h/l = 10$ with biaxial compression $(N_1^{(tr)}, N_2^{(tr)}, N_{12}^{(tr)} = 1, 1, 0)$ under uniform temperature distribution and simply supported

Theory	Mean	SD	Time(s)	Present
<i>rand</i> (0,1)	0.2630	0.0124	3611	0.2622
<i>rand</i> (0.1,0.9)	0.2628	0.0099	2156	
<i>rand</i> (0.2,0.8)	0.2624	0.0073	2116	
<i>rand</i> (0.3,0.7)	0.2624	0.0051	2107	
<i>rand</i> (0.4,0.6)	0.2623	0.0026	2066	
<i>rand</i> (0.4,0.7)	0.2589	0.0036	1952	
<i>rand</i> (0.4,0.9)	0.2523	0.0056	1999	

The results are computed with different random ranges $[a_1, b_1]$, length to thickness ratio $a/h = 20$, porous coefficient $\beta = 0.1$, power-index $p = 1$, material length scale parameter $h/l = 10$, biaxial compression $(N_1^{(tr)}, N_2^{(tr)}, N_{12}^{(tr)} = 1, 1, 0)$, and probability threshold $\zeta = 0.6$. It can be seen that as the random range steadily narrows, the standard deviation (SD) and computational time decreases. In comparison, the symmetry cases with *rand*(0.2,0.8), *rand*(0.3,0.7) and *rand*(0.4,0.6) show the rationality on the mean value and computational cost.



(a) Probability density function (PDF)



(b) Probability of exceedance (PoE)

Figure 4.21: Comparison of the efficiency of the *rand* coefficient differences for iBCMO algorithm of normalized thermal buckling load with biaxial compression, simply supported , $a/h = 20$, $p = 1$, $h/l = 10$, $\beta = 0.1$ under uniform distribution Moreover, in order to investigate the random range further, Fig. 4.21 displays the probability density function (PDF) and probability of exceedance (PoE) of normalized critical buckling temperature with various values of the random ranges. It is observed that the asymmetric ranges (0.4,0.7) and (0.4,0.9) provide significant deviations of the mean values with the exact value, therefore, the asymmetric ranges are not suitable for the present stochastic analysis. For the symmetric cases, it appears that the ranges of (0.3,0.7) and (0.4,0.6) present uneven graphs, while the

random range (0.2,0.8) is found to be appropriate for stochastic responses, therefore the random range $[a_1, b_1] = [0.2, 0.8]$ will be selected for the following numerical examples. Furthermore, Fig. 4.22 plots the probability density function of critical buckling loads of FGP microplates for different values of probabilistic threshold. It can be observed that the probability threshold coefficient $\zeta = 0.6$ has the most uniform data density, that numerically confirms the correctness of this coefficient in the computations.

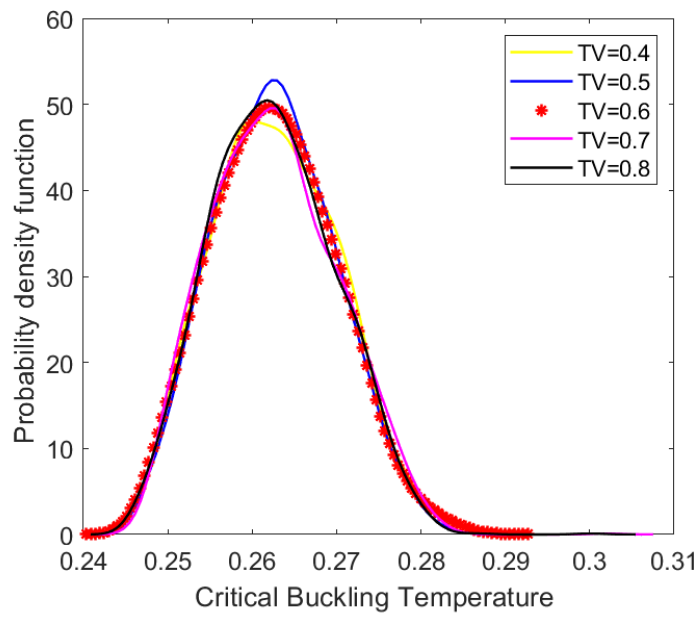


Figure 4.22: Comparison of the efficiency of the probabilistic threshold (TV) differences for iBCMO algorithm of normalized thermal buckling load with biaxial compression, simply supported , $a/h = 20$, $p = 1$, $h/l = 10$, $\beta = 0.1$ under uniform distribution

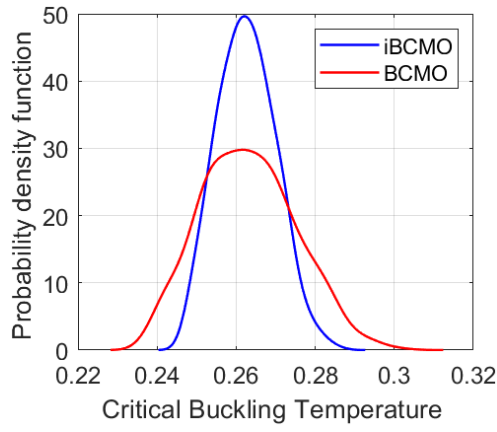
In order to demonstrate the performance of the present theory in predicting stochastic buckling temperatures of FGP microplates further, Table 4.8 introduces the comparison of both BCMO and iBCMO algorithm for normalized critical buckling temperature \bar{T}_{cr} of FGP microplates with $a/h = 20$, $\beta = 0.1$, $p = 1$ under uniform temperature distribution. It can be seen that the computational cost from the

iBCMO is lower about 1.7 times than that of the BCMO for different boundary conditions, with same mean values, the standard deviation from the iBCMO is much smaller than that from the BCMO.

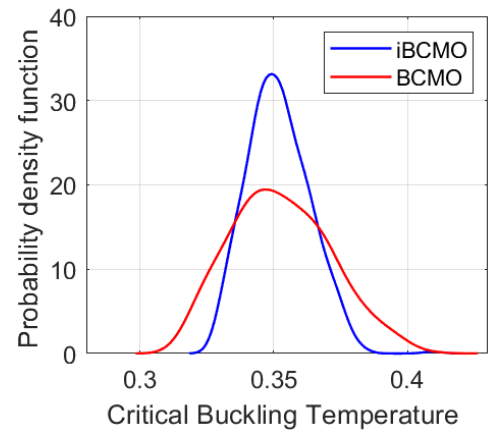
Table 4.8: Comparison between BCMO and iBCMO algorithms for the normalized critical buckling temperature \bar{T}_{cr} of Al/Al₂O₃ FGP square microplates with $a/h = 20$, $\beta = 0.1$, $p = 1$ with biaxial compression under uniform temperature distribution

BCs	h/l	Theory	Mean	SD	Time(s)	Present
SSSS	10	Ritz-BCMO	0.2634	0.0120	3611	0.2622
		Ritz-iBCMO	0.2624	0.0073	2116	
	1	Ritz-BCMO	4.4061	0.1996	3618	4.3917
		Ritz-iBCMO	4.3999	0.1169	2124	
SCSC	10	Ritz-BCMO	0.4250	0.0195	3683	0.4233
		Ritz-iBCMO	0.4243	0.0117	2127	
	1	Ritz-BCMO	7.1609	0.3134	3651	7.1462
		Ritz-iBCMO	7.1610	0.1900	2133	
CCCC	10	Ritz-BCMO	0.6860	0.0312	3653	0.6839
		Ritz-iBCMO	0.6850	0.0195	2123	
	1	Ritz-BCMO	11.6378	0.5202	3652	11.6128
		Ritz-iBCMO	11.6345	0.3095	2119	

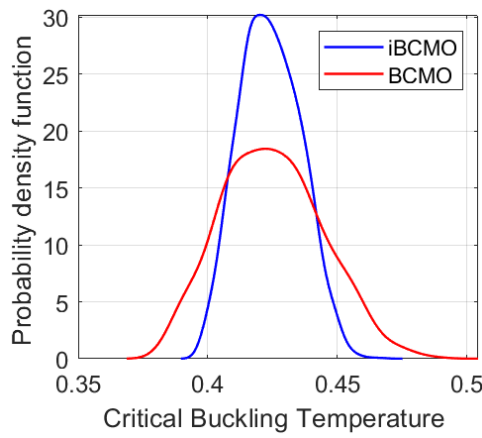
This is also verified in Fig. 4.23 which displays the probability density function of thermal buckling loads of FGP microplates with $a/h = 20$, $p = 1$ and $h/l = 10$ under uniform distribution.



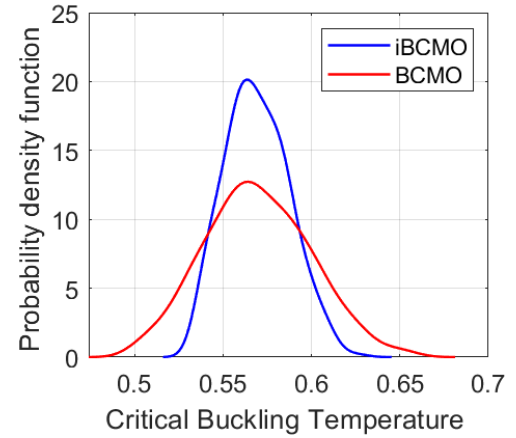
(a) SSSS, $\beta = 0.1$



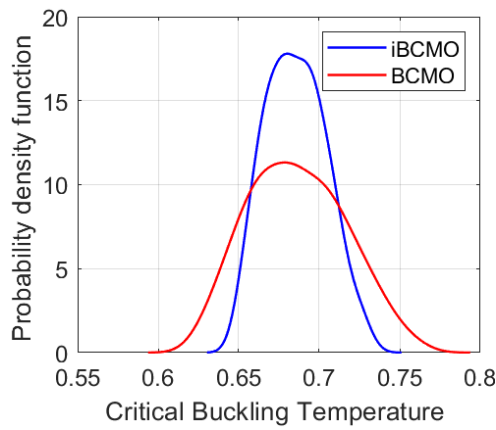
(b) SSSS, $\beta = 0.3$



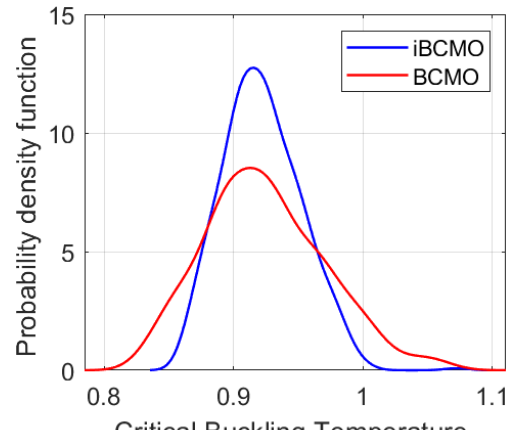
(c) SCSC, $\beta = 0.1$



(d) SCSC, $\beta = 0.3$



(e) CCCC, $\beta = 0.1$



(f) CCCC, $\beta = 0.3$

Figure 4.23: Comparison of the efficiency of iBCMO with the BCMO algorithm of normalized thermal buckling load , $a/h=20$, $p=1$, $h/l=10$ with biaxial compression under uniform distribution

In order to investigate stochastic critical buckling temperatures of FGP microplates, it is noted that five random variables of material properties ($E_{m,i}, E_{c,i}, \alpha_{t,i}, \alpha_{m,i}, \rho$) are designed to be randomly distributed with the same population size $NP = 2000$. Additionally, the data training was generated from the earlier analysis of Ritz-iBCMO solution. These values will be evaluated for the accuracy through the training process using the long short time memory model of the deep learning network. The initial normalization of the critical buckling temperatures is used as the output data for training samples, and these design factors are taken into consideration as the input data. Input-output pairs and randomly generated training samples are included in the data set, which is used to train the DNN. It is worthy to noticing that the DNN processing involves 500 iterations with one epoch between each one, the DNN structure is 110-110-4. The data were divided into two groups with 80% for the training set and 20% for the test set. The type of DNN is the long short time memory with tanh function for hidden layers and sigmoid function for output layer.

For Al/Al₂O₃ FGP microplates with three boundary conditions, the mean and standard deviation of normalized critical buckling temperatures from the Ritz-iBCMO and iBCMO-DNN models are shown in Tables 4.9–4.11. The critical buckling temperature responses are computed for the side-to-thickness ratio $a/h = 20$, porous parameter $\beta = 0.1$ and 0.3 , power-law index $p = 0.5$ and 2 , length scale parameter $h/l = 1$ and 10 . Obviously, the statistical moments of the critical buckling temperatures derived from the Ritz-iBCMO and iBCMO-DNN show good agreements for all cases. For all BCs, varied power-law indexes p , and porosity parameters β , the mean values of the critical buckling temperatures for the Ritz-iBCMO and iBCMO-DNN are close to the deterministic responses. As expected, the critical buckling temperatures rise with the increase of β and h/l . In comparison of the computational time between the theories, the iBCMO-DNN approach takes less computational times than the Ritz-iBCMO method. The

computational time of the iBCMO-DNN method is about 2/5 that of the Ritz-iBCMO method.

Table 4.9: Mean and standard deviation (SD) of normalized critical buckling temperature for FGP microplates with biaxial compression, $a/h = 20$, SSSS under uniform temperature distribution

β	P	h/l	Theory	Mean	SD	Time(s)	Present
0.1	0.5	10	Ritz-iBCMO	0.3291	0.0089	2123	0.3284
			iBCMO-DNN	0.3307	0.0091	845	
		1	Ritz-iBCMO	5.1633	0.1343	2125	5.1596
			iBCMO-DNN	5.1688	0.1347	844	
	2	10	Ritz-iBCMO	0.2239	0.0066	2124	0.2236
			iBCMO-DNN	0.2259	0.0071	845	
		1	Ritz-iBCMO	3.8358	0.1084	2123	3.8278
			iBCMO-DNN	3.8315	0.1082	846	
0.3	0.5	10	Ritz-iBCMO	0.4960	0.0152	2121	0.4952
			iBCMO-DNN	0.4995	0.0151	840	
		1	Ritz-iBCMO	8.6618	0.2454	2126	8.6440
			iBCMO-DNN	8.6669	0.2460	841	
	2	10	Ritz-iBCMO	0.2373	0.0122	2127	0.2370
			iBCMO-DNN	0.2389	0.0124	842	
		1	Ritz-iBCMO	6.2104	0.1712	2123	6.2009
			iBCMO-DNN	6.2155	0.1718	843	

Table 4.10: Mean and standard deviation (SD) of normalized critical buckling for FGP microplates with biaxial compression, $a/h = 20$, SCSC under uniform temperature distribution

β	p	h/l	Theory	Mean	SD	Time(s)	Present
0.1	0.5	10	Ritz-iBCMO	0.5307	0.0147	2129	0.5299
			iBCMO-DNN	0.5311	0.0146	841	
		1	Ritz-iBCMO	8.4103	0.2165	2127	8.3968
			iBCMO-DNN	8.4133	0.2173	845	
	2	10	Ritz-iBCMO	0.3614	0.0106	2124	0.3607
			iBCMO-DNN	0.3658	0.0108	843	
		1	Ritz-iBCMO	6.2261	0.1744	2122	6.2152
			iBCMO-DNN	6.2249	0.1740	840	
0.3	0.5	10	Ritz-iBCMO	0.8008	0.0243	2133	0.7999
			iBCMO-DNN	0.8014	0.0244	842	
		1	Ritz-iBCMO	14.1140	0.3999	2128	14.0821
			iBCMO-DNN	14.1184	0.4009	844	
	2	10	Ritz-iBCMO	0.3843	0.0195	2127	0.3839
			iBCMO-DNN	0.3849	0.0197	843	
		1	Ritz-iBCMO	10.1095	0.2818	2124	10.0882
			iBCMO-DNN	10.1109	0.2826	841	

Table 4.11: Mean and standard deviation (SD) of normalized critical buckling for FGP microplates with biaxial compression, $a/h = 20$, CCCC under uniform temperature distribution

β	p	h/l	Theory	Mean	SD	Time(s)	Present
0.1	0.5	10	Ritz-iBCMO	0.8568	0.0229	2122	0.8555
			iBCMO-DNN	0.8575	0.0231	840	
		1	Ritz-iBCMO	13.6636	0.3535	2125	13.6417
			iBCMO-DNN	13.6659	0.3541	841	
	2	10	Ritz-iBCMO	0.5831	0.0170	2124	0.5825
			iBCMO-DNN	0.5838	0.0172	840	
		1	Ritz-iBCMO	10.1182	0.2835	2124	10.1004
			iBCMO-DNN	10.1197	0.2842	843	
0.3	0.5	10	Ritz-iBCMO	1.2957	0.0395	2119	1.2936
			iBCMO-DNN	1.2967	0.0398	844	
		1	Ritz-iBCMO	22.9234	0.6409	2121	22.8856
			iBCMO-DNN	22.9287	0.6413	843	
	2	10	Ritz-iBCMO	0.6249	0.0316	2127	0.6233
			iBCMO-DNN	0.6255	0.0318	842	
		1	Ritz-iBCMO	16.4441	0.4720	2126	16.4167
			iBCMO-DNN	16.4458	0.4726	844	

Additionally, the performance of the current iBCMO-DNN algorithm in predicting buckling temperature responses is also shown in Figs. 4.24–4.26 in which the mean square error is almost nil for both training and test sets. Fig. 4.25 describes the probability density function of the critical buckling temperatures generated from the Ritz-iBCMO and iBCMO-DNN analysis. It can be seen again that the results of iBCMO-DNN are in good agreement with Ritz-iBCMO. This proves that the present model in capturing size effects with uncertainty of material properties based on the unified HSDT, Ritz solution and iBCMO-DNN is completely reliable.

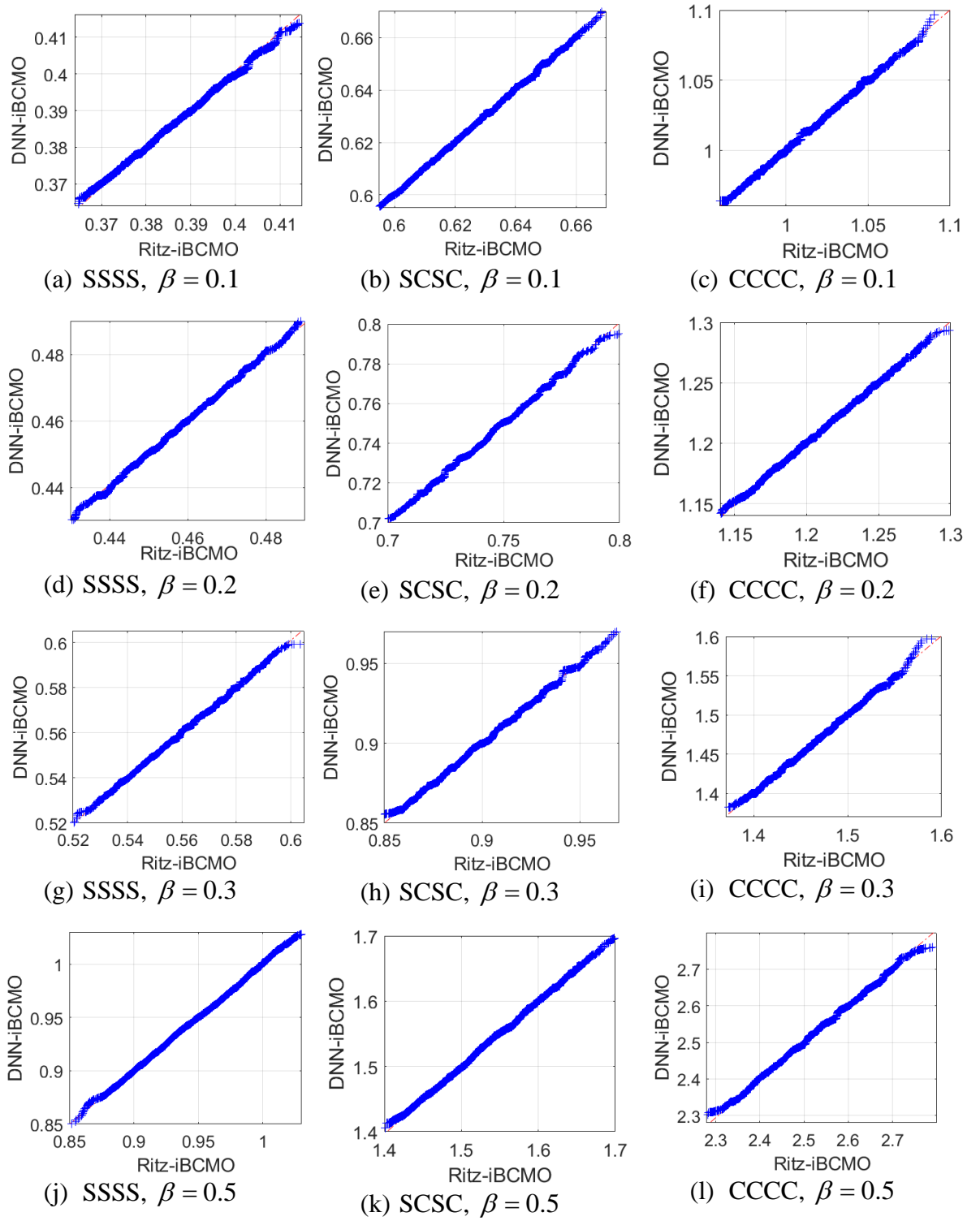


Figure 4.24: Quantile-quantile plot of the Ritz-iBCMO model with DNN-iBCMO, $a/h = 20$, $p = 1$, $h/l = 5$, biaxial compression under uniform distribution

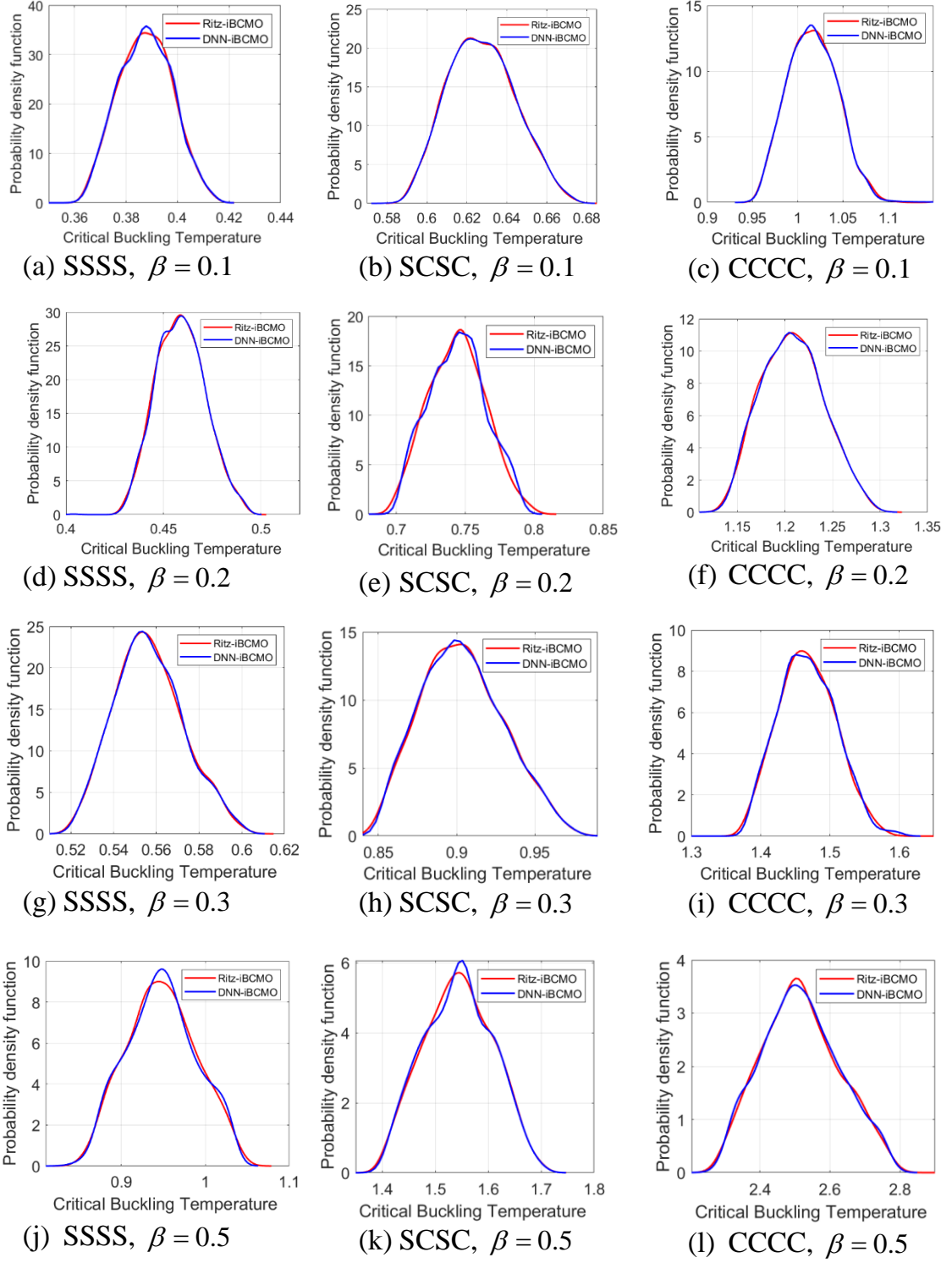
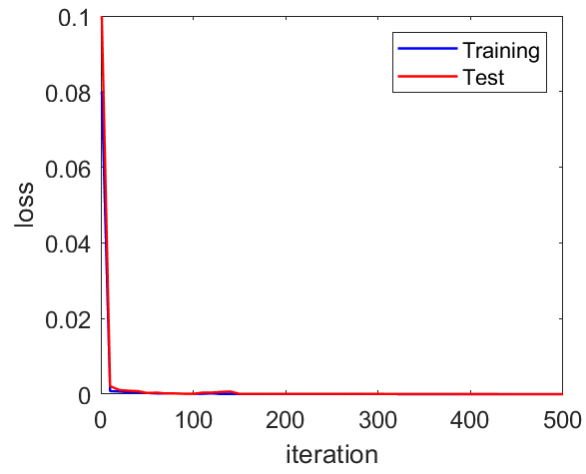
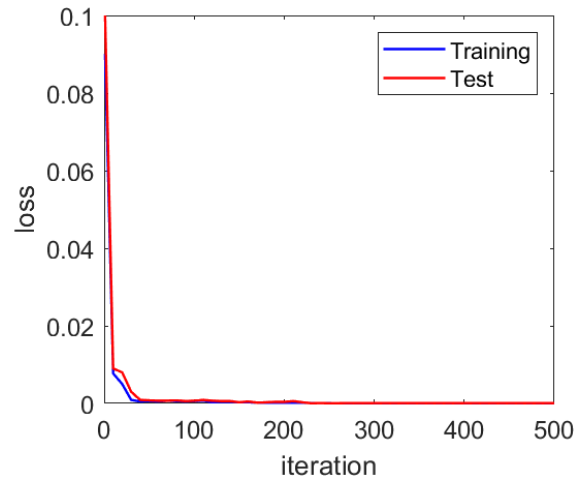


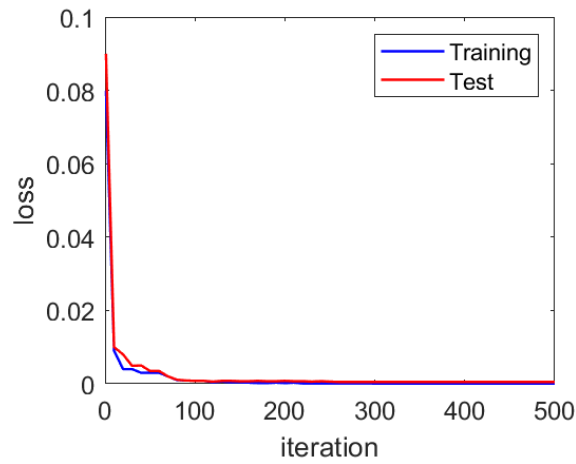
Figure 4.25: Probability density function (PDF) of Ritz-iBCMO and iBCMO-DNN methods the normalized thermal buckling with $a/h = 20$, $p = 1$, $h/l = 5$, biaxial compression under uniform distribution



(a) SSSS



(b) SCSC



(c) CCCC

Figure 4.26: Loss function of the normalized critical buckling temperature with $a/h = 20$, $h/l = 5$, $\beta = 0.3$

4.6. Conclusions

In order to investigate the stochastic responses of microplates under uncertainty in material properties, the Polynomial Chaos Expansion (PCE), Stochastic Collocation (SC) method, and Monte Carlo method are employed. Moreover, this research proposed a novel intelligent computational algorithm, iBCMO-DNN, for stochastic buckling temperature analysis of microplates with uncertainty of material properties. A combination of BCMO-ANN has been proposed to predict stochastic vibration behaviors of microplates subjected to uncertainties of material properties. The DNN with the long short-term memory model has been employed as a surrogate method to replace the time-consuming computational model, while the iBCMO for searching the set of optimal solutions. The deterministic responses of the microplates are obtained from a unified HSDT, MST and Ritz-type series approximation. The Ritz-BCMO, BCMO-ANN, the Ritz-iBCMO and iBCMO-DNN algorithms are developed for investigation of the impacts of material distribution, material length scale parameters, porosity density, temperature variations and boundary conditions on the static, natural frequencies, critical buckling loads and the critical buckling temperatures of microplates. The obtained numerical results showed the accuracy and efficiency of the present model in predicting stochastic behaviors of microplates. The following significant points might be deduced as follows:

- The proposed unified size dependent plate model presents the accuracy and efficiency in predicting stochastic vibration and buckling behaviors of the microplates.
- By applying the polynomial chaos expansion, only 256 and 16 samples are needed to compute stochastic fundamental frequency which is much less than the sample size of 10,000 of the Monte Carlo Simulation.
- In contrast to the Monte Carlo Simulation, which requires 10,000 samples, the stochastic collocation approach requires just 256 samples to calculate stochastic thermal buckling.

- Proposed BCMO-ANN algorithm allows to significantly save computational costs. The computational time of natural frequencies required by the BCMO-ANN method is about 1/55 times that of the Ritz-BCMO method.
- The computational cost of the proposed iBCMO algorithm is lower 1.7 times than that of the BCMO.
- The proposed iBCMO-DNN algorithm provides for substantial cost savings in computing. The computational time of critical buckling temperatures from the iBCMO-DNN approach requires approximately 2/5 that from the Ritz-iBCMO method.

Furthermore, metaheuristic optimization methods have recently such as BCMO and SGA been recognized as robust and reliable approaches for solving a wide range of complex optimization problems, attracting significant attention from the research community. Accordingly, in the following chapter, recent novel metaheuristic optimization techniques will be employed to optimize the fiber orientation of laminated composite plates. This will be carried out using the unified higher-order shear deformation theory in conjunction with the hybrid shape function proposed in Chapter three.

CHAPTER 5

META-HEURISTIC OPTIMIZATION ALGORITHMS FOR VIBRATION AND BUCKLING ANALYSIS OF LAMINATED COMPOSITE PLATES

This chapter applies meta-heuristic optimization algorithms for vibration and buckling analysis of laminated composite (LC) plates. It is a combination of unified higher-order shear deformation (HSDT) theory, Ritz method, and three optimization algorithms, namely shrimp and goby association search algorithm (SGA), balancing composite motion optimization (BCMO) and differential evolution (DE). The Ritz method with hybrid shape functions is utilized to solve the optimization problems by employing the Gram-Schmidt process to construct the approximation functions. The SGA and BCMO are employed for the first time to ascertain the optimal buckling loads and frequencies of laminated composite plates. Numerical examples are conducted to investigate the influence of fiber angle, modulus ratio, and different boundary conditions on the optimal results. It indicates that the BCMO and SGA are efficient and robust algorithms for addressing the optimization problems of laminated composite plates.

5.1. Introduction

Laminated composite plates have found extensive applications in engineering fields such as mechanical engineering, aerospace, construction, and more ([210-214]). Among the critical factors influencing their mechanical properties, the customization of fiber orientation is a pivotal element in shaping structural stiffness. In practice, achieving optimal fiber orientation demands a complex computational process, which has drawn the interest of numerous researchers employing various computational approaches.

In order to optimize responses of the laminated composite structures, meta-heuristic optimization methods have been recently considered as robust and reliable approaches for a wide range of complicated optimization problems. The core components of metaheuristic algorithms are exploration and exploitation. Exploration involves thoroughly searching the entire solution space to generate a variety of potential solutions, while exploitation focuses on refining the search within specific regions to identify the best solutions based on the knowledge gained from previous candidates. Randomization plays a crucial role in exploration, helping to avoid getting stuck in local optima. By such a way, metaheuristic optimization algorithms could approach to global optimization solutions. In general, meta-heuristic optimization algorithms [215] could be divided in three popular categories. The first category is inspired by the phenomenon of evolution observed in the natural world in which the algorithms are generally derived from the principles of Charles Darwin. Based on this approach, a number of optimization algorithms have been developed such as Differential Evolution (DE) [101], Genetic Algorithms (GA) [102]. In general, they directly utilize the objective function and constraints to seek optimal solutions. The selection of an optimal candidate for the next generation necessitates consideration of their capacity to adapt and thrive within their ecological surroundings. Some representative earlier works are herein cited for optimization of LC plates. Karakaya et al. [216] compared the optimal buckling results of GA method with the generalized pattern search algorithm. Ho et al. [217] employed the DE method and the smoothed FEM to analyze optimal buckling responses, taking into account fiber angle and layer thickness as design variables. By using the NSGA-II and GA algorithms, Kalantari et al. [218] investigated the minimum flexural strength of LC plates with design variables being fiber angle and fiber volume fraction. Drosopoulos et al. [219] used NSGA-II and FEM to scrutinize the maximum frequency of LC plate with layer thickness, fiber distribution, and fiber angles as design variables. Moreover, the second type of meta-heuristic optimization algorithms encompasses swarm-based approaches, from

which a number of optimization algorithms have been developed such as Ant colony optimization (ACO) [220], shrimp and goby association search algorithm (SGA)[110], dragonfly algorithm (DA) [221], particle swarm optimization (PSO) [222], salp swarm algorithm (SSA)[223]. The SGA is developed without depending on input parameters. Its concept is inspired by the symbiotic relationship between shrimp and goby fishes in their natural habitat. In this ecosystem, the goby uses the shrimp's burrow as a haven during the day and a regular resting place at night. Essentially, the security level of the shelter is contingent upon the shrimp's capacity to allure the gobiid fish. It is noted that the efficacy of these algorithms relies on the synchronization of a collective of particles, which impedes the ability to discern and independently assess individual particles. Instead, particles participate in collective communication to determine their subsequent course of action. A collective of agents engaged in continuous movement and interaction across several activities is often known as a particle swarm. The use of these algorithms for optimization of laminated composite plates could be mentioned in the following earlier works. By using a HSDT, isogeometric method (IGA) and the PSO algorithm, Shafei et al. [224] investigated the minimum frequency of LC plates. Based on the HSDT, FEM and PSO, Vosoughi et al. ([225, 226]) studied the optimal buckling loads of LC plates with design variables as fiber orientations. Finally, the third set of meta-heuristic optimization algorithms comprises those influenced by physical principles. In order to direct the movement of particles throughout the optimization process, these algorithms take their cues from the most fundamental scientific laws. Some examples of these types of algorithms are the balancing composite motion optimization (BCMO) [107], the curved space optimization (CSO) [227], and the water wave optimization (WWO) [228]. These principles include the dynamics of magnetic fields, the gravitational interactions among celestial bodies, electron charge transfers, chemical processes. More importantly, these algorithms typically necessitate interrelated parameters and involve substantial computational expenses. Besides, it can be observed that the recent development of the BCMO eliminates the

need for interdependent parameters to address this challenge. This approach draws inspiration from assuming the solution space operates within Cartesian coordinates, balancing the global and local search movements of potential solutions. Indeed, a potential solution can approach superior solutions to exploit local areas and extend further to explore the search landscape. Consequently, the highest-ranked individual in each generation can swiftly transition between spaces or enhance its existing local exploration.

A brief literature survey indicates that the BCMO and SGA algorithms are recognized as efficient methods for structural optimization. However, no research has been identified that specifically employs these algorithms for solving optimization problems related to laminated composite plates. This study aims to address this gap by proposing meta-heuristic optimization algorithms to determine the critical buckling loads and fundamental frequencies of laminated composite plates. Additionally, a new hybrid shape function for the Ritz method is also presented in this study. The theoretical framework incorporates a unified HSDT, Ritz method, BCMO, and SGA. To address the problems, the series-type solution employs OP generated through the Gram-Schmidt process. SGA and BCMO are employed to optimize the stiffness of LC plates, and their performance will be compared with the DE algorithm. Numerical examples of LC plates explore the impact of fiber angle, modulus ratio, and various BCs on the optimum results.

5.2. Theoretical formulation

The unified HSDT for LC plates in Fig. 5.1 is referenced by ([229]):

$$u_1(x_1, x_2, x_3, t) = \phi_1(x_1, x_2) \Psi_2(x_3) + u_{3,1}^0 \Psi_1(x_3) + u_1^0(x_1, x_2) \quad (5.1a)$$

$$u_2(x_1, x_2, x_3, t) = \phi_2(x_1, x_2) \Psi_2(x_3) + u_{3,2}^0 \Psi_1(x_3) + u_2^0(x_1, x_2) \quad (5.1b)$$

$$u_3(x_1, x_2, x_3, t) = u_3^0(x_1, x_2) \quad (5.1c)$$

where $\Psi_2(x_3) = H^s \Phi(x_3)$, $\Psi_1(x_3) = H^s \Phi(x_3) - x_3$; H^s is the transverse shear stiffness; $\Phi(x_3) = \int_0^{x_3} \frac{2(1+\nu)f_{,3}}{E(x_3)} dx_3 = \int_0^{x_3} \frac{f_{,3}}{\mu(x_3)} dx_3$, and $f(x_3)$ is a higher-order component that needs to fulfill a specific condition $f_{,3}\left(x_3 = \pm \frac{h}{2}\right) = 0$.

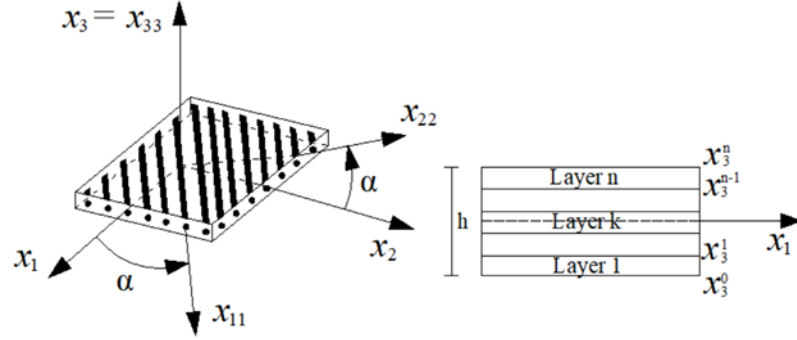


Figure 5.1: The geometric of laminated composite plates

The components of strains $\boldsymbol{\varepsilon}^T = [\varepsilon_{11} \quad \varepsilon_{22} \quad \gamma_{12} \quad \gamma_{13} \quad \gamma_{23}]$ are found as follows:

$$\boldsymbol{\varepsilon}^{(i)} = \Psi_3(x_3)\boldsymbol{\varepsilon}^{(3)} + \Psi_2(x_3)\boldsymbol{\varepsilon}^{(2)} + \Psi_1(x_3)\boldsymbol{\varepsilon}^{(1)} + \boldsymbol{\varepsilon}^{(0)} \quad (5.2)$$

where $\Psi_3(x_3) = \Phi_{,3}H^s$ with $\Phi_{,3}(x_3) = \frac{f_{,3}(x_3)}{\mu(x_3)}$ and,

$$\boldsymbol{\varepsilon}^{(0)} = \begin{Bmatrix} \varepsilon_{11}^{(0)} \\ \varepsilon_{22}^{(0)} \\ \gamma_{12}^{(0)} \\ \gamma_{13}^{(0)} \\ \gamma_{23}^{(0)} \end{Bmatrix} = \begin{Bmatrix} u_{1,1}^0 \\ u_{2,2}^0 \\ u_{1,2}^0 + u_{2,1}^0 \\ 0 \\ 0 \end{Bmatrix}, \quad \boldsymbol{\varepsilon}^{(1)} = \begin{Bmatrix} \varepsilon_{11}^{(1)} \\ \varepsilon_{22}^{(1)} \\ \gamma_{12}^{(1)} \\ \gamma_{13}^{(1)} \\ \gamma_{23}^{(1)} \end{Bmatrix} = \begin{Bmatrix} u_{3,11}^0 \\ u_{3,22}^0 \\ 2u_{3,12}^0 \\ 0 \\ 0 \end{Bmatrix} \quad (5.3a)$$

$$\boldsymbol{\varepsilon}^{(2)} = \begin{Bmatrix} \varepsilon_{11}^{(2)} \\ \varepsilon_{22}^{(2)} \\ \gamma_{12}^{(2)} \\ \gamma_{13}^{(2)} \\ \gamma_{23}^{(2)} \end{Bmatrix} = \begin{Bmatrix} \phi_{1,1} \\ \phi_{2,2} \\ \phi_{1,2} + \phi_{2,1} \\ 0 \\ 0 \end{Bmatrix}, \quad \boldsymbol{\varepsilon}^{(3)} = \begin{Bmatrix} \varepsilon_{11}^{(3)} \\ \varepsilon_{22}^{(3)} \\ \gamma_{12}^{(3)} \\ \gamma_{13}^{(3)} \\ \gamma_{23}^{(3)} \end{Bmatrix} = \begin{Bmatrix} 0 \\ 0 \\ 0 \\ \phi_1 + u_{3,1}^0 \\ \phi_2 + u_{3,2}^0 \end{Bmatrix} \quad (5.3b)$$

The relationship between the strains and stresses for the k layer is expressed as:

$$\boldsymbol{\sigma} = \begin{Bmatrix} \sigma_{11} \\ \sigma_{22} \\ \sigma_{12} \\ \sigma_{13} \\ \sigma_{23} \end{Bmatrix} = \begin{bmatrix} \bar{Q}_{11}^{(k)} & \bar{Q}_{12}^{(k)} & \bar{Q}_{16}^{(k)} & 0 & 0 \\ \bar{Q}_{12}^{(k)} & \bar{Q}_{22}^{(k)} & \bar{Q}_{26}^{(k)} & 0 & 0 \\ \bar{Q}_{16}^{(k)} & \bar{Q}_{22}^{(k)} & \bar{Q}_{66}^{(k)} & 0 & 0 \\ 0 & 0 & 0 & \bar{Q}_{55}^{(k)} & \bar{Q}_{45}^{(k)} \\ 0 & 0 & 0 & \bar{Q}_{45}^{(k)} & \bar{Q}_{44}^{(k)} \end{bmatrix} \begin{Bmatrix} \varepsilon_{11} \\ \varepsilon_{22} \\ \gamma_{12} \\ \gamma_{13} \\ \gamma_{23} \end{Bmatrix} = \bar{\mathbf{Q}}_e \boldsymbol{\varepsilon} \quad (5.4)$$

where

$$\bar{Q}_{11}^{(k)} = Q_{22}^{(k)} \sin^4 \alpha + Q_{11}^{(k)} \cos^4 \alpha + 2(2Q_{66}^{(k)} + Q_{12}^{(k)}) \cos^2 \alpha \sin^2 \alpha \quad (5.5a)$$

$$\bar{Q}_{12}^{(k)} = Q_{12}^{(k)} (\cos^4 \alpha + \sin^4 \alpha) + (Q_{11}^{(k)} - 4Q_{66}^{(k)} + Q_{22}^{(k)}) \cos^2 \alpha \sin^2 \alpha \quad (5.5b)$$

$$\bar{Q}_{22}^{(k)} = 2(2Q_{66}^{(k)} + Q_{12}^{(k)}) \cos^2 \alpha \sin^2 \alpha + Q_{11}^{(k)} \sin^4 \alpha + Q_{22}^{(k)} \cos^4 \alpha \quad (5.5c)$$

$$\bar{Q}_{16}^{(k)} = (2Q_{66}^{(k)} + Q_{12}^{(k)} - Q_{22}^{(k)}) \sin^3 \alpha \cos \alpha + (Q_{11}^{(k)} - (Q_{12}^{(k)} + 2Q_{66}^{(k)})) \sin \alpha \cos^3 \alpha \quad (5.5d)$$

$$\bar{Q}_{26}^{(k)} = (2Q_{66}^{(k)} + Q_{12}^{(k)} - Q_{22}^{(k)}) \sin \alpha \cos^3 \alpha + (Q_{11}^{(k)} - (Q_{12}^{(k)} + 2Q_{66}^{(k)})) \sin^3 \alpha \cos \alpha \quad (5.5e)$$

$$\bar{Q}_{66}^{(k)} = (Q_{22}^{(k)} + Q_{11}^{(k)} - 2(Q_{12}^{(k)} + Q_{66}^{(k)})) \cos^2 \alpha \sin^2 \alpha + Q_{66}^{(k)} (\cos^4 \alpha + \sin^4 \alpha) \quad (5.5f)$$

$$\bar{Q}_{44}^{(k)} = Q_{44}^{(k)} \cos^2 \alpha + Q_{55}^{(k)} \sin^2 \alpha \quad (5.5g)$$

$$\bar{Q}_{55}^{(k)} = Q_{44}^{(k)} \sin^2 \alpha + Q_{55}^{(k)} \cos^2 \alpha \quad (5.5h)$$

$$\bar{Q}_{45}^{(k)} = (Q_{55}^{(k)} - Q_{44}^{(k)}) \cos \alpha \sin \alpha \quad (5.5k)$$

with α is the fiber angle in each layer, $Q_{ij}^{(k)}$ of the orthotropic composite plates in the local coordinate system are given by:

$$Q_{11}^{(k)} = \frac{E_1}{1 - \nu_{12}\nu_{21}}, Q_{12}^{(k)} = \frac{\nu_{12}E_2}{1 - \nu_{12}\nu_{21}}, Q_{22}^{(k)} = \frac{E_2}{1 - \nu_{12}\nu_{21}} \quad (5.6a)$$

$$Q_{66}^{(k)} = G_{12}, Q_{44}^{(k)} = G_{23}, Q_{55}^{(k)} = G_{13} \quad (5.6b)$$

To obtain the equations of motion, Hamilton's principle is employed:

$$\int_{t_1}^{t_2} (\delta \Pi_{SE} + \delta \Pi_V - \delta \Pi_K) dt = 0 \quad (5.7)$$

The variation of the strain energy $\delta \Pi_{SE}$ is given by:

$$\delta \Pi_{SE} = \int_A \boldsymbol{\sigma} \delta \boldsymbol{\epsilon} dA = \int_A \left[\mathbf{N}_\varepsilon^{(0)} \delta \boldsymbol{\epsilon}^{(0)} + \mathbf{N}_\varepsilon^{(1)} \delta \boldsymbol{\epsilon}^{(1)} + \mathbf{N}_\varepsilon^{(2)} \delta \boldsymbol{\epsilon}^{(2)} + \mathbf{N}_\varepsilon^{(3)} \delta \boldsymbol{\epsilon}^{(3)} \right] dA \quad (5.8)$$

where the stress resultants can be derived based on the strains and their gradients using the following expressions:

$$\left(\mathbf{N}_\varepsilon^{(3)}, \mathbf{N}_\varepsilon^{(2)}, \mathbf{N}_\varepsilon^{(1)}, \mathbf{N}_\varepsilon^{(0)} \right) = \int_{-h/2}^{h/2} \left(\Psi_3, \Psi_2, \Psi_1, 1 \right) \boldsymbol{\sigma} dx_3 \quad (5.9)$$

$$\begin{Bmatrix} \mathbf{N}_\varepsilon^{(0)} \\ \mathbf{N}_\varepsilon^{(1)} \\ \mathbf{N}_\varepsilon^{(2)} \\ \mathbf{N}_\varepsilon^{(3)} \end{Bmatrix} = \begin{bmatrix} \mathbf{A}^\varepsilon & \mathbf{B}^\varepsilon & \mathbf{B}_s^\varepsilon & \mathbf{0} \\ \mathbf{B}^\varepsilon & \mathbf{D}^\varepsilon & \mathbf{D}_s^\varepsilon & \mathbf{0} \\ \mathbf{B}_s^\varepsilon & \mathbf{D}_s^\varepsilon & \mathbf{H}_s^\varepsilon & \mathbf{0} \\ \mathbf{0} & \mathbf{0} & \mathbf{0} & \mathbf{A}_s^\varepsilon \end{bmatrix} \begin{Bmatrix} \boldsymbol{\epsilon}^{(0)} \\ \boldsymbol{\epsilon}^{(1)} \\ \boldsymbol{\epsilon}^{(2)} \\ \boldsymbol{\epsilon}^{(3)} \end{Bmatrix} \quad (5.10)$$

where the stiffness components are given:

$$\left(\mathbf{A}^\varepsilon, \mathbf{B}^\varepsilon, \mathbf{D}^\varepsilon, \mathbf{H}_s^\varepsilon, \mathbf{B}_s^\varepsilon, \mathbf{D}_s^\varepsilon, \mathbf{A}_s^\varepsilon \right) = \int_{-h/2}^{h/2} \left(1, \Psi_1, \Psi_1^2, \Psi_2^2, \Psi_2, \Psi_1 \Psi_2, \Psi_3^2 \right) \mathbf{Q}_\varepsilon dx_3 \quad (5.11)$$

The change in the work done $\delta \Pi_V$ due to compressive membrane loads

($N_1^0 = N_2^0 = N_{12}^0 = N^0$) is expressed as:

$$\delta\Pi_V = -\int_A N^0 \left(u_{3,1}^0 \delta u_{3,1}^0 + u_{3,2}^0 \delta u_{3,2}^0 + 2u_{3,1}^0 \delta u_{3,2}^0 \right) dA \quad (5.12)$$

The variation of kinetic energy $\delta\Pi_K$ is calculated by:

$$\begin{aligned} \delta\Pi_K &= \frac{1}{2} \int_V \rho \left(\dot{u}_3 \delta \dot{u}_3 + \dot{u}_2 \delta \dot{u}_2 + \dot{u}_1 \delta \dot{u}_1 \right) dV \\ &= \frac{1}{2} \int_A \left[I_2 \left(\dot{u}_{3,1}^0 \delta \dot{u}_{3,1}^0 + \dot{u}_{3,2}^0 \delta \dot{u}_{3,2}^0 \right) + K_2 \left(\dot{\phi}_1 \delta \dot{\phi}_1 + \dot{\phi}_2 \delta \dot{\phi}_2 \right) \right. \\ &\quad I_0 \left(\dot{u}_1^0 \delta \dot{u}_1^0 + \dot{u}_2^0 \delta \dot{u}_2^0 + \dot{u}_3^0 \delta \dot{u}_3^0 \right) + I_1 \left(\dot{u}_1^0 \delta \dot{u}_{3,1}^0 + \dot{u}_{3,1}^0 \delta \dot{u}_1^0 + \dot{u}_2^0 \delta \dot{u}_{3,2}^0 + \dot{u}_{3,2}^0 \delta \dot{u}_2^0 \right) \\ &\quad + J_1 \left(\dot{u}_1^0 \delta \dot{\phi}_1 + \dot{\phi}_1 \delta \dot{u}_1^0 + \dot{u}_2^0 \delta \dot{\phi}_2 + \dot{\phi}_2 \delta \dot{u}_2^0 \right) \\ &\quad \left. + J_2 \left(\dot{u}_{3,1}^0 \delta \dot{\phi}_1 + \dot{\phi}_1 \delta \dot{u}_{3,1}^0 + \dot{u}_{3,2}^0 \delta \dot{\phi}_2 + \dot{\phi}_2 \delta \dot{u}_{3,2}^0 \right) \right] dA \end{aligned} \quad (5.13)$$

where $K_2, J_2, J_1, I_2, I_1, I_0$ are mass components of the laminated composite plate which are determined as:

$$(K_2, J_2, J_1, I_2, I_1, I_0) = \int_{-h/2}^{h/2} (\Psi_2^2, \Psi_1 \Psi_2, \Psi_2, \Psi_1^2, \Psi_1, 1) \rho dx_3 \quad (5.14)$$

5.3. Ritz method

The membrane and transverse displacements, as well as rotations $(u_1^0, u_2^0, u_3^0, \phi_1, \phi_2)$ can be represented through a series of shape functions in $x_1 -$, $x_2 -$ direction $(X_i(x_1)$ and $Y_j(x_2))$ and five unknowns variables $(u_{1ij}, u_{2ij}, u_{3ij}, x_{ij}, y_{ij})$, expressed as follows:

$$u_2^0(x_1, x_2, t) = \sum_{i=1}^{n_1} \sum_{j=1}^{n_2} u_{2ij}(t) Y_{j,2}(x_2) X_i(x_1) \quad (5.15a)$$

$$u_1^0(x_1, x_2, t) = \sum_{i=1}^{n_1} \sum_{j=1}^{n_2} u_{1ij}(t) Y_j(x_2) X_{i,1}(x_1) \quad (5.15b)$$

$$\phi_2(x_1, x_2, t) = \sum_{i=1}^{n_1} \sum_{j=1}^{n_2} y_{ij}(t) Y_{j,2}(x_2) X_i(x_1) \quad (5.15c)$$

$$\phi_1(x_1, x_2, t) = \sum_{i=1}^{n_1} \sum_{j=1}^{n_2} x_{ij}(t) Y_j(x_2) X_{i,1}(x_1) \quad (5.15d)$$

$$u_3^0(x_1, x_2, t) = \sum_{i=1}^{n_1} \sum_{j=1}^{n_2} u_{3ij}(t) Y_j(x_2) X_i(x_1) \quad (5.15e)$$

The shape functions are pivotal in dictating the convergence rates, accuracy, and susceptibility to numerical instabilities within the Ritz solution. Next, the admissible functions known as orthogonal polynomials (OP) which are constructed using the GS method [137]. These functions exhibit a rapid convergence rate, although they encounter challenges in determining the initial function. Using the GS approach is defined as follows:

$$\phi_1(x) = (x - A_1)\phi_0(x), \quad \phi_k(x) = (x - A_k)\phi_{k-1}(x) - D_k\phi_{k-2}(x) \quad (5.16a)$$

$$A_k = \frac{\int_c^d xw(x)\phi_{k-1}^2(x)dx}{\int_c^d w(x)\phi_{k-1}^2(x)dx}; \quad D_k = \frac{\int_c^d xw(x)\phi_{k-1}(x)\phi_{k-2}(x)dx}{\int_c^d w(x)\phi_{k-2}^2(x)dx} \quad (5.16b)$$

where $w(x)$ being the weighting function. The orthogonality is satisfied by the polynomials $\phi_k(x)$ as below:

$$\int_c^d w(x)\phi_k(x)\phi_l(x)dx = \begin{cases} 0 & \text{if } k \neq l \\ a_{kl} & \text{if } k = l \end{cases} \quad (5.17)$$

with $w(x) = 1$; $\phi_0(x) = 2x + 1$, and $[c, d] \in [-1, 1]$. The first five orthogonal polynomials are shown in Fig. 5.2. The shape functions $X_i(x_1)$ and $Y_j(x_2)$ are made to satisfy the BCs in which clamped (C) and the simply-supported (S) edges are as follows:

- Clamped (C): $\varphi_1 = \varphi_2 = u_1^0 = u_2^0 = u_3^0 = 0$ at $x_1 = 0, a$ and $x_2 = 0, b$
- Simply supported (S): $\varphi_2 = u_2^0 = u_3^0 = 0$ at $x_1 = 0, a$ and at $u_1^0 = u_3^0 = \varphi_1 = 0$ $x_2 = 0, b$

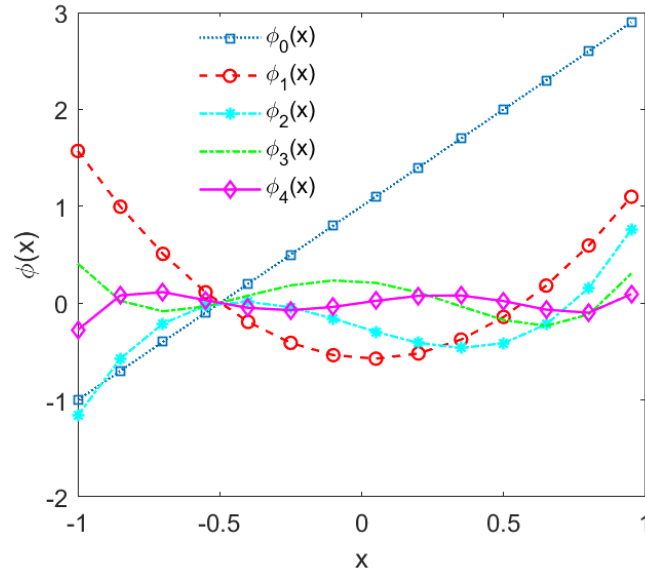


Figure 5.2: The first five orthogonal polynomials

The laminated composite plate's edge conditions, a mix of simply-supported and clamped boundaries (SSSS, CSCS, CCCC), are pivotal in numerical analyses (Table 5.1).

Table 5.1: Approximation functions of series-type solution

BCs	$X_j(x_1)$	$Y_j(x_2)$
SSSS	$x_1(a-x_1)\phi_j$	$x_2(b-x_2)\phi_j$
CSCS	$x_1^2(a-x_1)\phi_j$	$x_2^2(b-x_2)\phi_j$
CCCC	$x_1^2(a-x_1)^2\phi_j$	$x_2^2(b-x_2)^2\phi_j$

By incorporating Eq. (5.15) into Eqs. (5.8), (5.12), and (5.13), and the subsequent outcomes into Eq. (5.7), the characteristic motion equations are derived via the displacement vector \mathbf{d} , stiffness matrix \mathbf{K} and mass matrix \mathbf{M} as follows:

$$(\mathbf{K} - N^0 \mathbf{K}^g) \mathbf{d} + \mathbf{M} \ddot{\mathbf{d}} = \mathbf{0} \quad (5.18)$$

where

$$\mathbf{d} = [\mathbf{u}_1 \quad \mathbf{u}_2 \quad \mathbf{u}_3 \quad \mathbf{x} \quad \mathbf{y}]^T \quad (5.19a)$$

$$\mathbf{K} = \begin{bmatrix} \mathbf{K}^{11} & \mathbf{K}^{12} & \mathbf{K}^{13} & \mathbf{K}^{14} & \mathbf{K}^{15} \\ {}^T\mathbf{K}^{12} & \mathbf{K}^{22} & \mathbf{K}^{23} & \mathbf{K}^{24} & \mathbf{K}^{25} \\ {}^T\mathbf{K}^{13} & {}^T\mathbf{K}^{23} & \mathbf{K}^{33} & \mathbf{K}^{34} & \mathbf{K}^{35} \\ {}^T\mathbf{K}^{14} & {}^T\mathbf{K}^{24} & {}^T\mathbf{K}^{34} & \mathbf{K}^{44} & \mathbf{K}^{45} \\ {}^T\mathbf{K}^{15} & {}^T\mathbf{K}^{25} & {}^T\mathbf{K}^{35} & {}^T\mathbf{K}^{45} & \mathbf{K}^{55} \end{bmatrix} \quad (5.19b)$$

$$\mathbf{K}^g = \begin{bmatrix} \mathbf{0} & \mathbf{0} & \mathbf{0} & \mathbf{0} & \mathbf{0} \\ \mathbf{0} & \mathbf{0} & \mathbf{0} & \mathbf{0} & \mathbf{0} \\ \mathbf{0} & \mathbf{0} & \mathbf{K}^{g33} & \mathbf{0} & \mathbf{0} \\ \mathbf{0} & \mathbf{0} & \mathbf{0} & \mathbf{0} & \mathbf{0} \\ \mathbf{0} & \mathbf{0} & \mathbf{0} & \mathbf{0} & \mathbf{0} \end{bmatrix} \quad \text{with } K_{ijkl}^{g33} = H_{ik}^{11} S_{jl}^{00} + H_{ik}^{00} S_{jl}^{11} \quad (5.19c)$$

The components of \mathbf{K} is formulated as:

$$K_{ijkl}^{11} = A_{11} T_{ik}^{22} S_{jl}^{00} + 2A_{16} T_{ik}^{12} S_{jl}^{10} + A_{66} T_{ik}^{11} S_{jl}^{11}$$

$$K_{ijkl}^{12} = A_{12} T_{ik}^{02} S_{jl}^{20} + A_{16} T_{ik}^{21} S_{jl}^{01} + A_{26} T_{ik}^{10} S_{jl}^{12} + A_{66} T_{ik}^{11} S_{jl}^{11}$$

$$K_{ijkl}^{13} = B_{11} T_{ik}^{22} S_{jl}^{00} + B_{12} T_{ik}^{02} S_{jl}^{20} + 2B_{16} T_{ik}^{21} S_{jl}^{01} + B_{26} T_{ik}^{10} S_{jl}^{12} + 2B_{66} T_{ik}^{11} S_{jl}^{11}$$

$$K_{ijkl}^{14} = B_{s11} T_{ik}^{22} S_{jl}^{00} + 2B_{s16} T_{ik}^{21} S_{jl}^{01} + B_{s66} T_{ik}^{11} S_{jl}^{11}$$

$$K_{ijkl}^{15} = B_{s12} T_{ik}^{02} S_{jl}^{20} + B_{s16} T_{ik}^{21} S_{jl}^{01} + B_{s26} T_{ik}^{10} S_{jl}^{12} + B_{s66} T_{ik}^{11} S_{jl}^{11}$$

$$K_{ijkl}^{22} = A_{22} T_{ik}^{00} S_{jl}^{22} + 2A_{16} T_{ik}^{01} S_{jl}^{21} + A_{66} T_{ik}^{11} S_{jl}^{11}$$

$$K_{ijkl}^{23} = B_{12} T_{ik}^{20} S_{jl}^{02} + B_{22} T_{ik}^{00} S_{jl}^{22} + 2B_{16} T_{ik}^{10} S_{jl}^{12} + B_{26} T_{ik}^{21} S_{jl}^{01} + 2B_{66} T_{ik}^{11} S_{jl}^{11}$$

$$K_{ijkl}^{\varepsilon 24} = B_{s12} T_{ik}^{20} S_{jl}^{02} + B_{s16} T_{ik}^{10} S_{jl}^{12} + B_{s26} T_{ik}^{21} S_{jl}^{01} + B_{s66} T_{ik}^{11} S_{jl}^{11}$$

$$K_{ijkl}^{25} = B_{s22} T_{ik}^{00} S_{jl}^{22} + 2B_{s16} T_{ik}^{10} S_{jl}^{12} + B_{s66} T_{ik}^{11} S_{jl}^{11}$$

$$\begin{aligned} K_{ijkl}^{\varepsilon 33} &= D_{11} T_{ik}^{22} S_{jl}^{00} + D_{12} (T_{ik}^{02} S_{jl}^{20} + T_{ik}^{20} S_{jl}^{02}) + D_{22} T_{ik}^{00} S_{jl}^{22} + 4D_{66} T_{ik}^{11} S_{jl}^{11} \\ &+ 4D_{16} T_{ik}^{21} S_{jl}^{01} + 4D_{26} T_{ik}^{10} S_{jl}^{12} + A_{s44} T_{ik}^{00} S_{jl}^{11} + 2A_{s45} T_{ik}^{10} S_{jl}^{01} + \\ &+ A_{s55} T_{ik}^{11} S_{jl}^{00} - N^0 (T_{ik}^{11} S_{jl}^{00} + T_{ik}^{00} S_{jl}^{11}) \end{aligned}$$

$$\begin{aligned}
K_{ijkl}^{34} &= D_{s11} T_{ik}^{22} S_{jl}^{00} + D_{s12} T_{ik}^{20} S_{jl}^{02} + 2D_{s66} T_{ik}^{11} S_{jl}^{11} + 2D_{s16} T_{ik}^{12} S_{jl}^{10} \\
&+ D_{s16} T_{ik}^{01} S_{jl}^{21} + A_{s45} T_{ik}^{01} S_{jl}^{10} + A_{s55} T_{ik}^{11} S_{jl}^{00} \\
K_{ijkl}^{35} &= D_{s12} T_{ik}^{02} S_{jl}^{20} + D_{s22} T_{ik}^{00} S_{jl}^{22} + 2D_{s66} T_{ik}^{11} S_{jl}^{11} + D_{s16} T_{ik}^{21} S_{jl}^{01} \\
&+ 2D_{s26} T_{ik}^{10} S_{jl}^{12} + A_{s45} T_{ik}^{10} S_{jl}^{01} + A_{s44} T_{ik}^{00} S_{jl}^{11} \\
K_{ijkl}^{44} &= H_{s11} T_{ik}^{22} S_{jl}^{00} + H_{s66} T_{ik}^{11} S_{jl}^{11} + 2H_{s16} T_{ik}^{21} S_{jl}^{01} + A_{s55} T_{ik}^{11} S_{jl}^{00} \\
K_{ijkl}^{45} &= H_{s12} T_{ik}^{02} S_{jl}^{20} + H_{s16} T_{ik}^{21} S_{jl}^{01} + H_{s26} T_{ik}^{01} S_{jl}^{21} + H_{s66} T_{ik}^{11} S_{jl}^{11} + A_{s45} T_{ik}^{10} S_{jl}^{01} \\
K_{ijkl}^{55} &= H_{s22} T_{ik}^{00} S_{jl}^{22} + H_{s66} T_{ik}^{11} S_{jl}^{11} + 2H_{s16} T_{ik}^{10} S_{jl}^{12} + A_{s44} T_{ik}^{00} S_{jl}^{11}
\end{aligned} \tag{5.20}$$

where

$$T_{ik}^{rs} = \int_0^a \frac{\partial^r R_i}{\partial x_1^r} \frac{\partial^s R_k}{\partial x_1^s} dx_1, S_{jl}^{rs} = \int_0^b \frac{\partial^r P_j}{\partial x_2^r} \frac{\partial^s P_l}{\partial x_2^s} dx_2 \tag{5.21}$$

The components of \mathbf{M} are expressed as follows:

$$\begin{aligned}
M_{ijkl}^{11} &= I_0 T_{ik}^{11} S_{jl}^{00}, M_{ijkl}^{13} = I_1 T_{ik}^{11} S_{jl}^{00}, M_{ijkl}^{14} = J_1 T_{ik}^{11} S_{jl}^{00} \\
M_{ijkl}^{22} &= I_0 T_{ik}^{00} S_{jl}^{11}, M_{ijkl}^{23} = I_1 T_{ik}^{00} S_{jl}^{11}, M_{ijkl}^{25} = J_1 T_{ik}^{00} S_{jl}^{11} \\
M_{ijkl}^{33} &= I_2 (T_{ik}^{00} S_{jl}^{11} + T_{ik}^{11} S_{jl}^{00}) + I_0 T_{ik}^{00} S_{jl}^{00} \\
M_{ijkl}^{35} &= J_2 T_{ik}^{00} S_{jl}^{11}, M_{ijkl}^{34} = J_2 T_{ik}^{11} S_{jl}^{00}, M_{ijkl}^{55} = K_2 T_{ik}^{00} S_{jl}^{11}, M_{ijkl}^{44} = K_2 T_{ik}^{11} S_{jl}^{00}
\end{aligned} \tag{5.22}$$

Based on Eq. (5.18), the critical buckling loads N^{cr} of the microplate can be obtained by disregarding the mass inertia components, damping ratio and solving the characteristic equation $(\mathbf{K} - N^0 \mathbf{K}^g) \mathbf{d} = \mathbf{0}$. For free vibration analysis, it is supposed that $N^0 = 0$ and $\mathbf{d}(t) = \mathbf{d} e^{i\omega t}$, where $i^2 = -1$ represents the imaginary unit, and ω denotes the natural frequency of the microplate. By solving the equation $(\mathbf{K} - \omega^2 \mathbf{M}) \mathbf{d} = \mathbf{0}$, the natural frequencies will be determined.

5.4. Optimization solution

In this section, three algorithms are presented to identify the fiber angle α that maximize the critical buckling loads and frequencies of laminated composite plates, with the following objective functions.

Maximum $\bar{\omega} = f(\alpha_i^d)$ or $\bar{N}_{cr} = f(\alpha_i^d)$

$$\text{Subjected to } -90^\circ \leq \alpha_i^d \leq 90^\circ \quad (5.23)$$

with d is the number of layers.

Three algorithms including differential evolution (DE), shrimp and goby association search algorithm (SGA) and balancing composite motion optimization (BCMO) are used to solve the above optimization problem. More details about the DE, SGA, BCMO algorithms can be found in title 2.7.

5.5. Numerical examples

Several numerical examples are conducted to explore vibration and buckling behaviors of laminated composite plates. Convergence and verification are carried out first and then DE, SGA and BCMO algorithms are employed to determine their optimal frequencies and buckling loads. The analysis involves employing the shear function $\Phi(x_3) = \cot^{-1}(h/x_3) - (16x_3^3)/(15h^3)$ ([230]). The material properties are given as: $G_{12} = G_{13} = 0.6E_2$, $G_{23} = 0.5E_2$, $\nu_{12} = 0.25$, $\rho = 1$ ([231]). For simplicity, the following normalized parameters are used:

$$\bar{\omega} = \frac{\omega a^2}{h} \sqrt{\frac{\rho}{E_2}}; \quad \bar{N}_{cr} = \frac{N_{cr} a^2}{h^3 E_2} \quad (5.39)$$

Table 5.2: Convergence study for $[0^\circ / 90^\circ / 90^\circ / 0^\circ]$ plates with different BCs
($a/h = 10$, $E_1/E_2 = 40$)

BCs/Solution	Number of series $n = n_1 = n_2$					
	2	4	6	7	8	9
Normalized fundamental frequency						
SSSS	16.2797	15.5288	15.1192	15.1191	15.1192	15.1191
CSCS	21.1622	19.5302	19.2501	19.2502	19.2501	19.2501
CCCC	23.4273	22.3269	22.0249	22.0247	22.0248	22.0249
Normalized critical buckling load under uniaxial compression ($N_1^0, N_2^0, N_{12}^0 = 1, 0, 0$)						
SSSS	27.1409	25.1061	23.7876	23.3042	23.3043	23.3042
CSCS	36.5583	34.8010	34.6724	34.5755	34.5757	34.5755
CCCC	46.4065	44.3619	44.1133	44.0404	44.0403	44.0404

To examine the convergence of current solutions, Table 5.2 displays the results of the square $[0^\circ / 90^\circ / 90^\circ / 0^\circ]$ plates with $a/h = 10$ and $E_1 = 40E_2$. The outcomes are computed for three BCs (SSSS, CSCS and CCCC) with equal series-type solutions in the x_1 – and x_2 –directions ($n_1 = n_2 = n$). The results indicate swift convergences, observed at $n = 6$ for fundamental frequencies and $n = 7$ for buckling loads. Therefore, these values will be utilized in the numerical examples.

5.5.1. Verification study

Tables 5.3-5.5 provide the fundamental frequencies of $[0^\circ / 90^\circ / 90^\circ / 0^\circ]$, $[0^\circ / 90^\circ / 0^\circ]$ and $[0^\circ / 90^\circ]$ square plates with various BCs. For SSSS plates, the obtained solutions in Table 6.3 are compared with those who used the third-order shear deformation theory (TSDT) ([231], [232]) with $a/h = 10$ and Thai et al. [233] using HSDT and FEM with NS-DSG3 element with $a/h = 20$ and 25.

Table 5.3: The normalize fundamental frequencies of $[0^\circ / 90^\circ / 90^\circ / 0^\circ]$ plates

BCs	a/h	Theory	E_1/E_2				
			3	10	20	30	40
SSSS	10	TSDT [232]	7.240	9.847	12.225	13.987	15.112
		TSDT [231]	7.247	9.853	12.238	13.892	15.143
		Present	7.2137	9.8325	12.2395	13.8917	15.1192
	20	HSDT [233]	-	-	-	-	17.6620
		Present	7.4397	10.4096	13.4353	15.7603	17.6695
	25	HSDT [233]	-	-	-	-	18.0875
Present		7.4825	10.5176	13.6504	16.0987	18.1445	
CSCS	10	Present	9.8392	13.6002	16.4517	18.1279	19.2501
	20	Present	10.3734	15.1558	19.6100	22.7754	25.1996
CCCC	10	Present	12.7654	17.1590	19.8039	21.1663	22.0249
	20	Present	13.8842	20.5707	26.0621	29.5058	31.8833

For CCCC plates, the present results in Table 5.4 are compared with those previously reports by Thai et al.[233], Zhen and Wanji [234], Ferreira and Fasshauer [235], Ferreira et al. [236] for case $E_1/E_2 = 40$. The results listed in Table 5.5 are compared with those published by Noor [237] using 3D elasticity theory with $a/h = 5$ and Thai et al. [238] using a refined plate theory (RPT) with $a/h = 5, 10$ and 20 . It's evident that the present solutions exhibit strong agreement across all cases, with errors consistently below one percentage. Some new results are also provided in Tables 5.3-5.5 for other BCs with $a/h = 10$ and 20 . It can be seen that for all BCs when modulus ratio E_1/E_2 and a/h increase, the natural frequencies increase.

Table 5.4: The normalize fundamental frequencies of $[0^\circ / 90^\circ / 0^\circ]$ plates

$$(\bar{\omega}_1 = (\omega a^2 / \pi^2) / \sqrt{\rho h / (E_2 h^3 / (12(1 - \nu_{12}\nu_{21})))})$$

BCs	a / h	Theory	E_1 / E_2				
			3	10	20	30	40
CCCC	10	HSDT [234]	-	-	-	-	7.484
		RBF-PS [235]	-	-	-	-	7.4727
		FSDT [236]	-	-	-	-	7.4106
		HSDT [233]	-	-	-	-	7.4224
		Present	4.4887	5.9410	6.7371	7.1399	7.4022
	20	HSDT [234]	-	-	-	-	11.003
		RBF-PS [235]	-	-	-	-	10.968
		FSDT [236]	-	-	-	-	10.9528
		HSDT [233]	-	-	-	-	10.9042
		Present	4.8610	7.1875	9.0084	10.1035	10.8381
	100	HSDT [234]	-	-	-	-	14.601
		RBF-PS [235]	-	-	-	-	14.4305
		FSDT [236]	-	-	-	-	14.4455
		HSDT [233]	-	-	-	-	14.3626
		Present	4.9619	7.7474	10.4816	12.6081	14.3997
CSCS	10	Present	3.5360	4.8438	5.7655	6.2794	6.6146
	20	Present	3.6949	5.3958	6.9399	8.0117	8.8148
SSSS	10	Present	2.6389	3.6286	4.4577	4.9853	5.3561
	20	Present	2.6654	3.7800	4.8782	5.7026	6.3659

Table 5.5: The normalize fundamental frequencies of $[0^\circ / 90^\circ]$ plates

BCs	a/h	Theory	E_1/E_2				
			3	10	20	30	40
SSSS	5	3D [237]	6.2578	6.9845	7.6745	8.1763	8.5625
		RPT [238]	6.2167	6.9836	7.8011	8.4646	9.0227
		Present	6.2170	6.9676	7.7038	8.2126	8.5594
	10	RPT [238]	-	-	-	-	10.5480
		Present	6.7995	7.7912	8.8723	9.7954	10.6125
	20	RPT [238]	-	-	-	-	11.0997
Present		6.9819	8.0413	9.2036	10.2106	11.1161	
CSCS	10	Present	9.2150	10.8820	12.5490	13.8987	15.0435
	20	Present	9.6325	11.4996	13.4143	15.0219	16.4386
CCCC	10	Present	11.9659	14.3190	16.4770	18.0981	19.3846
	20	Present	12.8105	15.6519	18.4309	20.6918	22.6332

The critical buckling loads of $[0^\circ / 90^\circ / 90^\circ / 0^\circ]$ plates under uniaxial compression $(N_1^0, N_2^0, N_{12}^0 = 1, 0, 0)$ and $[0^\circ / 90^\circ / 0^\circ]$ plates under biaxial compression $(N_1^0, N_2^0, N_{12}^0 = 1, 1, 0)$, shear buckling $(N_1^0, N_2^0, N_{12}^0 = 0, 0, 1)$ are given in Tables 5.6-5.8 with different BCs. The numerical findings closely align with those reported in the literature for both uniaxial compression ([233, 239, 240]) and biaxial compression ([239-242]) cases. Hence, the present Ritz method is reliable for optimization vibration and buckling analysis of laminated composite plates. The first two free vibration mode shapes of the square LC plates are displayed for illustration purposes in Fig. 5.3.

Table 5.6: The normalize critical buckling of $[0^\circ / 90^\circ / 90^\circ / 0^\circ]$ plates under uniaxial compression $(N_1^0, N_2^0, N_{12}^0 = 1, 0, 0)$

BCs	a/h	Theory	E_1/E_2				
			3	10	20	30	40
SSSS	10	HSDT [233]	5.4418	10.0208	15.4010	19.7810	23.4383
		TSDT [239]	5.3933	9.9401	15.2945	19.6644	23.3401
		TSDT [240]	5.3884	9.9303	15.2841	19.6558	23.3152
		Present	5.3600	9.9008	15.4386	19.8632	23.3042
	20	TSDT [240]	-	-	-	-	31.6975
CSCS	10	Present	5.6353	11.0146	18.3350	25.2412	31.7690
		Present	8.4138	16.2424	24.3199	30.1327	34.5755
	20	Present	9.1960	19.6748	33.1939	45.2623	56.1154
CCCC	10	Present	13.0602	24.7163	34.3922	40.1873	44.0404
	20	Present	15.2033	34.0280	56.3164	74.5690	89.8246

Table 5.7: The normalize critical buckling of $[0^\circ / 90^\circ / 0^\circ]$ plates under biaxial compression ($N_1^0, N_2^0, N_{12}^0 = 1, 1, 0$)

BCs	a / h	Theory	E_1 / E_2				
			3	10	20	30	40
SSSS	10	HSDT [241]	-	4.963	7.516	9.056	10.259
		TSDT [242]	-	4.977	7.544	8.942	10.109
		TSDT [239]	-	4.916	7.448	8.820	9.9755
		TSDT [240]		4.9130	7.4408	8.7550	9.8795
		Present	2.7091	4.9492	7.5045	8.8676	10.0343
	20	TSDT [240]	-	-	-	-	13.0239
		Present	2.8325	5.5194	8.9582	11.0737	13.0866
CSCS	10	Present	4.3300	7.5574	9.8814	8.9119	12.8231
	20	Present	4.7207	9.2268	13.2198	16.5097	19.4522
CCCC	10	Present	6.7537	10.7581	13.1204	14.8401	16.2244
	20	Present	7.7957	14.2191	19.5382	23.9094	27.6485

Table 5.8: Normalized shear buckling of $[0^\circ / 90^\circ / 90^\circ / 0^\circ]$ plates ($N_1^0, N_2^0, N_{12}^0 = 0, 0, 1$), $a / h = 10$

BCs	E_1 / E_2				
	3	10	20	30	40
SSSS	11.0219	17.9481	24.2755	28.5083	31.4874
CSCS	13.4321	21.2794	19.2607	31.1782	33.5337
CCCC	15.5753	23.7884	29.5902	33.0073	35.3192
SFSF	0.6950	1.4574	2.5695	3.6911	4.8029

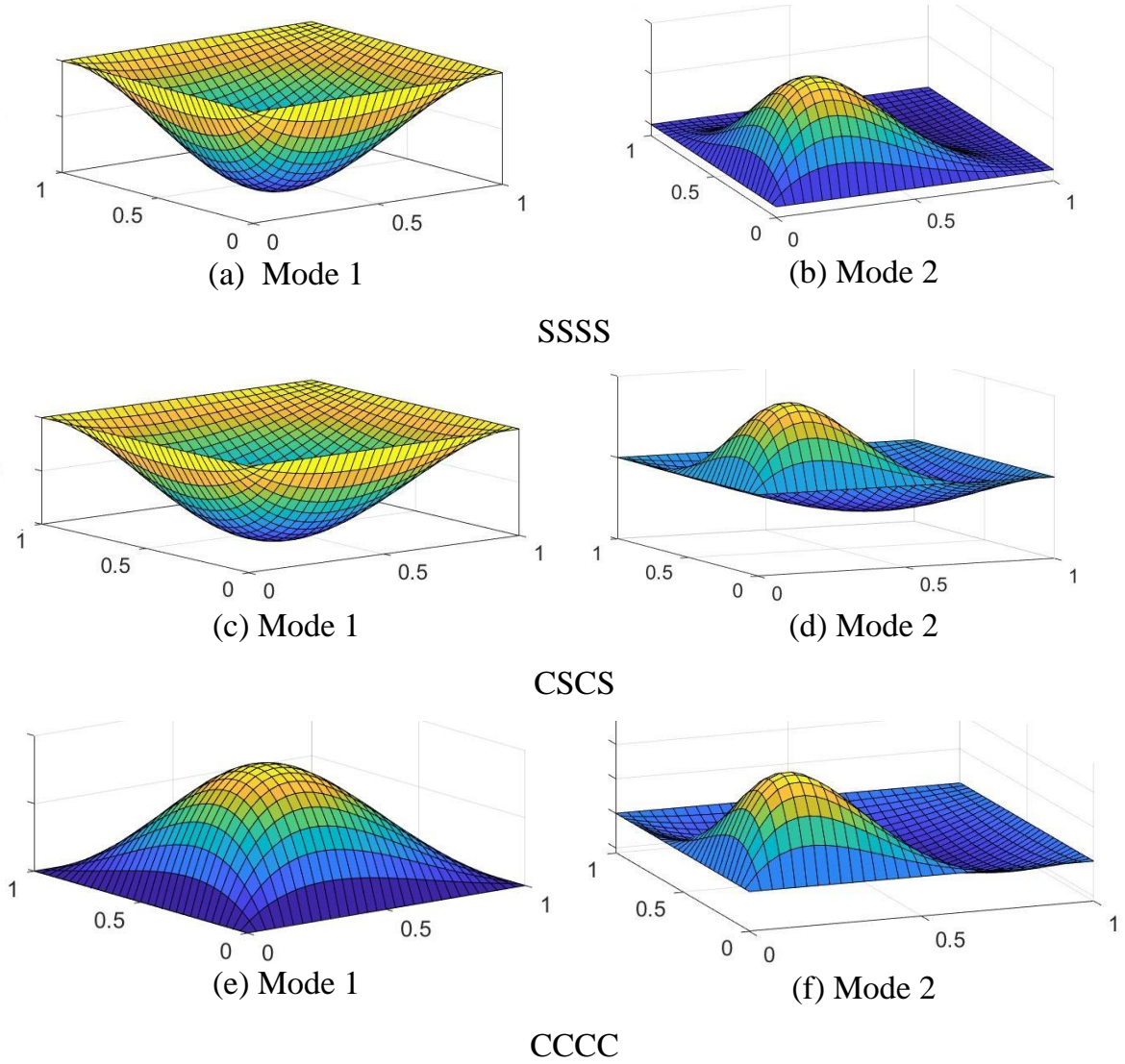


Figure 5.3: Mode shapes of vibration of laminated composite plates $a/h=10$, $E_1/E_2=40$, $[0^\circ/90^\circ/0^\circ]$, $\bar{\omega}_1 = (\omega a^2 / \pi^2) / \sqrt{\rho h / (E_2 h^3 / (12(1-\nu_{12}\nu_{21})))}$

5.5.2. Optimization study

In this section, the optimum results of the fundamental frequencies and buckling loads for uniaxial compression $(N_1^0, N_2^0, N_{12}^0 = 1, 0, 0)$ of four-layer square laminated composite plates ($a/h=10$, $E_1/E_2=40$) with different BCs are investigated. Tables 5.9-5.11 show the results of three different algorithms (DE, SGA, and BCMO) with the population distribution $NP=20$. By comparing the results from

Tables 5.9 and 5.10, it is evident that the optimal responses obtained in the present study are in agreement with those reported by Ho-Huu et al. [217] using FEM-DE for symmetric lay-up and by Keshtegar et al. [243] using Kriging-IPSO for arbitrary lay-up. For the buckling loads, the optimal fiber angles are $[-37^\circ / 39^\circ / 39^\circ / -37^\circ]$ for symmetric lay-up and $[37^\circ / -33^\circ / 36^\circ / -39^\circ]$ for arbitrary ones, corresponding to the entire three algorithms (BCMO, SGA and DE). However, the call functions are the biggest and smallest for DE and BCMO, respectively.

Table 5.9: Optimization critical buckling of symmetric SSSS square laminated composite plates with four layers ($a/h=10$, $E_1/E_2=40$, $NP=20$) under uniaxial compression ($N_1^0, N_2^0, N_{12}^0=1,0,0$)

Iterations	Solution`	Max values	$\alpha^{(1)}$	α^2	$\alpha^{(3)}$	$\alpha^{(4)}$	Call function	Determinate $[0^\circ / 90^\circ / 90^\circ / 0^\circ]$
SSSS								
500	FEM-DE [244]	30.7692	-39	42	42	-39	840	23.3042
100	Ritz-BCMO	36.9822	-37	39	39	-37	20	
	Ritz-SGA	36.9822	-37	39	39	-37	27	
	Ritz-DE	36.9822	-37	39	39	-37	50	
SFSF								
100	Ritz-BCMO	17.2807	30	-60	-60	30	20	4.7084
	Ritz-SGA	17.2807	30	-60	-60	30	27	
	Ritz-SGA	17.2807	30	-60	-60	30	50	
CSCS								
100	Ritz-BCMO	39.5512	31	-48	-48	31	20	34.5755
	Ritz-SGA	39.5512	31	-48	-48	31	27	
	Ritz-DE	39.5512	31	-48	-48	31	50	
CCCC								
100	Ritz-BCMO	44.4767	-10	85	85	-10	20	44.0404
	Ritz-SGA	44.4767	-10	85	85	-10	27	
	Ritz-DE	44.4767	-10	85	85	-10	50	

A comparative analysis related to cost computation (call function) of the performance is provided in Tables 5.9-5.11 in order to assess the effectiveness of optimization algorithms. Table 5.9 shows that the number of call function of the BCMO algorithm is the smallest, with 20 for the symmetric lay-up of buckling loads, whereas 27 and 50 are for the SGA and DE algorithms, respectively. Table 5.11 also shows new optimal fundamental frequencies for laminated composite plates with arbitrary lay-up. The optimal fiber angles of a SSSS square laminated composite plate are $[41^\circ / -55^\circ / 43^\circ / -43^\circ]$, as determined by the BCMO algorithm for 5 call functions. The results of the objective function (OF) for the BCMO algorithm are better than those of the SGA and DE algorithms.

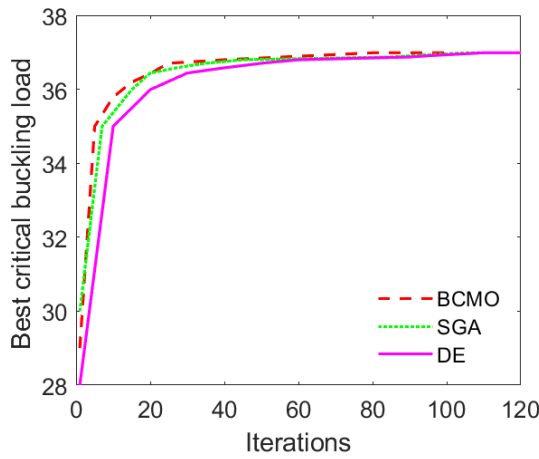
Table 5.10: Optimization critical buckling of SSSS square laminated composite plates with four layers ($a/h=10$, $E_1/E_2=40$, $NP=20$) under uniaxial compression ($N_1^0, N_2^0, N_{12}^0=1,0,0$)

BCs	Iterations	Solution	Max values	$\alpha^{(1)}$	α^2	$\alpha^{(3)}$	$\alpha^{(4)}$	Call function
SSSS	12	Kriging-IPSO [245]	35.4351	36	-37	36	-36	20
	20	Ritz-BCMO	36.9569	37	-33	36	-39	7
		Ritz-SGA	36.9569	37	-33	36	-39	12
		Ritz-DE	36.9569	37	-33	36	-39	25
CSCS	20	Ritz-BCMO	39.3736	33	-85	33	-25	7
		Ritz-SGA	39.3736	33	-85	33	-25	12
		Ritz-DE	39.3736	33	-85	33	-25	25
CCCC	20	Ritz-BCMO	44.6772	-20	75	-70	20	7
		Ritz-SGA	44.6772	-20	75	-70	20	12
		Ritz-DE	44.6772	-20	75	-70	20	25
SFSF	20	Ritz-BCMO	17.1737	36	-16	36	-33	7
		Ritz-SGA	17.1737	36	-16	36	-33	12
		Ritz-DE	17.1737	36	-16	36	-33	25

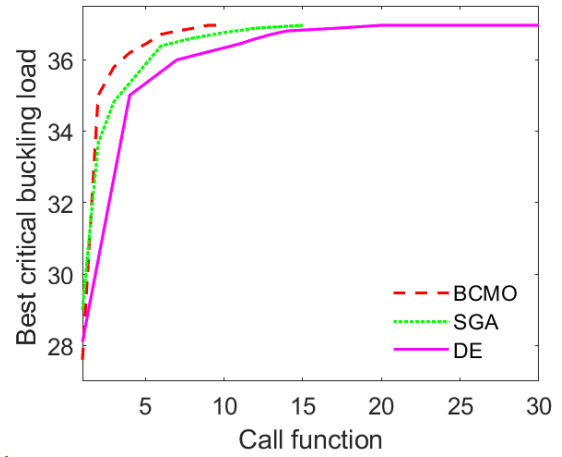
Table 5.11: Optimization fundamental frequencies of SSSS square laminated composite plates with four layers ($a/h=10$, $E_1/E_2=40$, $NP=20$)

BCs	Solution	Theory	Max values	$\alpha^{(1)}$	α^2	$\alpha^{(3)}$	$\alpha^{(4)}$	Call function
SSSS	Asymmetric	Ritz-DE	19.1344	41	-55	43	-43	20
		Ritz-SGA	19.1344	41	-55	43	-43	7
		Ritz-BCMO	19.1344	41	-55	43	-43	5
	Symmetric	Ritz-DE	18.7588	34	-43	-43	34	20
		Ritz-SGA	18.7588	34	-43	-43	34	7
		Ritz-BCMO	18.7588	34	-43	-43	34	5
SFSF	Asymmetric	Ritz-DE	9.0532	-33	40	-39	33	20
		Ritz-SGA	9.0532	-33	40	-39	33	7
		Ritz-BCMO	9.0532	-33	40	-39	33	5
	Symmetric	Ritz-DE	9.9969	30	-37	-37	30	20
		Ritz-SGA	9.9969	30	-37	-37	30	7
		Ritz-BCMO	9.9969	30	-37	-37	30	5
CSCS	Asymmetric	Ritz-DE	21.1601	-34	77	-35	51	20
		Ritz-SGA	21.1601	-34	77	-35	51	7
		Ritz-BCMO	21.1601	-34	77	-35	51	5
	Symmetric	Ritz-DE	21.2345	48	-34	-34	48	20
		Ritz-SGA	21.2345	48	-34	-34	48	7
		Ritz-BCMO	21.2345	48	-34	-34	48	5
CCCC	Asymmetric	Ritz-DE	22.9067	47	-39	33	-49	20
		Ritz-SGA	22.9067	47	-39	33	-49	7
		Ritz-BCMO	22.9067	47	-39	33	-49	5
	Symmetric	Ritz-DE	22.9472	49	-21	-21	49	20
		Ritz-SGA	22.9472	49	-21	-21	49	7
		Ritz-BCMO	22.9472	49	-21	-21	49	5

In order to compare the efficacy of various meta-heuristics, Figs. 5.4 and 5.5 show the convergence histories of natural frequencies and buckling loads of SSSS plates by three different solutions (DE, SGA, and BCMO). It can be seen that the SGA and BCMO algorithms converge faster than the DE one. For the same number of call functions, BCMO has the fewest iterations (Fig. 5.4a), and for the same number of iterations, it also has the fewest call functions (Fig. 5.4b). It should be noted that the comparison is not solely based on computational cost but extends to the effectiveness of the algorithms in achieving optimal solutions. Interestingly, while the call function of BCMO is better than SGA algorithm, their performance varies.



a) Symmetric layers



b) Arbitrary layers

Figure 5.4: Comparison the maximum buckling load (uniaxial compression) of SSSS square laminated composite plates with size population $NP = 20$ ($E_1 / E_2 = 40$)

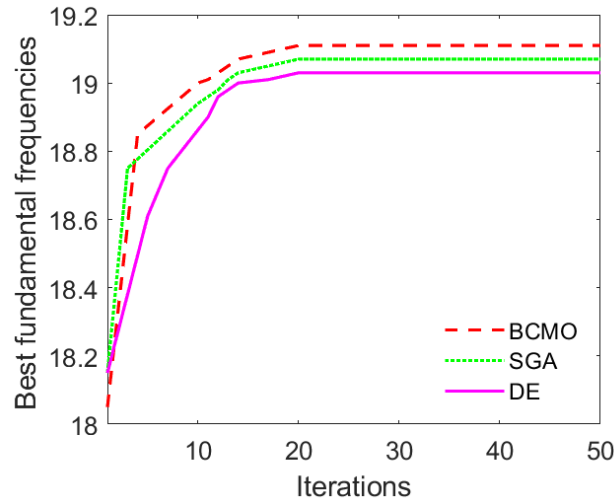
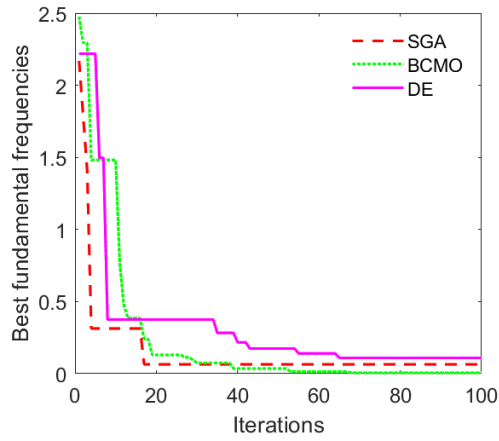
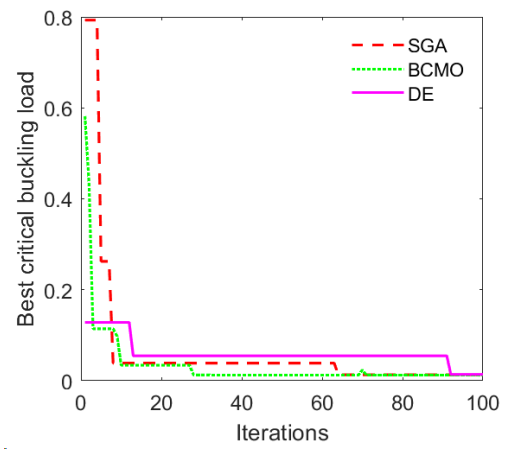


Figure 5.5: Comparison the maximum fundamental frequencies for SSSS square laminated composite plates with size population $NP = 20$ ($E_1 / E_2 = 40$)

The OF convergence histories of three algorithms for different BCs are presented in Figs. 5.6-5.8. The change in BCs from SSSS to CCCC impacts plate stiffness and subsequently affects frequencies and buckling load values. This variation is emphasized in Figs. 5.6 and 5.7, illustrating how these changes impact the numerical results produced by the algorithms.

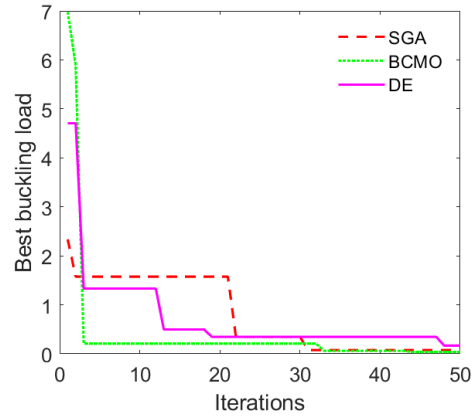
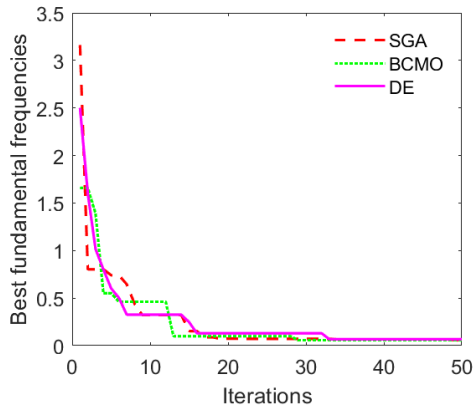


a) The fundamental frequencies

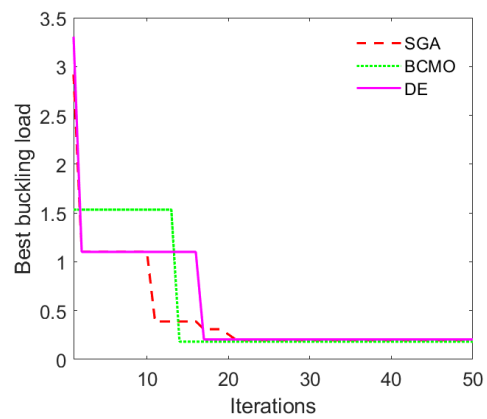
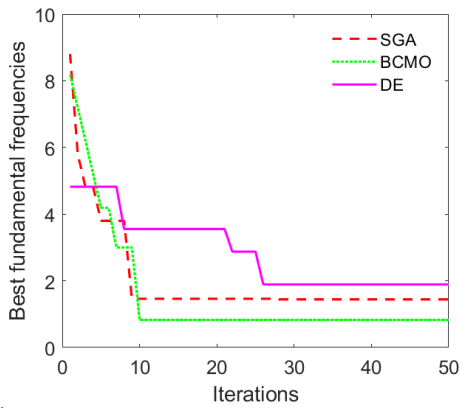


b) Biaxial compression

Figure 5.6: Comparison the minimum results of SSSS square laminated composite plates with size population $NP = 20$ ($E_1 / E_2 = 40$)



a) SSSS



b) CCCC

Figure 5.7: Comparison the minimum results of SSSS and CCCC square laminated composite plates with size population $NP = 50$ ($E_1 / E_2 = 40$)

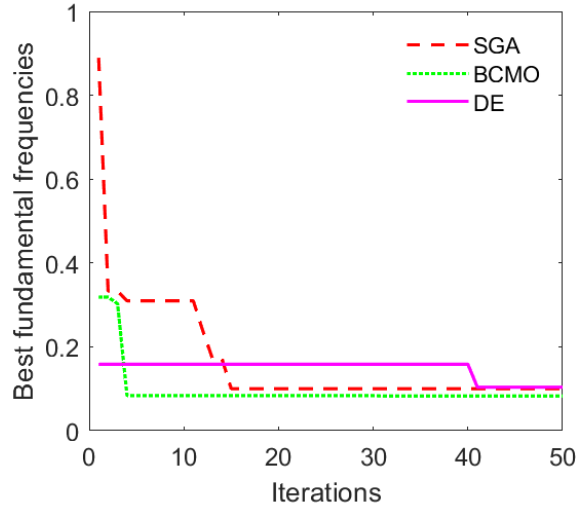


Figure 5.8: Comparison the minimum results for CSCS square laminated composite plates with size population $NP = 50$ ($E_1 / E_2 = 40$)

It is observed that the BCMO consistently attains the optimal solution with notably fewer iterations than the SGA and DE in nearly all cases at the maximum iteration. These findings contribute to understanding the comparative efficiency of meta-heuristic algorithms in tackling complex optimization problems in structural engineering.

5.6. Conclusions

This chapter studies meta-heuristic optimization algorithms for vibration and buckling analysis of laminated composite plates. The theoretical framework incorporates a unified HSDT, Ritz method, BCMO, and SGA. The obtained numerical results showed an efficiency and accuracy of the present theory in predicting the responses of laminated composite plates. The numerical findings demonstrate that:

- The novel hybrid shape functions require only the first six series to achieve the convergence and numerical stability for free vibration and seven for buckling analysis.
- The increase of side to thickness ratios and Young's modulus E_1 / E_2 ratios leads to the rising of the natural frequencies and critical buckling loads of

the laminated composite plates.

- The performance of Ritz-BCMO and Ritz-SGA, which are better than Ritz-DE when compared with the convergence rate and computation cost.
- For simply-supported square laminated composite plate, as determined by the BCMO algorithm, the optimal lay-up for the maximize fundamental frequencies is $[41^\circ / -55^\circ / 43^\circ / -43^\circ]$ and for the maximize buckling loads is $[37^\circ / -33^\circ / 36^\circ / -39^\circ]$.

CHAPTER 6

CONCLUSIONS AND RECOMMENDATIONS

6.1 Conclusions

The dissertation has developed new approximation functions for the Ritz method; developed stochastic models for analysis behaviors of FG, FG sandwich, FGP, PMF plates and microplates; developed two novel intelligent computation algorithms for solving the stochastic problems of microplates; proposed two optimization methods to search the optimal fiber directions of laminated composite plates. The unified higher-order shear deformation theory (HSDT) theory has been formulated to approximate of the displacement field. The modified gradient strain theory (MST) and the modified couple stress theory (MCT) are employed in the analysis of microplates, taking into account their size-dependent behavior. The governing equations of motion are obtained using Hamilton's principle. Convergence and verification studies are conducted to establish the precision of the proposed solution. This study presents numerical results investigating the influence of material distribution, material length scale parameters, porosity density, temperature variations, and boundary conditions on the natural frequencies, critical buckling loads, and deflections of functionally graded microplates. Based on the findings of this study, the following conclusions can be drawn:

- The thesis proposed new computational algorithms, which combined the Ritz method with novels OP, unified HSDT, MCT, and MST theory for analysis of microplates. Based on the findings of this study, the OP-Ritz shape functions proposed in this thesis are suitable for the behaviors analysis of microplates.
- Advanced computational methods for stochastic analysis behaviors of FG, FG sandwich, FGP plate and microplates. The Monte Carlo Simulation (MCS) method was also considered as the exact solution and used to

investigate the performance of the proposed PCE and SC models. The obtained numerical results showed that the PCE and SC give much better computation times than the MCS.

- The dissertation developed two novel intelligent computation algorithms by using the neural network systems (artificial neural network (ANN) and deep neural network (DNN)) integrated with the balancing composite motion optimization (BCMO) and improved BCMO to give the so-called BCMO-ANN and iBCMO-DNN algorithms for solving stochastic problems. The accuracy and efficiency of the proposed BCMO-ANN and iBCMO-DNN algorithms are validated through stochastic behaviors of microplates subjected to uncertainties in material properties.
- Thesis proposed meta-heuristic optimization algorithms (BCMO, SGA) for behaviors analysis of laminated composite plates. The performance the BCMO and SGA algorithms, which are better than a differential evolution (DE) algorithm when compared with the convergence rate and computation cost.

While the current shape functions have demonstrated effectiveness on two-dimensional microplates, their application on three-dimensional plates and microplates poses certain challenges. Furthermore, the present thesis fails to account for the behavioral characteristics of laminated composite microplates in situations where the fiber direction undergoes uncertain variations. The current methodology encounters challenges when dealing with plates that have arbitrary boundary conditions.

6.2. Recommendations

The following are some suggestions for how to proceed with the projected expansion of the study in the future:

- The novel shape functions can be developed to analysis behaviors of laminated composite microplates for two-dimensional and three-dimensional.

- Analysis of skew composite/FG microplates can be developed by extending present methods.
- A nonlinear model based on large displacements, rotations, and the Ritz method should be considered for the analysis of composite and FGP microplates under the arbitrary boundary conditions.
- Address the issue of microplates with periodic boundary conditions.

REFERENCES

1. Do, D.T.T., H. Nguyen-Xuan, and J. Lee, *Material optimization of tri-directional functionally graded plates by using deep neural network and isogeometric multimesh design approach*. Applied Mathematical Modelling, 2020. **87**: p. 501-533.
2. Carrera, E., et al., *Effects of thickness stretching in functionally graded plates and shells*. Composites Part B: Engineering, 2011. **42**(2): p. 123-133.
3. Dai, K.Y., et al., *A mesh-free method for static and free vibration analysis of shear deformable laminated composite plates*. Journal of Sound and Vibration, 2004. **269**(3): p. 633-652.
4. Hughes, T.J.R. and T.E. Tezduyar, *Finite Elements Based Upon Mindlin Plate Theory With Particular Reference to the Four-Node Bilinear Isoparametric Element*. Journal of Applied Mechanics, 1981. **48**(3): p. 587-596.
5. Jean-Louis, B., B. Klaus-JÜRgen, and H. Lee-Wing, *A study of three-node triangular plate bending elements*. International Journal for Numerical Methods in Engineering, 1980. **15**(12): p. 1771-1812.
6. Bletzinger, K.-U., M. Bischoff, and E. Ramm, *A unified approach for shear-locking-free triangular and rectangular shell finite elements*. Computers & Structures, 2000. **75**(3): p. 321-334.
7. Tessler, A. and T.J.R. Hughes, *A three-node mindlin plate element with improved transverse shear*. Computer Methods in Applied Mechanics and Engineering, 1985. **50**(1): p. 71-101.
8. N., D.E. and B. Klaus-Jürgen, *A continuum mechanics based four-node shell element for general non-linear analysis*. Engineering Computations, 1984. **1**(1): p. 77-88.
9. Lee, P.-S. and K.-J. Bathe, *Development of MITC isotropic triangular shell finite elements*. Computers & Structures, 2004. **82**(11): p. 945-962.
10. Lee, Y., K. Yoon, and P.-S. Lee, *Improving the MITC3 shell finite element by using the Hellinger–Reissner principle*. Computers & Structures, 2012. **110-111**: p. 93-106.
11. Jeon, H.-M., P.-S. Lee, and K.-J. Bathe, *The MITC3 shell finite element enriched by interpolation covers*. Computers & Structures, 2014. **134**: p. 128-142.
12. Liu, G.R., K.Y. Dai, and T.T. Nguyen, *A Smoothed Finite Element Method for Mechanics Problems*. Computational Mechanics, 2007. **39**(6): p. 859-877.
13. Nguyen, T.-K., et al., *Static and vibration analysis of isotropic and functionally graded sandwich plates using an edge-based MITC3 finite elements*. Composites Part B: Engineering, 2016. **107**: p. 162-173.
14. Chau-Dinh, T., Q. Nguyen-Duy, and H. Nguyen-Xuan, *Improvement on MITC3 plate finite element using edge-based strain smoothing enhancement for plate analysis*. Acta Mechanica, 2017. **228**(6): p. 2141-2163.
15. Nguyen-Hoang, S., et al., *A combined scheme of edge-based and node-based smoothed finite element methods for Reissner–Mindlin flat shells*. Engineering with Computers, 2016. **32**(2): p. 267-284.
16. Phung-Van, P., et al., *Geometrically nonlinear analysis of functionally graded plates using a cell-based smoothed three-node plate element (CS-MIN3) based on*

- the C0-HSDT*. Computer Methods in Applied Mechanics and Engineering, 2014. **270**: p. 15-36.
17. Phung-Van, P., et al., *A cell-based smoothed discrete shear gap method (CS-DSG3) based on the C0-type higher-order shear deformation theory for static and free vibration analyses of functionally graded plates*. Computational Materials Science, 2013. **79**: p. 857-872.
 18. Nguyen, T.-K., V.-H. Nguyen, and T. Chau-Dinh, *Cell- and Node-Based Smoothing MITC3-Finite Elements for Static and Free Vibration Analysis of Laminated Composite and Functionally Graded Plates*. International Journal of Computational Methods. **0**(0): p. 1850123.
 19. Hughes, T.J.R., J.A. Cottrell, and Y. Bazilevs, *Isogeometric analysis: CAD, finite elements, NURBS, exact geometry and mesh refinement*. Computer Methods in Applied Mechanics and Engineering, 2005. **194**(39): p. 4135-4195.
 20. Hung, P.T., P. Phung-Van, and C.H. Thai, *A refined isogeometric plate analysis of porous metal foam microplates using modified strain gradient theory*. Composite Structures, 2022. **289**: p. 115467.
 21. Cuong-Le, T., Hoang-Le, Minh, Ferreira, A. J. M., Abdel Wahab, Magd, *Small size-effect isogeometric analysis for linear and nonlinear responses of porous metal foam microplate*. Composite Structures, 2022. **285**: p. 115189.
 22. Thai, S., et al., *Post-buckling of functionally graded microplates under mechanical and thermal loads using isogeometric analysis*. Engineering Structures, 2017. **150**: p. 905-917.
 23. Farzam, A. and B. Hassani, *Size-dependent analysis of FG microplates with temperature-dependent material properties using modified strain gradient theory and isogeometric approach*. Composites Part B: Engineering, 2019. **161**: p. 150-168.
 24. Kant, T. and K. Swaminathan, *Analytical solutions for the static analysis of laminated composite and sandwich plates based on a higher order refined theory*. Composite Structures, 2002. **56**(4): p. 329-344.
 25. Joshan, Y.S., N. Grover, and B.N. Singh, *Analytical modelling for thermo-mechanical analysis of cross-ply and angle-ply laminated composite plates*. Aerospace Science and Technology, 2017. **70**: p. 137-151.
 26. Mantari, J.L. and C. Guedes Soares, *Bending analysis of thick exponentially graded plates using a new trigonometric higher order shear deformation theory*. Composite Structures, 2012. **94**(6): p. 1991-2000.
 27. Nguyen, T.-K., T.P. Vo, and H.-T. Thai, *Vibration and buckling analysis of functionally graded sandwich plates with improved transverse shear stiffness based on the first-order shear deformation theory*. Proceedings of the Institution of Mechanical Engineers, Part C: Journal of Mechanical Engineering Science, 2014. **228**(12): p. 2110-2131.
 28. Nguyen, V.-H., et al., *A new inverse trigonometric shear deformation theory for isotropic and functionally graded sandwich plates*. Composites Part B: Engineering, 2014. **66**: p. 233-246.
 29. Atashipour, S.R., U.A. Girhammar, and M. Al-Emrani, *Exact Lévy-type solutions for bending of thick laminated orthotropic plates based on 3-D elasticity and shear deformation theories*. Composite Structures, 2017. **163**: p. 129-151.

30. Bellman, R. and J. Casti, *Differential quadrature and long-term integration*. Journal of Mathematical Analysis and Applications, 1971. **34**(2): p. 235-238.
31. Faghih Shojaei, M. and R. Ansari, *Variational differential quadrature: A technique to simplify numerical analysis of structures*. Applied Mathematical Modelling, 2017. **49**: p. 705-738.
32. Sharma, P., *Efficacy of Harmonic Differential Quadrature method to vibration analysis of FGPM beam*. Composite Structures, 2018. **189**: p. 107-116.
33. Parashar, S.K. and P. Sharma, *Modal analysis of shear-induced flexural vibration of FGPM beam using Generalized Differential Quadrature method*. Composite Structures, 2016. **139**: p. 222-232.
34. Ahmed, S.R., A.B.M. Idris, and M.W. Uddin, *Numerical solution of both ends fixed deep beams*. Computers & Structures, 1996. **61**(1): p. 21-29.
35. Tanigawa, Y., H. Murakami, and Y. Ootao, *TRANSIENT THERMAL STRESS ANALYSIS OF A LAMINATED COMPOSITE BEAM*. Journal of Thermal Stresses, 1989. **12**(1): p. 25-39.
36. Ritz, W., *Über eine neue Methode zur Lösung gewisser Variationsprobleme der mathematischen Physik*. 2023: p. 1-61.
37. Reddy, J.N., *Mechanics of Laminated Composite Plates and Shells: Theory and Analysis*. Second Edition ed. 2003, Boca Raton: CRC Press.
38. Chen, D., J. Yang, and S. Kitipornchai, *Buckling and bending analyses of a novel functionally graded porous plate using Chebyshev-Ritz method*. Archives of Civil and Mechanical Engineering, 2019. **19**(1): p. 157-170.
39. Sun, S., D. Cao, and Q. Han, *Vibration studies of rotating cylindrical shells with arbitrary edges using characteristic orthogonal polynomials in the Rayleigh–Ritz method*. International Journal of Mechanical Sciences, 2013. **68**: p. 180-189.
40. Aydogdu, M., *Free Vibration Analysis of Angle-ply Laminated Beams with General Boundary Conditions*. 2006. **25**(15): p. 1571-1583.
41. Chai Gin, B., *Free vibration of rectangular isotropic plates with and without a concentrated mass*. Computers & Structures, 1993. **48**(3): p. 529-533.
42. Sayyad, A.S. and Y.M. Ghugal, *Modeling and analysis of functionally graded sandwich beams: A review*. Mechanics of Advanced Materials and Structures, 2018: p. 1-20.
43. Khandan, R., et al., *The development of laminated composite plate theories: a review*. Journal of Materials Science, 2012. **47**(16): p. 5901-5910.
44. Nguyen, T.-K., K. Sab, and G. Bonnet, *First-order shear deformation plate models for functionally graded materials*. Composite Structures, 2008. **83**(1): p. 25-36.
45. Mantari, J.L., A.S. Oktem, and C. Guedes Soares, *A new higher order shear deformation theory for sandwich and composite laminated plates*. Composites Part B: Engineering, 2012. **43**(3): p. 1489-1499.
46. Mantari, J.L. and C. Guedes Soares, *Generalized hybrid quasi-3D shear deformation theory for the static analysis of advanced composite plates*. Composite Structures, 2012. **94**(8): p. 2561-2575.
47. He, L., et al., *A size-dependent four variable refined plate model for functionally graded microplates based on modified couple stress theory*. Composite Structures, 2015. **130**: p. 107-115.

48. Farzam, A. and B. Hassani, *Isogeometric analysis of in-plane functionally graded porous microplates using modified couple stress theory*. Aerospace Science and Technology, 2019. **91**: p. 508-524.
49. Thai, C.H., A.J.M. Ferreira, and P. Phung-Van, *Free vibration analysis of functionally graded anisotropic microplates using modified strain gradient theory*. Engineering Analysis with Boundary Elements, 2020. **117**: p. 284-298.
50. Yang, F., et al., *Couple stress based strain gradient theory for elasticity*. International Journal of Solids and Structures, 2002. **39**(10): p. 2731-2743.
51. Lam, D.C.C., et al., *Experiments and theory in strain gradient elasticity*. Journal of the Mechanics and Physics of Solids, 2003. **51**(8): p. 1477-1508.
52. Mindlin, R.D., *Second gradient of strain and surface-tension in linear elasticity*. International Journal of Solids and Structures, 1965. **1**(4): p. 417-438.
53. Mindlin, R.D. and N.N. Eshel, *On first strain-gradient theories in linear elasticity*. International Journal of Solids and Structures, 1968. **4**(1): p. 109-124.
54. Kim, J., K. Żur, and J.N. Reddy, *Bending, free vibration, and buckling of modified couples stress-based functionally graded porous micro-plates*. Composite Structures, 2018. **209**.
55. Fan, F., et al., *Modified couple stress-based geometrically nonlinear oscillations of porous functionally graded microplates using NURBS-based isogeometric approach*. Computer Methods in Applied Mechanics and Engineering, 2020. **372**: p. 113400.
56. Thanh, C.-L., Tran, Loc V., Bui, Tinh Quoc, Nguyen, Hoang X., Abdel-Wahab, M., *Isogeometric analysis for size-dependent nonlinear thermal stability of porous FG microplates*. Composite Structures, 2019. **221**: p. 110838.
57. Guo, L., et al., *Dynamic response of porous E-FGM thick microplate resting on elastic foundation subjected to moving load with acceleration*. Thin-Walled Structures, 2022. **173**: p. 108981.
58. Eringen, A.C., *Nonlocal polar elastic continua*. International Journal of Engineering Science, 1972. **10**(1): p. 1-16.
59. Daneshmehr, A., A. Rajabpoor, and A. Hadi, *Size dependent free vibration analysis of nanoplates made of functionally graded materials based on nonlocal elasticity theory with high order theories*. International Journal of Engineering Science, 2015. **95**: p. 23-35.
60. Ashoori, A.R., E. Salari, and S.A. Sadough Vanini, *Size-dependent thermal stability analysis of embedded functionally graded annular nanoplates based on the nonlocal elasticity theory*. International Journal of Mechanical Sciences, 2016. **119**: p. 396-411.
61. Pham, Q.-H., P.-C. Nguyen, and T. Thanh Tran, *Dynamic response of porous functionally graded sandwich nanoplates using nonlocal higher-order isogeometric analysis*. Composite Structures, 2022. **290**: p. 115565.
62. Aria, A.I. and M.I. Friswell, *Computational hygro-thermal vibration and buckling analysis of functionally graded sandwich microbeams*. Composites Part B: Engineering, 2019. **165**: p. 785-797.
63. Shojaeefard, M.H., et al., *Micro temperature-dependent FG porous plate: Free vibration and thermal buckling analysis using modified couple stress theory with CPT and FSDT*. Applied Mathematical Modelling, 2017. **50**: p. 633-655.

64. Tung, H.V., *Thermal and thermomechanical postbuckling of FGM sandwich plates resting on elastic foundations with tangential edge constraints and temperature dependent properties*. Composite Structures, 2015. **131**: p. 1028-1039.
65. Ma, L.S. and T.J. Wang, *Nonlinear bending and post-buckling of a functionally graded circular plate under mechanical and thermal loadings*. International Journal of Solids and Structures, 2003. **40**(13): p. 3311-3330.
66. Zenkour, A.M. and M. Sobhy, *Thermal buckling of various types of FGM sandwich plates*. Composite Structures, 2010. **93**(1): p. 93-102.
67. Fazzolari, F.A. and E. Carrera, *Thermal Stability of FGM Sandwich Plates Under Various Through-the-Thickness Temperature Distributions*. Journal of Thermal Stresses, 2014. **37**(12): p. 1449-1481.
68. Daikh, A.A. and A. Megueni, *Thermal buckling analysis of functionally graded sandwich plates*. Journal of Thermal Stresses, 2018. **41**(2): p. 139-159.
69. Do, V.N.V. and C.-H. Lee, *Thermal buckling analyses of FGM sandwich plates using the improved radial point interpolation mesh-free method*. Composite Structures, 2017. **177**: p. 171-186.
70. Sahoo, B., et al., *Nonlinear vibration analysis of FGM sandwich structure under thermal loadings*. Structures, 2022. **44**: p. 1392-1402.
71. Mudhaffar, I.M., et al., *Hygro-thermo-mechanical bending behavior of advanced functionally graded ceramic metal plate resting on a viscoelastic foundation*. Structures, 2021. **33**: p. 2177-2189.
72. Daikh, A.A., *Thermal buckling analysis of functionally graded sandwich cylindrical shells*. Advances in aircraft and spacecraft science, 2020. **7**(4).
73. Nazarenko, L., H. Stolarski, and H. Altenbach, *Thermo-elastic properties of random particulate nano-materials for various models of interphase*. International Journal of Mechanical Sciences, 2017. **126**: p. 130-141.
74. Jiang, C., et al., *A new reliability analysis method for uncertain structures with random and interval variables*. International Journal of Mechanics and Materials in Design, 2012. **8**(2): p. 169-182.
75. Mode, C.J. and R.J. Gallop, *A review on Monte Carlo simulation methods as they apply to mutation and selection as formulated in Wright–Fisher models of evolutionary genetics*. Mathematical Biosciences, 2008. **211**(2): p. 205-225.
76. Nguyen, H.X., et al., *Stochastic buckling behaviour of laminated composite structures with uncertain material properties*. Aerospace Science and Technology, 2017. **66**: p. 274-283.
77. Jagtap, K.R., A. Lal, and B.N. Singh, *Stochastic nonlinear bending response of functionally graded material plate with random system properties in thermal environment*. International Journal of Mechanics and Materials in Design, 2012. **8**(2): p. 149-167.
78. Trinh, M.-C., et al., *Stochastic buckling quantification of laminated composite plates using cell-based smoothed finite elements*. Thin-Walled Structures, 2021. **163**: p. 107674.
79. Borges, R.A., et al., *Stochastic eigenfrequency and buckling analyses of plates subjected to random temperature distributions*. Mechanical Systems and Signal Processing, 2021. **147**: p. 107088.

80. Kumar, R.R., et al., *Stochastic buckling analysis of sandwich plates: The importance of higher order modes*. International Journal of Mechanical Sciences, 2019. **152**: p. 630-643.
81. Peng, X., et al., *Uncertainty analysis of composite laminated plate with data-driven polynomial chaos expansion method under insufficient input data of uncertain parameters*. Composite Structures, 2019. **209**: p. 625-633.
82. Umesh, K. and R. Ganguli, *Material Uncertainty Effect on Vibration Control of Smart Composite Plate Using Polynomial Chaos Expansion*. Mechanics of Advanced Materials and Structures, 2013. **20**(7): p. 580-591.
83. Chakraborty, S., et al., *Stochastic free vibration analysis of laminated composite plates using polynomial correlated function expansion*. Composite Structures, 2016. **135**: p. 236-249.
84. Sasikumar, P., et al., *A data driven polynomial chaos based approach for stochastic analysis of CFRP laminated composite plates*. Composite Structures, 2015. **125**: p. 212-227.
85. Shaker, A., et al., *Stochastic finite element analysis of the free vibration of laminated composite plates*. Computational Mechanics, 2008. **41**: p. 493-501.
86. Li, J., et al., *Stochastic thermal buckling analysis of laminated plates using perturbation technique*. Composite Structures, 2016. **139**: p. 1-12.
87. Franco Correia, V.M., et al., *Multiobjective optimization of ceramic-metal functionally graded plates using a higher order model*. Composite Structures, 2018. **183**: p. 146-160.
88. García-Macías, E., et al., *Metamodel-based approach for stochastic free vibration analysis of functionally graded carbon nanotube reinforced plates*. Composite Structures, 2016. **152**.
89. Xiu, D. and J.S. Hesthaven, *High-Order Collocation Methods for Differential Equations with Random Inputs*. SIAM Journal on Scientific Computing, 2005. **27**(3): p. 1118-1139.
90. Truong, T.T., T. Nguyen-Thoi, and J. Lee, *Isogeometric size optimization of bi-directional functionally graded beams under static loads*. Composite Structures, 2019. **227**: p. 111259.
91. Lieu, Q.X. and J. Lee, *A reliability-based optimization approach for material and thickness composition of multidirectional functionally graded plates*. Composites Part B: Engineering, 2019. **164**: p. 599-611.
92. Kaveh, A. and V. Kalatjari, *Topology optimization of trusses using genetic algorithm, force method and graph theory*. International Journal for Numerical Methods in Engineering, 2003. **58**(5): p. 771-791.
93. Khot, N.S., L. Berke, and V.B. Venkayya, *Comparison of Optimality Criteria Algorithms for Minimum Weight Design of Structures*. AIAA Journal, 1979. **17**(2): p. 182-190.
94. Sedaghati, R., *Benchmark case studies in structural design optimization using the force method*. International Journal of Solids and Structures, 2005. **42**(21): p. 5848-5871.
95. Mirjalili, S., *Moth-flame optimization algorithm: A novel nature-inspired heuristic paradigm*. Knowledge-Based Systems, 2015. **89**: p. 228-249.
96. Rashedi, E., H. Nezamabadi-pour, and S. Saryazdi, *GSA: A Gravitational Search Algorithm*. Information Sciences, 2009. **179**(13): p. 2232-2248.

97. Yang, X.-S. *Firefly Algorithms for Multimodal Optimization*. in *Stochastic Algorithms: Foundations and Applications*. 2009. Berlin, Heidelberg: Springer Berlin Heidelberg.
98. Neri, F. and C. Cotta, *Memetic algorithms and memetic computing optimization: A literature review*. *Swarm and Evolutionary Computation*, 2012. **2**: p. 1-14.
99. Dorigo, M. and L.M. Gambardella, *Ant colony system: a cooperative learning approach to the traveling salesman problem*. *IEEE Transactions on Evolutionary Computation*, 1997. **1**(1): p. 53-66.
100. Eberhart, R. and J. Kennedy. *A new optimizer using particle swarm theory*. in *MHS'95. Proceedings of the Sixth International Symposium on Micro Machine and Human Science*. 1995.
101. Storn, R. and K. Price, *Differential Evolution – A Simple and Efficient Heuristic for global Optimization over Continuous Spaces*. *Journal of Global Optimization*, 1997. **11**(4): p. 341-359.
102. Rocke, D.J.J.o.t.A.S.A., *Genetic Algorithms+ Data Structures= Evolution programs (3rd*. 2000. **95**(449): p. 347.
103. Dhiman, G. and V. Kumar, *Spotted hyena optimizer: A novel bio-inspired based metaheuristic technique for engineering applications*. *Advances in Engineering Software*, 2017. **114**: p. 48-70.
104. Do, D.T.T., D. Lee, and J. Lee, *Material optimization of functionally graded plates using deep neural network and modified symbiotic organisms search for eigenvalue problems*. *Composites Part B: Engineering*, 2019. **159**: p. 300-326.
105. Phuc, P.V., et al., *Optimal design of FG sandwich nanoplates using size-dependent isogeometric analysis*. *Mechanics of Materials*, 2019. **142**.
106. Taati, E. and N. Sina, *Multi-objective optimization of functionally graded materials, thickness and aspect ratio in micro-beams embedded in an elastic medium*. *Structural and Multidisciplinary Optimization*, 2018. **58**: p. 1-21.
107. Le-Duc, T., Q.-H. Nguyen, and H. Nguyen-Xuan, *Balancing composite motion optimization*. *Information Sciences*, 2020. **520**: p. 250-270.
108. Thanh Duong, H., et al., *Optimization design of rectangular concrete-filled steel tube short columns with Balancing Composite Motion Optimization and data-driven model*. *Structures*, 2020. **28**: p. 757-765.
109. Khatir, S., et al., *An improved Artificial Neural Network using Arithmetic Optimization Algorithm for damage assessment in FGM composite plates*. *Composite Structures*, 2021. **273**: p. 114287.
110. Sang-To Thanh, L.-M.H., Abdel Wahab Magd, Thanh Cuong Le, *A new metaheuristic algorithm: Shrimp and Goby association search algorithm and its application for damage identification in large-scale and complex structures*. *Advances in Engineering Software*, 2023. **176**: p. 103363.
111. Liu, X., F. Tao, and W. Yu, *A neural network enhanced system for learning nonlinear constitutive law and failure initiation criterion of composites using indirectly measurable data*. *Composite Structures*, 2020. **252**: p. 112658.
112. Liu, X., et al., *A review of artificial neural networks in the constitutive modeling of composite materials*. *Composites Part B: Engineering*, 2021. **224**: p. 109152.
113. Koizumi, M., *FGM activities in Japan*. *Composites Part B: Engineering*, 1997. **28**(1): p. 1-4.

114. Zenkour, A.M. and M.H. Aljadani, *Porosity effect on thermal buckling behavior of actuated functionally graded piezoelectric nanoplates*. European Journal of Mechanics - A/Solids, 2019. **78**: p. 103835.
115. Chi, S.-H. and Y.-L. Chung, *Mechanical behavior of functionally graded material plates under transverse load—Part I: Analysis*. International Journal of Solids and Structures, 2006. **43**(13): p. 3657-3674.
116. Alshabatat, N., K. Myers, and K. Naghshineh, *Design of in-plane functionally graded material plates for optimal vibration performance*. Noise Control Engineering Journal, 2016. **64**: p. 268-278.
117. Li, Q., V.P. Iu, and K.P. Kou, *Three-dimensional vibration analysis of functionally graded material sandwich plates*. Journal of Sound and Vibration, 2008. **311**(1): p. 498-515.
118. Barati, M.R. and A.M. Zenkour, *Investigating post-buckling of geometrically imperfect metal foam nanobeams with symmetric and asymmetric porosity distributions*. Composite Structures, 2017. **182**: p. 91-98.
119. Mindlin, R.D., *Influence of Rotatory Inertia and Shear on Flexural Motions of Isotropic, Elastic Plates*. Journal of Applied Mechanics, 2021. **18**(1): p. 31-38.
120. Sarangan, S. and B.N. Singh, *Higher-order closed-form solution for the analysis of laminated composite and sandwich plates based on new shear deformation theories*. Composite Structures, 2016. **138**: p. 391-403.
121. Thai, H.-T., et al., *A new simple shear deformation plate theory*. Composite Structures, 2017. **171**: p. 277-285.
122. Nguyen, T.N., T.D. Ngo, and H. Nguyen-Xuan, *A novel three-variable shear deformation plate formulation: Theory and Isogeometric implementation*. Computer Methods in Applied Mechanics and Engineering, 2017. **326**: p. 376-401.
123. Nguyen, T.N., C.H. Thai, and H. Nguyen-Xuan, *On the general framework of high order shear deformation theories for laminated composite plate structures: A novel unified approach*. International Journal of Mechanical Sciences, 2016. **110**: p. 242-255.
124. Neves, A.M.A., et al., *Free vibration analysis of functionally graded shells by a higher-order shear deformation theory and radial basis functions collocation, accounting for through-the-thickness deformations*. European Journal of Mechanics - A/Solids, 2013. **37**: p. 24-34.
125. Thai, H.-T., et al., *A quasi-3D hyperbolic shear deformation theory for functionally graded plates*. Acta Mechanica, 2014. **225**(3): p. 951-964.
126. Viola, E. and C. Gentilini, *Thickness Effect on the Dynamic Behavior of Three-Dimensional Plates by using the Ritz Method*, in *Mechanical Vibration: Where do we Stand?*, I. Elishakoff, Editor. 2007, Springer Vienna: Vienna. p. 57-81.
127. Moreno-García, P., J.V.A. dos Santos, and H. Lopes, *A Review and Study on Ritz Method Admissible Functions with Emphasis on Buckling and Free Vibration of Isotropic and Anisotropic Beams and Plates*. Archives of Computational Methods in Engineering, 2018. **25**(3): p. 785-815.
128. Nguyen, T.-K., et al., *Trigonometric-series solution for analysis of laminated composite beams*. Composite Structures, 2017. **160**: p. 142-151.
129. Ding, Z., *NATURAL FREQUENCIES OF RECTANGULAR PLATES USING A SET OF STATIC BEAM FUNCTIONS IN RAYLEIGH-RITZ METHOD*. Journal of Sound and Vibration, 1996. **189**(1): p. 81-87.

130. Lee, L.T. and D.C. Lee, *Free vibration of rectangular plates on elastic point supports with the application of a new type of admissible function*. Computers & Structures, 1997. **65**(2): p. 149-156.
131. Young, D., *Vibration of Rectangular Plates by the Ritz Method*. Journal of Applied Mechanics, 2021. **17**(4): p. 448-453.
132. Kim, Y.-W., *Temperature dependent vibration analysis of functionally graded rectangular plates*. Journal of Sound and Vibration, 2005. **284**(3): p. 531-549.
133. Gartner, J.R. and N. Olgac, *Improved numerical computation of uniform beam characteristic values and characteristic functions*. Journal of Sound and Vibration, 1982. **84**(4): p. 481-489.
134. Pao, Y.C. and K.A. Peterson, *Contour-Plot Simulation of Vibrational and Buckling Mode Shapes of Composite Plates*. Journal of Composite Materials, 1988. **22**(10): p. 935-954.
135. Dasgupta, A. and K.H. Huang, *A Layer-Wise Analysis for Free Vibrations of Thick Composite Spherical Panels*. Journal of Composite Materials, 1997. **31**(7): p. 658-671.
136. Bhat, R.B., *Natural frequencies of rectangular plates using characteristic orthogonal polynomials in rayleigh-ritz method*. Journal of Sound and Vibration, 1985. **102**(4): p. 493-499.
137. Chihara, T.S., *An Introduction to Orthogonal Polynomials*. 1978, London: Gordon and Breach Science Publishers.
138. Song, X., et al., *Traveling wave analysis of rotating cross-ply laminated cylindrical shells with arbitrary boundaries conditions via Rayleigh–Ritz method*. Composite Structures, 2015. **133**: p. 1101-1115.
139. Parashar, S.K. and A. Kumar, *Three-dimensional analytical modeling of vibration behavior of piezoceramic cylindrical shells*. Archive of Applied Mechanics, 2015. **85**(5): p. 641-656.
140. Kim, C.S., P.G. Young, and S.M. Dickinson, *On the flexural vibration of rectangular plates approached by using simple polynomials in the Rayleigh-Ritz method*. Journal of Sound and Vibration, 1990. **143**(3): p. 379-394.
141. Nguyen, T.-K., et al., *Vibration and buckling analysis of functionally graded sandwich beams by a new higher-order shear deformation theory*. Composites Part B: Engineering, 2015. **76**: p. 273-285.
142. Nguyen, T.-K., et al., *An analytical solution for buckling and vibration analysis of functionally graded sandwich beams using a quasi-3D shear deformation theory*. Composite Structures, 2016. **156**: p. 238-252.
143. Aydogdu, M., *Free Vibration Analysis of Angle-ply Laminated Beams with General Boundary Conditions*. Journal of Reinforced Plastics and Composites, 2006. **25**(15): p. 1571-1583.
144. Aydogdu, M., *Buckling analysis of cross-ply laminated beams with general boundary conditions by Ritz method*. Composites Science and Technology, 2006. **66**(10): p. 1248-1255.
145. Mantari, J.L. and F.G. Canales, *Free vibration and buckling of laminated beams via hybrid Ritz solution for various penalized boundary conditions*. Composite Structures, 2016. **152**: p. 306-315.

146. Nguyen, N.-D., T.P. Vo, and T.-K. Nguyen, *An improved shear deformable theory for bending and buckling response of thin-walled FG sandwich I-beams resting on the elastic foundation*. Composite Structures, 2020. **254**: p. 112823.
147. Dey, S., Mukhopadhyay, T., & Adhikari, S., *Uncertainty Quantification in Laminated Composites: A Meta-model Based Approach (1st ed.)*. 2019: CRC Press.
148. Xiu, D. and G. Karniadakis, *The Wiener--Askey Polynomial Chaos for Stochastic Differential Equations*. SIAM J. Sci. Comput., 2002. **24**: p. 619-644.
149. Crestaux, T., O. Le Maître, and J.-M. Martinez, *Polynomial chaos expansion for sensitivity analysis*. Reliability Engineering & System Safety, 2009. **94**(7): p. 1161-1172.
150. Nobile, F., R. Tempone, and C.G. Webster, *An Anisotropic Sparse Grid Stochastic Collocation Method for Partial Differential Equations with Random Input Data*. SIAM Journal on Numerical Analysis, 2008. **46**(5): p. 2411-2442.
151. Nobile, F., R. Tempone, and C.G. Webster, *A Sparse Grid Stochastic Collocation Method for Partial Differential Equations with Random Input Data*. SIAM Journal on Numerical Analysis, 2008. **46**(5): p. 2309-2345.
152. Mandic, D.a.C., Jonathon, *Recurrent neural networks for prediction: learning algorithms, architectures and stability*. 2001: Wiley.
153. Xavier, G. and B. Yoshua, *Understanding the difficulty of training deep feedforward neural networks*. PMLR. p. 249-256.
154. Gao, C., et al., *Long short-term memory-based deep recurrent neural networks for target tracking*. Information Sciences, 2019. **502**: p. 279-296.
155. Makridakis, S., et al., *The accuracy of extrapolation (time series) methods: Results of a forecasting competition*. Journal of Forecasting, 1982. **1**(2): p. 111-153.
156. Apicella, A., et al., *A survey on modern trainable activation functions*. Neural Networks, 2021. **138**: p. 14-32.
157. Russell Reed, R.J.M.I., *Neural Smithing: Supervised Learning in Feedforward Artificial Neural Networks*. 1999: Mit Press.
158. Makridakis, S., et al., *The accuracy of extrapolation (time series) methods: Results of a forecasting competition*. 1982. **1**(2): p. 111-153.
159. Riedmiller, M. and H. Braun. *A direct adaptive method for faster backpropagation learning: the RPROP algorithm*. in *IEEE International Conference on Neural Networks*. 1993.
160. H. Robbins, a.S.M., *A Stochastic Approximation Method*. The Annals of Mathematical Statistics, 1951. **22** p. 400-407.
161. Duchi, J., E. Hazan, and Y. Singer, *Adaptive Subgradient Methods for Online Learning and Stochastic Optimization*. 2011. **12**(null %J J. Mach. Learn. Res.): p. 2121-2159.
162. Kingma, D. and J. Ba, *Adam: A Method for Stochastic Optimization*. International Conference on Learning Representations, 2014.
163. Hinton, G.E., *A Practical Guide to Training Restricted Boltzmann Machines*, in *Neural Networks: Tricks of the Trade: Second Edition*, G. Montavon, G.B. Orr, and K.-R. Müller, Editors. 2012, Springer Berlin Heidelberg: Berlin, Heidelberg. p. 599-619.
164. Abdel-Basset, M., L. Abdel-Fatah, and A.K. Sangaiah, *Chapter 10 - Metaheuristic Algorithms: A Comprehensive Review*, in *Computational Intelligence for*

- Multimedia Big Data on the Cloud with Engineering Applications*, A.K. Sangaiah, M. Sheng, and Z. Zhang, Editors. 2018, Academic Press. p. 185-231.
165. Storn, R. and K. Price, *Differential evolution—a simple and efficient heuristic for global optimization over continuous spaces*. Journal of global optimization, 1997. **11**(4): p. 341-359.
 166. Fleetwood, K. *An introduction to differential evolution*. in *Proceedings of Mathematics and Statistics of Complex Systems (MASCOS) One Day Symposium, 26th November, Brisbane, Australia*. 2004.
 167. Banhart, J., *Manufacture, characterisation and application of cellular metals and metal foams*. Progress in Materials Science, 2001. **46**(6): p. 559-632.
 168. Salimon, A., et al., *Potential applications for steel and titanium metal foams*. Journal of Materials Science, 2005. **40**(22): p. 5793-5799.
 169. Wu, H., J. Yang, and S. Kitipornchai, *Mechanical Analysis of Functionally Graded Porous Structures: A Review*. International Journal of Structural Stability and Dynamics, 2020. **20**(13): p. 2041015.
 170. Saber, A.Y., Saidi, Ali Reza, Bahaadini, Reza, *Accurate solution for size-dependent free vibration analysis of functionally graded micro-plates with Levy boundary conditions*. Proceedings of the Institution of Mechanical Engineers, Part C: Journal of Mechanical Engineering Science, 2022. **236**(13): p. 7368-7386.
 171. Tran, V.-T., Nguyen, Trung-Kien, Nguyen, Phong T. T, Vo, Thuc P., *Stochastic vibration and buckling analysis of functionally graded microplates with a unified higher-order shear deformation theory*. Thin-Walled Structures, 2022. **177**: p. 109473.
 172. Tran, V.-T., Nguyen, Trung-Kien, Nguyen, Phong T. T., Vo, Thuc P., *Stochastic collocation method for thermal buckling and vibration analysis of functionally graded sandwich microplates*. Journal of Thermal Stresses, 2023. **46**(9): p. 909-934.
 173. Wang, Y.Q. and Z.Y. Zhang, *Bending and buckling of three-dimensional graphene foam plates*. Results in Physics, 2019. **13**: p. 102136.
 174. Pham-Tan, H., C.H. Thai, and P. Phung-Van, *NURBS-based refined plate theory for metal foam plates with porosities*. Thin-Walled Structures, 2022. **175**: p. 109246.
 175. Tu, T.M., Hoa, Le Kha, Hung, Dang Xuan, Hai, Le Thanh, *Nonlinear buckling and post-buckling analysis of imperfect porous plates under mechanical loads*. Journal of Sandwich Structures & Materials, 2018. **22**(6): p. 1910-1930.
 176. Sobhy, M., A.M. Zenkour, and M.A. Abazid, *Hygrothermal wave dispersion analysis of metal foam microplates strengthened by graphene embedded in a viscoelastic medium under 2D magnetic field effect*. Mechanics of Advanced Materials and Structures, 2022. **29**(28): p. 7592-7604.
 177. Shimpi, R.P., *Zeroth-Order Shear Deformation Theory for Plates*. 1999. **37**(4): p. 524-526.
 178. Ray, M.C., *Zeroth-Order Shear Deformation Theory for Laminated Composite Plates*. Journal of Applied Mechanics, 2003. **70**(3): p. 374-380.
 179. Reissner, E., *On transverse bending of plates, including the effect of transverse shear deformation*. International Journal of Solids and Structures, 1975. **11**(5): p. 569-573.

180. Shi, G., K.Y. Lam, and T.E. Tay, *On efficient finite element modeling of composite beams and plates using higher-order theories and an accurate composite beam element*. Composite Structures, 1998. **41**(2): p. 159-165.
181. Reddy, J.N., *A Simple Higher-Order Theory for Laminated Composite Plates*. Journal of Applied Mechanics, 1984. **51**(4): p. 745-752.
182. Tran, V.-T., et al., *Static and vibration analysis of functionally graded microplate with porosities based on higher-order shear deformation and modified strain gradient theory*. Vietnam Journal of Mechanics, 2023.
183. Van-Hau Nguyen, V.-T.T., Trung Kien Nguyen, *A BCMO-DNN algorithm for vibration optimization of functionally graded porous microplates*, in *Tuyển tập công trình khoa học Hội nghị Cơ học toàn quốc lần thứ XI (NACOME 2022)*. 2022, Nhà xuất bản Khoa học tự nhiên và Công nghệ. p. 577-588.
184. Sobhy, M., *Buckling and free vibration of exponentially graded sandwich plates resting on elastic foundations under various boundary conditions*. Composite Structures, 2013. **99**: p. 76-87.
185. Thai, C.H., et al., *An efficient size-dependent computational approach for functionally graded isotropic and sandwich microplates based on modified couple stress theory and moving Kriging-based meshfree method*. International Journal of Mechanical Sciences, 2018. **142-143**: p. 322-338.
186. thai Hoang, C., et al., *An efficient size-dependent computational approach for functionally graded isotropic and sandwich microplates based on modified couple stress theory and moving Kriging-based meshfree method*. International Journal of Mechanical Sciences, 2018. **142**.
187. Daikh, A.A. and A. Megueni, *Thermal buckling analysis of functionally graded sandwich plates*. Journal of Thermal Stresses, 2018. **41**(2): p. 139-159.
188. Thai, H.-T. and S.-E. Kim, *A size-dependent functionally graded Reddy plate model based on a modified couple stress theory*. Composites Part B: Engineering, 2013. **45**(1): p. 1636-1645.
189. Nguyen, H.X., et al., *A refined quasi-3D isogeometric analysis for functionally graded microplates based on the modified couple stress theory*. Computer Methods in Applied Mechanics and Engineering, 2017. **313**: p. 904-940.
190. Thai, S., et al., *Size-dependant behaviour of functionally graded microplates based on the modified strain gradient elasticity theory and isogeometric analysis*. Computers & Structures, 2017. **190**: p. 219-241.
191. Thai, C.H., A.J.M. Ferreira, and H. Nguyen-Xuan, *Isogeometric analysis of size-dependent isotropic and sandwich functionally graded microplates based on modified strain gradient elasticity theory*. Composite Structures, 2018. **192**: p. 274-288.
192. Tran, V.-T., et al., *Vibration and buckling optimization of functionally graded porous microplates using BCMO-ANN algorithm*. Thin-Walled Structures, 2023. **182**: p. 110267.
193. Tran, V.-T., T.-K. Nguyen, and H. Nguyen-Xuan, *An intelligent computational iBCMO-DNN algorithm for stochastic thermal buckling analysis of functionally graded porous microplates using modified strain gradient theory*. Journal of Thermal Stresses, 2024. **47**(9): p. 1188-1227.
194. Reddy, J.N., *Mechanics of Laminated Composite Plates and Shells*. 2nd Edition ed. 2003, Boca Raton: CRC Press.

195. Zhang, B., et al., *An efficient size-dependent plate theory for bending, buckling and free vibration analyses of functionally graded microplates resting on elastic foundation*. Applied Mathematical Modelling, 2015. **39**(13): p. 3814-3845.
196. Zenkour, A.M. and A.F. Radwan, *Hygrothermo-mechanical buckling of FGM plates resting on elastic foundations using a quasi-3D model*. International Journal for Computational Methods in Engineering Science and Mechanics, 2019. **20**(2): p. 85-98.
197. Yaghoobi, H. and M. Torabi, *Exact Solution for Thermal Buckling of Functionally Graded Plates Resting on Elastic Foundations with Various Boundary Conditions*. Journal of Thermal Stresses, 2013. **36**(9): p. 869-894.
198. Thai, H.-T., et al., *A review of continuum mechanics models for size-dependent analysis of beams and plates*. Composite Structures, 2017. **177**: p. 196-219.
199. Ashjari, M. and M.R. Khoshnavan, *Mass optimization of functionally graded plate for mechanical loading in the presence of deflection and stress constraints*. Composite Structures, 2014. **110**: p. 118-132.
200. Lieu, Q.X., et al., *Shape and size optimization of functionally graded sandwich plates using isogeometric analysis and adaptive hybrid evolutionary firefly algorithm*. Thin-Walled Structures, 2018. **124**: p. 588-604.
201. Moita, J.S., et al., *Material distribution and sizing optimization of functionally graded plate-shell structures*. Composites Part B: Engineering, 2018. **142**: p. 263-272.
202. Tran, T.T., P.-C. Nguyen, and Q.-H. Pham, *Vibration analysis of FGM plates in thermal environment resting on elastic foundation using ES-MITC3 element and prediction of ANN*. Case Studies in Thermal Engineering, 2021. **24**: p. 100852.
203. Stoffel, M., F. Bamer, and B. Markert, *Artificial neural networks and intelligent finite elements in non-linear structural mechanics*. Thin-Walled Structures, 2018. **131**: p. 102-106.
204. Lu, X., et al., *A data-driven computational homogenization method based on neural networks for the nonlinear anisotropic electrical response of graphene/polymer nanocomposites*. Computational Mechanics, 2019. **64**(2): p. 307-321.
205. Sudret, B., *Global sensitivity analysis using polynomial chaos expansions*. Reliability Engineering & System Safety, 2008. **93**(7): p. 964-979.
206. Marquardt, D.W., *An Algorithm for Least-Squares Estimation of Nonlinear Parameters*. Journal of the Society for Industrial and Applied Mathematics, 1963. **11**(2): p. 431-441.
207. Levenberg, K., *A METHOD FOR THE SOLUTION OF CERTAIN NON-LINEAR PROBLEMS IN LEAST SQUARES*. Quarterly of Applied Mathematics, 1944. **2**(2): p. 164-168.
208. Szandala, T., *Review and Comparison of Commonly Used Activation Functions for Deep Neural Networks*. 2021. p. 203-224.
209. Van Houdt, G., C. Mosquera, and G. Nápoles, *A Review on the Long Short-Term Memory Model*. Artificial Intelligence Review, 2020. **53**.
210. Bahreyni, B. and C. Shafai, *Application of twin-beam structures for estimation of material properties and sensor fabrication*. Canadian Journal of Electrical and Computer Engineering, 2006. **31**(2): p. 85-88.

211. Bargatin, I., I. Kozinsky, and M.L. Roukes, *Efficient electrothermal actuation of multiple modes of high-frequency nanoelectromechanical resonators*. Applied Physics Letters, 2007. **90**(9): p. 093116.
212. Jalili, N. and K. Laxminarayana, *A review of atomic force microscopy imaging systems: application to molecular metrology and biological sciences*. Mechatronics, 2004. **14**(8): p. 907-945.
213. Ozevin, D., *10 - Micro-electro-mechanical-systems (MEMS) for assessing and monitoring civil infrastructures*, in *Sensor Technologies for Civil Infrastructures*, M.L. Wang, J.P. Lynch, and H. Sohn, Editors. 2014, Woodhead Publishing. p. 265-302e.
214. Ilic, B.C., H. G. Krylov, S. Senaratne, W. Ober, C. Neuzil, P., *Attogram detection using nanoelectromechanical oscillators*. Journal of Applied Physics, 2004. **95**(7): p. 3694-3703.
215. Voß, S. *Meta-heuristics: The State of the Art*. in *Local Search for Planning and Scheduling*. 2001. Berlin, Heidelberg: Springer Berlin Heidelberg.
216. Karakaya, Ş. and Ö. Soykasap, *Buckling optimization of laminated composite plates using genetic algorithm and generalized pattern search algorithm*. Structural and Multidisciplinary Optimization, 2009. **39**(5): p. 477.
217. Ho-Huu, V.D.-T., T. D. Dang-Trung, H. Vo-Duy, T. Nguyen-Thoi, T., *Optimization of laminated composite plates for maximizing buckling load using improved differential evolution and smoothed finite element method*. Composite Structures, 2016. **146**: p. 132-147.
218. Kalantari, M., C. Dong, and I.J. Davies, *Effect of matrix voids, fibre misalignment and thickness variation on multi-objective robust optimization of carbon/glass fibre-reinforced hybrid composites under flexural loading*. Composites Part B: Engineering, 2017. **123**: p. 136-147.
219. Drosopoulos, G.A., C. Gogos, and G. Foutsitzi, *Multi-objective optimization for maximum fundamental frequency and minimum cost of hybrid graphene/fibre-reinforced nanocomposite laminates*. Structures, 2023. **54**: p. 1593-1607.
220. Dorigo, M., M. Birattari, and T. Stutzle, *Ant colony optimization*. IEEE computational intelligence magazine, 2006. **1**(4): p. 28-39.
221. Mirjalili, S., *Dragonfly algorithm: a new meta-heuristic optimization technique for solving single-objective, discrete, and multi-objective problems*. Neural computing and applications, 2016. **27**(4): p. 1053-1073.
222. Kennedy, J. and R. Eberhart. *Particle swarm optimization*. in *Proceedings of ICNN'95-international conference on neural networks*. 1995. IEEE.
223. Mirjalili, S.G., Amir H. Mirjalili, Seyedeh Zahra Saremi, Shahrzad Faris, Hossam Mirjalili, Seyed Mohammad, *Salp Swarm Algorithm: A bio-inspired optimizer for engineering design problems*. Advances in Engineering Software, 2017. **114**: p. 163-191.
224. Shafei, E., A. Shirzad, and T. Rabczuk, *Dynamic stability optimization of laminated composite plates: An isogeometric HSDT formulation and PSO algorithm*. Composite Structures, 2022. **280**: p. 114935.
225. Vosoughi, A.R., Darabi, A. Anjabin, N. Topal, U., *A mixed finite element and improved genetic algorithm method for maximizing buckling load of stiffened laminated composite plates*. Aerospace Science and Technology, 2017. **70**: p. 378-387.

226. Vosoughi, A.R., Darabi, A., Dehghani Forkhorji, H., *Optimum stacking sequences of thick laminated composite plates for maximizing buckling load using FE-GAs-PSO*. Composite Structures, 2017. **159**: p. 361-367.
227. Moghaddam, F.F., R.F. Moghaddam, and M. Cheriet, *Curved space optimization: a random search based on general relativity theory*. arXiv preprint arXiv:1208.2214, 2012.
228. Zheng, Y.-J., *Water wave optimization: a new nature-inspired metaheuristic*. Computers & Operations Research, 2015. **55**: p. 1-11.
229. Tran, V.-T., et al., *Meta-heuristic optimization algorithms for vibration and buckling analysis of laminated composite plates*. Engineering Analysis with Boundary Elements, 2024. **169**: p. 105974.
230. Nguyen, T.-K., Truong-Phong Nguyen, T. , Vo, Thuc P., Thai, Huu-Tai, *Vibration and buckling analysis of functionally graded sandwich beams by a new higher-order shear deformation theory*. Composites Part B: Engineering, 2015. **76**: p. 273-285.
231. Reddy, J.N.J.B.R., FL: CRC Press, . *Mechanics of laminated composite plates-Theory and analysis(Book)*. 1997.
232. Liu, L., L.P. Chua, and D.N. Ghista, *Mesh-free radial basis function method for static, free vibration and buckling analysis of shear deformable composite laminates*. Composite Structures, 2007. **78**(1): p. 58-69.
233. Thai, C.H., Tran, Loc V., Tran, Dung T., Nguyen-Thoi, T., Nguyen-Xuan, H., *Analysis of laminated composite plates using higher-order shear deformation plate theory and node-based smoothed discrete shear gap method*. Applied Mathematical Modelling, 2012. **36**(11): p. 5657-5677.
234. Zhen, W. and C. Wanji, *Free vibration of laminated composite and sandwich plates using global–local higher-order theory*. Journal of Sound and Vibration, 2006. **298**(1): p. 333-349.
235. Ferreira, A.J.M. and G.E. Fasshauer, *Analysis of natural frequencies of composite plates by an RBF-pseudospectral method*. Composite Structures, 2007. **79**(2): p. 202-210.
236. Ferreira, A.J.M., L.M.S. Castro, and S. Bertoluzza, *A high order collocation method for the static and vibration analysis of composite plates using a first-order theory*. Composite Structures, 2009. **89**(3): p. 424-432.
237. Noor, A.K., *Free vibrations of multilayered composite plates*. AIAA Journal, 1973. **11**(7): p. 1038-1039.
238. Thai, H.-T. and S.-E. Kim, *Free vibration of laminated composite plates using two variable refined plate theory*. International Journal of Mechanical Sciences, 2010. **52**(4): p. 626-633.
239. Thanh, C.-L., A.J.M. Ferreira, and M. Abdel Wahab, *A refined size-dependent couple stress theory for laminated composite micro-plates using isogeometric analysis*. Thin-Walled Structures, 2019. **145**: p. 106427.
240. Thai, C.H., Ferreira, A. J. M., Bordas, S. P. A., Rabczuk, T., Nguyen-Xuan, H., *Isogeometric analysis of laminated composite and sandwich plates using a new inverse trigonometric shear deformation theory*. European Journal of Mechanics - A/Solids, 2014. **43**: p. 89-108.

241. Khdeir, A.A. and L. Librescu, *Analysis of symmetric cross-ply laminated elastic plates using a higher-order theory: Part II—Buckling and free vibration*. Composite Structures, 1988. **9**(4): p. 259-277.
242. Thai, C.H., Nguyen-Xuan, H., Bordas, S. P. A., Nguyen-Thanh, N., Rabczuk, T., *Isogeometric Analysis of Laminated Composite Plates Using the Higher-Order Shear Deformation Theory*. Mechanics of Advanced Materials and Structures, 2015. **22**(6): p. 451-469.
243. Keshtegar, B., Nguyen-Thoi, Trung, Truong, Tam T., Zhu, Shun-Peng, *Optimization of buckling load for laminated composite plates using adaptive Kriging-improved PSO: A novel hybrid intelligent method*. Defence Technology, 2021. **17**(1): p. 85-99.
244. Ho-Huu, V., et al., *Optimization of laminated composite plates for maximizing buckling load using improved differential evolution and smoothed finite element method*. Composite Structures, 2016. **146**: p. 132-147.
245. Keshtegar, B., et al., *Optimization of buckling load for laminated composite plates using adaptive Kriging-improved PSO: A novel hybrid intelligent method*. Defence Technology, 2021. **17**(1): p. 85-99.

LIST OF PUBLICATIONS

I. Tạp chí khoa học trong danh mục WoS (SCIE, SSCI, AHCI, ESCI)

1. **Van-Thien Tran**, Trung-Kien Nguyen, P. T. T. Nguyen, and T. P. Vo, Stochastic collocation method for thermal buckling and vibration analysis of functionally graded sandwich microplates, Journal of Thermal Stresses, vol. 46, p. 909-934, 6/2023, **SCIE (Q2)**.
<https://doi.org/10.1080/01495739.2023.2217243>
2. **Van-Thien Tran**, Trung-Kien Nguyen, H. Nguyen-Xuan, Magd Abdel Wahab, Vibration and buckling optimization of porous functionally graded microplates using BCMO-ANN algorithm, Thin-Walled Structures, Thin-Walled Structures, vol. 182, p. 110267, 01/2023, **SCIE (Q1)**.
<https://doi.org/10.1016/j.tws.2022.110267>
3. **Van-Thien Tran**, Trung-Kien Nguyen, P. T. T. Nguyen, and T. P. Vo, Stochastic vibration and buckling analysis of functionally graded microplates with a unified higher-order shear deformation theory, Thin-Walled Structures, vol. 177, p.109473, 8/ 2022, **SCIE (Q1)**.
<https://doi.org/10.1016/j.tws.2022.109473>
4. **Van-Thien Tran**, Trung-Kien Nguyen, H. Nguyen-Xuan, An intelligent computational iBCMO-DNN algorithm for stochastic thermal buckling analysis of functionally graded porous microplates using modified strain gradient theory, Journal of Thermal Stresses, online, 7/2024, **SCIE (Q2)**.
<https://doi.org/10.1080/01495739.2024.2368054>
5. **Van-Thien Tran**, Trung-Kien Nguyen, H. Nguyen-Xuan, T. P. Vo, Meta-heuristic optimization algorithms for vibration and buckling analysis of laminated composite plates, Engineering Analysis with Boundary Elements, vol.169, Part A, 12/ 2024, 105974, **SCIE (Q1)**.
<https://doi.org/10.1016/j.enganabound.2024.105974>
6. **Van-Thien Tran**, Trung-Kien Nguyen, Van-Hau Nguyen, Thuc P. Vo, Novel computational algorithms for vibration, buckling, and transient analysis of porous metal foam microplates, Journal of Vibration Engineering & Technologies, 13, 203 (2025), **SCIE (Q2)**.
<https://doi.org/10.1007/s42417-024-01748-8>

II. Tạp chí khoa học trong danh mục Scopus

III. Tạp chí khoa học quốc tế có ISSN, có phản biện nhưng chưa xếp hạng WoS/Sopus

1. **Van-Thien Tran**, Van-Hau Nguyen, Trung-Kien Nguyen, T. P. Vo, Static and vibration analysis of functionally graded microplate with porosities based on higher-order shear deformation and modified strain gradient theory, Vietnam Journal of Mechanics, 2023, **ACI**.
<https://doi.org/10.15625/0866-7136/17552>

IV. Kỷ yếu hội nghị khoa học quốc tế có phản biện và có ISBN

1. **Van-Thien Tran**, Trung-Kien Nguyen, Van-Hau Nguyen, An Efficient Size-Dependent Computational Approach for Functionally Graded Porous Sandwich Microplates Based on Modified Couple Stress Theory, International Conference on Green Technology and Sustainable Development (GTSD 2022), Lecture Notes in Networks and Systems, vol 567, 82-96, 2023, **Scopus index (Q4)**.
https://doi.org/10.1007/978-3-031-19694-2_8
2. **Van-Thien Tran**, Trung-Kien Nguyen, A general framework of higher-order shear deformation theory for free vibration analysis of functionally graded microplates, Proceedings of the Second International Conference on Sustainable Civil Engineering and Architecture (ICSCEA-2021), Lecture Notes in Civil Engineering, vol.268, 713–727 2023, **Scopus index (Q4)**.
https://doi.org/10.1007/978-981-19-3303-5_64

V. Kỷ yếu hội nghị khoa học quốc gia có phản biện và có ISBN

1. Van-Hau Nguyen, **Van-Thien Tran**, Trung Kien Nguyen, A BCMO-DNN algorithm for vibration optimization of functionally graded porous microplates, Tuyển tập công trình khoa học Hội nghị Cơ học toàn quốc lần thứ XI (NACOME 2022), Nhà xuất bản Khoa học tự nhiên và Công nghệ, Tập 1, 577-588, 2022.